

Kern- und Teilchenphysik

**From Exotic Charmonia
to Scalar Glueballs
Light Hadron Final States at BESIII**

Inaugural-Dissertation
zur Erlangung des Doktorgrades
der Naturwissenschaften im Fachbereich Physik
der Mathematisch-Naturwissenschaftlichen Fakultät
der Westfälischen Wilhelms-Universität Münster

vorgelegt von
JOHANNES BLOMS
aus GEESTE

Münster 2021

Dekan:	Prof. Dr. Michael Rohlfing
Erster Gutachter:	Prof. Dr. Alfons Khoukaz
Zweiter Gutachter:	Prof. Dr. Anton Andronic

Tag der mündlichen Prüfung:

Tag der Promotion:

Abstract

Using data at 32 center-of-mass energies between $\sqrt{s} = 3.7730$ GeV and $\sqrt{s} = 4.7008$ GeV with an integrated luminosity of 22.7 fb^{-1} collected in e^+e^- annihilations with the BESIII detector, a precise determination of the Born cross sections $\sigma_b(e^+e^- \rightarrow \phi K^+K^-)$, $\sigma_b(e^+e^- \rightarrow \phi K_S^0 K_S^0)$ and $\sigma_b(e^+e^- \rightarrow p\bar{p}\eta')$ was performed for the first time in this energy regime.

In the first part of this thesis, the final states ϕK^+K^- and $\phi K_S^0 K_S^0$ were investigated. While the ϕ meson is reconstructed in its decay to K^+K^- , the K_S^0 meson is reconstructed in its decay to $\pi^+\pi^-$. In both channels, the ϕ meson was observed as a significant resonant structure on top of low background contributions. A partial wave analysis was carried out in order to perform a global reconstruction and selection efficiency correction. Born cross sections were determined, including statistical as well as systematic uncertainties. In the search for couplings of (exotic) vector charmonia to the $\phi K\bar{K}$ final state, a maximum likelihood fit was applied. Since no significant resonant contribution was observed, upper limits were calculated at 90% confidence level for various vector states.

In addition, the $K\bar{K}$ system recoiling off the ϕ meson was investigated using the data set at $\sqrt{s} = m_{\psi(2S)}$. Here, a formalism based on unitarity and analyticity was employed in order to properly describe the dynamical parts of the amplitudes of the present resonances in the scalar isoscalar sector. Also, the branching ratios $\mathcal{B}r(\psi(2S) \rightarrow \phi K^+K^-)$ and $\mathcal{B}r(\psi(2S) \rightarrow \phi K_S^0 K_S^0)$ were determined to be $(9.58_{-0.14}^{+0.14} \pm 0.45) \cdot 10^{-5}$ and $(3.45_{-0.13}^{+0.14} \pm 0.11) \cdot 10^{-5}$, respectively.

In the second part of this thesis, the final state $p\bar{p}\eta'$ was studied using the same data as above. The η' meson was reconstructed in its decays to $\eta\pi^+\pi^-$ and $\gamma\pi^+\pi^-$, while subsequent η mesons are reconstructed in $\gamma\gamma$. In both channels, the η' meson was significantly observed in the integrated data sample. Combined Born cross sections were determined for the first time in this energy regime, taking correlated systematic uncertainties between the channels and the data sets into account. The significance of a resonant contribution of the $\psi(4230)$ to the $p\bar{p}\eta'$ final state is 2.43σ . The data is in agreement with a resonant production of the $p\bar{p}$ pair via an intermediate J/ψ resonance, if the final state $p\bar{p}\eta'$ is produced via a resonant $\psi(4230)$.

Zusammenfassung

Unter Verwendung von Daten bei 32 Schwerpunktsenergien zwischen $\sqrt{s} = 3.7730$ GeV und $\sqrt{s} = 4.7008$ GeV mit einer integrierten Luminosität von 22.7 fb^{-1} , die in e^+e^- -Annihilationen mit dem BESIII-Detektor gesammelt wurden, wurde eine präzise Bestimmung der Bornschen Wirkungsquerschnitte $\sigma_b(e^+e^- \rightarrow \phi K^+ K^-)$, $\sigma_b(e^+e^- \rightarrow \phi K_S^0 K_S^0)$ und $\sigma_b(e^+e^- \rightarrow p\bar{p}\eta')$ zum ersten Mal in diesem Energiebereich durchgeführt.

Im ersten Teil dieser Arbeit wurden die Endzustände $\phi K^+ K^-$ und $\phi K_S^0 K_S^0$ untersucht. Während das ϕ -Meson im Zerfall nach $K^+ K^-$ rekonstruiert wurde, wurde das K_S^0 -Meson im Zerfall nach $\pi^+ \pi^-$ rekonstruiert. In beiden Kanälen wurde das ϕ -Meson als signifikante Resonanz mit geringen Untergrundbeiträgen beobachtet. Es wurde eine Partialwellenanalyse durchgeführt, um eine mehrdimensionale Rekonstruktions- und Selektionseffizienz vorzunehmen. Es wurden Bornsche Wirkungsquerschnitte bestimmt, die sowohl statistische als auch systematische Unsicherheiten enthalten. Bei der Suche nach Kopplungen von (exotischen) Vektor-Charmonia an den $\phi K\bar{K}$ -Endzustand wurde ein Maximum-Likelihood-Fit angewendet. Da kein signifikanter Resonanzbeitrag beobachtet wurde, wurden für verschiedene Vektorzustände obere Grenzwerte mit einem Konfidenzniveau von 90% errechnet.

Darüber hinaus wurde das $K\bar{K}$ -System, das vom ϕ -Meson rückstretet, anhand des Datensatzes bei $\sqrt{s} = m_{\psi(2S)}$ untersucht. Dabei wurde ein auf Unitarität und Analytizität basierender Formalismus verwendet, um die dynamischen Anteile der Amplituden der vorhandenen Resonanzen im skalaren isoskalaren Sektor korrekt zu beschreiben. Die Verzweungsverhältnisse $\mathcal{B}r(\psi(2S) \rightarrow \phi K^+ K^-)$ und $\mathcal{B}r(\psi(2S) \rightarrow \phi K_S^0 K_S^0)$ wurden zu $(9.58_{-0.14}^{+0.14} \pm 0.45) \cdot 10^{-5}$ bzw. $(3.45_{-0.13}^{+0.14} \pm 0.11) \cdot 10^{-5}$ bestimmt.

Im zweiten Teil dieser Arbeit wurde der Endzustand $p\bar{p}\eta'$ mit den gleichen Daten wie oben untersucht. Das η' -Meson wurde in seinen Zerfällen nach $\eta\pi^+\pi^-$ und $\gamma\pi^+\pi^-$ rekonstruiert, während die nachfolgenden η -Mesonen in $\gamma\gamma$ rekonstruiert wurden. In beiden Kanälen wurde das η' -Meson im integrierten Datensatz signifikant beobachtet. Kombinierte Bornsche Wirkungsquerschnitte wurden zum ersten Mal in diesem Energiebereich bestimmt, wobei korrelierte systematische Unsicherheiten zwischen den Kanälen und den Datensätzen berücksichtigt wurden. Die Signifikanz eines resonanten Beitrags des $\psi(4230)$ zum $p\bar{p}\eta'$ -Endzustand beträgt 2.43σ . Die Daten stimmen mit einer resonanten Erzeugung des $p\bar{p}$ -Paares über eine J/ψ -Zwischenresonanz überein, wenn der Endzustand $p\bar{p}\eta'$ über ein resonantes $\psi(4230)$ erzeugt wird.

Contents

1. Introduction	1
2. Theoretical Framework	5
2.1. The Standard Model of Particle Physics	5
2.2. Quantum Chromodynamics	7
2.3. Hadron Spectroscopy	10
2.3.1. Mesons	11
2.3.2. Baryons	19
2.3.3. Charmonia	19
2.3.4. Exotics	20
2.4. Elements of Scattering Theory	23
2.5. Dispersion Theory	25
2.5.1. S -matrix Theory	26
2.5.2. Analytical Properties of the S -Matrix	27
2.5.3. Breit-Wigner Formula	32
2.5.4. K -Matrix	34
2.5.5. Dispersion Integral	36
2.5.6. Elastic Approximation and Omnès Problem	37
2.6. A New Parametrization of the Scalar Pion Form Factor	38
2.7. Helicity Formalism	42
3. Experimental Setup	45
3.1. BEPCII Accelerator	45
3.2. BESIII Experiment	45
3.2.1. Multilayer Drift Chamber (MDC)	46
3.2.2. Time-of-Flight System (TOF)	49
3.2.3. Electromagnetic Calorimeter (EMC)	50
3.2.4. Muon Counter (MUC)	50
3.2.5. Trigger System	51
3.3. BESIII Data Sets	52
4. Event Selection	55
4.1. Charged Track Selection	55

4.2. Photon Candidate Selection	58
4.3. Kinematic Fit	59
5. Analysis of $e^+e^- \rightarrow \phi K\bar{K}$	63
5.1. Background Studies	64
5.2. Number of Observed Events	66
5.3. Efficiency	71
5.4. Higher Order Correction Factors	76
5.5. Born Cross Sections	77
5.5.1. Upper Limit on $e^+e^- \rightarrow \psi \rightarrow \phi K\bar{K}$	81
5.6. Systematic Uncertainties	83
5.6.1. Signal Region	84
5.6.2. Background Description	84
5.6.3. Kinematic Fit	84
5.6.4. Partial Wave Model	85
5.6.5. K_S^0 reconstruction	85
5.7. Partial Wave Analysis at $\sqrt{s} = m_{\psi(2S)}$	85
5.7.1. Determination of $\mathcal{B}r(\psi(2S) \rightarrow \phi K\bar{K})$	89
6. Analysis of $e^+e^- \rightarrow p\bar{p}\eta'$	95
6.1. Background Studies	95
6.2. Number of Observed Events	98
6.3. Efficiency	100
6.4. Systematic Uncertainties	100
6.5. Born Cross Sections	101
6.5.1. Upper Limit on $e^+e^- \rightarrow \psi \rightarrow p\bar{p}\eta'$	104
6.6. Comparison with $e^+e^- \rightarrow J/\psi\eta'$	105
7. Conclusions and Perspectives	111
A. Appendix	117
A.1. The Least-Squares Method	117
A.1.1. Least-Squares Fit	118
A.1.2. Goodness of Fit	119
A.2. Results for $e^+e^- \rightarrow \phi K^+K^-$, $e^+e^- \rightarrow \phi K_S^0 K_S^0$ and $e^+e^- \rightarrow p\bar{p}\eta'$	120
A.3. Invariant Mass Spectra of ϕ Meson Candidates for $e^+e^- \rightarrow \phi K^+K^-$	126
A.4. Invariant Mass Spectra of ϕ Meson Candidates for $e^+e^- \rightarrow \phi K_S^0 K_S^0$	132
A.5. Invariant Mass Spectra of η' Meson Candidates for $\eta' \rightarrow \eta\pi^+\pi^-$	138
A.6. Invariant Mass Spectra of η' Meson Candidates for $\eta' \rightarrow \gamma\pi^+\pi^-$	144

Bibliography	151
List of Figures	175
List of Tables	179

1. Introduction

What do Paul Tergat and the Belle collaboration have in common? Both caused ground-breaking events in September 2003. While Mr. Tergat set a new world record at the annual Berlin Marathon with the best time of 2 hours, 4 minutes and 55 seconds [1], the Belle collaboration published the discovery of the first exotic meson $X(3872)$, now called $\chi_{c1}(3872)$ [2]. Since the present work is thematically located more in particle physics and less in elite sports, we focus on the latter event in the following.

Before we can understand why the discovery of the $\chi_{c1}(3872)$ has opened Pandora's box and why this state is called exotic, we must return to the beginnings of the inward bound path of discovery unraveling the mysteries of matter and the forces that hold it together. This path culminated at the end of the twentieth century in a theory of fundamental forces of nature based on non-Abelian gauge fields, called the Standard Model of Particle Physics [3–6].

The journey began in 1897, when J. J. Thomson discovered the electron [7]. Since then, the understanding of particle physics has evolved rapidly. In 1911, E. Rutherford's scattering experiments showed [8], that an atom consists of a positively charged nucleus surrounded by a cloud of negatively charged electrons. One might ask why Rutherford has needed α -particles to make these insights into the atomic nucleus. The answer to that question comes from the basic principles of quantum mechanics: the resolution power of the observation depends on the wavelength λ of the spectator particle. Using visible light, only objects with diameters down to $0.2 - 0.3 \mu\text{m}$ can be resolved. Based on work from A. Einstein [9], who theorized that photons have both particle and wave properties simultaneously, L. de Broglie hypothesized that not only light, but also matter particles possess both such properties [10–12]. In fact, the wavelength λ of the α -particles used by Rutherford were in the order of 10^{-13} m, compared to $\lambda = \mathcal{O}(10^{-16}$ m) for high energy electrons and protons in today's particle accelerators.

After the discovery of the neutron by J. Chadwick in 1932 [13], the atomic nucleus with atomic number Z and mass number A was interpreted as a bound system of Z protons and $A - Z$ neutrons. It was Yukawa who argued in 1937 that the strong nuclear force that binds neutrons and protons in atomic nuclei is carried by a particle with a mass about 200 times that of an electron [14]. Shortly after Yukawa's prediction, such a particle was discovered in cosmic rays in 1947, called the π meson [15]. From this day on, a whole zoo of new particles with heavier masses and in general very short

lifetimes has been discovered, collectively called hadrons. The first structuring of these observations has been made within the static quark model by M. Gell-Mann and G. Zweig in 1964 [16, 17], classifying hadrons into spin-integer mesons ($q\bar{q}$) and spin-half-integer baryons (qqq) built up of spin $\frac{1}{2}$ building blocks called quarks q (or antiquarks \bar{q}). The following experimental milestones, including the first dynamic evidence for quarks at the Stanford Linear Accelerator Center (SLAC) from 1967 to 1973 [18], the discovery of the J/ψ meson at the Brookhaven National Laboratory [19] and at SLAC [20] in 1974, and first evidences for charmed baryons [21] as well as mesons [22, 23] in 1975 and 1976, respectively, have been accompanied by the development of modern theory of strong interactions, named **Quantum Chromodynamics (QCD)** [24–26]. It describes the interaction between quarks based on color symmetry, and particles with color interact strongly through the exchange of spin one particles named gluons. Observed hadrons are colorless combinations of colored quarks and gluons, described as confinement. As color neutrality of such states is the main constraint, the existence of other possible configurations beyond these conventional mesons and baryons was already discussed in the initial works on the quark model. These hypothetical exotic states include tetraquarks ($qq\bar{q}\bar{q}$), pentaquarks ($qqqq\bar{q}$), hybrids ($q\bar{q}g$) and glueballs (gg, ggg).

In past years, many exotic candidates have been discovered in the charmonium and charmonium-like spectrum, and their study is one of the most intensively studied topics in modern particle physics. Below the $D\bar{D}$ thresholds, the observed spectrum is in agreement with theoretical predictions from the **Non-Relativistic Quark Model (NRQM)** [27]. However, above this so-called open charm threshold, the description fails unexpectedly since a clear overpopulation of states is observed. The first exotic candidate in the charmonium and charmonium-like spectrum, the $\chi_{c1}(3872)$ as mentioned above, has been discovered in 2003 by the Belle collaboration in $B^\pm \rightarrow K^\pm J/\psi \pi^+ \pi^-$ as a very narrow resonance coupling to $J/\psi \pi^+ \pi^-$ [2]. Another exotic candidate that is examined in more detail in this work is the $\psi(4230)$, originally discovered by the BaBar experiment in 2005 as a strong resonant signal decaying to $J/\psi \pi^+ \pi^-$ [28]. BESIII reported this state in the process $e^+e^- \rightarrow J/\psi \pi^+ \pi^-$ [29] with a slightly lower mass, and also stated the need of a second heavier resonance $\psi(4360)$. Since the e^+e^- pair annihilates into a virtual photon γ^* , (exotic) vector charmonia can be produced directly at the BESIII experiment due to equal quantum numbers of the γ^* and, e.g. the $\psi(4230)$. This makes electron-positron colliders a very important tool for the study of exotic states in the charmonium region. In the analysis of $e^+e^- \rightarrow J/\psi \pi^+ \pi^-$, the discovery of the first charged charmonium-like state $Z_c(3900)$ coupling to $J/\psi \pi^\pm$ has been additionally made by both the BESIII [30] collaboration and the Belle [31] collaboration. Since it couples to $c\bar{c}$ and carries electrical charge, its minimal quark content is assumed to be $c\bar{c}u\bar{d}$.

As clear as the experimental observations regarding new exotic states are, as unclear are their theoretical interpretations. In recent years, a great deal of effort has been put

into the elaboration of theoretical models that attempt to classify exotic states, e.g. as tetraquarks ($qq\bar{q}\bar{q}$) [32–34], hadronic molecules ($q\bar{q}q\bar{q}$) [35–37] or hybrid charmonia ($c\bar{c}g$) [38,39]. Unfortunately, there is still no consensus on the inner structure of, e.g. the $\psi(4230)$ that would explain the observed properties. While only small couplings of the $\psi(4230)$ to the $D\bar{D}$ final state has been observed [38,40,41], it is prominently observed in charmonium transitions to $J/\psi\pi^+\pi^-$ [29], $h_c\pi^+\pi^-$ [42] and $\psi(2S)\pi^+\pi^-$ [43]. However, decays to light mesons or baryons have not been observed so far, e.g. to final states containing ϕ and K mesons [44–47] or a $p\bar{p}$ pair [48] with an additional light, unflavored meson π^0, η or ω [49,50].

In order to search for possible decay patterns of exotic vector charmonia to gain further understanding of these states, precise analyses using high luminosity data sets are needed. In the main part of this work, such data sets at center-of-mass energies between $\sqrt{s} = 3.7730$ GeV and $\sqrt{s} = 4.7008$ GeV accumulated at the BESIII experiment are used in order to perform a lineshape study of the energy-dependent Born cross section of the processes $e^+e^- \rightarrow \phi K^+K^-$, $e^+e^- \rightarrow \phi K_S^0 K_S^0$ and $e^+e^- \rightarrow p\bar{p}\eta'$ in the search for couplings of exotic vector charmonia to these light hadron states. Although the $\psi(4230)$ was only reported in final states containing a $c\bar{c}$ pair, either built into charmonium states or into pairs of charmed mesons, the cross section lineshapes of $\sigma_b(e^+e^- \rightarrow \text{light hadrons})$ do suggest contributions from amplitudes beyond simple continuum production. In [33], the $\psi(4230)$ is interpreted as a diquark antidiquark state $c\bar{s}\bar{c}s$, which implies the decay into final states containing $s\bar{s}$. This was observed in an amplitude analysis of $e^+e^- \rightarrow J/\psi\pi^+\pi^-$, with one of the dominant contributions coming from $\psi(4230) \rightarrow f_0(980)J/\psi$ [51]. The $f_0(980)$ meson is known to have large $s\bar{s}$ contributions [52,53]. In case the $c\bar{c}$ annihilates while the $s\bar{s}$ survives as a hidden strangeness meson, e.g. the ϕ meson, the decay $\psi(4230) \rightarrow \phi K\bar{K}$ is expected to occur. Such so-called charmless decays are also predicted by hybrid models [38]. Possible resonant contributions of various (exotic) vector charmonia including the $\psi(4230)$ to the Born cross section of $e^+e^- \rightarrow \phi K\bar{K}$ were investigated using maximum likelihood fits, and upper limits on their partial widths were determined.

Of special interest are final states involving a $p\bar{p}$ pair, since the partial width $\Gamma_{\psi \rightarrow p\bar{p}h}$ with h being a light, unflavored meson, can be related to the production cross section of $\sigma_{p\bar{p} \rightarrow \psi h}$ [54]. $p\bar{p}$ annihilation processes will be studied at the upcoming PANDA (Antiproton **A**nnihilation at **D**armstadt) experiment at the **F**acility for **A**ntiproton and **I**on **R**esearch (FAIR) [55]. So it is evidently crucial to obtain partial widths and, thus, production cross sections of potentially exotic vector charmonia with high accuracy for the PANDA physics program, both to formulate detection strategies and to evaluate luminosity requirements, as well as for detailed detector simulations with theoretically preferred final states. While $p\bar{p}\eta'$ decay widths for charmonium states below the open charm threshold, e.g. the J/ψ and $\psi(2S)$ have been already reported [56], information on the partial decay widths of higher lying charmonium and charmonium-like states,

e.g. the $\psi(4160)$ and $\psi(4230)$ is still lacking. In this work, the partial widths and their respective upper limits in case of no significant coupling of the $\psi(4160)$ and the $\psi(4230)$ to $p\bar{p}\eta'$ were extracted using maximum likelihood fits to the energy-dependent Born cross section. Since the J/ψ meson is significantly observed in the $p\bar{p}$ invariant mass spectrum, a cross check was performed in addition with results from a previous BESIII analysis of the reaction $e^+e^- \rightarrow J/\psi\eta'$ with $J/\psi \rightarrow l^+l^-$ [57].

Not only in the heavy charmonium sector, but also in the light scalar isoscalar sector, many interesting observations were made from experimental side. In the last decades, multiple states were discovered and discussed. At present time, five scalar isoscalar resonances, namely the $f_0(500)$, $f_0(980)$, $f_0(1370)$, $f_0(1500)$ and the $f_0(1710)$ are well-established and listed by the **P**article **D**ata **G**roup (PDG) [56]. However, the identification of scalar isoscalar mesons is a long-standing puzzle, since present resonances show large decay widths and, thus, a strong overlap between their decay amplitudes. To study such states, data has been obtained from $\pi\pi, K\bar{K}, \eta\eta, 4\pi$ and $\eta\eta'$ systems produced in S -wave. Both theoretical [58] and experimental [56] results are consistent with two nonets, one below and another one above $\sqrt{s} = 1\text{ GeV}$, with evidence for gluonic degrees of freedom. The observed phenomenon of multiplet doubling requires an effective chiral quark model, e.g. a coupled linear sigma model [59, 60] to provide an understanding of the light scalar spectrum. While both the $f_0(500)$ and the $f_0(980)$ are assigned to the lower nonet within the quark model, two of the three states $f_0(1370)$, $f_0(1500)$ and the $f_0(1710)$ must be assigned to the higher nonet. Simultaneously to this experimentally observed overpopulation, lattice QCD calculations predict the lightest glueball to have equal quantum numbers and to occur in the mass range between $1.6 - 1.7\text{ GeV}/c^2$ [61–64]. By studying the process $e^+e^- \rightarrow \phi K\bar{K}$ at BESIII, the scalar isoscalar sector can be investigated since a possible quantum number the $K\bar{K}$ system recoiling off the ϕ meson can carry is $J^{PC} = 0^{++}$. In addition, the associated production of scalar mesons with a ϕ meson would indicate a sizeable $s\bar{s}$ contribution of these. Sophisticated analyses need to be performed using theoretical models based on principles of scattering theory such as unitarity and analyticity in order to properly describe the dynamical parts of the amplitudes. In this work, such a formalism [65] having these features built in is employed within a partial wave analysis in order to study S -wave contributions to the $K\bar{K}$ spectrum in the process $e^+e^- \rightarrow \phi K\bar{K}$ at $\sqrt{s} = m_{\psi(2S)}$. D -wave contributions are described using a K -matrix approach. As an outlook, the $\pi^+\pi^-$ invariant mass spectrum for the process $e^+e^- \rightarrow \phi\pi^+\pi^-$ is also shown in order to be able to perform a coupled-channel analysis of both $\phi K\bar{K}$ and $\phi\pi^+\pi^-$ in the future.

2. Theoretical Framework

This chapter is intended to provide an introduction to the subject of hadron spectroscopy, within which the present work is situated. After the discussion of the Standard Model of Particle Physics, the underlying theory of the strong force, **Quantum Chromodynamics** (QCD), is presented. Bound states of QCD, e.g. mesons and baryons, are the subject of spectroscopy. They appear as resonances in measured variables such as invariant mass spectra or Born cross sections. The description of resonances as well as the extraction of resonance parameters requires a proper theoretical treatment of their amplitudes, based on elements of scattering theory such as analyticity and unitarity. A formalism which uses the principles of dispersion and S -matrix theory and therefore has these features built in by construction, concludes the chapter.

2.1. The Standard Model of Particle Physics

The Standard Model of Particle Physics is a **Quantum Field Theory** (QFT) of modern particle physics [3–6], describing the electromagnetic, weak, and strong interaction. The tremendous efforts to include gravitation [66] into the scheme were so far unsuccessful. Moreover, gravitation does not play a significant role in particle physics due to its small relative strength at such scales compared to the other fundamental forces and, therefore, can be neglected.

The elementary particles that make up matter are a set of fermions, interacting primarily through the exchange of vector bosons. These interactions are described by the Standard Model. Quarks, whose bound states, mesons and baryons (collectively called hadrons), form the particles with nuclear interactions, and leptons are the fundamental fermionic particles. While the latter only take part in the electromagnetic and weak interaction, quarks are also subject to the strong one. Figure 2.1 shows a schematic illustration of the Standard Model of Particle Physics and all elementary particles incorporated. Quarks and leptons come in three families, consisting of a doublet under the weak interaction: for leptons the electron and electron-neutrino (e^- , ν_e), the muon and muon-neutrino (μ , ν_μ) as well as the tauon and tauon-neutrino (τ , ν_τ), and for quarks the up- and down-quark (u, d), the charm- and strange-quark (c, s) as well as the top- and bottom-quark (t, b). For both quarks and leptons also antiparticles exist, carrying exactly the same mass and spin but oppositely charged quantum numbers.

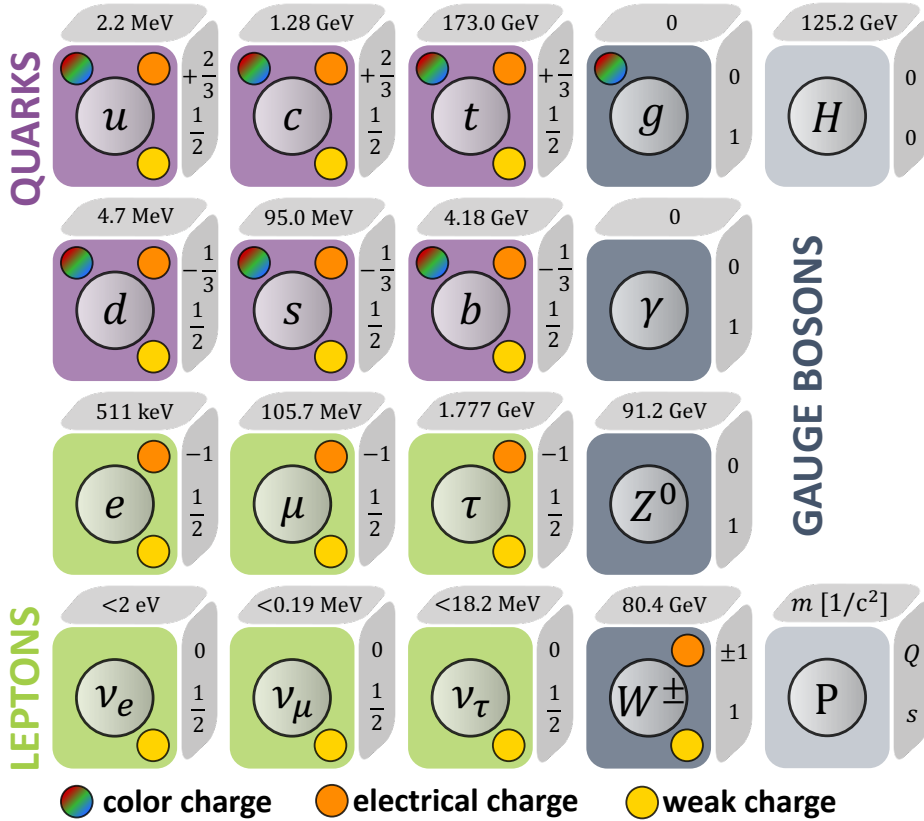


Figure 2.1.: Schematic illustration of the Standard Model of Particle Physics, including the elementary fermions (six quarks and six leptons), the force-mediating vector bosons of the strong, weak, and electromagnetic interaction as well as the recently discovered Higgs boson. The color charge, the electrical charge and the weak charge are represented by colored circles. The values of both the electrical charge Q and the intrinsic spin s are given on the right of each box. The masses m of the particles are given on the top of each box. In case of the neutrinos, which have a non-vanishing mass as indicated by, e.g. neutrino oscillations [67–69], no mechanism to produce their masses is established yet. Values are taken from [56].

Theoretically, the strong, weak, and electromagnetic interactions are combined within the Standard Model into a $SU(3)_c \times SU(2)_L \times U(1)_Y$ gauge theory, with $SU(3)_c$ denoting the gauge color group of the strong interaction and $SU(2)_L \times U(1)_Y$ denoting the gauge group of the electroweak interaction [4, 70, 71]. Assuming local gauge symmetries, so-called gauge bosons need to be introduced as shown in Figure 2.1, mediating the fundamental forces between the elementary quarks and leptons.

The exchange boson of the *electromagnetic interaction* is the massless photon γ . The underlying QFT is **Q**uantum **E**lectrodynamics (QED) and its Lagrangian is given by [72]

$$\mathcal{L}_{\text{QED}} = \bar{\psi}(i\gamma^\mu D_\mu - m)\psi - \frac{1}{4}F_{\mu\nu}F^{\mu\nu}, \quad (2.1)$$

with γ^μ being the Dirac matrices, $D_\mu = \partial_\mu + iqA_\mu$ being the gauge covariant derivative with electromagnetic vector potential A_μ , $F_{\mu\nu} = \partial_\mu A_\nu - \partial_\nu A_\mu$ being the electromagnetic field tensor, q being the electric charge and ψ being the bispinor field of a fermion. In the fifties and sixties, renormalization procedures in QFT have been established for singularities of QED by Dyson, Feynman, Schwinger and others [73–81].

Correspondingly, the massive exchange bosons of the *weak interaction* are the charged W^\pm , with $m_{W^\pm} = (80.379 \pm 0.012) \text{ GeV}/c^2$ [56], and the neutral Z^0 , with $m_{Z^0} = (91.1876 \pm 0.0021) \text{ GeV}/c^2$ [56], coupling to the weak isospin T of a particle. However, a mass term of the W^\pm and Z^0 would break the $SU(2)_L$ -symmetry. This is why masses need to be introduced dynamically via the Higgs mechanism [82, 83]. The Higgs boson was experimentally confirmed in 2012 [84, 85]. The corresponding complex scalar Higgs field transforms as a doublet under $SU(2)_L$ and is coupled via a Yukawa term to the quark and lepton fields. Since its potential has a non-trivial degenerate vacuum, the gauge symmetry is broken spontaneously. By this, the quarks and leptons as well as W^\pm and Z^0 gain an effective mass.

The theory of *strong interaction* is governed by a QFT named **Q**uantum **C**hromodynamics (QCD) [6, 24]. Its gauge bosons are the $3 \times 3 - 1 = 8$ gluons which couple to the color charge. A detailed discussion about QCD is given in the next section.

2.2. Quantum Chromodynamics

This section is intended to give a basic introduction to QCD [6, 24] before describing the e^+e^- annihilation into hadrons in more detail. At the very end, the asymptotic states of the theory, bound states of gluons and quarks, called either mesons or baryons, are highlighted. The color hypothesis mentioned in Chapter 1 was phenomenologically successful, but raised the question of what mechanism could ensure that all hadron wave functions are color singlets. The answer to that is a non-Abelian gauge theory with color symmetry as its corresponding gauge group, with the colors being the gauge quantum numbers of the quarks. Hence, the model of strong interaction can be considered as a system of quarks of the various flavors (u, d, s, c, b, t) each assigned to the fundamental representation of the local gauge group $SU(3)_c$. Gluons are the gauge bosons of this group. As a $SU(3)_c$ gauge theory, QCD considers quarks q_i , antiquarks \bar{q}_i and gluons A_μ^C as degrees of freedom. Its Lagrangian is given by [56]

$$\mathcal{L}_{\text{QCD}} = \sum_{f=u,d,s,c,b,t} \bar{q}_f^a \left(iD_\mu^{ab} \gamma^\mu - m_f \delta^{ab} \right) q_f^b - \frac{1}{4} (G^a)_{\mu\nu} (G^a)^{\mu\nu} , \quad (2.2)$$

with q_f^a being the quark-field spinor for a quark of flavor f , mass m_f and color a ,

$$D_\mu^{ab} = \partial_\mu \delta^{ab} - ig\lambda_c^{ab} A_\mu^c \quad \text{and} \quad (G^a)_{\mu\nu} = \partial_\mu A_\nu^a - \partial_\nu A_\mu^a + gf^{abc} A_\mu^b A_\nu^c \quad (2.3)$$

being the covariant derivative and the gluonic field strength tensor with gluonic field A_μ^a , respectively, and λ_c^{ab} being the adjoint representation of the $SU(3)_c$ generators with structure constants f^{abc} defined through

$$[\lambda_a, \lambda_b] = if^{abc}\lambda_c. \quad (2.4)$$

Note that the last term in Equation (2.3) allows for gluon self-interaction, resulting in an effective range of very short distances for the strong force since gluons carry color charge themselves.

In the left part of Equation (2.3), g denotes the coupling constant of QCD. It becomes very small in the high-energy regime (high transferred momentum Q), which is called asymptotic freedom, and perturbation theory converges for $Q > 4\text{ GeV}$, while the perturbative expansion breaks down for smaller energy scales. In case of strong couplings, QCD exhibits *confinement* of colors, which means that the asymptotic states of the theory are those that are singlets of the $SU(3)_c$ group. Qualitatively speaking, separating a color-singlet state into colored components produces a flux tube of gauge fields (or gluons) between color charged objects carrying energy. Since this tube has fixed radius and energy density, the increase of the distance (or decrease of the momentum transfer) between the two sources grows the energy costs proportionally to the separation. The energy density will increase to a point such that it is energetically more favorable to break the flux tube and generate a color-anticolor pair from the vacuum and therefore two color neutral objects. This effect is known as hadronization.

Before a more detailed discussion about the coupling constant and its properties is given, the simplest example of elementary interactions among quarks and gluons that can be observed in high-energy experiments such as BESIII, namely the e^+e^- annihilation into hadrons $e^+e^- \rightarrow q\bar{q}$, is presented. The lowest order total cross section of this process is given by [72]

$$\sigma(e^+e^- \rightarrow \text{hadrons})(s) = \sigma_0(s) \cdot 3 \sum_f Q_f^2, \quad (2.5)$$

with $\sigma_0(s)$ being the QED cross section for $e^+e^- \rightarrow \mu^+\mu^-$ with coupling constant $\alpha_{\text{QED}} \approx \frac{1}{137}$ at energy s

$$\sigma_0(s) = \frac{4\pi\alpha_{\text{QED}}^2}{3s}. \quad (2.6)$$

The factor 3 denotes the number of colors and Q_f is the electric charge of a quark with flavor f . The value of this cross section is affected by leading order corrections such as gluon exchange and emission. Taking these corrections into account, the total cross section becomes

$$\sigma(e^+e^- \rightarrow \text{hadrons})(s) = \sigma_0(s) \cdot 3 \sum_f Q_f^2 \cdot \left[1 + \frac{\alpha_s}{\pi} + \mathcal{O}(\alpha_s^2) \right], \quad (2.7)$$

with $\alpha_s = \frac{g^2}{4\pi}$ being the strong coupling constant. This coupling constant must be defined at some renormalization point M , which may be chosen at a large momentum scale where the coupling is small. By this, α_s can be used to predict results of various scattering processes with any large momentum transfer. After renormalization, the strong coupling constant reads [72]

$$\alpha_s(Q) = \frac{2\pi}{b_0 \log(Q/\Lambda_{\text{QCD}})}, \quad (2.8)$$

with $b_0 = 11 - \frac{2}{3}n_f$ and n_f being the number of quark flavors, and Λ_{QCD} being the QCD Landau pole experimentally measured to be $\Lambda_{\text{QCD}} \approx 200 - 400$ MeV [56]. Equation (2.8), also known as the *running of the coupling constant*, easily shows that $\alpha_s(Q)$ becomes small for large Q . Note that QCD perturbation theory is valid for momentum transfers larger than Λ_{QCD} , e.g. $Q = 1$ GeV or $\alpha_s(Q) \approx 0.4$. Figure 2.2 shows the coupling constant for different values of Q .

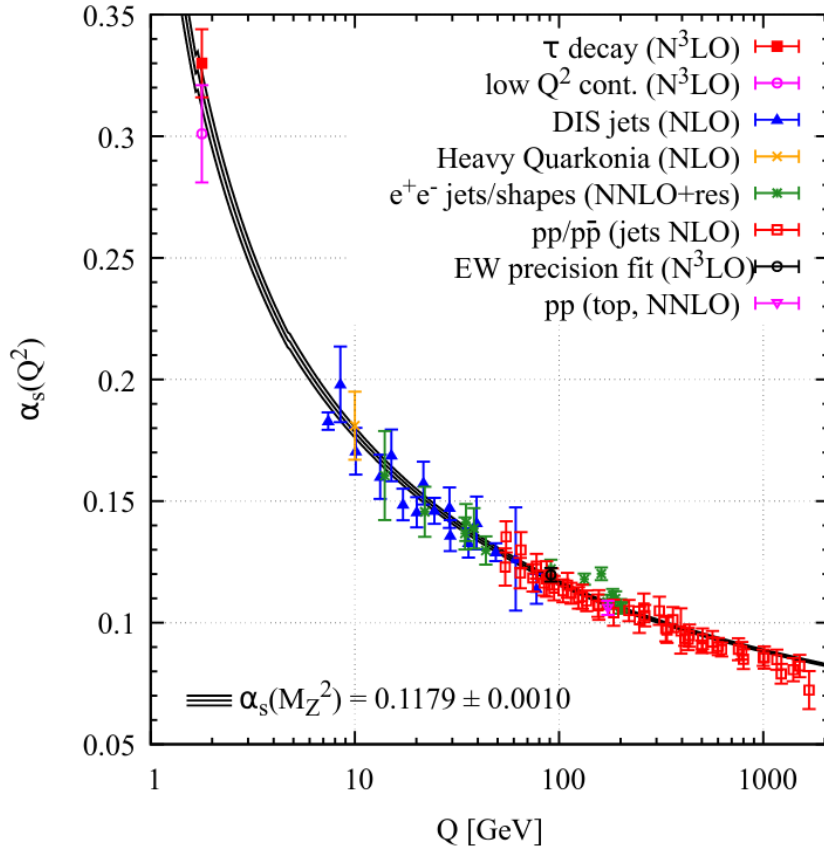


Figure 2.2.: Summary of measurements of α_s as a function of the energy scale Q . The respective degree of QCD perturbation theory used in the extraction of α_s is indicated in brackets (NLO: next-to-leading order; NNLO: next-to-next-to-leading order; NNLO+res.: NNLO matched to a resummed calculation; N³LO: next-to-NNLO). Figure taken from [56].

After having introduced the basic concepts of QCD, it is necessary to get better insights into the theory by measuring the interaction between quarks and gluons with experiments. Since neither of them can be observed in isolation in experiments due to confinement phenomena, but only within hadrons, the strong interaction is examined by studying hadronic spectra. This approach is similar to QED, where information about the underlying theory can be inferred from atomic spectra. Hence, hadronic states will be discussed in the following.

2.3. Hadron Spectroscopy

Hadronic states X appear either in production processes

$$I_1 + I_2 \rightarrow X + (S) \rightarrow F_1 + F_2 + \cdots + F_n + (S)$$

with an eventual spectator particle S or in decays

$$I \rightarrow X + (S) \rightarrow F_1 + F_2 + \cdots + F_n + (S).$$

They show up as resonant structures, e.g. in the corresponding cross sections or invariant mass spectra of their daughter particles. Note that also other kinematic phenomena such as threshold cusps and triangle singularities may produce similar structures [86]. However, partial wave amplitude analyses have to be carried out in order to get a proper understanding of the underlying processes. Constructed amplitudes need to rely on the basic principles of scattering theory, such as unitarity and analyticity. A detailed presentation of the basics of scattering theory is given in Sections 2.4 and 2.5. In the following, QCD bound states, so-called hadrons, will be discussed.

In principle, a hadron consists of an indefinite number of quarks and gluons such that together they form a color singlet. Their quarkonic component can be distinguished into so-called *valence quarks* and *sea quarks*. While the latter are present as quark-antiquark pairs producing small vacuum fluctuations, valence quarks are usually responsible for the quantum numbers of a hadron (there are exceptions, such as the proton spin crisis [87]). These contain the electric charge \mathcal{Q} , total angular momentum J , parity \mathcal{P} , charge conjugation \mathcal{C} , baryon number \mathcal{B} ($\mathcal{B}_q = \frac{1}{3}$, $\mathcal{B}_{\bar{q}} = -\frac{1}{3}$), as well as the flavor quantum numbers, which are the isospin \mathcal{I} (and its third component \mathcal{I}_3), strangeness \mathcal{S} , charmness \mathcal{C} , bottomness \mathcal{B} and topness \mathcal{T} . The additive flavor and electric charge quantum numbers of the six quarks are summarized in Table 2.1. Multiplicative quantum numbers are the parity, whose operator $\hat{\mathcal{P}}$ reverses spatial coordinates \mathbf{x} so that $\hat{\mathcal{P}}\psi(t, \mathbf{x}) = \psi(t, -\mathbf{x})$, and the charge conjugation, whose operator $\hat{\mathcal{C}}$ transforms all particles into their antiparticles $\hat{\mathcal{C}}\psi = \bar{\psi}$.

Within the conventional quark model [16, 17], hadrons are classified into those which are

Table 2.1.: Additive quantum numbers of the quarks: electrical charge \mathcal{Q} , isospin \mathcal{I} and its third component \mathcal{I}_3 , strangeness \mathcal{S} , charmness \mathcal{C} , bottomness \mathcal{B} and topness \mathcal{T} [56].

	d	u	s	c	b	t
\mathcal{Q}	$-\frac{1}{3}$	$+\frac{2}{3}$	$-\frac{1}{3}$	$+\frac{2}{3}$	$-\frac{1}{3}$	$+\frac{2}{3}$
\mathcal{I}	$\frac{1}{2}$	$\frac{1}{2}$	0	0	0	0
\mathcal{I}_3	$-\frac{1}{2}$	$+\frac{1}{2}$	0	0	0	0
\mathcal{S}	0	0	-1	0	0	0
\mathcal{C}	0	0	0	+1	0	0
\mathcal{B}	0	0	0	0	-1	0
\mathcal{T}	0	0	0	0	0	+1

made up of a quark-antiquark pair (mesons, $q\bar{q}$), and those consisting of three quarks (baryons, qqq), representing the most simple quark configurations of color singlet states. As color-neutrality of such states is the main constraint of QCD, the existence of other possible configurations beyond these conventional mesons and baryons were also predicted back then [16]. States like tetraquarks ($qq\bar{q}\bar{q}$), hybrids ($q\bar{q}g$) or glueballs (gg, ggg) are called exotic states. The next sections give a detailed insight into conventional and exotic states, as well as the current status of experimental observations.

2.3.1. Mesons

Conventional mesons are the simplest configurations allowed by the quark model. They consist of a quark-antiquark pair $q\bar{q}$. In fact, the role of mesons in QCD shows many parallels to that of the hydrogen atom in QED. For example, their spin and orbital angular momentum structure is very similar. Being made up of two fermions, an orbital angular momentum of $L = 0, 1$ in combination with either parallel or antiparallel spin configurations S yield total angular momenta of $J = 0, 1, 2$ of the $q\bar{q}$ system. Note that in general J is given by $|L - S| \leq J \leq |L + S|$ [88].

Within hadron spectroscopy, hadronic states are commonly classified using the notation J^{PC} . Since the strong interaction is symmetric under parity, its eigenvalues P are ± 1 . In case of a $q\bar{q}$ system $P = (-1)^{L+1}$, where the factors $(-1)^L$ and $(-1)^1$ arises from the action of \hat{P} on the spatial wave function and the opposite intrinsic parities of fermions and antifermions, respectively. The C -parity is given by $C = (-1)^{L+S}$ due to the Pauli principle which states that the wave function needs to be antisymmetric with respect to interchange of the two fermions [56]. Consequently, the lightest mesonic states ($L = 0, 1$) carry the J^{PC} quantum numbers 0^{-+} (*pseudoscalar*), 1^{--} (*vector*), 0^{++} (*scalar*), $1^{++,+}$ (*axial*) and 2^{++} (*tensor*). By this, mesons can be constructed based on their spatial quantum numbers. However, any observed mesonic state that does not carry the aforementioned quantum numbers allowed by the quark model can safely be considered

2. Theoretical Framework

exotic, e.g. $J^{PC} = 0^{--}$ or the $\pi_1(1400)$ and the $\pi_1(1600)$ with $J^{PC} = 1^{-+}$ [89–91].

Considering the flavor quantum numbers of the lightest quarks (u, d, s), mesonic states will show up as an octet and a singlet in SU(3) flavor symmetry according to $3 \otimes \bar{3} = 8 \oplus 1$. The corresponding nonets of the pseudoscalar as well as vector mesons are shown in Figure 2.3 with respect to their strangeness \mathcal{S} and their third component of the isospin \mathcal{I}_3 . While

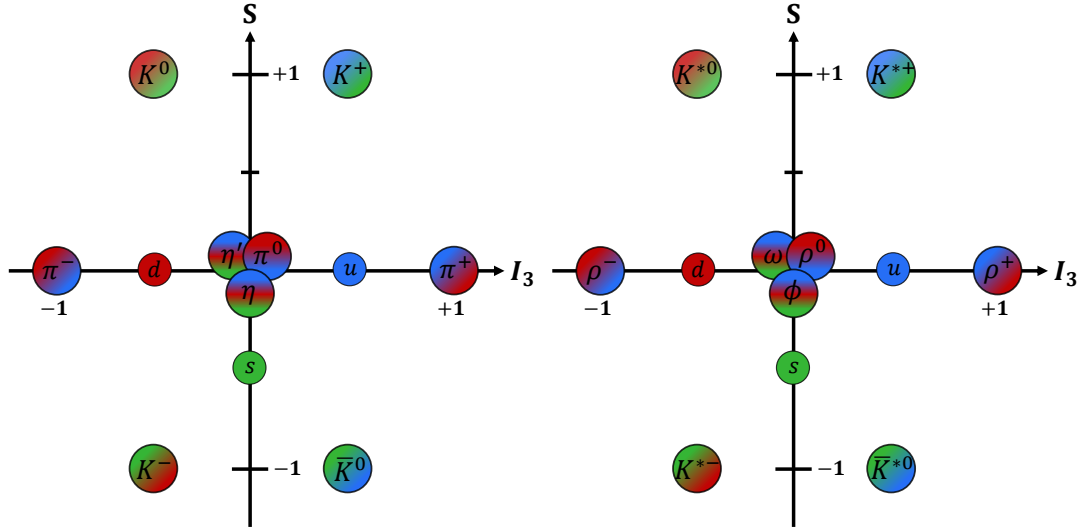


Figure 2.3.: Schematic representation of the nonet of pseudoscalar mesons (left), $q\bar{q}$ pairs with $J^{PC} = 0^{-+}$, and vector mesons (right), $q\bar{q}$ pairs with $J^{PC} = 1^{--}$, depending on the third component of their isospin \mathcal{I}_3 (abscissa) and their strangeness \mathcal{S} (ordinate). Colors indicate different quark flavors of the three lightest quarks, u (blue), d (red) and s (green). The three mesons in the center ($\mathcal{I}_3 = 0$) are mixtures of $u\bar{u}$, $d\bar{d}$ and $s\bar{s}$, while the other six mesons are quark-antiquark combinations with different flavors.

states at the corners of the hexagon (kaons K^+ , K^- , K^0 , \bar{K}^0 and pions π^+ , π^- for $J^{PC} = 0^{-+}$ as well as excited kaons K^{*+} , K^{*-} , K^{*0} , \bar{K}^{*0} and rho mesons ρ^+ , ρ^- for $J^{PC} = 1^{--}$) are rather easily distinguishable in terms of \mathcal{S} and \mathcal{I}_3 , the wave functions of the centered states with $\mathcal{S} = \mathcal{I}_3 = 0$ (π^0 , η , η' for $J^{PC} = 0^{-+}$ and ρ^0 , ϕ , ω for $J^{PC} = 1^{--}$) are superpositions of the combinations ($u\bar{u}$, $d\bar{d}$, $s\bar{s}$), as listed in Table 2.2. A brief explanation about the signs and weights contained in these superpositions follows. QCD approximately does not distinguish between u and d due to the fact that the strong interaction couples to the color charge and their similar masses. Thus, they are considered as two states of

Table 2.2.: Quark content of the lightest pseudoscalar (left) and vector (right) mesons m , where ψ_f is the flavor wave function [56]. For states with $\mathcal{S} = \mathcal{I}_3 = 0$ the case of ideal SU(2) and SU(3) is shown on the left, whereas the case where the two isosinglet states are ideally mixed (pure $s\bar{s}$ and $u\bar{u} + d\bar{d}$) is shown on the right.

m	ψ_f	m	ψ_f
π^+	$u\bar{d}$	ρ^+	$u\bar{d}$
π^-	$d\bar{u}$	ρ^-	$d\bar{u}$
K^+	$u\bar{s}$	K^{+*}	$u\bar{s}$
K^-	$s\bar{u}$	K^{-*}	$s\bar{u}$
K^0	$d\bar{s}$	K^{0*}	$d\bar{s}$
\bar{K}^0	$s\bar{d}$	\bar{K}^{0*}	$s\bar{d}$
π^0	$\frac{1}{\sqrt{2}}(u\bar{u} - d\bar{d})$	ρ^0	$\frac{1}{\sqrt{2}}(u\bar{u} - d\bar{d})$
η_8	$\frac{1}{\sqrt{6}}(u\bar{u} + d\bar{d} - 2s\bar{s})$	ϕ	$\approx s\bar{s}$
η_1	$\frac{1}{\sqrt{3}}(u\bar{u} + d\bar{d} + s\bar{s})$	ω	$\approx \frac{1}{\sqrt{2}}(u\bar{u} + d\bar{d})$

an isospin doublet $(u, d) = (+\frac{1}{2}, -\frac{1}{2})$ and correspondingly $(+\frac{1}{2}, -\frac{1}{2}) = (\bar{d}, -\bar{u})$ [92]. The combination of the isodoublet with the one of its antiparticles yields

$$|\mathcal{I} = 0, \mathcal{I}_3 = 0\rangle = \frac{1}{\sqrt{2}}|u\bar{u} + d\bar{d}\rangle \quad (2.9)$$

$$|\mathcal{I} = 1, \mathcal{I}_3 = 0\rangle = \frac{1}{\sqrt{2}}|u\bar{u} - d\bar{d}\rangle, \quad (2.10)$$

with the first state being the isosinglet, behaving like a scalar under flavor SU(2), and the second state being the neutral partner of the three isovectors, which are in case of the pseudoscalar mesons the pions π^+ , π^- and π^0 . If the s -quark is introduced, the combination $|\eta_1\rangle$ of the aforementioned singlet and octet can be build, which behaves like a scalar under flavor SU(3). Additionally, by requiring orthogonality to these first two states, the third one $|\eta_8\rangle$ in the center can be found:

$$|\eta_1\rangle = \frac{1}{\sqrt{3}}|u\bar{u} + d\bar{d} + s\bar{s}\rangle \quad (2.11)$$

$$|\eta_8\rangle = \frac{1}{\sqrt{6}}|u\bar{u} + d\bar{d} - 2s\bar{s}\rangle. \quad (2.12)$$

It can easily be seen that hidden strangeness \mathcal{S} is mixed with $u\bar{u} + d\bar{d}$ in a certain ratio. This mixture of $|\eta_1\rangle$ and $|\eta_8\rangle$ yields to the physically observed η and η' mesons, described by

$$\begin{pmatrix} |\eta\rangle \\ |\eta'\rangle \end{pmatrix} = \begin{pmatrix} \cos\theta_P & -\sin\theta_P \\ \sin\theta_P & \cos\theta_P \end{pmatrix} \cdot \begin{pmatrix} |\eta_8\rangle \\ |\eta_1\rangle \end{pmatrix}, \quad (2.13)$$

where the pseudoscalar mixing angle θ_P is measured to be between -10° and -20° [56]. In case of the vector mesons with $J^{PC} = 1^{--}$, the ϕ and ω mesons are the mixtures of the octet and singlet states with an approximately ideal mixing angle θ_V . Thus, the ϕ meson can be considered as a pure $s\bar{s}$ state [56].

According to the reactions studied in this work, special remarks on the properties of kaons as well as scalar mesons are presented below. After that, mesons containing heavier charmed quarks are introduced, so-called charmonia, as well as their exotic neighbors.

Kaons

The parity P and charge conjugation C were introduced above. Thus, their combination, CP parity, may transform a left-handed electron e_L^- into a right-handed positron e_R^+ . In electromagnetic and strong interactions, observed phenomena are C - and P -symmetric, and therefore also CP -symmetric. Weak interaction processes violate C and P separately, but still preserve CP parity in most cases. However, indirect CP violating processes were discovered in neutral K decays [93] (or more precisely, in $K^0 - \bar{K}^0$ mixing) and later established in, e.g. B meson decays [94, 95]. Direct CP violating processes have been observed in [96]. For an overview of CP violation in the quark sector we refer to [56].

Neutral kaons are produced in two different quark compositions $K^0(d\bar{s})$ and $\bar{K}^0(s\bar{d})$ and thus carry strangeness $S_{K^0} = +1$ and $S_{\bar{K}^0} = -1$. When propagating, they can transform between each other. This mixing leads to experimentally observable kaons $K_S^0 \equiv K_S$ (short) and $K_L^0 \equiv K_L$ (long) with similar masses [56] but different lifetimes, in fact $\tau_{K_S} = 8.954(4) \cdot 10^{-11}$ s and $\tau_{K_L} = 5.116(21) \cdot 10^{-8}$ s [56]. As pseudoscalar mesons with $J^{PC} = 0^{-+}$, the following P , C and CP relations hold:

$$P|K^0\rangle = -|K^0\rangle, \quad P|\bar{K}^0\rangle = -|\bar{K}^0\rangle \quad (2.14)$$

$$C|K^0\rangle = -|\bar{K}^0\rangle, \quad C|\bar{K}^0\rangle = -|K^0\rangle \quad (2.15)$$

$$CP|K^0\rangle = |\bar{K}^0\rangle, \quad CP|\bar{K}^0\rangle = |K^0\rangle. \quad (2.16)$$

Consequently, the states K^0 and \bar{K}^0 of the strong interaction are no CP eigenstates. However, such eigenstates can easily be constructed as

$$|K_1\rangle = \frac{1}{\sqrt{2}} \left(|K^0\rangle + |\bar{K}^0\rangle \right), \quad CP|K_1\rangle = +|K_1\rangle \quad (2.17)$$

$$|K_2\rangle = \frac{1}{\sqrt{2}} \left(|K^0\rangle - |\bar{K}^0\rangle \right), \quad CP|K_2\rangle = -|K_2\rangle. \quad (2.18)$$

Experimentally, the decays $K_S \rightarrow \pi\pi$ and $K_L \rightarrow \pi\pi\pi$ are mainly observed, which also determines their aforementioned life times. In case of a decay into $\pi\pi$, the pions must be in an $L = 0$ state to conserve angular momentum. Hence, P , C and CP are given by

$$P(\pi\pi) = (-1)^L P(\pi)P(\pi) = 1 \cdot (-1) \cdot (-1) = 1, \quad C(\pi\pi) = 1, \quad CP(\pi\pi) = 1. \quad (2.19)$$

This implies that the K_S could be identified with the K_1 from Equation (2.17). In case of a decay into $\pi\pi\pi$, one may define the angular momentum \vec{L}_1 of two pions and the angular momentum \vec{L}_2 of the third pion with respect to the center-of-mass of the pair, yielding $\vec{L} = \vec{L}_1 + \vec{L}_2$ with $|L_1| = |L_2|$ due to the conservation of angular momentum. Hence, P , C and CP are given here as

$$P(\pi\pi\pi) = (-1)^{L_1}(-1)^{L_2}P(\pi)^3 = -1, \quad C(\pi\pi\pi) = 1, \quad CP(\pi\pi\pi) = -1. \quad (2.20)$$

Analogously, the K_L can be identified with K_2 from Equation (2.17). Contrary to expectations, the decay $K_L \rightarrow \pi\pi$ was observed in [93], indicating CP violation in weak interactions. This effect can be described by two possible sources: first, the Hamiltonian can introduce indirect CP violation in the $K^0 - \bar{K}^0$ mixing, meaning that the physical K_L were not purely CP eigenstates but the result of a mixing between both CP odd K_2 and CP even K_1 . Second, the decay $K_L \rightarrow \pi\pi$ directly violates CP since an odd state decayed into an even state.

To introduce $K^0 - \bar{K}^0$ mixing, one may write the Hamiltonian equation of motion for the $K^0\bar{K}^0$ system as [97]

$$i\frac{d}{dt} \begin{pmatrix} K^0 \\ \bar{K}^0 \end{pmatrix} = \begin{pmatrix} M_{11} - \frac{i}{2}\Gamma_{11} & M_{12} - \frac{i}{2}\Gamma_{12} \\ M_{21} - \frac{i}{2}\Gamma_{21} & M_{22} - \frac{i}{2}\Gamma_{22} \end{pmatrix} \begin{pmatrix} K^0 \\ \bar{K}^0 \end{pmatrix}, \quad (2.21)$$

with M_{ij} denoting mass terms containing the quark masses and the potential energy of the interactions between quarks and Γ_{ij} being decay rates determined by, e.g., the Fermi golden rule. CPT^1 invariance requires $M_{11} = M_{22} = M$, $\Gamma_{11} = \Gamma_{22} = \Gamma$, $M_{12} = M_{21}^*$ and $\Gamma_{12} = \Gamma_{21}^*$ [98]. By diagonalizing the mixing matrix, the physical propagating eigenstates of the Hamiltonian can be obtained as [98]

$$|K_S\rangle = \frac{1}{\sqrt{1+|\bar{\epsilon}|^2}} (|K_1\rangle + \bar{\epsilon}|K_2\rangle) \quad (2.22)$$

$$|K_L\rangle = \frac{1}{\sqrt{1+|\bar{\epsilon}|^2}} (|K_2\rangle + \bar{\epsilon}|K_1\rangle), \quad (2.23)$$

¹The operator of the T -parity transforms the time t according to $\hat{T} : t \mapsto -t$.

with the parameter $\bar{\varepsilon}$ defined by

$$\frac{1 - \bar{\varepsilon}}{1 + \bar{\varepsilon}} = \left(\frac{M_{12}^* - \frac{i}{2}\Gamma_{12}^*}{M_{12} - \frac{i}{2}\Gamma_{12}} \right). \quad (2.24)$$

Equation (2.24) shows that the physical states $K_S(K_L)$ would correspond to the CP eigenstates $K_1(K_2)$ for real M_{12} and Γ_{12} . Indirect CP violation can be measured in, e.g., semi-leptonic decays via the asymmetry parameter δ given by [97]

$$\delta \equiv \frac{\Gamma[K_L \rightarrow \pi^- l^+ \nu_L] - \Gamma[K_L \rightarrow \pi^+ l^- \nu_L]}{\Gamma[K_L \rightarrow \pi^- l^+ \nu_L] + \Gamma[K_L \rightarrow \pi^+ l^- \nu_L]} = \frac{2\text{Re}(\bar{\varepsilon})}{(1 + |\bar{\varepsilon}|^2)}, \quad (2.25)$$

with l and ν being a lepton and its related neutrino, respectively. Experimentally, this value was measured to be $\delta = (3.322 \pm 0.058_{\text{stat}} \pm 0.047_{\text{sys}}) \cdot 10^{-3}$ [99], showing a clear evidence for CP violation due to $K^0 - \bar{K}^0$ mixing.

Additionally, any observed difference between a decay rate $\Gamma(i \rightarrow f)$ and its CP conjugate $\Gamma(\bar{i} \rightarrow \bar{f})$ indicates a direct violation of CP in the decay amplitude. The decay amplitudes can be written as

$$\begin{aligned} A(i \rightarrow f) &= M_1 e^{i\phi_1} e^{i\alpha_1} + M_2 e^{i\phi_2} e^{i\alpha_2} \\ A(\bar{i} \rightarrow \bar{f}) &= M_1 e^{-i\phi_1} e^{i\alpha_1} + M_2 e^{-i\phi_2} e^{i\alpha_2}, \end{aligned} \quad (2.26)$$

with ϕ_i being the weak phases (and thus switches sign under CP conjugation), α_i being the strong final-state phases and M_i being real moduli of the matrix elements [97]. Consequently, their asymmetry reads

$$\frac{\Gamma(i \rightarrow f) - \Gamma(\bar{i} \rightarrow \bar{f})}{\Gamma(i \rightarrow f) + \Gamma(\bar{i} \rightarrow \bar{f})} = \frac{-2M_1 M_2 \sin(\phi_1 - \phi_2) \sin(\alpha_1 - \alpha_2)}{|M_1|^2 + |M_2|^2 + 2M_1 M_2 \cos(\phi_1 - \phi_2) \cos(\alpha_1 - \alpha_2)}. \quad (2.27)$$

According to Equation (2.27), a non-zero asymmetry is achieved if there are at least two interfering amplitudes M_i with both different weak and strong phases ϕ_i and α_i , respectively. In order to experimentally investigate CP violation in the decay of neutral kaons, where also $K^0 - \bar{K}^0$ mixing occurs, the following observables can be defined [56]

$$\eta_{+-} \equiv \frac{A[K_L \rightarrow \pi^+ \pi^-]}{A[K_S \rightarrow \pi^+ \pi^-]}, \quad (2.28)$$

$$\eta_{00} \equiv \frac{A[K_L \rightarrow \pi^0 \pi^0]}{A[K_S \rightarrow \pi^0 \pi^0]}, \quad (2.29)$$

$$\varepsilon \equiv \frac{A[K_L \rightarrow (\pi\pi)_{I=0}]}{A[K_S \rightarrow (\pi\pi)_{I=0}]}, \quad (2.30)$$

$$\frac{\sqrt{2}\varepsilon'}{\varepsilon} = \frac{A[K_L \rightarrow (\pi\pi)_{I=2}]}{A[K_L \rightarrow (\pi\pi)_{I=0}]} - \frac{A[K_S \rightarrow (\pi\pi)_{I=2}]}{A[K_S \rightarrow (\pi\pi)_{I=0}]}. \quad (2.31)$$

Note that in Equation (2.31) the parameter ε' is related to direct CP violation only, whereas ε is related to indirect CP violation. The observables are related via $\eta_{+-} = \varepsilon + \varepsilon'$ and $\eta_{00} = \varepsilon - 2\varepsilon'$. By this, the measured ratio $\frac{\varepsilon'}{\varepsilon}$ is

$$\operatorname{Re}\left(\frac{\varepsilon'}{\varepsilon}\right) = \frac{1}{6} \left\{ 1 - \frac{\Gamma[\mathbf{K}_L \rightarrow \pi^+\pi^-]/\Gamma[\mathbf{K}_S \rightarrow \pi^+\pi^-]}{\Gamma[\mathbf{K}_L \rightarrow \pi^0\pi^0]/\Gamma[\mathbf{K}_S \rightarrow \pi^0\pi^0]} \right\}. \quad (2.32)$$

Its value was measured to be $\operatorname{Re}\left(\frac{\varepsilon'}{\varepsilon}\right) = (1.66 \pm 0.16) \cdot 10^{-3}$ [100], which cannot be reliably predicted by the Standard Model [101–103]. Comparing the experimental values from direct and indirect CP violation, it can easily be seen that the contribution from $\mathbf{K}^0 - \bar{\mathbf{K}}^0$ mixing is approximately twice as large as the contribution from the decay of neutral kaons.

Scalar Isoscalar Sector

Figure 2.3 has already introduced the pseudoscalar as well as the vector mesons. However, *scalar* mesons with $J^{PC} = 0^{++}$ also play an important role in this work. Hence, they are discussed in the following. Although the $\mathcal{I} = \frac{1}{2}$ and $\mathcal{I} = 1$ states would have to be assigned a separate chapter, this work restricts to the scalar isoscalar sector ($\mathcal{I} = 0$). For a detailed discussion on light exotics see [104].

Contrary to pseudoscalar and vector mesons, the identification of scalar isoscalar mesons is a long-standing puzzle. Present resonances show large decay widths [56] and, thus, a strong overlap between their decay amplitudes. Additionally, several inelasticities like the opening of decay channels (e.g. at the $\mathbf{K}\bar{\mathbf{K}}, \eta\eta$ mass thresholds) producing cusps in the lineshapes of neighbored resonances have to be taken into account. A detailed overview about the dynamical parts of such amplitudes is given in Section 2.5.

In the last decades, multiple states with scalar quantum numbers were discovered and discussed. At present time, five scalar isoscalar resonances, namely the broad $\mathbf{f}_0(500)$ (or σ), the $\mathbf{f}_0(980)$, the broad $\mathbf{f}_0(1370)$, the comparatively narrow $\mathbf{f}_0(1500)$ and the $\mathbf{f}_0(1710)$ are well-established and listed by the **P**article **D**ata **G**roup (PDG) [56]. To study the scalar isoscalar sector, data has been obtained from $\pi\pi, \mathbf{K}\bar{\mathbf{K}}, \eta\eta, 4\pi$ and $\eta\eta'$ systems produced in S -wave. Both theoretical [58] and experimental [56] results are consistent with two nonets, one below and another one above $\sqrt{s} = 1 \text{ GeV}$, with evidence for gluonic degrees of freedom. The observed phenomenon of multiplet doubling requires an effective chiral quark model, e.g. a coupled linear sigma model [59,60] to provide an understanding of the light scalar spectrum. Within this model, the lightest scalars may be interpreted as Higgs-like bosons for the non-perturbative low-energy strong interaction.

Simultaneously to the experimentally observed overpopulation of states, lattice QCD calculations predict the lightest glueball to have quantum numbers $J^{PC} = 0^{++}$ and a mass around $1.6 - 1.7 \text{ GeV}/c^2$ [61–64]. There are several signatures expected for

glueballs, for example isoscalar states that do not fit into ordinary $q\bar{q}$ nonets, an enhanced production in gluon-rich channels such as radiative J/ψ decays [105], decay branching fractions incompatible with $SU(N)$ predictions for $q\bar{q}$ states or reduced $\gamma\gamma$ coupling. Due to the possible mixing of glueballs with nearby isoscalar $q\bar{q}$ states of the same quantum numbers, these signatures may be affected, e.g., leading to a supernumerary isoscalar state in the heavier nonet above $\sqrt{s} = 1$ GeV [61, 106–110]. A brief overview about the experimental status of the scalar isoscalar resonances as well as current interpretations is given in the following, starting with the $f_0(980)$.

The nature of the $f_0(980)$ is still inconclusive as it can be described both in the tetraquark picture [111–114] and as a $K\bar{K}$ molecule [115] due to its large branching ratio into $K\bar{K}$. Data from radiative ϕ meson decays into $f_0(980)$ [116–119] seemed to favor the tetraquark description [120, 121]. In contradiction to that, measurements of ratios of decay rates of $B_{(s)} \rightarrow J/\psi\pi\pi$ [52, 53] show an evident deviation from the tetraquark picture [122] as well as stating substantial $s\bar{s}$ content of the $f_0(980)$. This result was later put into question by a dispersive analysis [123].

The $f_0(1370)$ and the $f_0(1500)$ decay prominently into 4π [124, 125], while the heavier $f_0(1710)$ favors to decay into the $K\bar{K}$ final state [126]. According to the quark model, these observed decay patterns suggest an $u\bar{u} + d\bar{d}$ structure for the $f_0(1370)$ and the $f_0(1500)$, and $s\bar{s}$ for the $f_0(1710)$. The latter is further justified by the suppressed production rate in $p\bar{p}$ annihilation [127, 128], as expected from the OZI suppression [129] for an $s\bar{s}$ state. However, experimental results from $\gamma\gamma$ collisions, which are sensible to glue mixing with $q\bar{q}$ [130], have shown contradictions to this naive assumption. The $f_0(1500)$ is not observed in $\gamma\gamma \rightarrow K\bar{K}$ [131–133] nor in $\gamma\gamma \rightarrow \pi\pi$ [134, 135]. The absence of the $f_0(1500)$ in the $\pi\pi$ channel in $\gamma\gamma$ collisions as well as its small $K\bar{K}$ decay branching ratio does not favor a large $u\bar{u} + d\bar{d}$ nor $s\bar{s}$ structure, respectively, but mainly a gluonic one.

According to the mixing scheme in [130] based on recent hadronic J/ψ data from BESIII [136, 137], glue is shared between the $f_0(1370)$, the $f_0(1500)$ and the $f_0(1710)$, indicating almost pure $u\bar{u} + d\bar{d}$ content for the $f_0(1370)$, mainly glue content for the $f_0(1500)$ and dominantly $s\bar{s}$ for the $f_0(1710)$. Using the same data, the $f_0(1500)$ is observed with a much smaller contribution than the $f_0(1710)$ in $J/\psi \rightarrow \gamma\pi\pi$ [138] and $J/\psi \rightarrow \gamma\eta\eta$ [139], in disagreement with a glueball interpretation of the $f_0(1500)$. However, clarification about the inner structure of the resonances in the scalar isoscalar sector is still lacking. Sophisticated analyses need to be redone using higher luminosity data sets as well as theoretical models based on principles of scattering theory such as unitarity. An example for a formalism having these features built in, allowing for an extraction of resonance properties while mapping smoothly onto the well constrained low-energy amplitudes at $\sqrt{s} < 1$ GeV is presented in Section 2.6. For a broader discussion of the scalar isoscalar states as well as their $\mathcal{I} = \frac{1}{2}$ and $\mathcal{I} = 1$ partners we refer to the “Non- $q\bar{q}$ Mesons” as well as to the “Scalar Mesons below 2 GeV” mini-review of the PDG [56].

2.3.2. Baryons

Conventional baryons consist of three quarks qqq and thus carry baryon number $B = 1$. Using group theory, the baryon wave function can be decomposed into the subspaces

$$|qqq\rangle = |\text{color}\rangle \otimes |\text{space}\rangle \otimes |\text{spin}\rangle \otimes |\text{flavor}\rangle. \quad (2.33)$$

As half-odd-integer particles they obey the Fermi statistics, requiring a fully antisymmetric wave function under the exchange of two quarks. Since the color wave function of the lightest multiplet needs always to be in an antisymmetric color singlet, the remaining wave functions need to be symmetric. Further, the spin wave function can be decomposed into the subspaces [72]

$$2 \otimes 2 \otimes 2 = (2)_M \oplus (2)_M \oplus (4)_S, \quad (2.34)$$

with M and S denoting mixed and full symmetry, respectively. The flavor wave function can be decomposed according to $SU(3)$ flavor symmetry into

$$3 \otimes 3 \otimes 3 = (10)_S \oplus (8)_M \oplus (8)_M \oplus (1)_A, \quad (2.35)$$

with A denoting fully asymmetric. Finally, the space wave function can be identified as a representation of $SO(3)$ spacial symmetry using Jacobi coordinates [72], thus denoting it by an angular momentum L . For $L = 0$ the baryon octet with $J^P = \frac{1}{2}^+$ and decuplet with $J^P = \frac{3}{2}^+$ can be build, as shown in Figure 2.4. Furthermore, a rich spectrum of excited baryon states for higher angular momentum L can be obtained accordingly, whose resonances are experimentally well confirmed. However, knowledge on the fundamental degrees of freedom present in the excited baryon spectrum is still lacking [140].

2.3.3. Charmonia

Mesons containing c, \bar{c} quarks are charmed D mesons ($c\bar{d}, c\bar{u}$), flavorless charmonia ($c\bar{c}$) or exotics, e.g. tetraquarks $c\bar{c}q\bar{q}$. The experimentally observed charmonium and charmonium-like spectrum is shown in Figure 2.5, having the η_c with $J^{PC} = 0^{-+}$ as its ground state and covering a mass range approximately up to $5 \text{ GeV}/c^2$. Hence, charmonium spectroscopy is a powerful tool to investigate the transition region between perturbative and non-perturbative QCD.

Among many, the most prominent representative is the vector charmonium J/ψ , which was simultaneously observed by experiments led by Burton Richter [20] and Samuel C. C. Ting [19] in 1974. Below the $D\bar{D}$ thresholds, the observed spectrum can be well described by the **Non-Relativistic Quark Model** (NRQM) [27]. Above these so-called open charm thresholds, where conventional charmonia are dominantly expected to decay OZI-allowed [129] into $D\bar{D}$ pairs, the description fails unexpectedly. Instead, a clear overpopulation

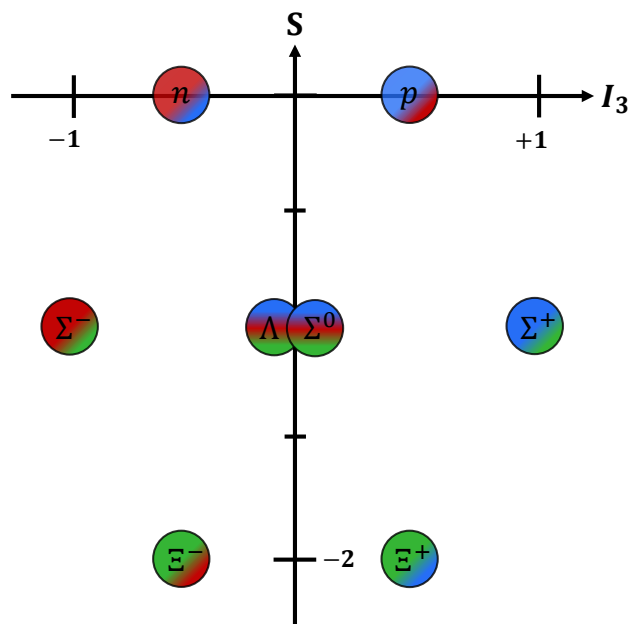


Figure 2.4.: Schematic representation of the octet of baryons, build up of three quarks qqq with $J^P = \frac{1}{2}^+$. The third component of the isospin I_3 is shown on the abscissa and the strangeness S on the ordinate. Colors indicate different quark flavors of the three lightest quarks, u (blue), d (red) and s (green).

of states is observed in recent years which do not fit into the NRQM. These states are called exotic and will be discussed in the next section.

2.3.4. Exotics

The rich spectrum observed by experiments involving heavy quarks such as the charm quark contains interesting new exotic states, especially above the various $D\bar{D}$ thresholds. In contrast to the scalar isoscalar sector, these states are mostly well separated from each other. However, they are typically measured in three-particle decays, leading to many crossed-channel resonances due to the large phase space which needs to be taken into account. Their interference necessarily has to be described by proper theoretical frameworks, from which many interpretations about the inner structure of exotic states have been arisen. They are mainly based on the assumption, that more complex configurations of quarks and gluons, despite the conventional mesons and baryons, are allowed to exist. As already predicted by Gell-Mann [16], group theory allows for color singlets consisting of more than a quark-antiquark pair or three quarks. Mesons and baryons may be easily extended to tetraquarks and molecules ($qq\bar{q}\bar{q}$) or pentaquarks ($qqqq\bar{q}$), respectively. Due to the self coupling of gluons in QCD, also hybrids ($q\bar{q}g$) or glueballs (gg, ggg) may exist. Experimental evidences for states beyond the conventional

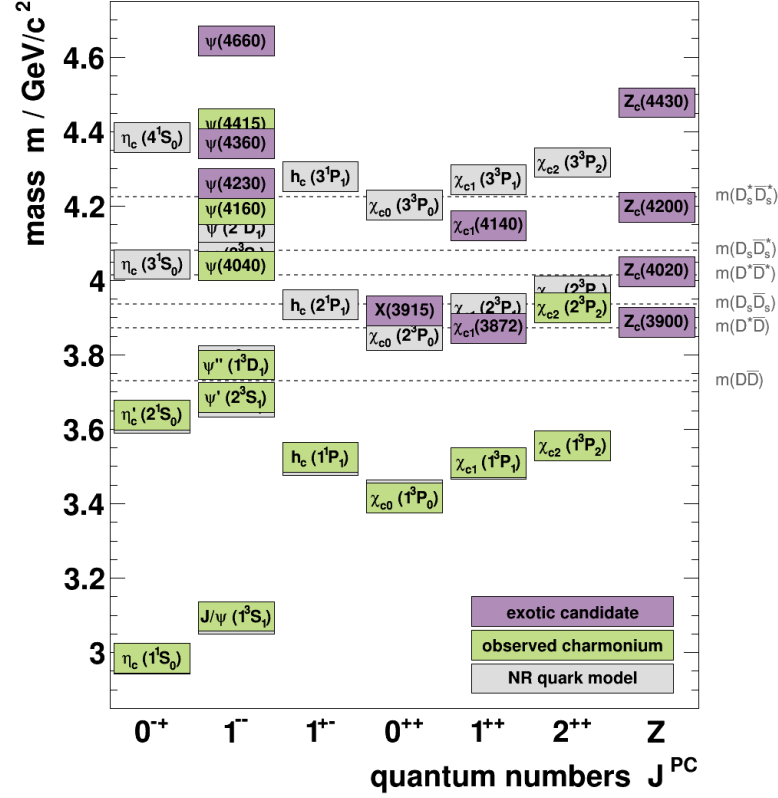


Figure 2.5.: Schematic representation of the charmonium spectrum in the mass region available at BESIII with quantum numbers in spin-parity notation J^{PC} . Charged charmonium-like states Z are shown in a separate column, since they are not conventional charmonium states ($c\bar{c}$). States predicted in the non-relativistic quark model but not yet discovered are represented by gray boxes. Experimentally confirmed states are shown by green boxes, while purple boxes represent exotic candidates that do not fit the conventional charmonium spectrum. Dashed lines indicate different open charm thresholds.

quark model in the heavy quark sector accumulated in recent years are presented in the following.

Since the discovery of the exotic $\chi_{c1}(3872)$ in $B^\pm \rightarrow K^\pm \chi_{c1}(3872)$ with $\chi_{c1}(3872) \rightarrow J/\psi \pi^+ \pi^-$ by Belle in 2003 [2] and later confirmed by BaBar [141], many new exotics have been searched for and also successfully discovered. The states being well-established and confirmed by the PDG within the charmonium sector are the four charged $Z_c(3900)^\pm$, $Z_c(4020)^\pm$, $Z_c(4200)^\pm$, $Z_c(4430)^\pm$ and the four neutral $\chi_{c1}(3872)$, $\psi(4230)$, $\psi(4360)$, $\psi(4460)$ [56]. The $\psi(4230)$ was originally discovered by BaBar decaying to $J/\psi \pi^+ \pi^-$ in initial state radiation $e^+ e^- \rightarrow \gamma(e^+ e^- \rightarrow \psi(4230))$ in 2005 [28]. BESIII reported this state in Born cross section studies of $e^+ e^- \rightarrow J/\psi \pi^+ \pi^-$ [29] using improved statistics with a slightly lower mass, and also stated the need of a second heavier resonance $\psi(4360)$. While a simple Breit-Wigner ansatz in [29] needs two distinct resonances to describe the region around $\sqrt{s} = 4.23$ GeV, the $D_1 \bar{D}$ molecular model accurately describes the

data using only one pole [142, 143]. Further experimental insights into the $\psi(4230)$ may have been revealed with the observations of $\psi(4230) \rightarrow \pi^\mp Z_c(3900)^\pm$ [30] and $\psi(4230) \rightarrow \gamma \chi_{c1}(3872)$ [144] at BESIII, which both can be explained with a dominant $D_1 \bar{D}$ component in the $\psi(4230)$ [145, 146].

Since no significant coupling of the $\psi(4230)$ to the $D\bar{D}$ final state has been observed [38, 40, 41], current interpretations also describe this state as a hybrid charmonium with spin-1 $c\bar{c}$ [147, 148] or a spin-0 $c\bar{c}$ [149, 150] core. The former may be ruled out by the observation of $\psi(4230) \rightarrow h_c \pi^+ \pi^-$ [151] due to the zero spin of the $c\bar{c}$ system in h_c , which is assumed to be conserved in the decay. Additionally, other models have been proposed to interpret the $\psi(4230)$ as a tetraquark state [33, 34].

However, a common consensus about the inner structure of the $\psi(4230)$ is still missing. Thus, precise analyses using high luminosity data sets are needed in order to search for possible decay patterns as well as production mechanisms of the $\psi(4230)$ or exotic states generally. Possible decay mechanisms include radiative or hadronic transitions to lighter charmonia, open charm decays to $D\bar{D}$ pairs or decays to light mesons or baryons. Especially the latter are of high interest, since they have not been observed so far, e.g. in the processes $e^+e^- \rightarrow p\bar{p}\pi^0$ [49], $\phi\phi\phi$, $\phi\phi\omega$ [45], $\rho K_S^0 \bar{n} K^-$ [152], $K_S^0 K^\pm \pi^\mp$ [46], $K_S^0 K^\pm \pi^\mp \pi^0$, $K_S^0 K^\pm \pi^\mp \eta$ [47], $2(p\bar{p})$ [48], $\phi\lambda\lambda$ [44], $p\bar{p}\eta$ and $p\bar{p}\omega$ [50]. In this work, the final states $\phi K\bar{K}$ and $p\bar{p}\eta'$ are studied in the search for couplings of the $\psi(4230)$ to these light mesons and baryons. Of special interest are final states involving a $p\bar{p}$ pair, since the partial width $\Gamma_{V \rightarrow p\bar{p}h}$ with V being a vector charmonium or charmonium-like state and h being a light meson, can be related to the production cross section $\sigma_{p\bar{p} \rightarrow Vh}$ using [54]

$$\sigma_{p\bar{p} \rightarrow Vh}(s) = 4\pi^2 (2S_V + 1) \frac{M_V^3}{A_D} \Gamma_{V \rightarrow p\bar{p}h} \left[\frac{p_{h,cm}}{p_{p,cm}} s^{-1} \right], \quad (2.36)$$

with S_V and M_V being the spin and mass of particle V , respectively, A_D being the area of the Dalitz plot and $p_{i,cm}$ being the momentum of particle i in the center-of-mass system. In light of the upcoming PANDA (Antiproton Annihilation at Darmstadt) experiment at the Facility for Antiproton and Ion Research (FAIR) [55], it is important to obtain partial widths and, thus, production cross sections of potentially exotic vector charmonia with high accuracy.

The BESIII experiment is well suited for such studies, since exotic states like the $\psi(4230)$ with $J^{PC} = 1^{--}$ can be produced directly from e^+e^- annihilation due to the fixed quantum numbers $J^{PC} = 1^{--}$ of the initial state [153]. For a broader discussion on the current theoretical and experimental status of exotic states, we refer to the ‘‘Non- $q\bar{q}$ Mesons’’ mini-review of the PDG [56], as well as to [154].

2.4. Elements of Scattering Theory

Particle accelerator experiments provide an excellent opportunity for hadron spectroscopy. Among the many open questions that need to be answered, sophisticated analysis techniques like partial wave analyses become more and more important. Compared to previous experiments, nowadays statistics available are more than suitable to carry out those analyses on a level of precision which could not have been achieved before.

One of the most important necessities of such experiments is the study of analytical properties of amplitudes, since the discovery and investigation of new particles base mainly on the study of leading singularities in the amplitudes. Scattering amplitudes can be separated into a *spin part*, describing the spin structure of the scattering (or production) process, and a *dynamical part*, describing the energy-dependence of the amplitude. In this work, the spin structure of all processes involved is described by the so-called helicity formalism [155], which will be described in Section 2.7. However, a more detailed discussion of the dynamical part of amplitudes will be provided in the next paragraphs.

Scattering in Quantum Mechanics

Before the discussion about the different representations of partial wave amplitudes is given, it is important to derive a general expression for the scattering amplitude. Starting with non-relativistic two-particle elastic scattering of spinless particles (e.g., $\pi\pi \rightarrow \pi\pi$ or $KK \rightarrow KK$), the Hamiltonian of such a process is equal to

$$\hat{H} = -\frac{1}{2m_1}\Delta_1 - \frac{1}{2m_2}\Delta_2 + V(r), \quad (2.37)$$

with m_i and $\Delta_i = \frac{\partial^2}{\partial x_i^2} + \frac{\partial^2}{\partial y_i^2} + \frac{\partial^2}{\partial z_i^2}$ being the mass and the Laplace operator for the coordinates of particle i , respectively, and $V(r)$ being the interaction potential depending on the distance $r = |\vec{r}| = |\vec{r}_1 - \vec{r}_2|$ between particles 1 and 2. In the center of inertia, the Hamiltonian can be reduced to a sum of two independent terms: a free movement of the center-of-mass and an interaction of the particles. Equivalently, the two particle wave function $\psi(\vec{r}_1, \vec{r}_2)$ can be written in the factorized form

$$\psi(\vec{r}_1, \vec{r}_2) = \phi(\vec{R})\psi(\vec{r}), \quad (2.38)$$

with $\phi(\vec{R})$ and $\psi(\vec{r})$ representing the center-of-mass movement and the relative movement of particles 1 and 2 (which is equal to the movement of a particle with mass m in the centrally symmetrical field $V(r)$), respectively.

In spherical coordinates, $\psi(\vec{r})$ reads $\psi(\vec{r}) = R(r)Y_{l,m}(\theta, \phi)$ with the radial wave function

$R(r)$ and the angular-dependent function $Y_{l,m}(\theta, \phi)$ with angular momentum l and its projection m . At large distances, where $V(r)$ can be neglected, the radial wave function $R(r)$ obeys the equation

$$\frac{1}{r} \frac{d^2(rR)}{dr^2} + k^2 R = 0, \quad (2.39)$$

with $k = \sqrt{2mE}$ and E being the energy. Its general solution can be written as

$$R \approx \sqrt{\frac{2}{\pi}} \frac{\sin(kr - l\pi/2 + \delta_l)}{r}, \quad (2.40)$$

with δ_l being the so-called *phase shift*, defining the behavior of $R(r)$ at comparatively small r [88].

The scattering of two particles can be reformulated as a scattering of one particle on the stationary field $V(r)$. In the center-of-mass system, where the total momentum is $\vec{P}(1+2) = 0$, the two particle wave function is determined by $\psi(\vec{r})$ only (since $\phi(\vec{R}) = 1$ without loss of generality). Assuming the movement of a free incoming particle along the z -axis before scattering, which can be described by a plane wave e^{ikz} , and an outgoing particle after scattering, which can be described (at asymptotically large distances) by a spherical outgoing wave

$$f(\theta) \frac{e^{ikr}}{r} \quad (2.41)$$

with scattering amplitude $f(\theta)$, the wave function can be written as

$$\psi(r) \simeq e^{ikz} + \frac{f(\theta)}{r} e^{ikr}. \quad (2.42)$$

Note that $f(\theta)$ is fully determined by the phase shifts δ_l . Equation (2.42) is called the asymptotic expression for the wave function. It describes the flux of incoming particles with density v and the flux of outgoing particles. Scattered particles may go through an element of the surface $dS = r^2 d\Omega$ with the probability

$$v |\psi_{\text{out}}|^2 d\Omega = v |f(\theta)|^2 d\Omega. \quad (2.43)$$

The cross section is defined by its ratio to the flux of the incoming particles

$$d\sigma = |f(\theta)|^2 d\Omega = 2\pi |f(\theta)|^2 \sin\theta d\theta. \quad (2.44)$$

In case of elastic scattering, the scattering amplitude $f(\theta)$ can be expressed as

$$f(\theta) = \frac{1}{2ik} \sum_l (2l+1) (e^{2i\delta_l} - 1) P_l(\cos\theta), \quad (2.45)$$

with $P_l(\cos\theta)$ being some standard Legendre-polynomials and

$$f_l = \frac{1}{2ik}(e^{2i\delta_l} - 1) = \frac{1}{k}e^{i\delta_l} \sin \delta_l \quad (2.46)$$

defining a partial wave amplitude. Note that in case of scattering with absorption (inelastic scattering, e.g., $\pi\pi \rightarrow \text{KK}$ or $\text{KK} \rightarrow \pi\pi$), the intensities of incoming and outgoing waves are no longer equal. The inelasticity parameter η_l with $0 \leq \eta_l \leq 1$ incorporates such processes in the corresponding partial wave amplitude

$$f_l = \frac{1}{2ik}\eta_l(e^{2i\delta_l} - 1). \quad (2.47)$$

Inelastic processes ($\eta_l \neq 1$) contribute to the imaginary part of the scattering amplitude [88].

In the following, an overview about the framework of *dispersion theory* is given. After the S -matrix is introduced, describing the probability for the transition from the initial to the final state, the dispersion integral as well as the homogeneous Omnès problem will be discussed.

2.5. Dispersion Theory

In Section 2.2 the theory of strong interaction, QCD, was introduced. It leads to a wide range of phenomena, which still need to be understood. As already discussed in Section 2.3, many experiments showed the abundant existence of bound states compared to the most simple quark model predictions. In order to gain insights into their nature, theoretically sound studies are required, preserving fundamental physical properties such as Lorentz invariance, causality and probability conservation. Since the standard perturbation theory approach in the strong coupling constant is not applicable at the hadronic scale, proper alternatives have to be carried out. One of them is dispersion theory, including analyticity, unitarity and crossing symmetry by construction. Unfortunately, the application of dispersion theory is restricted to low energies due to the opening of inelastic channels. Therefore, an effective high-energy extension of the dispersive framework [156] is presented in Section 2.6.

While the renormalization procedure in QFT has been established for singularities of QED in the fifties and sixties by Dyson, Feynman, Schwinger and others [73–81], the description of the strong force with QFT proved to be difficult and has only been provided in the seventies [24–26]. In the meantime, there was some prejudice that a solution outside field theory has to be found, namely the S -matrix theory [157–162]. Being based on dispersion theory [163, 164], the S -matrix relates the infinite past to the infinite future in one step, without being decomposable into intermediate steps corresponding to time-

slices. The coming passages intend to present its basic theory as well as their analytic properties.

2.5.1. S-matrix Theory

In an experiment, in which, for the sake of clarity, only a short ranged interaction (e.g. QCD) of the involved particles is considered, initial states i and final states f are prepared in the distant past and future, respectively, by [163]

$$|i, \text{in}\rangle = |i, t \rightarrow -\infty\rangle \quad \text{and} \quad |f, \text{out}\rangle = |f, t \rightarrow +\infty\rangle, \quad (2.48)$$

where t denotes the time. These states are normalized ($\langle i, \text{in}|j, \text{in}\rangle = \langle i, \text{out}|j, \text{out}\rangle = \delta_{ij}$) and fulfill the completeness relation (e.g. for the initial states)

$$1 = \sum_m |m, \text{in}\rangle \langle m, \text{in}|. \quad (2.49)$$

The probability for the transition from the initial to the final state

$$|\langle f, \text{out}|i, \text{in}\rangle|^2 = |\langle f, \text{in}|S|i, \text{in}\rangle|^2 = |\langle f, \text{out}|S|i, \text{out}\rangle|^2 \quad (2.50)$$

is described by the so-called S -matrix. Its unitarity (probability conservation) reads

$$SS^\dagger = S^\dagger S = 1. \quad (2.51)$$

Since the momenta of relativistic particles are easier to measure than their position, it is common to work in momentum space, where each state $|i\rangle$ is a state consisting of n particles with quantum numbers β_j and momenta p_j with $j = 1, \dots, n$

$$|i\rangle = |\beta_1, p_1\rangle \otimes |\beta_2, p_2\rangle \otimes \dots \otimes |\beta_n, p_n\rangle. \quad (2.52)$$

All particles fulfill the on-shell condition $p_j^2 = m_j^2$ and thus the normalization for each single-particle state is [163]

$$\langle \beta_i, p|\beta_j, k\rangle = 2p^0 \delta_{\beta_i, \beta_j} (2\pi)^3 \delta^3(\vec{p} - \vec{k}). \quad (2.53)$$

Because the particles have a defined momentum, they are not localized in position space due to the Heisenberg uncertainty principle. Hence, they will pass each other without interacting. The S -matrix can then be written as

$$S = 1 + iR, \quad (2.54)$$

separating off the interaction part R , which is usually defined as a distribution (following overall momentum conservation as well as Lorentz invariance)

$$\langle f|R|i\rangle = (2\pi)^4 \delta^4(p_i - p_f) \langle f|T|i\rangle, \quad (2.55)$$

with p_i and p_f being the overall momenta of the initial and final state, respectively, and transition amplitude T . Further, the unitarity of the S -matrix (Equation (2.51)) can be invoked to write

$$\langle f|R|i\rangle - \langle f|R^\dagger|i\rangle = i \langle f|R^\dagger R|i\rangle. \quad (2.56)$$

The unitarity relation for T can then be obtained after some calculations as [163]

$$\langle f|T|i\rangle - \langle i|T|f\rangle^* = i \sum_m (2\pi)^4 \delta^4(p_i - p_m) \langle m|T|f\rangle^* \langle m|T|i\rangle, \quad (2.57)$$

which can be simplified using $\langle i|S|f\rangle = \langle f|S|i\rangle$ to

$$2i \operatorname{Im} \langle f|T|i\rangle = i \sum_m (2\pi)^4 \delta^4(p_i - p_m) \langle f|T|m\rangle^* \langle m|T|i\rangle. \quad (2.58)$$

2.5.2. Analytical Properties of the S -Matrix

Besides unitarity, analyticity is another important property of the S -matrix, which is related to the micro-causality condition for some arbitrary field operator $\phi(x)$

$$[\phi(x), \phi(y)] = 0 \quad \text{if} \quad (x - y)^2 < 0. \quad (2.59)$$

This equation ensures that information cannot be transmitted faster than the speed of light. From now on we restrict ourselves to the scattering process of four scalar particles

$$\phi_1(p_1) + \phi_2(p_2) \rightarrow \phi_3(p_3) + \phi_4(p_4) \quad (2.60)$$

to illustrate further properties of the S -matrix. In the presence of spins, the helicity formalism (see Section 2.7) developed by Jacob and Wick [165,166] may be used to ensure the proper description of the spin structure of the processes investigated. Commonly, decays are described within the *isobar model*, treating sequential decays as a coherent sum of two-body interactions.

All momenta are restricted by the mass-shell condition $p_a^2 = m_a^2$ with $a = 1, \dots, 4$. For scalar particles, T will only depend on the momenta [163]

$$\langle \phi_3(p_3) \phi_4(p_4) | T | \phi_1(p_1) \phi_2(p_2) \rangle = T^{fi}(p_1, p_2; p_3, p_4). \quad (2.61)$$

2. Theoretical Framework

In order to preserve Lorentz invariance, the amplitude T can only depend on the Lorentz invariant products [163, 167]

$$s_{xy} = p_x \cdot p_y \quad \text{with} \quad x, y = 1, \dots, 4 \quad (2.62)$$

and

$$\epsilon_{abcd} = \epsilon_{\mu\nu\alpha\beta} p_a^\mu p_b^\nu p_c^\alpha p_d^\beta, \quad (2.63)$$

with $\epsilon_{\mu\nu\alpha\beta}$ being the antisymmetric fourth-order tensor. This can be written as

$$T^{fi}(p_1, p_2; p_3, p_4) = T_s^{fi}(s_{xy}) + \epsilon_{abcd} T_{abcd}^{fi}(s_{xy}). \quad (2.64)$$

The first term on the right-hand side of Equation (2.64) transforms even under parity, the second term changes sign. Since the strong interaction is parity conserving, the last term can be neglected. Not all possible contractions s_{xy} are independent of each other. In fact, only two of them are necessary to describe the amplitude due to the on-shell conditions and momentum conservation. Commonly, the Mandelstam variables [168] are chosen given by

$$s = (p_1 + p_2)^2, \quad t = (p_1 - p_3)^2 \quad \text{and} \quad u = (p_1 - p_4)^2. \quad (2.65)$$

The transition amplitude can now be expressed as

$$T^{fi}(p_1, p_2; p_3, p_4) = T^{fi}(s, t, u) \quad (2.66)$$

with the relation

$$s + t + u = m_1^2 + m_2^2 + m_3^2 + m_4^2. \quad (2.67)$$

If the scattering is described in the center-of-mass system (CMS), the momenta can be written as

$$p_1 = \begin{pmatrix} p_1^0 \\ \vec{p}_{12} \end{pmatrix}, p_2 = \begin{pmatrix} p_2^0 \\ -\vec{p}_{12} \end{pmatrix}, p_3 = \begin{pmatrix} p_3^0 \\ \vec{p}_{34} \end{pmatrix} \quad \text{and} \quad p_4 = \begin{pmatrix} p_4^0 \\ -\vec{p}_{34} \end{pmatrix} \quad (2.68)$$

with

$$\begin{aligned} p_{1/2}^0 &= \sqrt{|\vec{p}_{12}|^2 + m_{1/2}^2} \quad , \quad |\vec{p}_{12}|^2 = \frac{\lambda(s, m_1^2, m_2^2)}{4s} \\ p_{3/4}^0 &= \sqrt{|\vec{p}_{34}|^2 + m_{3/4}^2} \quad , \quad |\vec{p}_{34}|^2 = \frac{\lambda(s, m_3^2, m_4^2)}{4s} \end{aligned} \quad (2.69)$$

and the Källén function $\lambda(a, b, c)$

$$\lambda(a, b, c) = \left(a - (\sqrt{b} + \sqrt{c})^2 \right) \left(a - (\sqrt{b} - \sqrt{c})^2 \right). \quad (2.70)$$

Using this notation, the Mandelstam variables t and u can be expressed through s and the scattering angle θ_s between \vec{p}_{12} and \vec{p}_{34} as

$$t = \frac{1}{2} \left(\sum_{i=1}^4 m_i^2 - s + (m_2^2 - m_1^2)(m_3^2 - m_4^2) + 4|\vec{p}_{12}||\vec{p}_{34}|\cos\theta_s \right) \quad (2.71)$$

and

$$u = \frac{1}{2} \left(\sum_{i=1}^4 m_i^2 - s - (m_2^2 - m_1^2)(m_3^2 - m_4^2) - 4|\vec{p}_{12}||\vec{p}_{34}|\cos\theta_s \right). \quad (2.72)$$

Further, T can be partial wave projected, which reads for scalar particles [163]

$$T^{fi}(s, t, u) = T(s, \cos\theta_s) = 8\pi \sum_{l=0}^{\infty} (2l+1) P_l(\cos\theta_s) t_l^{fi}(s), \quad (2.73)$$

with $P_l(\cos\theta_s)$ being the standard Legendre-polynomials and $t_l(s)$ being the partial wave amplitude (see Equation (2.46)). The unitarity equation for $t_l(s)$ in case of two-particle intermediate states with masses m_a and m_b reads

$$\text{Im } t_l^{fi}(s) = \sum_{m=\{m_a, m_b\}} (t_l^{fm})^*(s) \sigma(s, m_a, m_b) t_l^{mi}(s) \quad (2.74)$$

with the phase space factor

$$\sigma(s, m_a, m_b) = \frac{\sqrt{\lambda(s, m_a^2, m_b^2)}}{s} \theta(s - (m_a + m_b)^2). \quad (2.75)$$

This derivation only applies for $s > \max\{(m_1 + m_2)^2, (m_3 + m_4)^2\}$ as the initial and final states were assumed to be asymptotic states [169].

Using the *CPT*-theorem in QFT [170–173], the s -channel process can be related to the t -channel and the u -channel processes by replacing a particle in an incoming state with an antiparticle in an outgoing state with reversed momentum. A three body decay of m_1 may then be written as

$$\phi_1(p_1) \rightarrow \bar{\phi}_2(-p_2) + \phi_3(p_3) + \phi_4(p_4). \quad (2.76)$$

In the framework of S -matrix theory, the s -, t - and u -channels are related by requiring crossing symmetry. Here, they are described by the same amplitude $T(s, t, u)$ which

is continued into different energy regions of the Mandelstam variables s, t and u (see Figure 2.6). The s -channel produces imaginary parts for

$$s > \max\{(m_1 + m_2)^2, (m_3 + m_4)^2\} = s_{\text{thr}} \quad (2.77)$$

and correspondingly the t - and u -channel for

$$\begin{aligned} t &> \max\{(m_1 + m_3)^2, (m_2 + m_4)^2\} = t_{\text{thr}} \\ u &> \max\{(m_1 + m_4)^2, (m_2 + m_3)^2\} = u_{\text{thr}}. \end{aligned} \quad (2.78)$$

Hence, the partial wave amplitude in the s -channel does not only have an imaginary part for $s > s_{\text{thr}}$, a so-called right-hand cut, but also an imaginary part extending to $-\infty$, a so-called left-hand cut, which is introduced due to the projection of $T(s, t, u)$ onto the s -channel process [169].

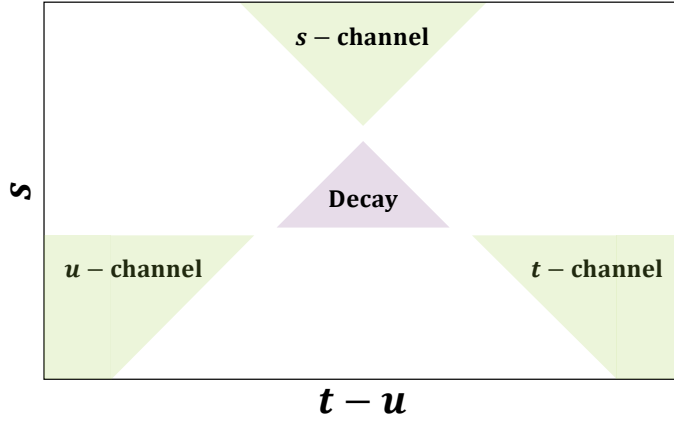


Figure 2.6.: Mandelstam plane, showing the s -, t - and u -channel as well as the decay region.

However, $t_l(s)$ can be analytically continued to the upper complex s -plane, without encountering singularities. In addition, it can also be defined in the entire complex s -plane using the Schwarz reflection principle $t_l(s) = t_l^*(s^*)$. The mentioned left- and right-hand cuts will then show up as discontinuities

$$\text{disc } t_l(s) = \lim_{\epsilon \rightarrow 0} (t_l(s + i\epsilon) - t_l(s - i\epsilon)) = 2i \text{Im } t_l(s). \quad (2.79)$$

$t_l(s)$ is therefore an analytic function in the entire first sheet of the complex s -plane, except for the discontinuities along the real axis and possible bound states below the lowest threshold. It follows, that the S -matrix is assumed to be analytic as well up to the aforementioned kinematic singularities and poles. These phenomena can be distinguished into *branch points*, *bound states*, *virtual states* and *resonances*.

Branch points can be distinguished into the aforementioned right- and left-hand cuts. While right-hand cuts occur at each threshold for a kinematically allowed process (e.g. at the KK threshold in the $\pi\pi$ scattering amplitude), left-hand cuts become present when reactions in the crossed channel become possible (e.g. in the reaction $e^+e^- \rightarrow \phi\text{K}\bar{\text{K}}$ at the K^* threshold with $\text{K}^* \rightarrow \phi\text{K}$ in the $\text{K}\bar{\text{K}}$ scattering amplitude). In fact, left-hand cuts are located in the unphysical region ($s < 0$) for the reaction under investigation but can still influence significantly their energy dependence.

Bound states appear as poles on the physical sheet ($s > 0$) and are only allowed to occur on the real s -axis below the lowest threshold.

Virtual states appear on the real s -axis on the unphysical sheet [174].

Resonances

Resonances appear as poles on the unphysical sheets close to the physical one. They show up either in formation experiments such as

$$e^+e^- \rightarrow \psi \rightarrow \phi\text{K}\bar{\text{K}}, \quad (2.80)$$

where they become visible in energy scans of the Born cross section, or in combination with a spectator particle m as an associated production in production experiments of the kind

$$e^+e^- \rightarrow m + f_J \rightarrow m + \text{K}\bar{\text{K}}, \quad (2.81)$$

with m being, i.e., the ϕ meson. The characteristics of interest are the pole position s_R in the complex s -plane and its residue \mathcal{R} . Usually, if the observed structure is narrow and if there are no relevant thresholds or other resonances nearby, a standard Breit-Wigner parametrization (see Subsection 2.5.3) may be employed in order to extract the resonance properties such as the mass M_R and width Γ_R . Their relation to the pole position is given by [56]

$$\sqrt{s_R} = M_R - i\Gamma_R/2. \quad (2.82)$$

However, in case one of these requirements is not satisfied, unitarity and analyticity get violated, and more sophisticated parametrizations need to be used. Examples are the K -matrix approach (see Subsection 2.5.4) or methods based on dispersion theory (see Section 2.6). Note that in case of broad resonances, Equation (2.82) is no longer valid so that the Breit-Wigner parameters deviate from the pole position.

A residue quantifies the coupling of a resonance to a certain channel and allows for the definition of branching ratios. Close to the resonance pole, the scattering matrix \mathcal{M} can be written as

$$\lim_{s \rightarrow s_R} (s - s_R)\mathcal{M}_{ba} = -\mathcal{R}_{ba}. \quad (2.83)$$

\mathcal{R}_{ab} can be calculated via an integration along a closed contour around the pole and its factorization $(\mathcal{R}_{ba})^2 = \mathcal{R}_{aa} \times \mathcal{R}_{bb}$ allows the introduction of pole couplings according to

$$\tilde{g}_a = \mathcal{R}_{ba} / \sqrt{\mathcal{R}_{bb}} \quad (2.84)$$

as well as the definition of a partial width and a branching fraction as [56]

$$\Gamma_{R \rightarrow a} = \frac{|\tilde{g}_a|^2}{M_R} \rho_a(M_R^2) \quad \text{and} \quad \text{Br}_{R \rightarrow a} = \Gamma_{R \rightarrow a} / \Gamma_R, \quad (2.85)$$

with $\rho_a(M_R^2)$ being a factor related to the two-body phase space. Note that both the pole position s_R and the pole coupling \tilde{g}_a (and therefore the partial decay width $\Gamma_{R \rightarrow a}$) are independent of the reaction studied. Similar to Equation (2.82) regarding the mass of a resonance, Equation (2.85) is equal to the commonly used definition of a branching fraction in case of narrow resonances which is discussed further below [56].

In general, there is no universal model-independent recipe to construct the scattering amplitude. However, extracted resonance parameters should not depend on the parametrization used. The most common parametrizations such as the Breit-Wigner parametrization, the K -matrix approach as well as a method based on dispersion theory will be presented in the following. Their limitations, although already indicated in the previous passages, are also discussed.

2.5.3. Breit-Wigner Formula

The simplest form of a production amplitude of some resonance R coupling to channel a is the constant-width Breit-Wigner parametrization

$$\mathcal{A}_a(s) = \frac{\alpha g_a}{M_R^2 - s - iM_R \Gamma_R}, \quad (2.86)$$

with α being the resonance-source coupling. This parametrization holds if $2(M_R - \sqrt{s_{\text{thr}_a}}) / \Gamma_R \gg 1$, with $\sqrt{s_{\text{thr}_a}}$ being the sum of the nominal masses of the daughter particles of resonance R in channel a . In case of the ϕ meson, which is produced close to the K^+K^- threshold, an energy-dependent width $\Gamma(m)$ has to be used in order to account for the threshold behavior. Additionally, it is common to replace s by m^2 , which is the running invariant mass squared. The corresponding amplitude is then given by [175,176]

$$\mathcal{A}_a(m) = \frac{p_{\phi \rightarrow K^+K^-}^{L_{\phi \rightarrow K^+K^-}}}{M_\phi^2 - m^2 - im\Gamma(m)} \cdot \frac{B_L(p_{\phi \rightarrow K^+K^-})}{B_L(p'_{\phi \rightarrow K^+K^-})}, \quad (2.87)$$

with $L = 1$ being the lowest allowed orbital angular momentum between the daughter particles K^+K^- , p and p' with

$$p(m) = \sqrt{\left(\frac{m - 2m_K}{2} + m_K\right)^2 - m_K^2}, \quad p'(M_\phi) = \sqrt{\left(\frac{M_\phi - 2m_K}{2} + m_K\right)^2 - m_K^2} \quad (2.88)$$

being the momentum of the K^+K^- pair in the ϕ meson rest frame and evaluated at $m = M_\phi$, respectively, and $B_L(p)/B_L(p')$ being the corresponding L -dependent Blatt-Weisskopf form factors given by [175, 176]

$$\begin{aligned} B_0(p) &= 1 \\ B_1(p) &= \frac{1}{\sqrt{1 + (Rp)^2}} \\ B_2(p) &= \frac{1}{\sqrt{1 + \frac{(Rp)^2}{3} + \frac{(Rp)^2}{9}}}. \end{aligned} \quad (2.89)$$

$R = 3 \text{ GeV}^{-1}$ denotes some properly chosen momentum scale. The energy-dependent width $\Gamma(m)$ is defined as [175, 176]

$$\Gamma(m) = \left(\frac{p}{p'}\right)^{2L_{\phi \rightarrow K^+K^-} + 1} \left(\frac{M_\phi}{m}\right) \Gamma_\phi \left[\frac{B_1(p_{\phi \rightarrow K^+K^-})}{B_1(p'_{\phi \rightarrow K^+K^-})} \right]. \quad (2.90)$$

The Breit-Wigner parametrization is no longer correct if one tries to describe more than one resonance in one partial wave that significantly couples to the same channel, although often done. It violates unitarity constraints, which can be easily seen as follows. Generally, a resonance is uniquely characterized by its pole position s_r and its residue \tilde{g} (see Subsection 2.5.2). For the corresponding transition matrix element T [174]

$$T_{ab} = - \sum_r \frac{\tilde{g}_a^r \tilde{g}_b^r}{s - s_r} \quad (2.91)$$

a relation to the S -matrix exists via $S_{ab} = \delta_{ab} - 2i\sqrt{\sigma_a}T_{ab}\sqrt{\sigma_b}$, with σ_i being the phase space factor of channel i and \tilde{g}_i^r being the residue for the coupling of resonance r to channel i . Equation (2.91) is a sum over Breit-Wigner functions. For a demonstration of unitarity violation one may start with the unitarity condition in the single channel case

$$\text{Im}(T) = \sigma|T|^2. \quad (2.92)$$

Considering the T -matrix with two resonances a and b

$$T = - \frac{(\tilde{g}^{(a)})^2}{s - M_a^2 + iM_a\Gamma_a} - \frac{(\tilde{g}^{(b)})^2}{s - M_b^2 + iM_b\Gamma_b} \quad (2.93)$$

leads to

$$\begin{aligned} \text{Im}(T) - \sigma|T|^2 = & \frac{(\tilde{g}^{(a)})^2 (\Gamma_a M_a - \sigma (\tilde{g}^{(a)})^2)}{(s - M_a^2)^2 + M_a^2 \Gamma_a^2} + \frac{(\tilde{g}^{(b)})^2 (\Gamma_b M_b - \sigma (\tilde{g}^{(b)})^2)}{(s - M_b^2)^2 + M_b^2 \Gamma_b^2} \\ & + \text{Re} \left(\frac{2\sigma (\tilde{g}^{(a)} \tilde{g}^{(b)})^2}{(s - M_a^2 + iM_a \Gamma_a)(s - M_b^2 - iM_b \Gamma_b)} \right). \end{aligned} \quad (2.94)$$

The right-hand side of Equation (2.94) needs to vanish for unitarity to be satisfied. With the unitarity condition for a single resonance ($\Gamma_i M_i = \sigma (\tilde{g}^{(i)})^2$) and kinematically well separated resonances ($M_1 - M_2 \gg (M_1 \Gamma_1 + M_2 \Gamma_2) / (M_1 + M_2)$), this may be achieved [174]. However, especially for the scalar isoscalar sector (see Subsection 2.3.1), where many broad and overlapping resonances are present, the sum of Breit-Wigner functions violates unitarity significantly. Hence, the parameters extracted for the resonances will not be correct and, in fact, reaction dependent. This makes sum of Breit-Wigner amplitudes far unfavorable for spectroscopy. A more refined method, the K -matrix approach, is described in the following section.

2.5.4. K -Matrix

The K -matrix provides a clear improvement compared to the Breit-Wigner parametrization for the treatment of two-body coupled-channel scattering processes, since two-body unitarity is built in by construction. Additionally, the P -vector approach can be used to provide an effective description for the production mechanisms as well as for the effect of rescattering.

The S -matrix of scattering processes of the type $a + b \rightarrow c + d$ can be written as a sum of a term describing no interaction and a term describing interaction [177]

$$S = I + 2iT \quad (2.95)$$

$$= I + 2i\sqrt{\sigma}\hat{T}\sqrt{\sigma}, \quad (2.96)$$

with \hat{T} being the Lorentz-invariant transition matrix element, I being the identity and σ being the phase space diagonal matrix. The relation to the K -matrix is defined as

$$T(s) = (I + K(s)C(s))^{-1}K(s), \quad (2.97)$$

with s being the squared energy of the two-body system and $C(s)$ being the diagonal Chew-Mandelstam matrix where $\text{Im} C_{ii}(s) = -\sigma_{ii}(s)$. The elements of the phase space

matrix in case of a decay into two stable particles with masses m_1 and m_2 can be written as

$$\sigma_{ii}(s, m_1, m_2) = \sqrt{\left(1 - \frac{(m_1 + m_2)^2}{s}\right) \cdot \left(1 - \frac{(m_1 - m_2)^2}{s}\right)}. \quad (2.98)$$

For the reaction channels i and j , the symmetric and real valued K -matrix can be written as a sum over a number of resonances r plus a sum over polynomial background contributions n [177]

$$K_{ij}(s) = \sum_r B_{Lr_i}(p_i, p_{r_i}) \cdot B_{Lr_j}(p_j, p_{r_j}) \cdot \frac{g_{r_i}^{\text{bare}} g_{r_j}^{\text{bare}}}{(m_r^{\text{bare}})^2 - s} + \sum_n c_{nij} s^n, \quad (2.99)$$

with B_{Lr_i} being the aforementioned Blatt-Weisskopf barrier factors in channel i , and $g_{r_i}^{\text{bare}}$ as well as m_r^{bare} being the coupling strength of the resonance r to channel i and its mass in the K -matrix representation, respectively. The s -dependent polynomial background term of the order n can be added while still conserving unitarity. It is important to note that the properties of the resonances r in the K -matrix representation are not identical to the properties in the T -matrix description (which are the real physical properties). In fact, if left-hand cuts are neglected, the K -matrix can be transferred into the T -matrix via the Chew-Mandelstam matrix using Equation (2.97), which then allows for the extraction of the physical properties of the resonance r .

In order to describe also processes of the type $a \rightarrow b+c+d$ with a resonance r being present in the channel $r \rightarrow c+d$, the P -vector approach is used. It describes the production of two particles in the initial decay, which then undergo a scattering of the type $a+\bar{b} \rightarrow c+d$ so that the K -matrix formalism can be employed. A Lorentz-invariant F -vector, which is equivalent to the T -matrix of the two-body scattering process, can be defined as [177]

$$F_i^p(s) = \sum_j (I + K(s)C(s))_{ij}^{-1} \cdot P_j^p, \quad (2.100)$$

with P_j^p being one element of the P -vector taking into account the production of the wave or resonance. The sum runs over all channels relevant for the partial wave under consideration. Since P has to exhibit the same pole structures as the K -matrix, it can be written as [177]

$$P_i^p(s) = \sum_r B_{Lr_i}(p_i, p_{r_i}) \cdot \frac{\beta_r^p g_{r_i}^{\text{bare}}}{(m_r^{\text{bare}})^2 - s} + \sum_n c_{ni}^p s^n, \quad (2.101)$$

with β_r^p being a complex parameter representing the strength of the production process of resonance r . Note that both the coupling strength and the mass are equal to the ones in Equation (2.99). Usually, a K -matrix analysis of the scalar isoscalar sector (see Subsection 2.3.1) needs to consider the channels $\pi\pi, K\bar{K}, \eta\eta, \eta\eta'$ and 4π . In this analysis,

data is available for the $K\bar{K}$ channel. Accordingly, the remaining channels are constrained by using data available in the literature or by introducing effective channels.

2.5.5. Dispersion Integral

In general, scattering amplitudes and vertex functions will contain both real and imaginary parts. As already mentioned in Subsection 2.5.1, causality implies certain properties for the analytic structure of the amplitudes that allows to relate real and imaginary parts via so-called dispersion relations [163, 164].

An amplitude $f(s)$, which is holomorphic in the entire complex s -plane, except for a left-hand cut ($C_L = \{s \in \mathbb{R} | s < s_L\}$), a right-hand cut ($C_R = \{s \in \mathbb{R} | s > s_R\}$) and a bound state pole at s_p , can be written as

$$f(s) = \frac{1}{2\pi i} \int_C dz \frac{f(z)}{z - s} \quad (2.102)$$

for any $s \in \mathbb{C}$ with $s \notin C_L \cup C_R \cup \{s_p\}$. C denotes any closed path with the mathematical positive orientation encircling $z = s$ but not any of the non-analyticities mentioned above [169]. This is shown in Figure 2.7 (left). The integration path can be deformed

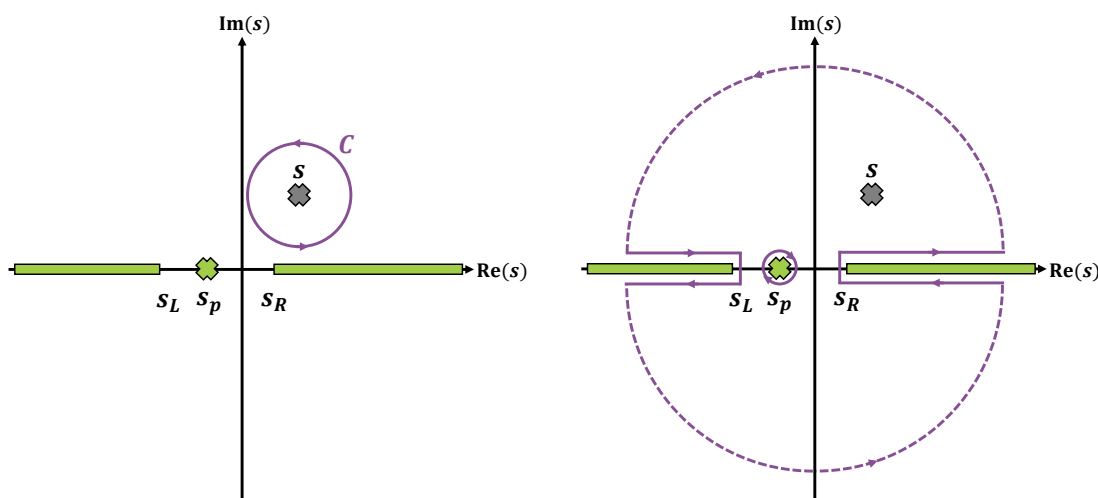


Figure 2.7.: Closed path C (purple line) encircling $z = s$ (left) and its deformation using Cauchy's theorem (right) for the dispersive representation in the complex s -plane. The left-hand cut s_L , the right-hand cut s_R and the pole at s_p are marked in green.

using Cauchy's theorem as shown in Figure 2.7 (right). It is important to note that

singularities such as the cuts and the pole have to be avoided. The integration path can be obtained by subtracting the residue at s_p

$$R\left(\frac{f(z)}{s-z}, s_p\right) = \text{Res}\left(\frac{f(z)}{z-s}\right)\Big|_{z=s_p} \quad (2.103)$$

due to the clockwise orientation of the integral around s_p . Usually, the whole integral can be separated into an integration along the real axis and a part along the complex arc. For sufficiently convergent $f(s)$ ($|f(s)| \rightarrow 0$ for $|s| \rightarrow \infty$), the contribution of the complex arc vanishes and $f(s)$ can be written as

$$f(s) = -R\left(\frac{f(z)}{s-z}, s_p\right) + \frac{1}{2\pi i} \left[\int_{-\infty}^{s_L} dz \frac{\text{disc } f(z)}{z-s} + \int_{s_R}^{\infty} dz \frac{\text{disc } f(z)}{z-s} \right] \quad (2.104)$$

$$= -R\left(\frac{f(z)}{s-z}, s_p\right) + \frac{1}{2\pi i} \left[\int_{-\infty}^{s_L} dz \frac{\text{disc } f(z)}{z-s-i\epsilon} + \int_{s_R}^{\infty} dz \frac{\text{disc } f(z)}{z-s-i\epsilon} \right], \quad (2.105)$$

where in the last step the values on the cuts are accessed by an analytic continuation of $f(s)$ by approaching with the prescription $s \rightarrow s + i\epsilon$. Note that using Equation (2.79), the amplitude is nothing but an integral over its imaginary part, which may be provided by experimental data.

2.5.6. Elastic Approximation and Omnès Problem

The simplest application of dispersion theory is the elastic approximation, or homogeneous Omnès problem [178]. Consider a two particle amplitude $f(s)$ of a given isospin \mathcal{I} and angular momentum l which is analytic in the complex s -plane except a right-hand cut starting at s_0 . In fact, we apply dispersion theory to the transition of a source ψ with spin l to a final state consisting of two particles ϕ_1 and ϕ_2

$$\langle f|S|i\rangle = \langle \phi_1(p_1), \phi_2(p_2) | T | \psi(p_1 + p_2) \rangle \propto F_l^f\left((p_1 + p_2)^2\right), \quad (2.106)$$

with F_l^f being a so-called form factor [179–182]. We may consider a vector of form factors $F_l^f(s)$ ($f = 1, \dots, n$ denotes the open channels taking part in the rescattering process in a fixed partial wave l) which fulfill the following unitarity condition (see Equation (2.74))

$$\text{Im } F_l^f(s) = \sum_{m=1}^n \left(t_l^{fm}(s)\right)^* \sigma_m(s) F_l^m(s), \quad (2.107)$$

with $\sigma_m(s)$ being the phase space of the channel m and t_l^{fm} being the partial wave scattering amplitude between channels f and m . A form factor can be determined as

$$F_l^f(s) = \sum_{k=1}^n \Omega_l^{fk}(s) P^k(s), \quad (2.108)$$

with $\Omega_l^{fk}(s)$ being an Omnès matrix and $P^k(s)$ being a polynomial from a Taylor expansion [169]. From now on the discussion restricts to a single channel as final and intermediate state (elastic approximation). In this case, the Omnès function can be determined analytically and the partial wave amplitude $t_l(s)$ above $s = s_0$ can be entirely described by the phase shift $\delta_l(s)$

$$t_l(s) = \frac{\sin\delta_l(s)}{\sigma_1(s)} e^{i\delta_l(s)}. \quad (2.109)$$

In the elastic region (below some inelastic thresholds $s_{\text{inel}} > s_0$) the Watson theorem holds [183], which states that since the imaginary part is a real number, the phase of both $F_l(s)$ and $\Omega_l(s)$ needs to be equal to the phase shift $\delta_l(s)$ (or: the phase of the amplitude is equal to the corresponding two particle scattering amplitude $f(s) = e^{i\delta(s)}|f(s)|$). The unitarity condition reads

$$\text{disc log } \Omega_l(s) = 2i\delta_l(s). \quad (2.110)$$

Using the dispersion relation, the Omnès function can finally be written as

$$\Omega(s) = \exp\left(\frac{s}{\pi} \int_{s_0}^{\infty} \frac{dz}{z} \frac{\delta_l(z)}{z - s - i\epsilon}\right). \quad (2.111)$$

In case of present left-hand cuts, the Omnès problem becomes inhomogeneous. However, in practice such inelasticities do not play a significant role in low energy pion physics up to 1 GeV ($K\bar{K}$ threshold). That is why one often assumes an approximation of keeping only the elastic channels. For an overview of the inhomogeneous Omnès problem we refer to [169].

2.6. A New Parametrization of the Scalar Pion Form Factor

In this section, a formalism aiming to parametrize the scalar pion form factor while being consistent with the general principles of analyticity and unitarity is presented. Regarding the low energy regime up to an energy of about $s = (1.1 \text{ GeV})^2$, the two-pion system is well understood: sophisticated investigations based on dispersion theory have in particular derived the $\pi\pi - K\bar{K}$ phase shifts and inelasticities with high accuracy [184–189]. From that, the scalar strange (and also non-strange) form factors for both pions and kaons may be constructed, already capturing the physics of the $f_0(500)$ and the $f_0(980)$ [123, 179, 190–195]. However, in order to be able to describe also the higher energy regime, where many inelasticities like resonances start being present, a model needs to be employed. Such a model is presented in [65], whose amplitudes match smoothly to those constructed from dispersion relations only. In addition, resonance properties may be extracted since the extension of the low energy regime is performed in a way consistent

with analyticity.

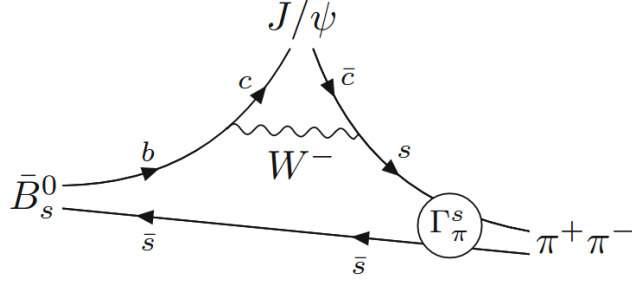


Figure 2.8.: Dominant tree-level diagram for the weak transition on the quark level for the decay process $\bar{B}_s^0 \rightarrow J/\psi \pi^+ \pi^-$. The hadronization of the $s\bar{s}$ pair into $\pi^+ \pi^-$ (S -wave dominated) is given by the scalar form factor Γ_π^s . Figure taken from [65].

This derived formalism was primarily used as an application for extracting resonance properties of excited scalar mesons [65] from high accuracy LHCb data of the process $\bar{B}_s^0 \rightarrow J/\psi \pi \pi / K \bar{K}$ (see Figure 2.8) [52, 196]. In that case the production of the $\pi^+ \pi^-$ pair (and also of the $K \bar{K}$ pair) can be seen as evolving from a pure $s\bar{s}$ source. That is why the strange pion and kaon scalar form factor Γ_i^s can be extracted up to about 2 GeV using the data mentioned above according to

$$\Gamma_i^s = \Omega_{im} [1 - V_R \Sigma]_{mn}^{-1} M_n. \quad (2.112)$$

In the following, Equation (2.112) is explained in detail. Its derivation can be found in [65]. Note that due to the fact that both the scalar isoscalar $\pi\pi$ and the $K\bar{K}$ channels are strongly coupled via the $f_0(980)$ resonance, a coupled channel description is mandatory. In addition to $\pi\pi$ and $K\bar{K}$, an effective 4π channel, modeled either by the $\rho\rho$ or $\sigma\sigma$, is used in this three-channel model [65].

The Omnès matrix Ω [178] and the corresponding matrix elements Ω_{im} are given by

$$\Omega = \begin{pmatrix} \Omega_{11} & \Omega_{12} & 0 \\ \Omega_{21} & \Omega_{22} & 0 \\ 0 & 0 & 1 \end{pmatrix}, \quad \Omega_{im}(s) = \frac{1}{2\pi i} \int_{4M_\pi^2}^{\infty} dz \frac{\text{disc } \Omega_{im}(z)}{z - s - i\epsilon}, \quad (2.113)$$

with the discontinuity $\text{disc } \Omega_{im} = 2i(T_0)_{ij}^* \sigma_j \Omega_{jm}$. Here, $\sigma_j(s) = \sqrt{1 - 4M_j^2/s}$ is the two-body phase space of channel j and

$$T_0 = \begin{pmatrix} \frac{\eta_0 e^{2i\delta_0} - 1}{2i\sigma_\pi} & g_0 e^{i\psi_0} & 0 \\ g_0 e^{i\psi_0} & \frac{\eta_0 e^{2i(\psi_0 - \delta_0)} - 1}{2i\sigma_K} & 0 \\ 0 & 0 & 0 \end{pmatrix} \quad (2.114)$$

is the T -matrix for the energy regime below 1 GeV. In Equation (2.114), δ_0 denotes the scalar isoscalar $\pi\pi$ phase shift, ψ_0 the phase of the $\pi\pi \rightarrow K\bar{K}$ scattering amplitude, g_0 its absolute value and

$$\eta_0 = \sqrt{1 - 4(g_0)^2 \sigma_\pi \sigma_K \Theta(s - 4M_K^2)} \quad (2.115)$$

the inelasticity [65]. The Omnès matrix elements Ω_{im} must already be provided in terms of a dispersively constructed coupled-channel Omnès matrix (which basically means phase shift studies, see Equation (2.114)), e.g. from [197] and can then be used as input for the form factor calculation. An extension up to five channels (e.g. $\eta\eta$ and $\eta\eta'$) can be made in a straightforward manner. In this case the 2×2 Omnès submatrix for the additional channels is equal to the identity matrix I .

The self-energy matrix $\Sigma = G\Omega$ with loop operator G and discontinuity given by

$$\text{disc } \Sigma_{ij}(s) = 2i\Omega_{im}^\dagger(s) \text{disc } G_{mm}(s)\Omega_{mj}(s) \quad (2.116)$$

can be written as a once-subtracted dispersion integral according to

$$\Sigma_{ij}(s) = \Sigma_{ij}(0) + \frac{s}{\pi} \int \frac{dz}{z} \frac{\text{disc } \Sigma_{ij}(z)}{z - s - i\epsilon}. \quad (2.117)$$

In Equation (2.116), Ω is the Omnès matrix from Equation (2.113) and $\text{disc } G_{mm}(s)$ for channel m reads

$$\begin{aligned} \text{disc } G_{11} &= 2i\sigma_\pi = 2i\sqrt{1 - 4M_\pi^2/s} \\ \text{disc } G_{22} &= 2i\sigma_K = 2i\sqrt{1 - 4M_K^2/s} \\ \text{disc } G_{33}^k &= 2i \int_{4M_\pi^2}^{\infty} dm_1^2 dm_2^2 \rho_k(m_1^2) \rho_k(m_2^2) \frac{\lambda^{1/2}(s, m_1^2, m_2^2)}{s}. \end{aligned} \quad (2.118)$$

Here, $\lambda(a, b, c)$ is the Källén function from Equation (2.70) and $\rho_k(m^2)$ is the spectral density for the state k (ρ or σ), which can be written as

$$\rho_k(q^2) = \frac{1}{\pi} \frac{m_k \Gamma_k(q^2)}{(q^2 - m_k^2)^2 + m_k^2 \Gamma_k^2(q^2)}, \quad (2.119)$$

with the energy-dependent width

$$\Gamma_k(s) = \frac{\Gamma_k m_k}{\sqrt{s}} \left(\frac{p_\pi(s)}{p_\pi(m_k^2)} \right)^{2L_k+1} \left(F_R^{(L_k)}(s) \right)^2, \quad (2.120)$$

with $p_\pi(s) = \frac{\sqrt{s}}{2} \sigma_\pi(s)$, the nominal width (mass) $\Gamma_k(m_k)$ of the resonance, the angular momentum of the decay $L_k = 1$ and $L_k = 0$ for the ρ and the σ , respectively, and the barrier factors $F_R^{(L)}(s)$ [198]. By this, the finite width of the two intermediate mesons is

taken into account, which ensures the proper treatment of a four body phase space. In case of an extension up to five channels the off-diagonal elements are $\Sigma_{45,54} = 0$ [169], whereas the diagonal elements for the self-energy matrix read for a real and positive Källén function $\lambda = \lambda(s, m_a, m_b)$ (see Equation (2.70))

$$\begin{aligned} \Sigma_{44,55}(s, m_a, m_b) = & \frac{-4m_a m_b}{16\pi^2} \left(\left(\frac{m_a^2 - m_b^2}{s} - \frac{m_a^2 + m_b^2}{m_a^2 - m_b^2} \right) \log \left(\frac{m_a}{m_b} \right) - 1 \right. \\ & \left. + \frac{\sqrt{\lambda}}{s} \left(\log \left(\frac{s - m_a^2 - m_b^2 + \sqrt{\lambda}}{s - m_a^2 - m_b^2 - \sqrt{\lambda}} \right) \right) - 2i\pi\Theta \left(s - (m_a + m_b)^2 \right) \right) \end{aligned} \quad (2.121)$$

and otherwise

$$\begin{aligned} \Sigma_{44,55}(s, m_a, m_b) = & \frac{-4m_a m_b}{16\pi^2} \left(\left(\frac{m_a^2 - m_b^2}{s} - \frac{m_a^2 + m_b^2}{m_a^2 - m_b^2} \right) \log \left(\frac{m_a}{m_b} \right) - 1 \right. \\ & \left. + \frac{\sqrt{-\lambda}}{s} \left(\arctan \left(\frac{m_a^2 - m_b^2 + s}{\sqrt{-\lambda}} \right) - \arctan \left(\frac{m_a^2 - m_b^2 - s}{\sqrt{-\lambda}} \right) \right) \right). \end{aligned} \quad (2.122)$$

The potential V_R describes resonances above 1 GeV and can be written as

$$(V_R)_{ij} = \sum_r g_{r_i} \frac{s}{m_r^2(m_r^2 - s)} g_{r_j}, \quad (2.123)$$

with bare resonance masses m_r and bare resonance-channel coupling constants g_{r_i} . They are universal (means reaction-independent) parameters and may be determined by a fit to data.

The analytic term M describing the transition from the source to the channel n reads

$$M_i = c_i + \gamma_i s + \dots - \sum_r g_{r_i} \frac{s}{m_r^2 - s} \alpha_r, \quad (2.124)$$

with the normalizations $c_i = \Gamma_i^s(0)$ for channel i , the resonance-source couplings α_r and some slope parameters γ_i (which are not necessarily $\neq 0$). Note that c_i can be fixed based on χPT^2 as they depend on the source only (in this case a $s\bar{s}$ source) [123].

In this work, the presented formalism is applied to BESIII data in Section 5.7 in order to describe the dynamical part of the amplitudes of the $K\bar{K}$ system with $J^{PC} = 0^{++}$ in the reaction $e^+e^- \rightarrow \phi K\bar{K}$.

²**Chiral Perturbation Theory** (χPT) is an effective field theory that provides a systematic framework for studying strong interaction processes at low energies, in contrast to a perturbative treatment of QCD at high momentum transfers in terms of *the running coupling constant*. For an introduction to χPT we refer to [199].

2.7. Helicity Formalism

The final states investigated in the present analysis are treated as stable and are described by a chain of two-body decays of short-lived intermediate resonances within the isobar model. By this, the observed amplitude is decomposed into partial wave contributions. The spin structure of the decay is described in the helicity formalism [165,166]. Figure 2.9 shows the most important kinematic variables for the production as well as decay reference frames. The considered angles are the azimuthal and polar angle of the production of the intermediate resonance X in the e^+e^- rest frame with respect to the direction of the beam and of the decay of the single resonance (or partial wave containing several resonances) in its helicity system, in which the y -axis is defined to be parallel to the normal vector of the production plane.

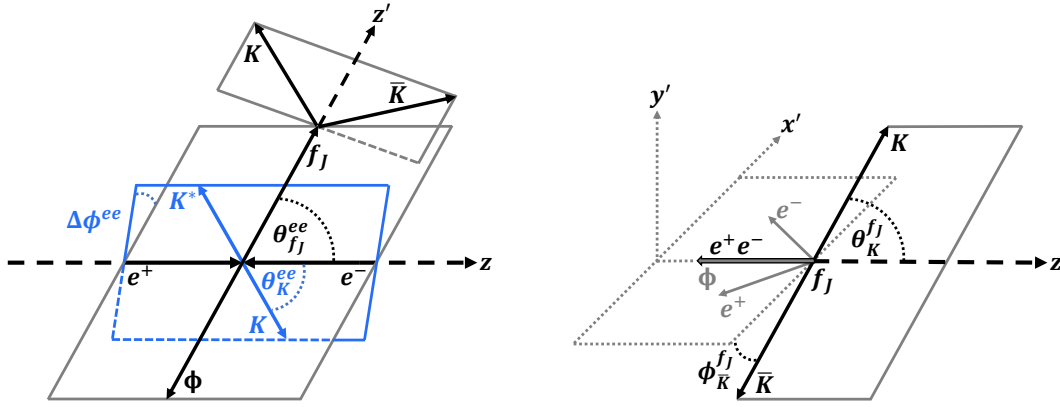


Figure 2.9.: Graphical representation of the most important kinematic variables for the production (**left**) and decay (**right**) reference frames. Exemplary, the process $e^+e^- \rightarrow \phi K K$ is shown. In the production, the z -axis is defined as the flight direction of the e^+ , while the directions of the x - and y -axes are arbitrary and only defined in the laboratory frame by convention (y -axis pointing up in vertical direction). The e^+e^- pair annihilates either into ϕf_J with $f_J \rightarrow K K$ (black) or into $K^* K$ with $K^* \rightarrow \phi K$ (blue). $\Delta\phi_{e^+e^-}$ denotes the angle between the planes of these two decay branches. In the helicity frame of the f_J depicted on the right-hand side, the z' -axis is defined as the opposite direction of the e^+e^- system or equivalently of the ϕ meson. The $x' - z'$ -plane is given by the production plane, spanned by the flight directions of the e^- and e^+ . Accordingly, the y' -axis is perpendicular to this production plane.

Relativistic particles with momentum \vec{p} can properly be described in the helicity reference system by first rotating the coordinate system so that, e.g., the z -axis is aligned with \vec{p}

$$\hat{r}(\alpha, \beta, \gamma) |j, m\rangle = \sum_{m'} D_{mm'}^j(\alpha, \beta, \gamma) |j, m'\rangle, \quad (2.125)$$

with $\hat{r}(\alpha, \beta, \gamma)$ being the unitary rotation operator acting on the state $|j, m\rangle$ (with angular momentum j and its projection m along the direction of motion), α, β, γ being the Euler angles and $D_{mm'}^j(\alpha, \beta, \gamma)$ being the complex unitary Wigner-D-matrices, which can be found in [56].

Since the helicity λ is defined as the projection of the total angular momentum \vec{J} to a quantization axis along \vec{p} , $\lambda = \vec{J} \cdot \frac{\vec{p}}{|\vec{p}|}$, it is invariant under rotations around and boosts along that axis. The decay amplitude of a particle a with a total angular momentum \vec{J} and a helicity λ_a decaying to daughters b and c with $\lambda = \lambda_b - \lambda_c$ can be written as [165, 166]

$$A_{\lambda_b, \lambda_c}^{J_a, \lambda_a}(a \rightarrow b + c) = \sqrt{\frac{2J_a + 1}{4\pi}} \cdot D_{\lambda_a, \lambda}^{J_a*}(\varphi, \theta, 0) \cdot F_{\lambda_b, \lambda_c}^{J_a}, \quad (2.126)$$

with φ and θ being the azimuthal and polar angle, respectively. Since the total spin S as well as the orbital angular momentum L are good quantum numbers, the amplitude can be transformed into the so-called LS -basis, enabling to write the parameter $F_{\lambda_b, \lambda_c}^{J_a}$ as follows [155]

$$F_{\lambda_b, \lambda_c}^{J_a} = \sum_{L, S} \sqrt{\frac{2L + 1}{2J_a + 1}} \langle L, 0; S, \lambda | J_a, \lambda \rangle \langle J_b, \lambda_b; J_c, -\lambda_c | S, \lambda \rangle \cdot \alpha_{LS}^{J_a}. \quad (2.127)$$

L and S are limited by $|J_b - J_c| \leq |J_b + J_c|$ and $|L - S| \leq J_a \leq |L + S|$. $\langle L, 0; S, \lambda | J_a, \lambda \rangle$ and $\langle J_b, \lambda_b; J_c, -\lambda_c | S, \lambda \rangle$ are Clebsch-Gordan coefficients, which can be found in [56]. The free, complex parameter $\alpha_{LS}^{J_a}$ has to be determined in the fit. This amplitude is employed for each L, S combination possible between the two daughter particles of the former mother resonance.

Exemplary, the process $e^+e^- \rightarrow \phi K\bar{K}$ with a subsequent $\phi \rightarrow K^+K^-$ decay is investigated. Assuming only resonances in the $K\bar{K}$ system, the full decay amplitude can be written as

$$\begin{aligned} \mathcal{A} = & \sum_{\lambda_{e^+e^-} = -1, 1} \left| \left(\sum_R \sum_{\lambda_R} \sum_{\lambda_\phi} \sum_L \sum_S \sqrt{\frac{2L + 1}{4\pi}} \cdot D_{\lambda_{e^+e^-}, \lambda_R - \lambda_\phi}^{1*}(\varphi_R, \theta_R, 0) \right. \right. \\ & \cdot \langle L, 0; S, \lambda_R - \lambda_\phi | 1, \lambda_R - \lambda_\phi \rangle \cdot \langle J_R, \lambda_R; 1, -\lambda_\phi | S, \lambda_R - \lambda_\phi \rangle \cdot \alpha_{LS}^1 \cdot B_L(p) \\ & \cdot \sqrt{\frac{2J_R + 1}{4\pi}} \cdot D_{\lambda_R, 0}^{J_R*}(\varphi_K, \theta_K, 0) \cdot \langle J_R, 0; 0, 0 | J_R, 0 \rangle \cdot \alpha_{J_R 0}^{J_R} \cdot \tilde{F}_{J_R, R} \\ & \left. \left. \cdot \sqrt{\frac{3}{4\pi}} \cdot D_{\lambda_\phi, 0}^{1*}(\varphi_{K^+}, \theta_{K^+}, 0) \cdot \langle 1, 0; 0, 0 | 1, 0 \rangle \cdot \alpha_{10}^1 \cdot \tilde{F}_{1, \phi} \right) \right|^2. \quad (2.128) \end{aligned}$$

In Equation (2.128), $\lambda_{e^+e^-}$ denotes the helicity of the e^+e^- initial state, which is due to the annihilation into a virtual photon equal to -1 or 1. R denotes a resonance in the $K\bar{K}$ system and J_R as well as λ_R its total spin and helicity, respectively. λ_ϕ is the helicity of the ϕ meson. The sum over R runs through all resonances incorporated into the specific

model. These may be the scalar isoscalar resonances listed in the PDG [56]. The sums over λ_R and λ_ϕ run from $-J_R$ to J_R and -1 to 1 , respectively. L and S are the orbital angular momentum and spin of the $\phi - R$ system from above. Since kaons do not have spin, for both $f_J \rightarrow K\bar{K}$ and $\phi \rightarrow K^+K^-$ decays the spin of the kaon system necessarily is zero. Hence, the orbital angular momentum between the two kaons is equal to the total spin J of the mother particle. While the index K denotes the kaon coming from the resonance R , the index K^+ denotes the K^+ from the decay of the ϕ meson. The values of $J_\phi = 1$ and $J_K = J_{K^+} = 0$ have already been inserted in Equation (2.128).

The functions $\tilde{F}_{J_R,R}$ and $\tilde{F}_{1,\phi}$ contain the whole dynamics of the resonances R and ϕ . They also include the barrier factors and thus additionally depend on the angular momentum between their daughter particles given by J_R and 1 , respectively. Since only the product $\alpha_{LS}^1 \cdot \alpha_{J_R 0}^{J_R} \cdot \alpha_{10}^1$ can be determined in the fit, the factors $\alpha_{J_R 0}^{J_R}$ and α_{10}^1 describing the decay strength and phase of the decays $f_J \rightarrow K\bar{K}$ and $\phi \rightarrow K^+K^-$ can be fixed to $1 + i \cdot 0$.

3. Experimental Setup

The analyses performed in this work are based on data at center-of-mass energies between $\sqrt{s} = 3.7730 - 4.7008$ GeV collected in e^+e^- annihilations with the **B**eijing **S**pectrometer (BESIII) operating at the **B**eijing **E**lectron-**P**ositron **C**ollider **II** (BEPCII). In this section, the accelerator, the detector components as well as the trigger system used for the acquisition of tremendous amounts of data are presented. While BESIII was initially designed to meet the current physics program [153], several detector upgrades are planned and partially already realized in order to do so also for the future program [200].

3.1. BEPCII Accelerator

BEPCII is a symmetric double-ring e^+e^- collider which serves the purpose of both high-energy physics and synchrotron radiation, designed to provide a peak luminosity of $1 \cdot 10^{33} \text{ cm}^{-2}\text{s}^{-1}$ at a beam energy of 1.89 GeV corresponding to the center-of-mass energy of the $\psi(2S)$. Before being injected into two separate storage rings, both electrons and positrons are pre-accelerated up to an energy of $E_{\text{inj}} = 2.5$ GeV by a linear accelerator with a length of 202 m [201]. The beams are circulating at a design beam current of 910 mA with 93 bunches per beam. Inside the BESIII detector they are brought to collision under a small angle of 2×11 mrad at a well-defined interaction point (IP). The two major upgrades of BEPCII in past years were the increase of the maximum beam energy up to 2.5 GeV and the opportunity for a top-up injection mode, which is a highly efficient operation scheme for the accelerator providing a nearly constant beam current as well as increased integrated luminosity [200, 202]. Figure 3.1 gives an overview of the BEPCII facility and a summary of the operational parameters is listed in Table 3.1.

3.2. BESIII Experiment

The BESIII detector is designed to suffice the physics requirements as well as the technical requirements for a high luminosity, multi-bunch collider [200]. It consists of four sub-detector systems, covering 93% of 4π solid angle: A small-cell, helium based (60 % He, 40 % C_3H_8) **M**ultilayer **D**rift **C**hamber (MDC) surrounded by a solenoid magnet that provides a 1 T magnetic field within the tracking volume, a **T**ime-**o**f-**F**light system (TOF) based on plastic scintillators, an **E**lectromagnetic **C**alorimeter (EMC) to measure

photons and the **Muon Counter** (MUC) to effectively distinguish muons from charged pions and protons. Since two particles with identical mass and opposite momentum are brought to collision, the center-of-mass system of the e^+e^- pair is approximately at rest. Therefore, the sub-detector systems are built cylindrically symmetric around the beam axis with the interaction point in the center. By combining the information from all detector components, an excellent resolution as well as particle identification is achieved, enabling high accuracy measurements with the BESIII experiment. Figure 3.2 shows a schematic drawing of the BESIII detector and its components. In the following, an overview of each sub-detector system is given. For a more detailed review we refer to the design and construction report [205] as well as to the future physics program [200] by the BESIII collaboration.

3.2.1. Multilayer Drift Chamber (MDC)

Particles which are produced in e^+e^- annihilations and penetrating the beryllium beam pipe have to traverse the innermost detector system, the MDC. This cylindrical wire drift chamber is used to measure the momentum and energy of electrically charged particles very precisely by measuring points along its trajectory in a well-defined magnetic field of 1 T as well as the particle type by measuring the specific energy deposit dE/dx in the chamber. The MDC consists of inner and outer chambers without any intervening wall, sharing a common gas volume. Thus, a potential major source of multiple scattering is eliminated. As a main constraint on the momentum resolution, multiple scattering is further minimized by the use of thin gold-plated aluminum field wires with a diameter of $110\ \mu\text{m}$ for field shaping and a specific helium-based gas mixture of helium (60%) and propane C_3H_8 (40%) with a radiation length of 550 m. The single wire position

Table 3.1.: Relevant operational parameters of BEPCII [201].

Parameter	Unit	BEPCII
Center-of-mass energy	GeV	2 – 5.0
Circumference	m	237.5
Peak luminosity (at 2×1.89 GeV)	$\text{cm}^{-2}\text{s}^{-1}$	$\sim 10^{33}$
Number of bunches		2×93
Beam current	A	2×0.91
Bunch spacing	m/ns	2.4/8
Bunch length σ_z	cm	1.5
Bunch size ($\sigma_x \times \sigma_y$)	$\mu\text{m} \times \mu\text{m}$	$\sim 380 \times 5.7$
Relative energy spread		$5 \cdot 10^{-4}$
Crossing angle	mrad	± 11

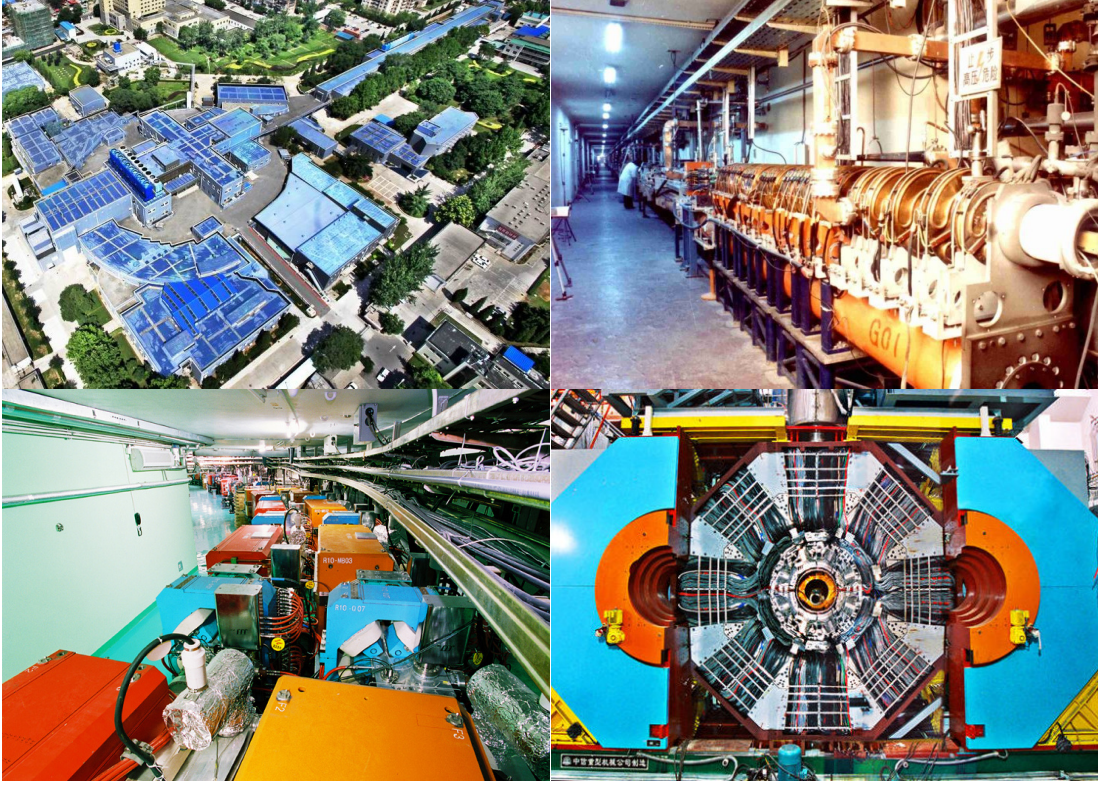


Figure 3.1.: Pictures of the BESIII and BEPCII facilities. **Top left:** Bird view on the facilities. **Top right:** The linear accelerator. **Bottom left:** The two storage rings. **Bottom right:** Front view of the BESIII detector. Images are taken from [203, 204].

resolution is expected to be $\sim 130 \mu\text{m}$ in $r\phi$ plane and $\sim 2 \text{ mm}$ in z direction, which gives a momentum resolution of $\sigma_p/p < 0.5\%$ at $1 \text{ GeV}/c$. Ions and electrons start drifting within the electric field and produce electric signals at the corresponding sense wires which are made of gold-plated tungsten-rhenium with a diameter of $25 \mu\text{m}$. They are arranged with alternating orientations to allow for a three-dimensional track reconstruction.

Technically, the chamber has an inner radius of 59 mm , an outer radius of 810 mm and a maximum length of 2.582 m . In order to place the focusing quadrupole as close as possible to the IP, the end plates of the chamber have a stepped conical shape with an achieved minimal polar angle coverage of $|\cos\vartheta| \leq 0.83$ and a solid angle coverage of $\Delta\Omega/4\pi = 93\%$. The chamber is divided into 43 sense wire layers of small drift cells, containing a total of 6796 sense wires and 21844 additional field wires [205].

With the measured curvature in the magnetic field and the energy loss dE/dx of a charged track a first particle identification (PID) can be performed. The normalized pulse height, which is proportional to the energy loss of incident particles, is a function of $\beta\gamma = p/m$, with p and m being the momentum and mass of a charged particle, respectively [206]. These include electrons e^\pm , muons μ^\pm , pions π^\pm , kaons K^\pm and protons

3. Experimental Setup

p or antiprotons \bar{p} , which are considered stable when traversing the MDC. Using dE/dx pulse heights, protons can be clearly separated from all other particles up to a momentum of ~ 1 GeV/c. A well e/π separation is achieved above 0.4 GeV/c, whereas a 3σ π/K separation is achieved up to 0.6 GeV/c. Both leptons e^- , μ and pions π can not be well separated around 0.2 GeV/c [206]. In order to improve the PID of the BESIII detector, the information of MDC are married to the one from the TOF system as described in

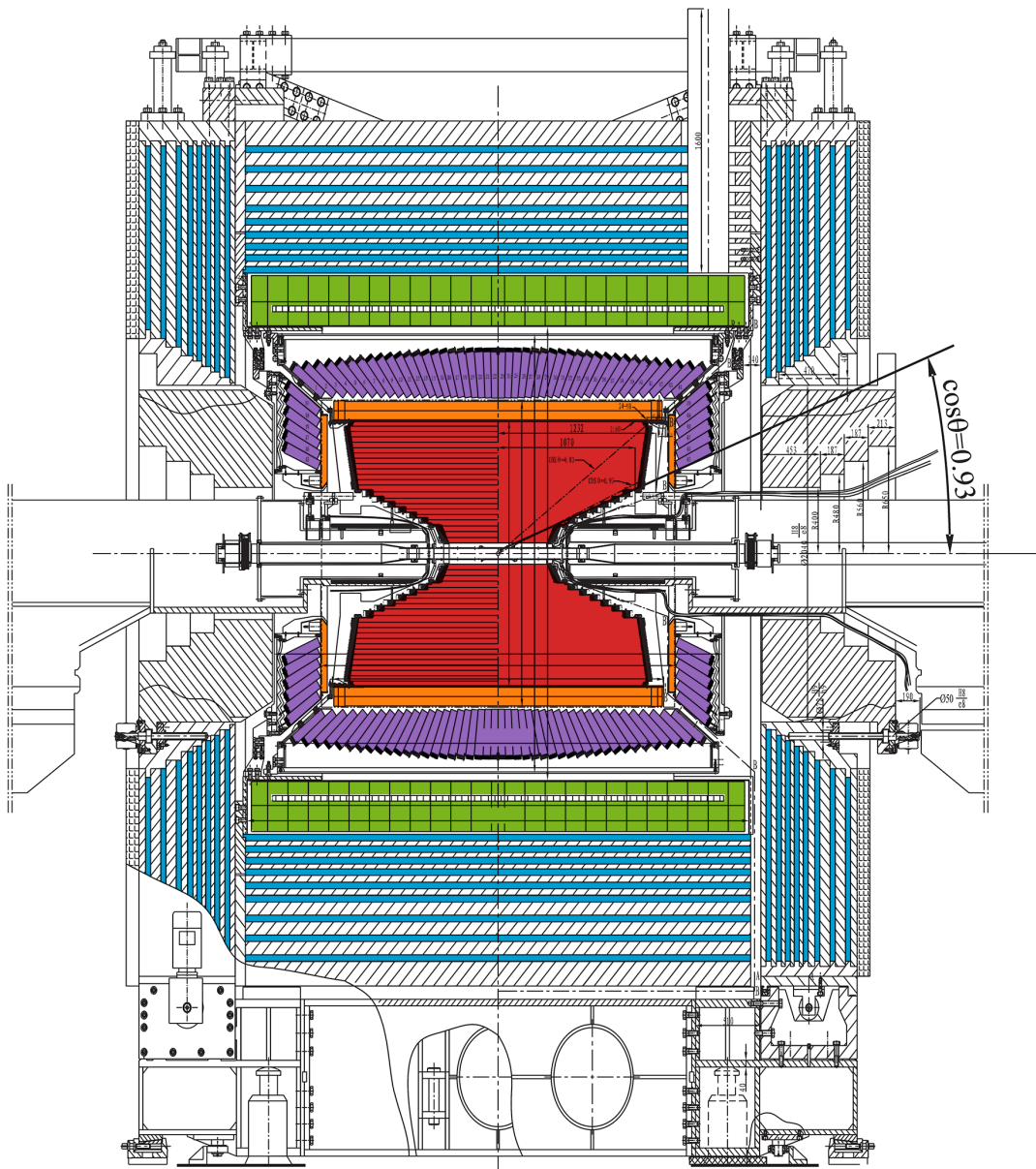


Figure 3.2.: Schematic drawing of the BESIII detector and its subdetector components. **Red:** Multilayer drift chamber. **Orange:** Time-of-flight system. **Purple:** Electromagnetic calorimeter. **Green:** Solenoid magnet. **Blue:** Muon counter. The beam line goes horizontally through the detector in z -direction. The interaction point is situated at the geometrical center of the detector. Image edited from its original version [205].

the next section.

Aging problems due to beam-induced background have caused the cell gains of the inner chamber to drop about 40% [207], leading to a degradation of the spatial resolution and reconstruction efficiency. Therefore, a **Cylindrical Gas Electron Multiplier (CGEM)** has been suggested as one option among other for an upgrade. The main advantages of a CGEM are a high counting rate capability as well as a low sensitivity to aging [200]. Many studies have to be performed in order to test if the CGEM can reach the required performance so that the MDC still meets the future physics program. The current status and development details can be found in [200, 208].

3.2.2. Time-of-Flight System (TOF)

The TOF system, made up of plastic scintillator bars and read out by fine-mesh photomultiplier tubes directly attached to the two end faces of the bars, is mounted directly between the MDC and the EMC. It is composed of a barrel part and two endcaps, measuring the flight time of charged particles in order to improve the PID efficiency. The barrel part consists of two layers, each with 88 plastic scintillation bars of 2.3 m length and a trapezoidal cross section with a thickness of 50 mm. The two endcaps contain only a single layer of 48 fan-shaped scintillation counters, 480 mm in length and 50 mm thick. They are read out by a single photomultiplier tube attached to the end of each segment. While the barrel part covers a polar angle range of $|\cos \vartheta| < 0.83$, the endcaps cover the polar angle regions with $0.85 < |\cos \vartheta| < 0.95$. Thus, a small acceptance gap exists, due to the needed space for the mechanical support structure of the MDC. Achieved time resolutions in the barrel and end cap regions are $\sigma_t \approx 100$ ps and $\sigma_t \approx 110$ ps, respectively. They mainly depend on the intrinsic TOF time resolution caused by the characteristics of the scintillator and the photomultiplier as well as time resolution and jitter in the readout electronics [153].

As mentioned in the previous section, TOF measurements enable PID. The mass m of a charged particle can be calculated using the velocity β [206] by

$$m^2 = p^2 \cdot \frac{1 - \beta^2}{\beta^2} \quad \text{with} \quad \beta = \frac{L}{ct}, \quad (3.1)$$

with t being the measured time-of-flight, p being the momentum of the charged particle measured in the MDC with corresponding flight path length L and c being the speed of light in vacuum. Note that the start time can be determined from reconstructed tracks of charged particles in the MDC [209]. A 2σ K/π separation is achieved for particle momenta of up to 0.9 GeV/c [206]. However, the PID performance strongly relies on the time resolution.

In order to even improve the capability of PID of the BESIII experiment, the endcaps were

upgraded with a **M**ulti-gap **R**esistive **P**late **C**hambers technology (MRPC), yielding an overall time resolution for pions with momentum around 0.8 GeV/c of about 65 ps. For a detailed overview of the MRPC see [210].

3.2.3. Electromagnetic Calorimeter (EMC)

The EMC is the third and outermost sub-detector system surrounded by the solenoid magnet. It allows the energy and direction of flight of incoming particles to be measured. While charged particles emit energy in the form of photons as radiation, those from the IP or from decays of short-lived resonances such as π^0 and η are measured directly. Due to the many sources the photons may come from, the EMC has to cover a wide energy range from ~ 20 MeV up to 2.3 GeV. This is achieved with 6240 thallium doped cesium iodide CsI(Tl) crystals. Each crystal has a length of 28 cm, which corresponds to 15.1 radiation lengths X_0 of CsI. Front and rear faces have a typical size of $5.2 \text{ cm} \times 5.2 \text{ cm}$ to $6.4 \text{ cm} \times 6.4 \text{ cm}$, respectively. Similar to the TOF, the EMC is divided into a cylindrical barrel part and two endcaps. A total of 5280 crystals arranged in 44 layers make up the barrel part and each endcap is composed of 480 crystals arranged in 6 layers. All crystals are slightly tilted by $\sim 1.5^\circ$, pointing to a region $\pm 10 \text{ cm}$ off the interaction point to avoid missing photons that could pass exactly between two crystals. The EMC polar angle coverage of the barrel and endcaps is $|\cos \vartheta| < 0.82$ and $0.83 < |\cos \vartheta| < 0.93$, respectively. The expected energy and spatial resolutions are $\sigma_E/E \leq 2.5\%$ and $\sigma_z \leq 0.6 \text{ cm}$ at a photon energy of 1 GeV, respectively [206].

Not only the energy deposition, but also the shape of the shower produced in the EMC allow for PID. While muons and pions lose almost no energy passing through the EMC, electrons and positrons are stopped completely and deposit all of their energy, thus showing a ratio of deposit energy to the track momentum $\Delta E/p$ which is approximately unity. However, the shape of the shower can be characterized by the energies E_{seed} , $E_{3 \times 3}$ and $E_{5 \times 5}$, denoting the energy deposit in the central crystal, in the central 3×3 crystal array and in the central 5×5 crystal array, respectively. Moreover, the second-moment S is defined as [206]

$$S = \frac{\sum_i E_i \cdot d_i^2}{\sum_i E_i}, \quad (3.2)$$

with E_i being the energy deposit in the i -th crystal and d_i being the distance between the i -th crystal and the center position of the reconstructed shower. The ratios $E_{\text{seed}}/E_{3 \times 3}$ and $E_{3 \times 3}/E_{5 \times 5}$ as well as S can be used as additional input for PID at BESIII.

3.2.4. Muon Counter (MUC)

The muon counter is the only sub-detector system which is mounted outside the coil of the superconducting solenoid. It allows distinguishing between muons and pions by

exploiting the feature of muons to penetrate large amounts of heavy material, while pions tend to be stopped either in the EMC or the coil of the superconducting solenoid. Both pions and muons produce almost the same specific energy loss and time-of-flight signals due to the proximity of their masses as well as their equal charges. Hence, using only information from the inner detector systems would not allow for a μ/π separation. Therefore, the magnetic flux return yoke has been instrumented with **Resistive Plate Counters (RPC)**. The barrel part is organized into octanes, each of which consists of nine layers. Endcaps include eight layers of RPC modules, organized into quadrants. The full solid angle coverage amounts to $\sim 89\%$. The active detector volume is filled with a gas mixture of Argon Ar, Tetrafluoroethane $C_2F_4H_2$ and n-Butan C_4H_{10} (50%/42%/8%), providing an average single gap RPC efficiency of 96% at a working voltage of 8 kV and a dark current of less than $1 \mu A/m^2$. Investigating the penetration depth for muons and pions, a clear μ/π separation is achieved at a cut-off length of ~ 4 cm [206].

3.2.5. Trigger System

The trigger system is required to select physics events with a high efficiency while simultaneously suppressing cosmic ray and beam related backgrounds. It is composed of a two-stage trigger. The first trigger (L1 trigger) is realized as a hardware trigger utilizing field-programmable gate array (FPGA) driven front-end boards. Once a signal is accepted by the L1 trigger logic, the complete readout buffer is transmitted to an online event filter. The second trigger level (L3 trigger) is a software event filter, further reducing the background rate based on various event filters, such as MDC track finding and EMC cluster shaping algorithms. After an event is accepted, it is permanently stored to disk with approximately 42 Mb/s during normal operation, which corresponds to an event rate of about 2 kHz at the mass of the J/ψ . The expected event as well as background rates after both the L1 and L3 triggers are shown in Table 3.2.

Table 3.2.: Expected event and background rates of the BESIII trigger system at a center-of-mass energy corresponding to the J/ψ mass before and after the L1 and L3 triggers. Values are taken from [205].

Processes	Event rate (kHz)	After L1 (kHz)	After L3 (kHz)
Physics	2	2	2
Bhabha	0.8	Pre-scaled	Pre-scaled
Cosmic ray	< 2	~ 0.2	~ 0.1
Beam background	$> 10^4$	< 2	< 1
Total	$> 10^4$	4	3

3.3. BESIII Data Sets

In recent years, BESIII have accumulated several high statistics data sets in order to cover its physics programs [153, 200]. Besides the world's largest data set at the J/ψ resonance containing about ten billion of events for precision studies of light hadrons, a large data sample at the $\psi(2S)$ resonance containing about three billion of events was taken for detailed studies of charmonium transitions and decay studies of non-vector charmonia. Additionally, a large amount of high luminosity data sets at various center-of-mass energies between $\sqrt{s} = 3.7$ GeV and $\sqrt{s} = 5.0$ GeV enable dedicated studies of exotic charmonia, in the following called XYZ data. The BESIII experiment is therefore the world leading experiment in the study of exotic particles in the charmonium region thanks to the ability to directly produce them in large numbers, with multiple important contributions to the field of charmonium spectroscopy as mentioned in Subsection 2.3.4. Figure 3.3 summarizes the current data available at BESIII above 3.7 GeV.

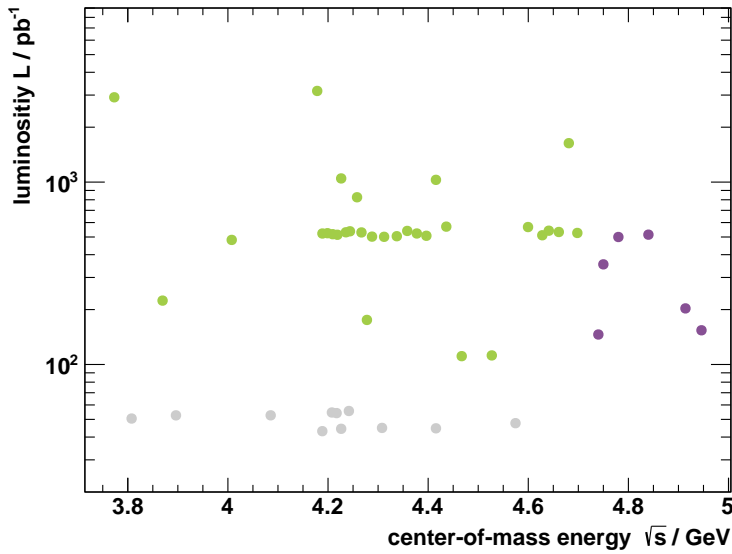


Figure 3.3.: Luminosities of the high luminosity BESIII XYZ data sets at center-of-mass energies above 3.7 GeV. **Green:** Data sets used in this work. **Purple:** Recently taken data sets, but not finally calibrated yet. **Gray:** Low luminosity scan data sets. Values are taken from [211–213].

Since this work aims for both the search for couplings of exotic charmonia ψ to light hadron final states and the investigation of the scalar isoscalar sector, the data at the $\psi(2S)$ resonance as well as the XYZ data are used, with the latter including a total integrated luminosity L of 22.7 fb^{-1} measured based on the Bhabha scattering process $e^+e^- \rightarrow (\gamma)e^+e^-$ [214].

All data as well as Monte Carlo (MC) simulations are reconstructed and analyzed in the object-oriented **BESIII Offline Software System** (BOSS) [215], which is based on

the GAUDI framework [216]. It provides tools for event and detector simulation, data processing as well as physics analysis. While the detector simulation is realized using the GEANT4-based [217] simulation software BOOST (**BESIII Object-Oriented Simulation Tool**) [218], including a geometric description of the BESIII detector, its response as well as performance and running conditions, the MC generator software package KKMC [219] is used for event generation. It is constructed in the framework of BesEvtGen [220], an adaptation of the EvtGen [221] package, allowing to precisely calculate correction factors for initial-state radiation (ISR) and vacuum polarization (VP) factors as well as to obtain efficiencies for the processes under investigation.

Typically, data events are not distributed evenly in phase space. In order to allow for a proper efficiency correction using MC generated events, a partial wave analysis (PWA) is carried out which uses signal MC samples containing evenly distributed phase space events as input to obtain a new, weighted signal MC sample as an effective description of data. The theoretical basis was already discussed in Sections 2.4 and 2.5 and its practical application is shown in Chapter 5.

Furthermore, the so-called inclusive MC sample at $\sqrt{s} = 4.178 \text{ GeV}$ provided by the BESIII collaboration is used for background studies. To minimize statistical uncertainties, it contains an equivalent integrated luminosity of about 40 times the data luminosity, including open charm processes, continuum production of hadrons, QED and initial-state radiation processes. The branching fractions of all known decay modes are set to world average values from the Particle Data Group (PDG) [56] and are generated with EvtGen [221, 222]. The remaining unmeasured decay modes are generated by LUNDCHARM [223–226]. Note that for the production of resonances in EvtGen a relativistic Breit-Wigner according to Equation (2.87) is used as its lineshape.

4. Event Selection

The data sets used in this work require a pre-selection due to the tremendous amount of events accumulated with state of the art high-energy physics experiments like BESIII. Standardized selection conditions for charged tracks and photon candidates, so-called initial event selection criteria, will be presented in the following. Charged tracks are reconstructed with a track fitting algorithm based on the Kalman filter method [227] and are combined with the photon candidates to one of the analyzed final states $K^+K^-K^+K^-$, $K^+K^-K_S^0K_S^0$, $p\bar{p}\pi^+\pi^-\eta$ and $p\bar{p}\pi^+\pi^-\gamma$ if satisfying the aforementioned initial event selection criteria.

4.1. Charged Track Selection

Particle identification In a first step, the particle identification system (PID) of BESIII [153,206] assigns a probability to each measured charged track for being a charged particle of species $\mathcal{H} \in \{e^\pm, \mu^\pm, \pi^\pm, K^\pm, p, \bar{p}\}$. Since the PID capabilities are quite different for each sub-detector and for each momentum range, it is necessary to combine the available information in the most optimal way in order to improve the PID performance. In general, the response of a detector to each particle species is given by a probability density function (PDF) $\mathcal{P}(x;p,\mathcal{H})$, which describes the probability that a particle of the aforementioned species leaves a signature x described by a vector of measurements $(dE/dx, t, m^2, \Delta E/p, \dots)$. $\mathcal{P}(x;p,\mathcal{H})dx$ is the probability for the detector (element) to respond to a track of momentum p and type \mathcal{H} with a measurement in the range $(x, x+dx)$ and consequently $\int \mathcal{P}(x;p,\mathcal{H})dx = 1$. Note that x may describe a single or several measurements in one or several detectors which may be correlated with respect to a single hypothesis (e.g. $\Delta E/p$ and the shower shape of electrons in the EMC) or to different detectors (e.g. the energy deposited in the EMC and the muon chambers by charged pions). While in many cases these correlations are reasonably small and may be neglected, they need sophisticated and powerful algorithms such as the likelihood method [153] to take them into account if necessary. In case of highly correlated measurements, near-optimal discrimination variables may be constructed using neural networks [228]. They can be applied to the BESIII PID algorithm and are implemented in ROOT [229,230] as a multilayer perceptron (MLP) neural network.

In this work however, a $\chi^2(i)$ value for each sub-detector system is assigned to each

charged track in an event for being a particle of the type \mathcal{H}_i . The $\chi^2(i)$ values are added in quadrature for each sub-detector system used for PID according to

$$\chi_{\text{PID}}^2(i) = \chi_{\text{dE/dx}}^2(i) + \chi_{\text{TOF}}^2(i), \quad (4.1)$$

with $\text{NDF}_{\text{PID}} = 2$ being the number of degrees of freedom in the $\chi_{\text{PID}}^2(i)$ determination. The probability of a charged track for being a particle of type \mathcal{H}_i is calculated as

$$\text{Prob}_{\text{PID}}(i) = \text{Prob}(\chi_{\text{PID}}^2(i), \text{NDF}_{\text{PID}}). \quad (4.2)$$

A minimal combined probability of 10^{-5} is required for pions, kaons and protons to be identified in order to reduce background with tracks, where the PID system is unable to assign a clear particle hypothesis \mathcal{H} .

The number of charged tracks measured in each event is limited to two in addition to the number of charged particles in the final state. Therefore, combinations can be formed that are to be considered valid and used for further analysis if they satisfy the following energy and momentum balance:

$$\left| \left(\sum_{i=1}^n E_i \right) - E_{\text{initial}} \right| < 0.25 \text{ GeV}, \quad \left| \left(\sum_{i=1}^n \vec{p}_i \right) - \vec{p}_{\text{initial}} \right| < 0.25 \text{ GeV}/c, \quad (4.3)$$

with E_i and \vec{p}_i being the energy and the momentum of track i , and E_{initial} and \vec{p}_{initial} being the initial energy and the initial momentum right after the collision of the e^+e^- system, respectively. Furthermore, in the case of $e^+e^- \rightarrow \phi K\bar{K}$ the invariant mass $m(K^+K^-)$ of at least one combination of an oppositely charged kaon pair has to satisfy $2m_{\text{K}} \leq m(K^+K^-) < 1.5 \text{ GeV}/c^2$ in the considered event, with $2m_{\text{K}}$ being the nominal mass of two kaons. Thereby, a first $\phi \rightarrow K^+K^-$ selection is performed.

Vertex fit Most of the hadronic resonances produced right after the annihilation of the e^+e^- pair as well as during the subsequent decay processes leading to the investigated final states decay via the strong interaction. Hence, they have a very short lifetime which results in the assumption of a common point of origin of all charged tracks, the so-called initial (primary) vertex. All charged tracks coming from this initial vertex are constrained by a vertex fit to a helix model, varying their reconstructed track parameters within its measured uncertainties. This fit contains five parameters $\vec{a} = (d_\rho, \phi_0, \kappa, d_z, \lambda)$, with d_ρ being the signed distance on the transverse $x - y$ plane from the helix center to the interaction point (pivot), ϕ_0 being the azimuthal angle specifying the interaction point with respect to the helix center, $\kappa = 1/P_t$ being the reciprocal of the transverse momentum P_t (the sign of κ represents the charge of the track), d_z being the signed distance of the helix center from the interaction point in z direction and $\tan \lambda$ being the

slope of the track with λ being the dip angle [231]. Their geometrical meaning is illustrated in Figure 4.1. Hence, a charged particle in a uniform magnetic field is represented by a helical trajectory and its position along this helix is given by

$$\begin{aligned} x &= x_0 + d_\rho \cos \phi_0 + \frac{\alpha}{\kappa} (\cos \phi_0 - \cos (\phi_0 + \phi)) \\ y &= y_0 + d_\rho \sin \phi_0 + \frac{\alpha}{\kappa} (\sin \phi_0 - \sin (\phi_0 + \phi)) \\ z &= z_0 + d_z - \frac{\alpha}{\kappa} \tan \lambda \cdot \phi, \end{aligned} \quad (4.4)$$

with $\alpha = 1/cB$ being the magnetic field constant and ϕ being the turning angle and determines the location. Commonly, the helix parameters \vec{a} are defined at the interaction point $\vec{x}_0 = (x_0, y_0, z_0)^T$. Further, the helix center in $x - y$ plane is

$$\begin{aligned} x_c &= x_0 + \left(d_\rho + \frac{\alpha}{\kappa} \right) \cos \phi_0 \\ y_c &= y_0 + \left(d_\rho + \frac{\alpha}{\kappa} \right) \sin \phi_0 \end{aligned} \quad (4.5)$$

and the signed radius of the circle is given by $\rho = \alpha/\kappa$. Consequently, the track momentum can be expressed as $P_t = 1/|\kappa|$ [231]. For the actual primary vertex reconstruction all

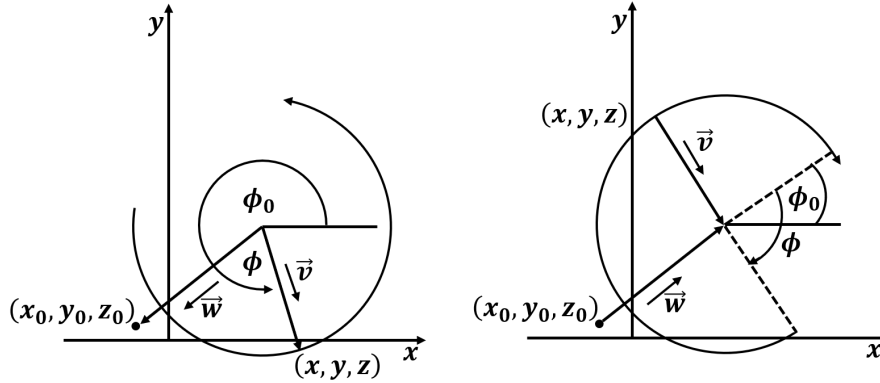


Figure 4.1.: Schematic representation of the helix parametrization for negative (**left**) and positive (**right**) charged tracks. The vectors are defined by $\vec{x} = \vec{x}_0 + (d_\rho + \rho) \cdot \vec{w} - \rho \cdot \vec{v}$, with $\vec{w} = (\cos \phi_0, \sin \phi_0)^T$ and $\vec{v} = (\cos (\phi_0 + \phi), \sin (\phi_0 + \phi))^T$.

reconstructed tracks are used as input. Here, first loose selection criteria are applied: Charged tracks are required to be measured within $|\cos \vartheta| < 0.93$ with θ being the polar angle and its track parameters have to satisfy $|d_z| < 20$ cm with d_z being the coordinate of the closest point approaching the origin along the z -axis [232]. Accepted tracks are regarded as the seed tracks for primary vertex fitting. In a next step, the pair of tracks with the smallest distance is used as the first two candidates for vertex fitting, and the remaining tracks are added to the pre-determined vertex one after the other. During the fit procedure, the vertex position, the track helix parameters and therefore the 3-

momentum vector are continuously updated. The 3-position vector is taken as the value for the vertex position in the last Kalman filter step [232]. The χ^2 of the primary vertex reconstruction is set in order to minimize the distance d between the common vertex, i.e., the point with the smallest distance to all charged particle trajectories, and the run dependent interaction point (see Figure 4.2). After vertex fitting, selection conditions for

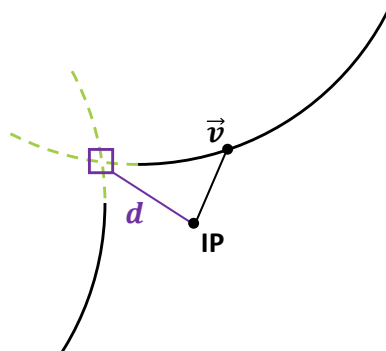


Figure 4.2.: Illustration of the trajectories of two charged tracks with common vertex (purple box). Its distance d to the run dependent interaction point (IP) is minimized in the vertex fit. Constraints on the fit result are set with respect to the point of the closest approach \mathbf{v} to the run dependent interaction point according to Equation (4.6).

the point of the closest approach $\mathbf{v} = (v_x, v_y, v_z)$ to the run dependent interaction point are set to

$$\begin{aligned} v_r = \sqrt{v_x^2 + v_y^2} < 1 \text{ cm} , \\ |v_z| < 10 \text{ cm} . \end{aligned} \tag{4.6}$$

K_S^0 mesons are reconstructed via their decay into two charged pions. This weak decay with a mean lifetime of $\tau = (8.954 \pm 0.004) \cdot 10^{-11}$ s [56] leads to a second vertex. Hence, for the process $e^+e^- \rightarrow \phi K_S^0 K_S^0$ an additional secondary vertex fit is performed, reconstructing two tracks of oppositely charged pions to a common vertex where a possible K_S^0 decay could have happened. The only requirement is that the fit converges.

In case of $e^+e^- \rightarrow p\bar{p}\eta'$, selection conditions on photon candidates are applied before the kinematic fit is performed. The photon candidate selections are discussed in the following.

4.2. Photon Candidate Selection

When a photon hits the EMC and interacts with one or more CsI(Tl) crystals, it is transformed into a e^+e^- pair by γ -conversion. This e^+e^- pair emits further photons through bremsstrahlung, leading to an alternating continuation of these processes. By this, an electromagnetic shower is produced, which develops laterally and longitudinally as well as loses energy in one or several connected crystals.

A cluster finding algorithm identifies these geometrically related crystals and combines them to clusters [233]. Note that a cluster can be the result of one or more showers. Hence, each shower is recognized by a seed, which is the local maxima of energy deposit among its neighbors. For example, a high momentum π^0 meson is likely to create a cluster containing two showers. In that case, every crystal involved will be assigned a weight from each seed and thus contributes a certain shared energy to each shower. The position of the primary hit is calculated as the weighted mean [233]

$$x_c = \frac{\sum_i W_i(E_i)x_i}{\sum_i W_i(E_i)}, \quad (4.7)$$

with the weight $W_i(E_i)$ being a function of energy deposited in the i th crystal and x_i being the coordinate of the crystal center at the front face. The simplest assumption is a linear weighting function $W_i(E_i) = E_i$. A minimal energy deposit ΔE is required in order to suppress background photons in the EMC

$$\begin{aligned} \Delta E &> 25 \text{ MeV in the barrel region } |\cos \vartheta| < 0.8, \\ \Delta E &> 50 \text{ MeV in the endcap regions } 0.86 < |\cos \vartheta| < 0.92. \end{aligned}$$

The higher threshold for photon detection in the endcap regions is set to reduce low-energetic photons from beam backgrounds. Further, a cut on the timing information T from the EMC with respect to the event start time further suppresses electronic noise and energy deposits unrelated to the event

$$0 \text{ ns} \leq T \leq 700 \text{ ns}.$$

Additionally, a cut is applied on the angle between straight lines from the vertex to the position of the shower and the extrapolated position of the closest charged track t in the EMC

$$\angle(t, \gamma) > 10^\circ.$$

4.3. Kinematic Fit

Tracks that survive the previously described selection conditions are combined to different final states, as depicted in Table 4.1. While K_S^0 mesons are reconstructed via their decay into two charged pions, η mesons are reconstructed via their subsequent electromagnetic decays into two photons. In case of final states involving photons, the number of photon candidates is only restricted to being greater than or equal to the number of photons in the final state due to noise in the EMC.

For each combination, a kinematic fit is performed in order to improve the mass and

momentum resolution of the measured quantities. Several kinematic constraints r can be applied, such as the conservation of energy and momentum (four constraints) in the initial production or additional mass constraints on charged pion (constrained to the K_S^0 mass) or photon pairs (constrained to the η mass). The fitting algorithm is based on the Lagrange multiplier method [234] and uses the MDC information for charged tracks and EMC information for neutral particles. It is assumed that the constraint equations can be linearized and summarized in two matrices \mathbf{D} and \mathbf{d} . The r constraint functions can be written as [153]

$$\mathbf{H}(\alpha) \equiv 0, \quad \text{where} \quad \mathbf{H} = (H_1 H_2 \dots H_r), \quad (4.8)$$

with α being a column vector representing the parameters for a set of n tracks. α_0 are the unconstrained values of the initial track parameters after vertex fitting and before kinematic fitting. The constraint functions can be expanded around some point α_A , yielding the linearized equations

$$0 = \frac{\partial H(\alpha_A)}{\partial \alpha} (\alpha - \alpha_A) + H(\alpha_A) = \mathbf{D}\delta\alpha + \mathbf{d}, \quad (4.9)$$

with $\delta\alpha = \alpha - \alpha_A$ and thus $D_{ij} = \frac{\partial H_i}{\partial \alpha_j}$ and $d_i = H_i(\alpha_A)$. Further, the χ^2 can be written as a sum of two terms [153]

$$\chi^2 = (\alpha - \alpha_0)^T V_{\alpha_0}^{-1} (\alpha - \alpha_0) + 2\lambda^T (\mathbf{D}\delta\alpha + \mathbf{d}), \quad (4.10)$$

with λ being a vector of r unknown Lagrange multipliers. The final equations after minimizing the χ^2 with respect to α and λ can be written as

$$\alpha = \alpha_0 - V_{\alpha_0} \mathbf{D}^T \lambda = 0 \quad (4.11)$$

$$\lambda = V_{\mathbf{D}} (\mathbf{D}\delta\alpha_0 + \mathbf{d}) \quad (4.12)$$

$$V_{\alpha} = V_{\alpha_0} - V_{\alpha_0} \mathbf{D}^T V_{\mathbf{D}} \mathbf{D} V_{\alpha_0}, \quad (4.13)$$

with $V_{\mathbf{D}} = (\mathbf{D} V_{\alpha_0} \mathbf{D}^T)^{-1}$ being the $r \times r$ constraint covariance matrix and

$$\chi^2 = \lambda^T V_{\mathbf{D}}^{-1} \lambda = \lambda^T (\mathbf{D}\delta\alpha_0 + \mathbf{d}) \quad (4.14)$$

being the final χ^2 expression. In order to perform kinematic fitting, it is necessary to choose a track representation that uses physically meaningful quantities. Typically, the so-called four-parameter W format is adopted, using the four-momentum $\alpha = (p_x, p_y, p_z, E)$. Here, the aforementioned five helix parameters are used for charged tracks in MDC track fitting, whereas for photon candidates the parameters used in EMC reconstruction serves as input [234].

Table 4.1.: Branching fractions $\mathcal{B}r$ [56] and reconstruction patterns of the analyzed final states as well as the number of additional mass constraints r used in the kinematic fit.

Mode i	$\mathcal{B}r$ (Γ_i/Γ)	N_p	$N_{\bar{p}}$	N_{K^+}	N_{K^-}	N_{π^+}	N_{π^-}	N_γ	r
<hr/>									
$e^+e^- \rightarrow \phi K\bar{K}$									
ϕK^+K^-		0	0	2	2	0	0	0	0
$\phi K_S^0 K_S^0$		0	0	1	1	2	2	0	2
$\phi \rightarrow K^+K^-$	$(49.2 \pm 0.5)\%$								
$K_S^0 \rightarrow \pi^+\pi^-$	$(23.6 \pm 0.2)\%$								
<hr/>									
$e^+e^- \rightarrow p\bar{p}\eta'$									
$p\bar{p}\eta\pi^+\pi^-$		1	1	0	0	1	1	≥ 2	1
$p\bar{p}\gamma\pi^+\pi^-$		1	1	0	0	1	1	≥ 1	0
$\eta' \rightarrow \eta\pi^+\pi^-$	$(42.6 \pm 0.7)\%$								
$\eta' \rightarrow \gamma\pi^+\pi^-$	$(29.5 \pm 0.4)\%$								
$\eta \rightarrow \gamma\gamma$	$(39.4 \pm 0.2)\%$								

The most common kinematic constraint in high energy physics is the energy-momentum conservation (four-momentum). It states that the sum of four-vectors of all final-state particles must be equal to the four-vector of the initial state. Additional constraints used in this analysis are invariant mass constraints, forcing several tracks to have an invariant mass m_c that satisfies $E^2 - p_x^2 - p_y^2 - p_z^2 - m_c^2 = 0$, e.g. in decays such as $K_S^0 \rightarrow \pi^+\pi^-$ or $\eta \rightarrow \gamma\gamma$. In case of more than one combination in an event, the one yielding the smallest χ_{NC}^2 value is kept for further analysis.

Another important validation of the kinematic fitting process is the study of so-called pull distributions of the track parameters (a brief discussion of the Least-Squares method and pulls is given in Appendix A.1). The pull of the i^{th} -track parameter is defined as

$$(\text{pull})_i = \frac{\alpha_i - \alpha_{0i}}{\sqrt{(V_{\alpha_0})_{ii} - (V_\alpha)_{ii}}}. \quad (4.15)$$

It is assumed that the pull distribution follows a Gaussian distribution with unit width centered at $x = 0$. If a deviation is observed, proper correction parameters for the covariance matrix of the helix parameters have to be determined. In this analysis the values determined in [235] are used and implemented in the MC production. A detailed description of how to extract correction parameters is given in [236].

5. Analysis of $e^+e^- \rightarrow \phi K\bar{K}$

In this chapter, a lineshape study of the energy-dependent Born cross section σ_b for the processes $e^+e^- \rightarrow \phi K^+K^-$ and $e^+e^- \rightarrow \phi K_S^0 K_S^0$ is carried out in the search for couplings of (exotic) vector charmonia to the investigated light hadron final states, using the BESIII data sets accumulated at center-of-mass energies from $\sqrt{s} = 3.7730$ GeV to $\sqrt{s} = 4.7008$ GeV. The Born cross section, which is per definition the lowest order cross section (see Section 5.4), is given by

$$\sigma_b(e^+e^- \rightarrow \phi K\bar{K}) = \frac{N_{\text{obs}}}{L \cdot (1 + \delta_r) \cdot (1 + \delta_v) \cdot \varepsilon \cdot \mathcal{B}r} , \quad (5.1)$$

with N_{obs} being the number of observed signal events in data, L being the integrated luminosity (see Section 3.3), $(1 + \delta_r)$ and $(1 + \delta_v)$ being correction factors for initial state radiation and vacuum polarization, respectively, ε being the detection efficiency and $\mathcal{B}r$ being the product of the branching ratios of $\phi \rightarrow K^+K^-$ and, if present, $K_S^0 \rightarrow \pi^+\pi^-$ decays. The determination of these parameters required to calculate the Born cross section is presented in the following sections including the study of their respective statistical and systematic uncertainties.

After the initial event selection discussed in Chapter 4, also a reaction-dependent final event selection is applied in order to identify all final state particles. While charged kaons recoiling off the ϕ meson can be assumed as stable and can be measured directly with the BESIII detector, K_S^0 mesons recoiling off the ϕ meson are reconstructed in their decay $K_S^0 \rightarrow \pi^+\pi^-$ with $\mathcal{B}r(K_S^0 \rightarrow \pi^+\pi^-) = (69.20 \pm 0.05)\%$ [56]. In order to identify the K_S^0 mesons properly, a mass window is applied given by

$$|m(\pi^+\pi^-) - m_{K_S^0, \text{PDG}}| < 12.0 \text{ MeV}/c^2 . \quad (5.2)$$

Additionally, a flight significance $\frac{L}{\sigma}$ with L and σ being the distance between the common vertex of the $\pi^+\pi^-$ pair and the primary vertex and its error, respectively, is defined. Commonly, for both K_S^0 mesons $\frac{L}{\sigma} > 2$ is required [237].

As a light, short-lived meson, the ϕ meson is reconstructed in its decay $\phi \rightarrow K^+K^-$ with $\mathcal{B}r(\phi \rightarrow K^+K^-) = (49.2 \pm 0.5)\%$ [56]. ϕ meson candidates can be identified by investigating the invariant mass spectra of their daughter particles after all selection criteria as shown in Figure 5.1. A clear resonant structure is observed almost background free at the nominal mass of the ϕ meson [56] in both final states. The number of observed

signal events in data N_{obs} can be obtained by a fit to data, including individual functional forms for the signal and background contributions, respectively, and integrating the signal part. However, one has to ensure that no background processes are present which may lead to resonant structures around the mass of the ϕ meson. Therefore, background studies are performed in the next section.

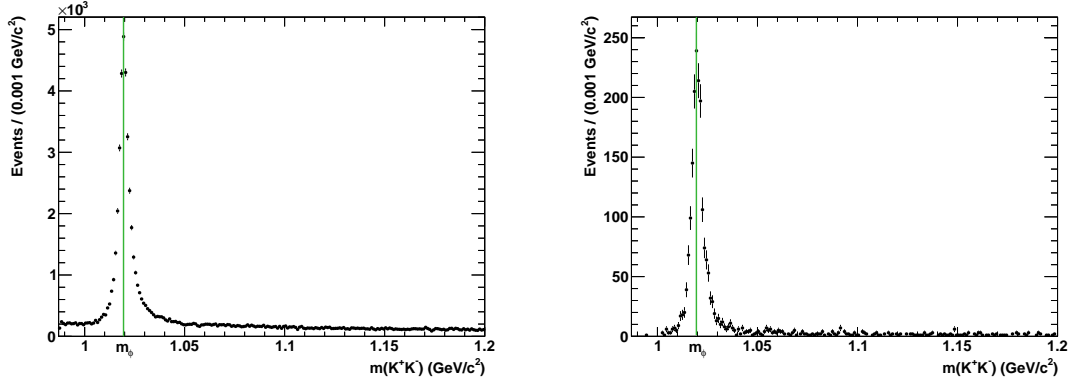


Figure 5.1.: Invariant mass spectrum of ϕ candidates for $e^+e^- \rightarrow \phi K^+K^-$ (left) and $e^+e^- \rightarrow \phi K_S^0 K_S^0$ (right) for the summed data set after all selection criteria. The green vertical lines represent the world average value $m_\phi = (1019.461 \pm 0.016) \text{ MeV}$ from the PDG [56]. A clear resonant structure is observed almost background free at the mass of the ϕ meson in both final states.

5.1. Background Studies

Using the inclusive MC sample at $\sqrt{s} = 4.178 \text{ GeV}$, a proper analysis of reactions contributing to both the signal and to the background events left after the aforementioned selection criteria can be performed. The cross sections of reactions incorporated into this inclusive MC sample were obtained from the PDG [56]. Since most of these processes are poorly measured, if measured at all, the raw ratio of signal and background processes does not necessarily match the observed data. Therefore, both signal and background contributions are scaled separately using scale parameters determined by a fit to data. The ϕ meson invariant mass spectra was chosen as the reference spectrum as shown in Figure 5.2. An overall good agreement is observed, despite a deviation between the right shoulder of the signal part of the inclusive MC sample (red) and the resonant structure at the ϕ meson mass in data for $m(K^+K^-) \in [1.03 \text{ GeV}/c^2, 1.10 \text{ GeV}/c^2]$. The reason for this is a lower and upper limit on the invariant mass of the ϕ meson on generator level which was set by the BESIII collaboration. Also, the description of the recoiling $K\bar{K}$ invariant mass spectrum is lacking due to incomplete cross sections for processes involving f_0 and f_2 mesons.

However, important information can be gained from the inclusive MC sample. An

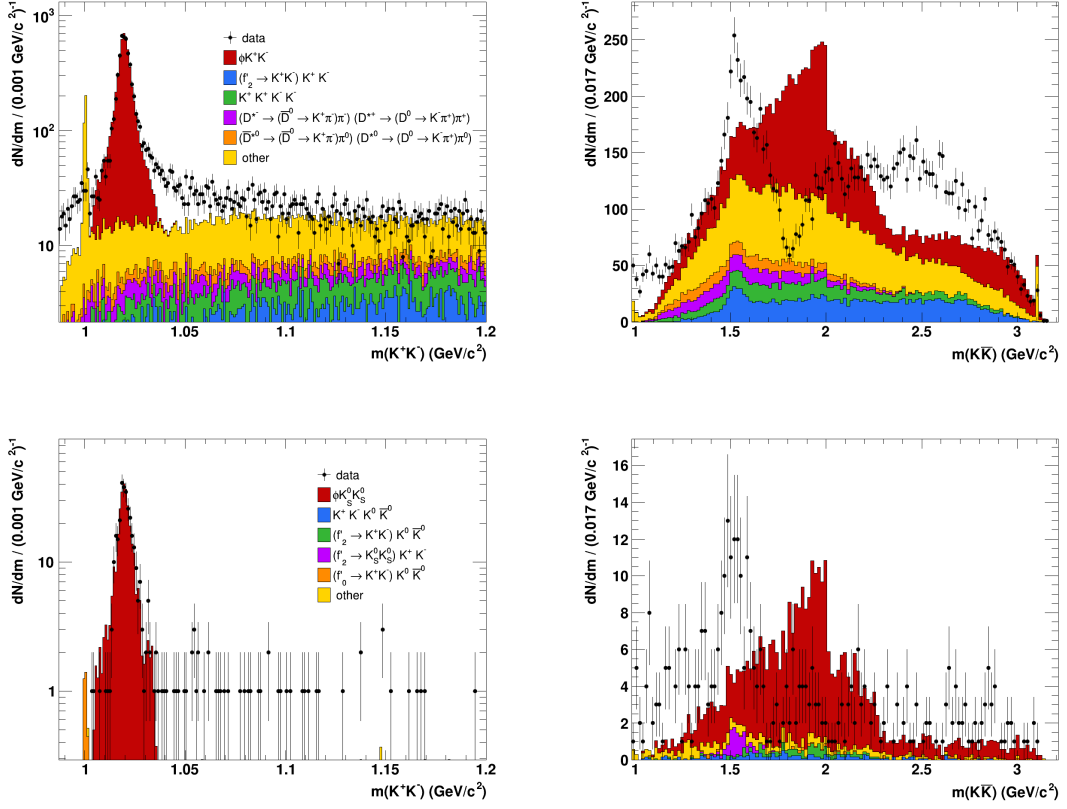


Figure 5.2.: Fit of the signal and background contributions extracted from the inclusive MC sample to the invariant mass spectrum of ϕ candidates (**left**) and respective recoiling $K\bar{K}$ invariant mass spectrum (**right**) for $e^+e^- \rightarrow \phi K^+K^-$ (**top**) and $e^+e^- \rightarrow \phi K_S^0 K_S^0$ (**bottom**) for $\sqrt{s} = 4.178$ GeV. Data (black dots with error bars), the signal contribution (red) as well as main background contributions are shown.

overview of the surviving contributions is given in Table 5.1. In both final states, the resonant structure observed at the ϕ meson mass fully relates to the signal processes $e^+e^- \rightarrow \phi K^+K^-$ and $e^+e^- \rightarrow \phi K_S^0 K_S^0$ while no peaking background is observed. Additionally, the main background contributions lead to the same final state as the signal, e.g. $e^+e^- \rightarrow f_2'(1525)(\rightarrow K^+K^-)K^+K^-$ or $e^+e^- \rightarrow K_S^0 K_S^0 K^+K^-$ where no ϕ meson is involved. Hence, their kinematic χ_{NC}^2 value is equal to that of the signal processes. A significant amount of background processes contributing in $e^+e^- \rightarrow \phi K^+K^-$ comes from the misidentification of kaons as pions, e.g. in $e^+e^- \rightarrow (D^{*-} \rightarrow (\bar{D}^0 \rightarrow K^+\pi^-)\pi^-) + (D^{*+} \rightarrow (\bar{D}^0 \rightarrow K^-\pi^+)\pi^+)$. Due to the different masses of the K and π mesons, the χ_{NC}^2 value of these processes is likely to be different compared to signal. The signal significance with respect to these background processes, which lead to different

Table 5.1.: Inclusive MC events that survive the selection criteria identified as the $K^+K^-K^+K^-$ or $K^+K^-K_S^0K_S^0$ final state. **Green:** Signal contributions. **White:** Background contributions. The listed processes are sorted according to their yield. Processes with lower yields are denoted by remaining. Note that the number of events is indicative, as the inclusive MC samples does not accurately describe data.

Reaction	Number of events
$\phi(\rightarrow K^+K^-)K^+K^-$	63360
$\phi(\rightarrow K^+K^-)f_2'(1525)(\rightarrow K^+K^-)$	8
$f_2'(1525)(\rightarrow K^+K^-)K^+K^-$	12077
$K^+K^-K^+K^-$	7107
$(D^{*-} \rightarrow (\bar{D}^0 \rightarrow K^+\pi^-)\pi^-) + (D^{*+} \rightarrow (\bar{D}^0 \rightarrow K^-\pi^+)\pi^+)$	4380
$(D^{*0} \rightarrow (\bar{D}^0 \rightarrow K^+\pi^-)\pi^0) + (D^{*0} \rightarrow (\bar{D}^0 \rightarrow K^-\pi^+)\pi^0)$	3840
$(\bar{D}^{*0} \rightarrow (\bar{D}^0 \rightarrow K^+\pi^-)\pi^0) + (D^0 \rightarrow K^-\pi^+)$	2918
$(\bar{D}^0 \rightarrow K^+\pi^-)\pi^0 + (D^{*0} \rightarrow (D^0 \rightarrow K^-\pi^+)\pi^0)$	2862
sum of remaining	26363
$\phi(\rightarrow K^+K^-)K_S^0K_S^0$	3730
$K_S^0K_S^0K^+K^-$	265
$f_2'(1525)(\rightarrow K^+K^-)K_S^0K_S^0$	246
$f_2'(1525)(\rightarrow K_S^0K_S^0)K^+K^-$	192
$f_0(980)(\rightarrow K^+K^-)K_S^0K_S^0$	61
$f_0(1710)(\rightarrow K^+K^-)K\bar{K}$	47
$K^-K^0a_2(1320)(\rightarrow K^+K^0)$	42
sum of remaining	753

final states, can be maximized using the so-called figure of merit (FOM, see Figure 5.3). It is defined as

$$f(\chi_{\text{cut}}^2) = \frac{S}{\sqrt{S+B}}, \quad (5.3)$$

with S and B being the scaled number of signal and background events left after a selection condition on the χ_{NC}^2 value at χ_{cut}^2 , respectively. A maximum signal significance is achieved for selection conditions of $\chi_{4C}^2 < 93$ and $\chi_{6C}^2 < 227$ for the processes $e^+e^- \rightarrow \phi K^+K^-$ and $e^+e^- \rightarrow \phi K_S^0K_S^0$, respectively.

5.2. Number of Observed Events

The remaining invariant mass distributions of the ϕ meson candidates are depicted in Figure 5.4 after applying all selection criteria discussed in the previous sections. Since no peaking background contributions are present around the ϕ meson mass, a fit to data can be applied in order to extract the number of observed events N_{obs} for both

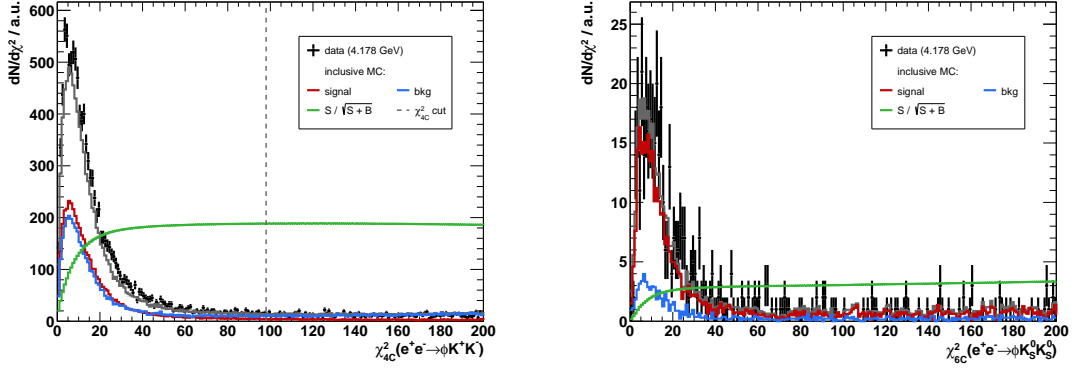


Figure 5.3.: χ_{NC}^2 distributions (gray line) obtained using the inclusive MC sample at $\sqrt{s} = 4.178$ GeV with signal (red line) and background (blue line) contributions, as well as the resulting FOM (green line) and data (black dots with error bars) for the processes $e^+e^- \rightarrow \phi K^+K^-$ (left) and $e^+e^- \rightarrow \phi K_S^0 K_S^0$ (right). The vertical dashed gray line indicates the selection condition on the χ_{NC}^2 value of the kinematic fit.

final states. The signal $f_{\text{sig}}(x)$ is described using the Breit-Wigner function $h(x)$ from Equation (2.87) convolved with a Gaussian $g(x)$ to account for the energy resolution of the detector system

$$f_{\text{sig}}(x) = \int h(x)g(x - \tau)d\tau, \quad (5.4)$$

with x being the invariant mass of the ϕ meson candidates. The width of the Breit-Wigner function is fixed to the world average value $\Gamma_\phi = (4.249 \pm 0.013)$ MeV from the PDG [56]. Background contributions of both the $K^+K^-K^+K^-$ and $K^+K^-K_S^0K_S^0$ final state are described by a first order polynomial. A maximum likelihood fit is performed to the sum of all 32 data samples in the XYZ regime from $\sqrt{s} = 3.7730$ GeV to $\sqrt{s} = 4.7008$ GeV as shown in Figure 5.4. The nominal values for the mass m_ϕ and the Gaussian widths $\sigma_{K^+K^-}$ and $\sigma_{K_S^0K_S^0}$ from the fit result are

$$\begin{aligned} \sigma_{K^+K^-} &= 0.95 \text{ MeV} \\ \sigma_{K_S^0K_S^0} &= 0.92 \text{ MeV} \\ m_\phi &= 1.01979 \text{ GeV}/c^2. \end{aligned} \quad (5.5)$$

Figure 5.4 also shows two colored regions. The green shaded box represents the signal region in which the number of observed events N_{obs} is extracted. It contains 95% of the signal portion and is set symmetrically around m_ϕ . In principle, this region can be chosen arbitrarily (systematic studies can be found in Subsection 5.6.1), but should contain a known percentage close to 100% of the signal component. The number of signal events could instead not be determined in a fixed region defined by left and right bounds in the invariant mass of the ϕ meson, because the same bounds in the accepted MC might

5. Analysis of $e^+e^- \rightarrow \phi K\bar{K}$

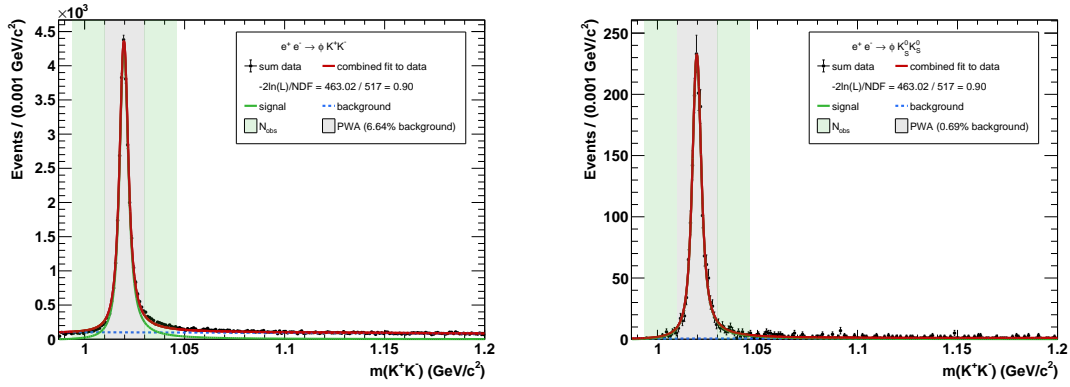


Figure 5.4.: Invariant mass spectrum of ϕ candidates for $e^+e^- \rightarrow \phi K^+K^-$ (left) and $e^+e^- \rightarrow \phi K_S^0 K_S^0$ (right) for all data sets used. Data (black dots with error bars), a combined fit to data (red), the signal and background contribution (solid green and blue dotted, respectively) as well as signal regions to obtain the number of observed events N_{obs} and a global efficiency using a partial wave analysis (green and gray shaded, respectively) can be seen.

not correspond to the same percentage of the total signal in data and MC due to, e.g. possible differences in resolution.

The gray shaded box is set to $[m_\phi - 0.01 \text{ GeV}/c^2, m_\phi + 0.01 \text{ GeV}/c^2]$ and represents the signal events used for the partial wave analysis (PWA). This region is chosen in such a way that the background portion is negligibly small in contrast to the signal. According to the fit to the invariant mass distributions, the amount of background compared to signal events in the blue region is approximately 6.64% and 0.69% for $e^+e^- \rightarrow \phi K^+K^-$ and $e^+e^- \rightarrow \phi K_S^0 K_S^0$, respectively, and therefore can be safely neglected in the partial wave analysis. Furthermore, for the $\phi K_S^0 K_S^0$ final state, the background component is omitted in the following. In the case of significantly larger background portions, these would have to be taken into account in the PWA. For example, sidebands can be defined whose events are assigned negative weights. The assumption here is that the events in the sidebands describe the background in the signal region sufficiently well. However, since the ϕ meson is produced close to the K^+K^- threshold, no suitable left sideband can be defined. Furthermore, due to its asymmetric lineshape, there is a long signal tail, so that the right sideband could only be defined very far away from the nominal mass of the ϕ meson. This means that the background in the signal range can no longer be described sufficiently well. Another alternative would be to include the main background reactions in the PWA model, e.g. $e^+e^- \rightarrow K^+K^- K\bar{K}$. However, in order to have sufficient statistics close to the K^+K^- threshold in the accepted MC sample, a disproportionately large number of events would have to be generated. After the PWA using the events in the blue region, the solution can be extended to the region in which N_{obs} is obtained in order to extract a weighted Monte Carlo sample as an effective and proper description

of data to determine an efficiency correction for each data set.

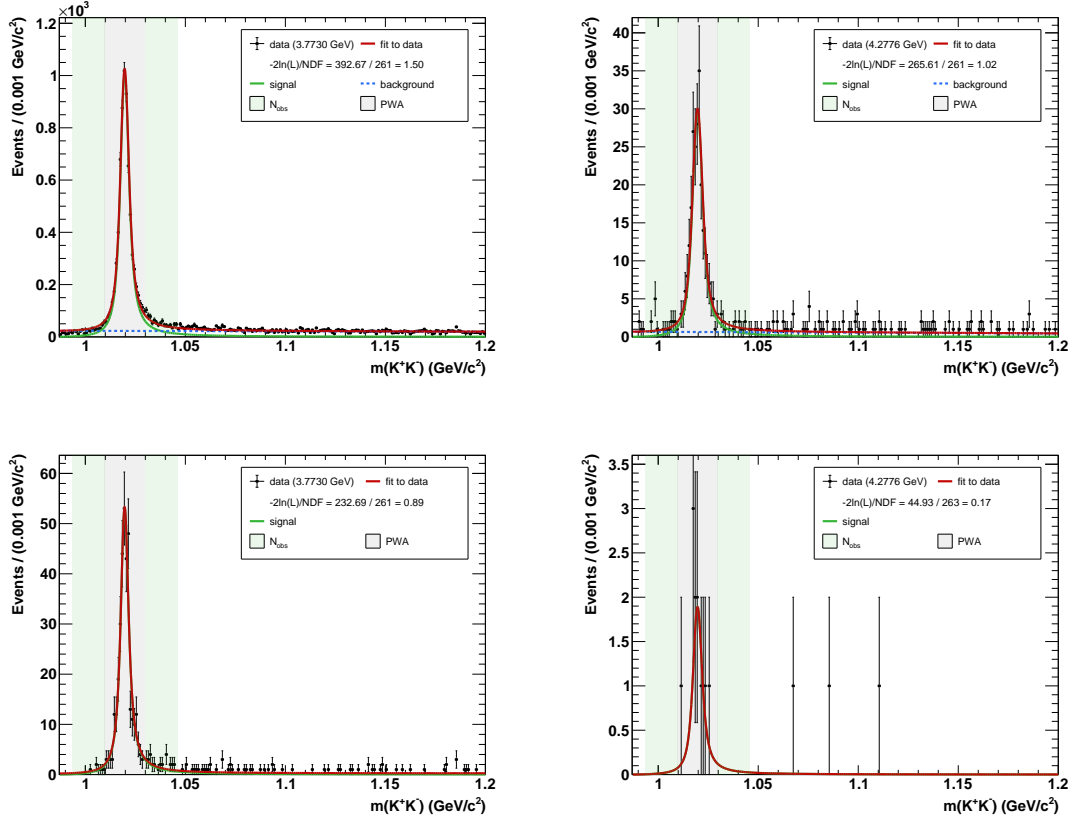


Figure 5.5.: Invariant mass spectrum of ϕ candidates for data (black dots with error bars) at $\sqrt{s} = 3.7730$ GeV (**left**) and $\sqrt{s} = 4.2776$ GeV (**right**). A fit (red line) with a Breit-Wigner function convolved with a Gaussian function as signal (green line) and a first-order polynomial as background (dashed blue line) is applied. The green and gray shaded areas depict the signal regions in which the number of observed events N_{obs} is extracted and for which a PWA is performed to determine a global efficiency, respectively. **Top:** $e^+e^- \rightarrow \phi K^+K^-$. **Bottom:** $e^+e^- \rightarrow \phi K_S^0 K_S^0$.

A maximum likelihood fit is performed for each data set individually with the mass parameter in the Breit-Wigner function fixed to m_ϕ from Equation (5.5), as shown in Figure 5.5 exemplarily for the high statistics data sample at $\sqrt{s} = 3.7730$ GeV and the small statistics data sample at $\sqrt{s} = 4.2776$ GeV. Fit results of all other data sets can be found in Appendices A.3 and A.4. The number of signal events N_{obs} in data is extracted by integrating the signal part of the fit result. In order to account for asymmetric statistical uncertainties due to Poisson statistics, a likelihood scan of N_{obs} is performed by fixing the

5. Analysis of $e^+e^- \rightarrow \phi K\bar{K}$

signal amplitude to suitable values around its nominal value. The resulting distribution can be described by an asymmetric Gaussian function

$$\mathcal{G}(N) = \frac{1}{\sqrt{2\pi}\sigma_k} e^{-\frac{(N-\mu)^2}{2\sigma_k^2}} \quad \text{with} \quad \sigma_k = \begin{cases} \sigma_L, & N \leq \mu \\ \sigma_R, & N > \mu \end{cases}, \quad (5.6)$$

with μ being the mean (here N_{obs}) and σ_L and σ_R being the asymmetrical widths of the Gaussian. Those widths correspond to the lower (σ_L) and upper (σ_R) statistical uncertainty of N_{obs} . The fit results and fit parameters can be found in Figure 5.6 and Tables A.2 and A.4, respectively.

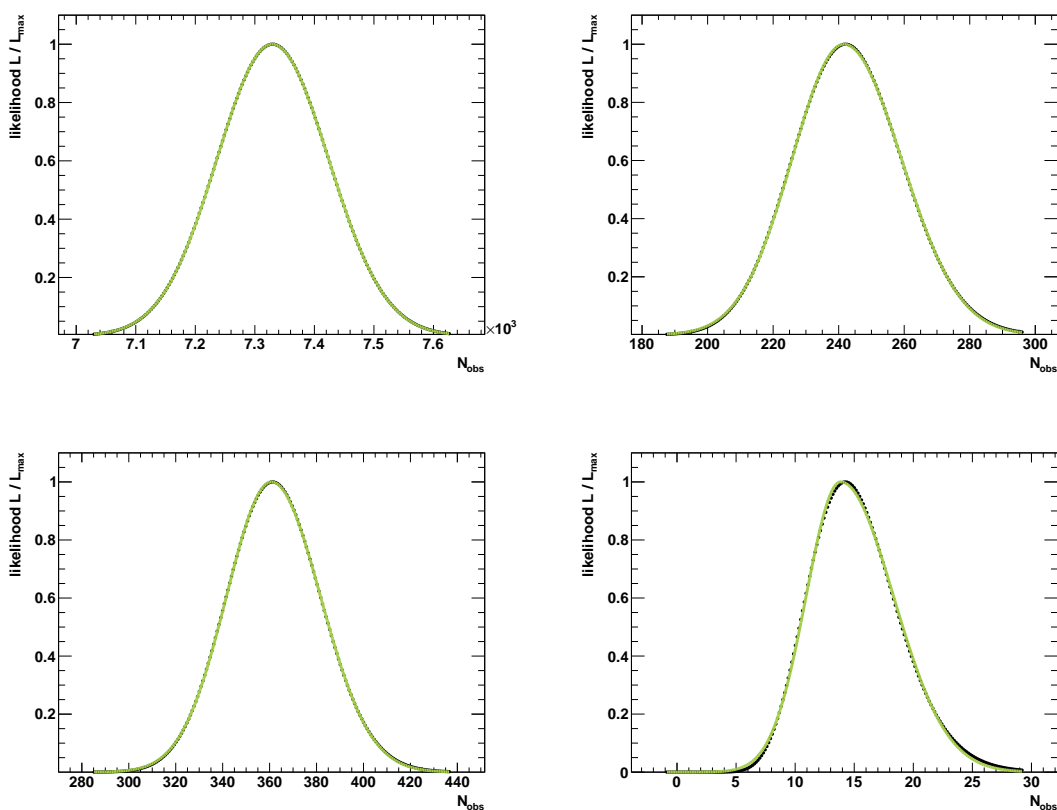


Figure 5.6.: Fit results (green line) of the likelihood scans of the number of observed events N_{obs} in the ϕ candidates invariant mass spectrum (black dots) at $\sqrt{s} = 3.7730$ GeV (**left**) and $\sqrt{s} = 4.2776$ GeV (**right**). **Top:** $e^+e^- \rightarrow \phi K^+K^-$. **Bottom:** $e^+e^- \rightarrow \phi K_S^0 K_S^0$.

5.3. Efficiency

The efficiency ε can be defined according to

$$\varepsilon = \frac{N_{\text{acc}}}{N_{\text{gen}}}, \quad (5.7)$$

with N_{acc} and N_{gen} being the number of reconstructed and generated signal MC events, respectively. In case of events that are not equally distributed over the full n -particle phase-space, Equation (5.7) only holds if the signal MC sample properly reflects data in all relevant coordinates $\vec{x} = \{p_\phi, \theta_\phi, \phi_\phi, p_{K\bar{K}}, \theta_{K\bar{K}}, \phi_{K\bar{K}}, \dots\}$. Since its distribution is a priori unknown, a partial wave analysis of the data is performed in order to re-weight the signal MC sample. The principles of such analyses were already discussed in Sections 2.4 to 2.7.

Within the isobar model, the processes $e^+e^- \rightarrow \gamma^* \rightarrow \phi K^+ K^-$ and $e^+e^- \rightarrow \gamma^* \rightarrow \phi K_S^0 K_S^0$ are decomposed into a sequence of two-body decays. Each is described in the helicity formalism (see Section 2.7). The K_S^0 meson is treated as a stable particle. For the lineshape of the ϕ meson, the signal MC simulations are employed that are used for normalization in the partial wave analysis. Blatt-Weisskopf barrier factors according to [238] are used for both the production $\gamma^* \rightarrow \phi f_J$ and the two-body decays $\phi \rightarrow K^+ K^-$ as well as $f_J \rightarrow K\bar{K}$. The final model includes processes of the type $e^+e^- \rightarrow \phi f_J$ only, with $f_J \rightarrow K^+ K^-$ or $f_J \rightarrow K_S^0 K_S^0$. Due to limited statistics, the possible quantum numbers of the f_J resonances are restricted to $J^{PC} = 0^{++}$ and $J^{PC} = 2^{++}$ in this work. The dynamical part of the scalar isoscalar resonances are described by a K -matrix approach (see Subsection 2.5.4) based on data up to $m(K\bar{K}) \leq 1.9$ GeV, incorporating the five channels $\pi\pi, K\bar{K}, \eta\eta, \eta\eta'$ and 4π with five fixed poles [239]. For higher invariant masses, an additional single $J^{PC} = 0^{++}$ resonance is included, while the $J^{PC} = 2^{++}$ contributions are described by four single resonances. They are parametrized as relativistic Breit-Wigner amplitudes according to Equation (2.87) with masses and widths as free parameters in the fit. No significant contributions from processes of the type $e^+e^- \rightarrow K K^*$ with $K^* \rightarrow \phi K$ were found (see Figures 5.9 and 5.10). Note that the aim of this partial wave analysis is only to describe the data accurately enough to enable a proper determination of the efficiency. This is why, as already mentioned previously in Section 5.1, the remaining background events underneath the ϕ meson peak ($|m_{\phi, \text{PDG}} - m(K^+ K^-)| < 0.01$ GeV/ c^2) are neglected in the partial wave analysis. It is performed as an unbinned maximum likelihood fit using the software package PAWIAN (**P**artial **W**ave **I**nteractive **A**nalysis) [240]. Details on likelihood construction in PAWIAN can be found in [177, 240, 241].

A special comment has to be given regarding the $\phi K_S^0 K_S^0$ final state. Due to low statistics, the fit is performed simultaneously over the energy range from $\sqrt{s} = 3.8720$ GeV to $\sqrt{s} = 4.7008$ GeV with all amplitudes fully constrained between the data sets apart from

5. Analysis of $e^+e^- \rightarrow \phi K\bar{K}$

an overall scaling factor. In case of the data set at $\sqrt{s} = 3.7730$ GeV statistics allow for a separate fit. The fit results at $\sqrt{s} = 4.1784$ GeV are displayed in Figures 5.9 and 5.10, showing an overall good quality in all coordinates \vec{x} .

Event weights $w(\vec{x}_j)$ can be obtained from the partial wave analysis for each energy point as a function of the coordinates \vec{x} in the n -particle phase-space. They are used to determine the global efficiency ε as

$$\varepsilon = \frac{\sum_{j=1}^{N_{\text{acc}}} w(\vec{x}_j)}{\sum_{j=1}^{N_{\text{gen}}} w(\vec{x}_j)}. \quad (5.8)$$

Results are listed in Tables A.2 and A.4. The efficiencies calculated using the PWA are compared to the PHSP values in Figure 5.7. In case of $e^+e^- \rightarrow \phi K^+K^-$, the efficiencies calculated using the PWA are generally higher compared to the one-dimensional estimates. The opposite behavior can be seen for $e^+e^- \rightarrow \phi K_S^0 K_S^0$. In order to understand these results, the difference of the momentum distributions of the kaons recoiling off the ϕ meson between the simple signal MC sample and the re-weighted MC sample using the PWA result are investigated in Figure 5.8 at $\sqrt{s} = 4.1784$ GeV. According to the PWA solution, a shift to higher momenta for $e^+e^- \rightarrow \phi K^+K^-$ and to lower momenta for $e^+e^- \rightarrow \phi K_S^0 K_S^0$ can be observed. Slow K_S^0 mesons result in lower reconstruction efficiencies due to the reduced flight length and correspondingly decreasing resolution of the secondary vertex.

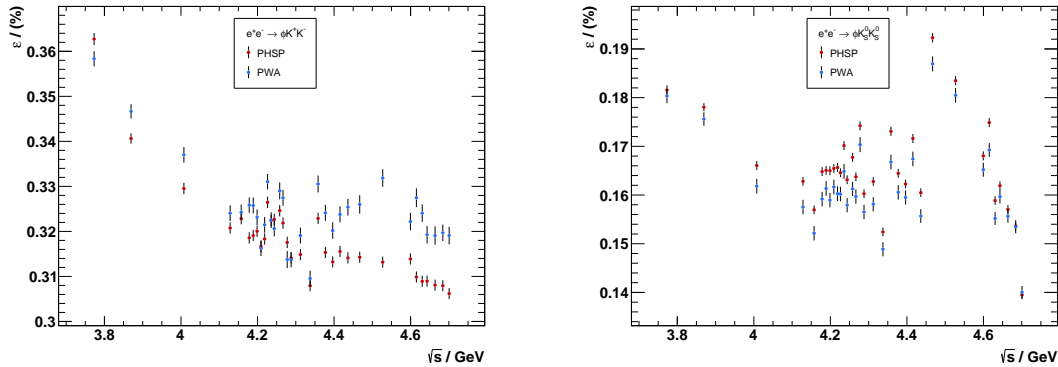


Figure 5.7.: Efficiencies for $e^+e^- \rightarrow \phi K^+K^-$ (left) and $e^+e^- \rightarrow \phi K_S^0 K_S^0$ (right) calculated using the PWA result (blue dots) and the signal MC simulation (red dots) for all data sets used in this work.

It is important to note that these changes are nearly constant over the full energy range and thus can not produce any unphysical structures in the resulting Born cross section. Additionally, small fluctuations in the energy-dependence of the efficiency can be observed for both the PWA and the PHSP case. This can be explained by the fact that the data

sets used in this work were accumulated at different beam times and correspondingly with different detector properties due to aging. Therefore, no exactly flat energy-dependence can be expected a priori.

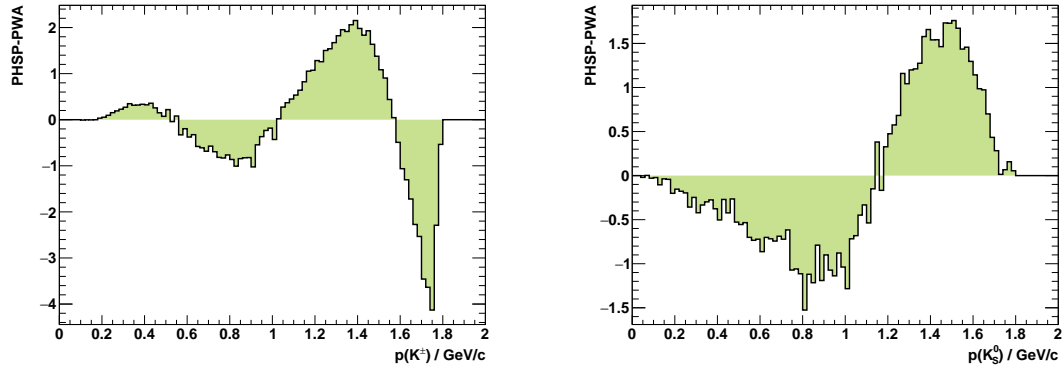


Figure 5.8.: Difference of the momentum distributions of the $K\bar{K}$ system recoiling off the ϕ meson between the signal MC sample and the re-weighted MC sample using the PWA result at $\sqrt{s} = 4.1784$ GeV for $e^+e^- \rightarrow \phi K^+K^-$ (**left**) and $e^+e^- \rightarrow \phi K_S^0 K_S^0$ (**right**).

5. Analysis of $e^+e^- \rightarrow \phi K\bar{K}$

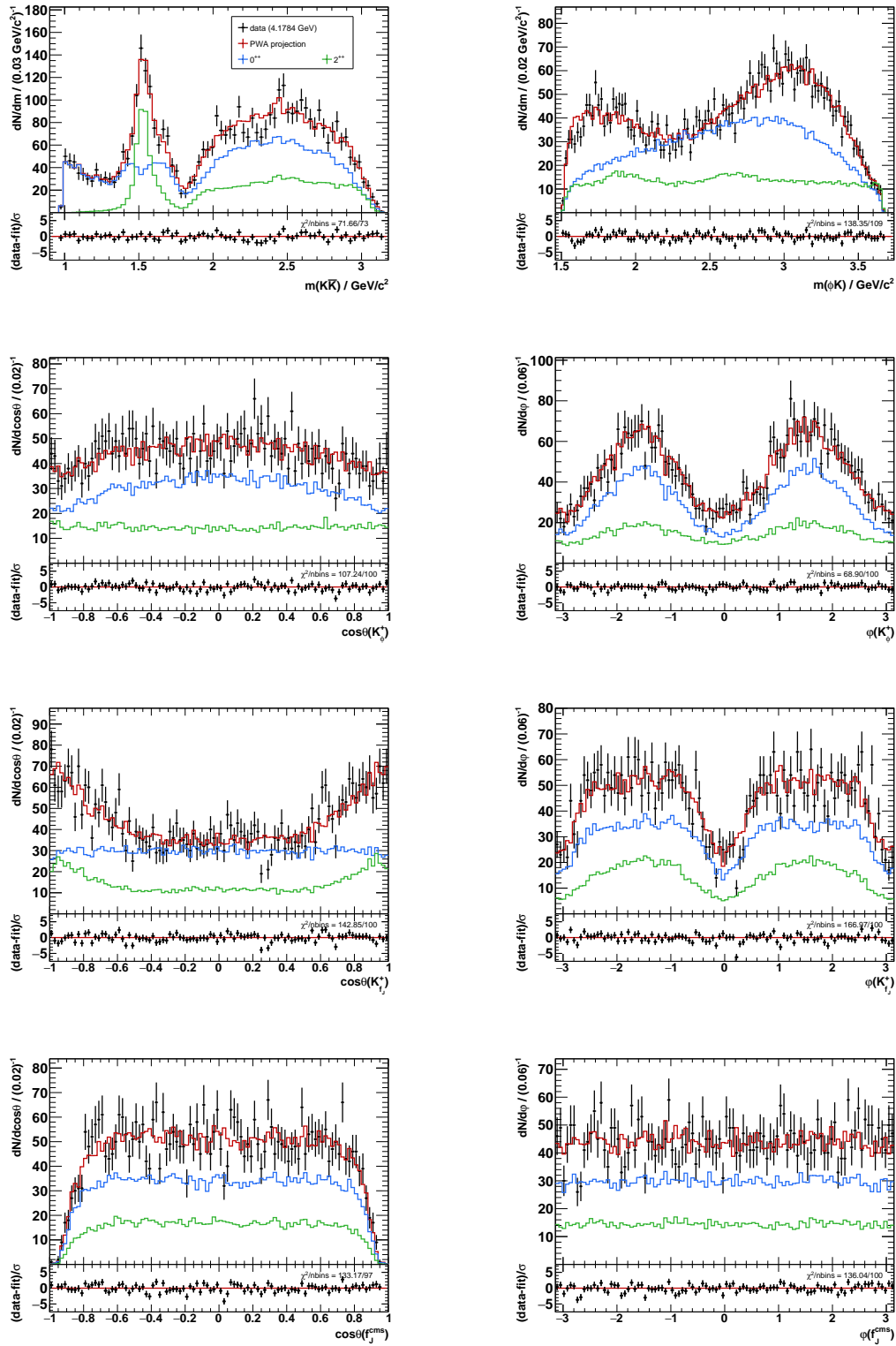


Figure 5.9.: Fit results of the partial wave analysis for $e^+e^- \rightarrow \phi K^+K^-$ at $\sqrt{s} = 4.1784$ GeV. Data (black dots with error bars), the total PWA projection (red solid line), the 0^{++} (blue solid line) as well as the 2^{++} contributions (green solid line) are shown.

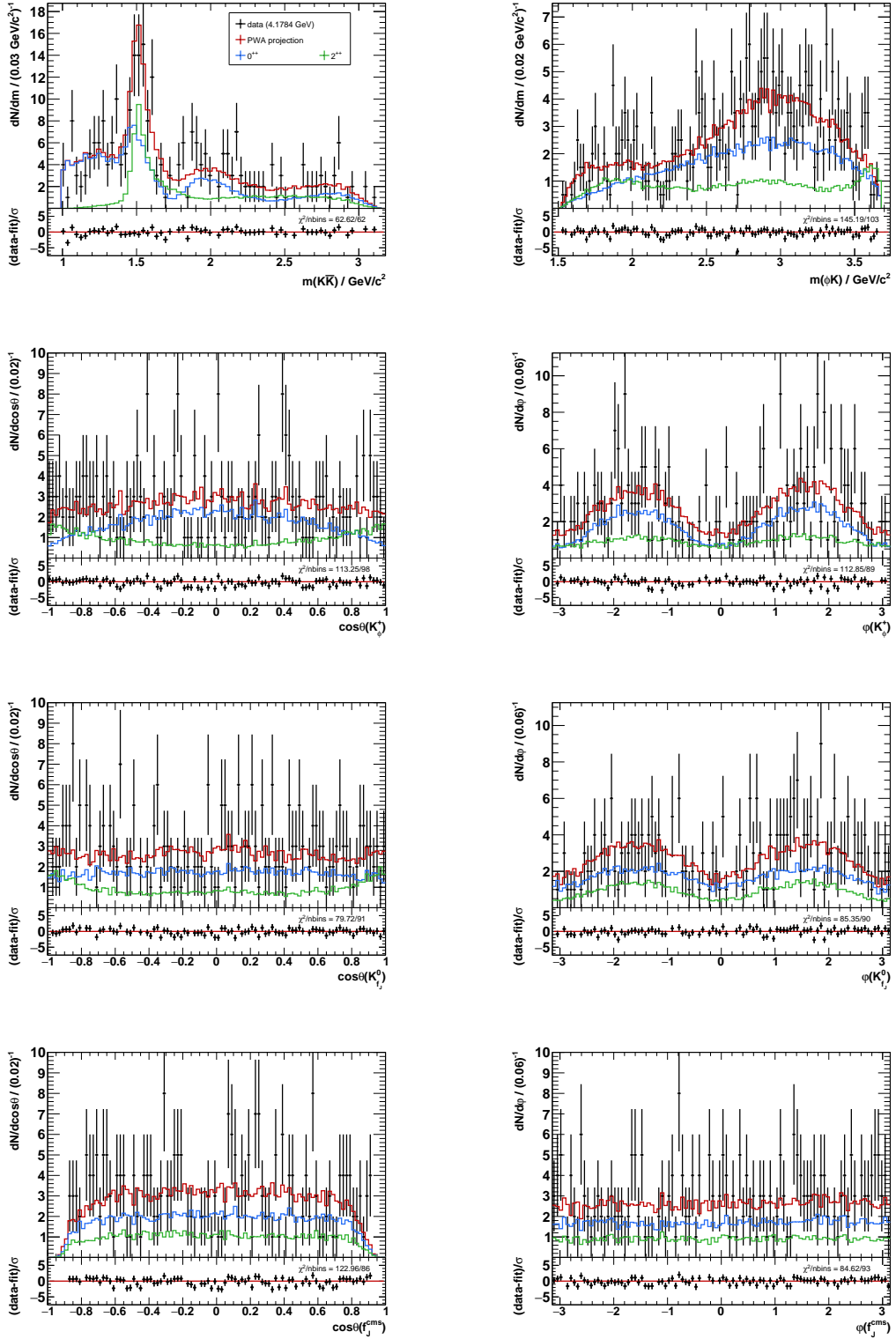


Figure 5.10.: Fit results of the partial wave analysis for $e^+e^- \rightarrow \phi K_S^0 K_S^0$ at $\sqrt{s} = 4.1784$ GeV. Data (black dots with error bars), the total PWA projection (red solid line), the 0^{++} (blue solid line) as well as the 2^{++} contributions (green solid line) are shown.

5.4. Higher Order Correction Factors

In addition to the Born-level production, which describes the lowest order scattering process, the initial state radiation (ISR) and the vacuum polarization (VP) processes contribute to the observed hadronic cross sections of $e^+e^- \rightarrow \phi K\bar{K}$. ISR describes the emission of one or more photons of either the electron or positron (or both) before colliding at the interaction point, resulting in a reduced center-of-mass energy for this event. Thus, the measured cross section for such processes involves the lineshape of the Born cross section from the production threshold up to the nominal collision center-of-mass energy due to ISR. The number of observed signal events has to be corrected for this higher order scattering process to compare the results with those of theoretical calculations. Note that one of the initial state leptons may reabsorb an ISR photon for which a vertex correction is performed internally. Processes studied in this work at leading order as well as three higher order contributions are shown in Figure 5.11.

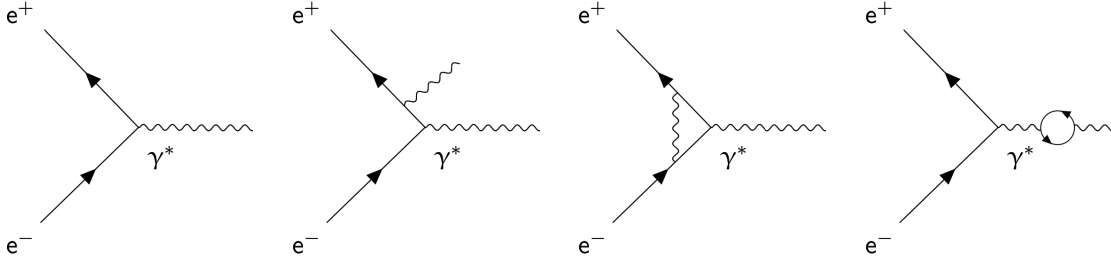


Figure 5.11.: Schematic drawings of the main processes included in the measured cross section for the reaction $e^+e^- \rightarrow \phi K\bar{K}$. From left to right: Born approximation, initial state radiation, vertex smearing and vacuum polarization.

At BESIII, the KKMC generator [219] is used in combination with BesEvtGen [220] to generate Monte Carlo events for e^+e^- annihilation processes. While KKMC is used to generate the intermediate states by considering the ISR and the beam energy spread, BesEvtGen is used to generate the final states of the intermediate state decays including FSR effects. As mentioned above, the ISR correction factors depend on the lineshape of the observed hadronic cross section. Thus, an iterative approach as described in the following is used to obtain these correction factors.

The cross section can be corrected to a cross section without ISR contributions, the so-called *dressed* cross section, given by

$$\sigma_{\text{dressed}} = \frac{\sigma_{\text{obs}}}{(1 + \delta_r)} = \frac{N_{\text{obs}}}{L \cdot (1 + \delta_r) \cdot \varepsilon \cdot \mathcal{B}r}. \quad (5.9)$$

This can be further corrected to the Born cross section $\sigma_b = \frac{\sigma_{\text{dressed}}}{(1 + \delta_v)}$ as shown in Equation (5.1). ISR correction factors and the efficiency are obtained from ISR events

generated with KKMC. In order to generate these events, the lineshape of the energy-dependent Born cross section is used as input. For the first iteration a flat lineshape is used as a starting point. Within the simulation procedure, the dressed cross section is roughly obtained from Equation (5.9), re-evaluating the efficiency and the ISR correction factors. The resulting cross section is used as input for the next iteration until the ISR-dependent quantity $\beta = \varepsilon \cdot (1 + \delta_v)$ converges. Convergence is achieved if the ratio β_i/β_{i-1} of two successive iterations is equal to one within its statistical uncertainties. During the iterative procedure, the efficiency is obtained from the weighted MC sample extracted from the partial wave analysis result.

Vacuum polarization processes describe the spontaneous production of a fermion-antifermion pair from the virtual photon, which then annihilates again into a new virtual photon. It can be described as a small correction to the leading order process given by

$$(1 + \delta_v) = \frac{1}{|1 - \Pi(s)|^2}, \quad (5.10)$$

with $\Pi(s)$ being the vacuum polarization tensor depending on the available center-of-mass energy squared s . Correction factors for VP, including leptonic and hadronic contributions, are calculated with the alphaQED software package [242] with an accuracy of 0.5 %.

5.5. Born Cross Sections

In the previous sections, all parameters that serve to determine the Born cross section according to Equation (5.1) were determined. The results are listed in Tables A.2 and A.4 and graphically shown in Figure 5.12, including statistical as well as systematic uncertainties. The determination of the latter will be discussed in the next section. The processes $e^+e^- \rightarrow \phi K^+K^-$ and $e^+e^- \rightarrow \phi K_S^0 K_S^0$ were successfully observed in all data sets used in this work. These results enable the search for possible couplings of (exotic) vector charmonia ψ to the light hadron final state $\phi K\bar{K}$ in the following. Therefore, a maximum likelihood fit to the Born cross section at each center-of-mass energy from $\sqrt{s} = 3.7730$ GeV to $\sqrt{s} = 4.7008$ GeV is performed.

A likelihood $\mathcal{L}(x|\Theta)$ can be defined for given data x and set of model parameters Θ . In case of a fit to the energy-dependent Born cross section including several uncorrelated, fixed data sets, the overall likelihood can be written as a product given by

$$\mathcal{L}(\Theta) = \prod_i \mathcal{L}_i(\Theta), \quad (5.11)$$

with \mathcal{L}_i being the likelihood function of the model parameters Θ for data set i . In this work, \mathcal{L}_i depends only on one parameter, e.g. the expected number of signal events to be observed $N_i(\Theta)$, given by

$$N_i(\Theta) = \sigma_b(x_i|\Theta) \cdot L_i \cdot (1 + \delta_r)(1 + \delta_v)_i \cdot \varepsilon_i \cdot \mathcal{B}r. \quad (5.12)$$

$\sigma_b(x_i|\Theta)$ is the cross section hypothesis under investigation. The functions $\mathcal{L}_i(N_i)$ have already been determined in Section 5.2 including statistical uncertainties only. In order to account also for the systematic uncertainties, the likelihood function is written as

$$\mathcal{L}_i(N_i) = \frac{1}{\sqrt{2\pi(\sigma_{k,i}^2 + \sigma_{\text{sys},i}^2)}} e^{-\frac{(N_i - \mu_i)^2}{2(\sigma_{k,i}^2 + \sigma_{\text{sys},i}^2)}} \quad \text{with} \quad \sigma_{k,i} = \begin{cases} \sigma_{L,i}, & N_i \leq \mu_i \\ \sigma_{R,i}, & N_i > \mu_i \end{cases}, \quad (5.13)$$

with $\sigma_{\text{sys},i}$ being the total systematic uncertainty for data set i . The cross section hypothesis under investigation is discussed in the following.

Continuum production processes of the type $e^+e^- \rightarrow \gamma^* \rightarrow \phi K\bar{K}$ in this energy regime can be described by [49]

$$\sigma_{\text{con}} = \left(\frac{C}{\sqrt{s}} \right)^\lambda, \quad (5.14)$$

with \sqrt{s} being the center-of-mass energy and the exponent λ being a priori unknown. C and λ are free parameters in the fit. Potential resonant contributions from processes such as $e^+e^- \rightarrow \psi \rightarrow \phi K\bar{K}$ are described by a Breit-Wigner amplitude according to [57]

$$\mathcal{A}_{\text{BW}} = \frac{\sqrt{12\pi\Gamma_{e^+e^-}\mathcal{B}r(\psi \rightarrow \phi K\bar{K})\Gamma}}{s - m^2 + im\Gamma}, \quad (5.15)$$

with m and Γ being the mass and width of the possible resonant contribution ψ , respectively, $\Gamma_{e^+e^-}$ being its electronic width and $\mathcal{B}r(\psi \rightarrow \phi K\bar{K})$ being the branching ratio of $\psi \rightarrow \phi K\bar{K}$. The product $\sigma_\psi \equiv \Gamma_{e^+e^-} \cdot \mathcal{B}r(\psi \rightarrow \phi K\bar{K})$ is a free parameter in the fit. In case of no interference with the continuum production of $\phi K\bar{K}$, the resonant contribution is added incoherently as

$$\sigma_{\text{incoh}} = \sigma_{\text{con}} + \left| \frac{\sqrt{12\pi\sigma_\psi\Gamma}}{s - m^2 + im\Gamma} \right|^2. \quad (5.16)$$

Furthermore, the resonant contribution is added coherently if an interference is allowed, which may be constructive or destructive. In this case, the full amplitude reads

$$\sigma_{\text{coh}} = \left| \sqrt{\sigma_{\text{con}}} + \frac{\sqrt{12\pi\sigma_\psi\Gamma}}{s - m^2 + im\Gamma} e^{i\phi} \right|^2, \quad (5.17)$$

with ϕ being the relative phase between the amplitudes of continuum and resonant production. To test the contribution of ψ states, the mass and width in Equation (5.15) can be fixed to the corresponding world average values from the PDG [56]. As already mentioned in Chapter 1, the $\psi(4230)$ is of particular interest because it has not been observed in decays to light hadrons so far. Its mass and width is $m_\psi = 4.2187 \text{ GeV}/c^2$ and $\Gamma_\psi = 0.044 \text{ GeV}$, respectively.

Unbinned maximum likelihood fits are performed for continuum processes and an additional incoherent or coherent resonant contribution using the `Minuit` optimizer of `ROOT` [243], as shown in Figure 5.12. The significance of a resonant contribution is calculated based on the likelihood ratio for the hypotheses of continuum production and an additional resonant contribution using the function `RooStats::PValueToSignificance()` from the `RooStats` package [244]. The p -values are assumed to follow a χ^2 distribution and, thus, are obtained via `TMath::Prob(|2 log $\mathcal{L}_{\text{res}} - 2 \log \mathcal{L}_{\text{con}}|, \text{NDF}_{\text{res}} - \text{NDF}_{\text{con}})$` , with $\text{NDF}_{\text{res}} - \text{NDF}_{\text{con}} = 1$ (2) being the difference of the number of degrees of freedom in both fits in the incoherent (coherent) case. According to the fit results, the significance of a resonant contribution of the $\psi(4230)$ to the production of the $\phi K \bar{K}$ final state for the coherent and incoherent case is 0.57σ and 0.03σ (1.02σ and 1.37σ) for $\phi K^+ K^-$ (for $\phi K_S^0 K_S^0$), respectively. Hence, upper limits for these processes will be determined in the next section. These results indicate that the $\psi(4230)$ strongly prefers to preserve its charm content in decays, as in charmonium transitions to $\psi(2S)$ or J/ψ under the emission of a $\pi\pi$ pair.

The results of the Born cross sections are compared for the $\phi K^+ K^-$ and $\phi K_S^0 K_S^0$ final states in Figure 5.13. A linear fit is performed, yielding a proportionality factor of 3.85 ± 0.01 , which differs significantly from the value of two if assuming isospin symmetry. However, since the continuum production of the final states investigated goes through a virtual photon γ^* , isospin is a priori not conserved. Thus, the determined proportionality factor is not unexpected. A more detailed discussion is given in Section 5.7.

5. Analysis of $e^+e^- \rightarrow \phi K\bar{K}$

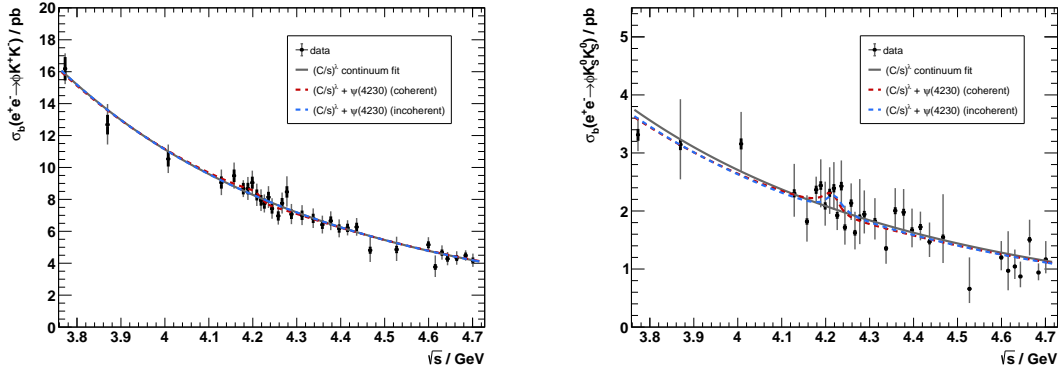


Figure 5.12.: Born cross section (black dots with thick and thin error bars, denoting statistical and systematic uncertainties, respectively) for $e^+e^- \rightarrow \phi K^+K^-$ (**left**) and $e^+e^- \rightarrow \phi K_S^0 K_S^0$ (**right**) at center-of-mass energies from $\sqrt{s} = 3.7730$ GeV to $\sqrt{s} = 4.7008$ GeV. Maximum likelihood fits are performed according to Equations (5.14), (5.16) and (5.17), assuming pure continuum production (solid gray line) and an additional coherent (dashed red line) or incoherent (dashed blue line) resonant contribution of the $\psi(4230)$.

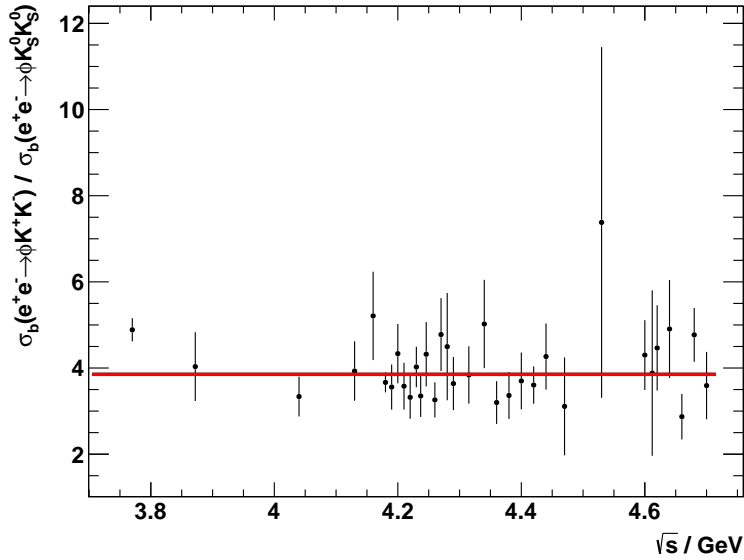


Figure 5.13.: Ratio of the Born cross section of $e^+e^- \rightarrow \phi K^+K^-$ and $e^+e^- \rightarrow \phi K_S^0 K_S^0$ at center-of-mass energies from $\sqrt{s} = 3.7730$ GeV to $\sqrt{s} = 4.7008$ GeV (black dots with error bars). A linear fit (red line) is performed, yielding a proportionality factor of 3.85 ± 0.01 .

5.5.1. Upper Limit on $e^+e^- \rightarrow \psi \rightarrow \phi K \bar{K}$

Since no obvious resonant structure in the Born cross sections $\sigma_b(e^+e^- \rightarrow \phi K \bar{K})$ was observed, upper limits on $e^+e^- \rightarrow \psi \rightarrow \phi K^+ K^-$ and $e^+e^- \rightarrow \psi \rightarrow \phi K_S^0 K_S^0$ will be set using a Bayesian approach [42, 245, 246]. The observable for which an upper limit σ_ψ^{UL} is calculated is $\sigma_\psi = \Gamma_{e^+e^-} \cdot \mathcal{B}r(\psi \rightarrow \phi K \bar{K})$, given by

$$C.L. = \frac{\int_{-\infty}^{\sigma_\psi^{\text{UL}}} \mathcal{L}(\Theta) \pi(\Theta) d\sigma_\psi}{\int_{-\infty}^{+\infty} \mathcal{L}(\Theta) \pi(\Theta) d\sigma_\psi}, \quad (5.18)$$

for a confidence level $C.L.$ typically chosen to be equal to 90%. The prior $\pi(\Theta)$ for the model parameters Θ

$$\pi(\Theta) = \begin{cases} 1, & \sigma_\psi \geq 0 \\ 0, & \sigma_\psi < 0 \end{cases} \quad (5.19)$$

excludes unphysical negative cross section values. Here, $\mathcal{L}(\Theta)$ is the product of likelihood functions $\mathcal{L}_i(\Theta)$ (see Equation (5.11)), which have already been determined in Equation (5.13). Figure 5.14 shows the resulting likelihood scans in case of the hypothesis of a resonant $\psi(4230)$ contribution. In the coherent case, the fit shows two solutions with exactly the same fit quality, which is a direct result of the interference effect between both the continuum production process and the resonant amplitude, incorporating constructive and destructive interference, corresponding to smaller and larger values of σ_ψ , respectively [247]. The upper limits for the $\psi(4230)$ hypothesis calculated using Equation (5.18) are $\sigma_{\psi, \text{coh}}^{\text{UL}} = 1.75 \text{ eV}$ and $\sigma_{\psi, \text{incoh}}^{\text{UL}} = 0.019 \text{ eV}$ for $e^+e^- \rightarrow \psi(4230) \rightarrow \phi K^+ K^-$ and $\sigma_{\psi, \text{coh}}^{\text{UL}} = 0.47 \text{ eV}$ and $\sigma_{\psi, \text{incoh}}^{\text{UL}} = 0.025 \text{ eV}$ for $e^+e^- \rightarrow \psi(4230) \rightarrow \phi K_S^0 K_S^0$.

Motivated by the still lacking knowledge of the masses and widths of ψ states around $m = 4.23 \text{ GeV}/c^2$, upper limit scans were performed for possible resonant contributions with masses $m \in [4.15 \text{ GeV}/c^2, 4.45 \text{ GeV}/c^2]$ and widths $\Gamma \in [0.04 \text{ GeV}, 0.24 \text{ GeV}]$. This ensures that possible contributions from the $\psi(4160)$ and $\psi(4415)$ as lowest and highest mass representatives for vector charmonia in the energy range studied are taken into account. Results for the coherent case are shown in Figure 5.15. While the upper limit does not seem to depend on the mass for a fixed width bin, it increases with larger widths for a fixed mass bin. Furthermore, no obvious region can be observed in which the upper limits may show any discrepancy from these behaviors. Consequently, no specific pair of mass and width can be identified, which could be assigned to a possible resonant contribution. The observation that these vector charmonia also do not couple to the investigated final state thus provides information about their inner structure since they seem to preserve its charm content in decays, as in charmonium transitions to $\psi(2S)$ or J/ψ under the emission of a $\pi\pi$ pair.

5. Analysis of $e^+e^- \rightarrow \phi K\bar{K}$

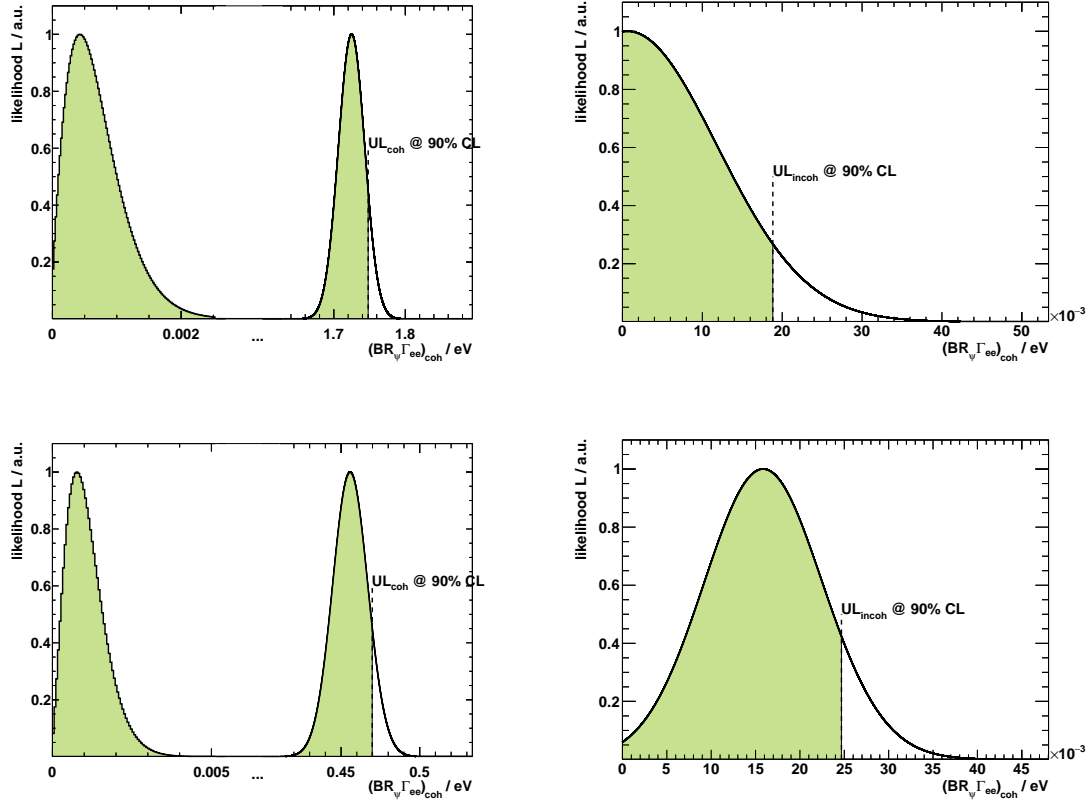


Figure 5.14.: Likelihood distribution for a coherent (**left**) and incoherent (**right**) resonant contribution of the $\psi(4230)$ to the Born cross section of $e^+e^- \rightarrow \phi K^+K^-$ (**top**) and $e^+e^- \rightarrow \phi K_S^0 K_S^0$ (**bottom**). Upper limits indicated by the dashed lines are calculated at 90% *C.L.* according to Equation (5.18).

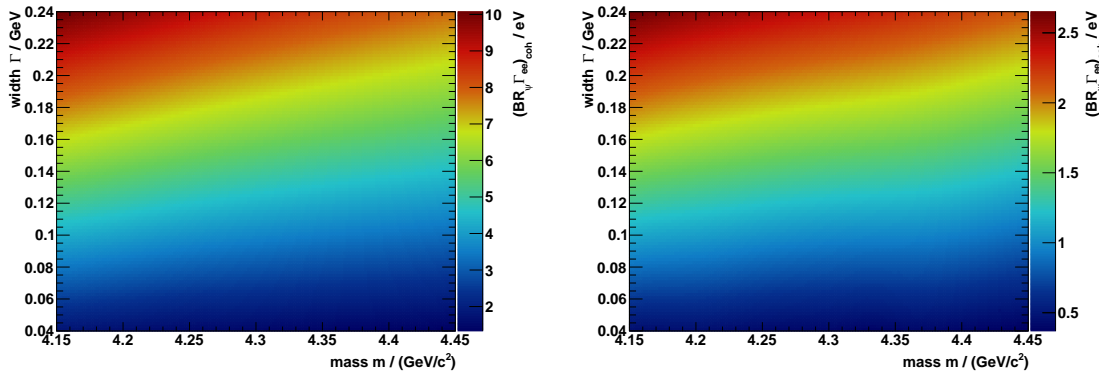


Figure 5.15.: Upper limits for a possible coherent resonant contribution ψ with mass m and width Γ to the Born cross section of $e^+e^- \rightarrow \phi K^+K^-$ (**left**) and $e^+e^- \rightarrow \phi K_S^0 K_S^0$ (**right**).

5.6. Systematic Uncertainties

In order to reach maximum sensitivity in the search for rare processes, the careful evaluation of sources of uncertainties is very important. Especially the results of the Born cross sections as well as for the upper limit determination strongly depend on a proper uncertainty estimation. While the statistical uncertainties arise from finite data and signal MC samples, systematic effects and their uncertainties appear, e.g. due to fixed selection criteria in the analysis. Furthermore, combining the information from many data sets gathered throughout ten years of measurement time over a wide energy range is very complicated and requires careful investigation of many possible sources of systematic uncertainties. Examples are differences between data and signal MC, aging of detector components, and different measurement conditions, although every data set is accumulated with a very high accuracy and precision. Therefore, it is of special importance to perform the study of systematic uncertainties properly and diligently.

Beyond systematic effects due to fixed selection criteria specifically depending on the analysis, more general systematic uncertainties which have been determined by the BESIII collaboration in previous studies are summarized in Table 5.2. For each data set, an uncertainty of 1% [214] is assigned to the integrated luminosities which were measured based on the Bhabha scattering process $e^+e^- \rightarrow (\gamma)e^+e^-$. Using a $J/\psi \rightarrow p\bar{p}\pi^+\pi^-$ control sample [248], the systematic uncertainty of the tracking efficiency is determined to be 1% per charged track in the final state. Branching fractions are taken from the PDG [56]. In case of $K_S^0 \rightarrow \pi^+\pi^-$ decays the systematic uncertainty related to the reconstruction efficiency is treated separately in Subsection 5.6.5.

Table 5.2.: Systematic uncertainties for the luminosity [214], the tracking efficiency [248] as well as the branching ratio [56] in % for the reactions $e^+e^- \rightarrow \phi K^+K^-$ and $e^+e^- \rightarrow \phi K_S^0 K_S^0$.

	$e^+e^- \rightarrow \phi K^+K^-$	$e^+e^- \rightarrow \phi K_S^0 K_S^0$
Luminosity	1.0	1.0
Tracking efficiency	4.0	2.0
Branching ratio	1.0	1.0
Total	4.2	2.4

Additional systematic effects are studied by varying fixed parameters like selection conditions within the analysis around its nominal values and investigate a possible deviation in the results. Since all other parameters in the Born cross section formula are constant, only the number of observed signal events N_i and the efficiency ε_i for a variation i are investigated compared to its nominal values N_{ref} and ε_{ref} by calculating the ratio

$$R_i = \frac{\sigma_i^{\text{B}}}{\sigma_{\text{ref}}^{\text{B}}} = \frac{N_i \cdot \varepsilon_{\text{ref}}}{\varepsilon_i \cdot N_{\text{ref}}} \quad (5.20)$$

and its uncertainty

$$\Delta R_i = \sqrt{\sum_{j=1}^m \left(\frac{\partial R_i}{\partial x_j} \Delta x_j \right)^2 + 2 \sum_{j=1}^{m-1} \sum_{k=j+1}^m \frac{\partial R_i}{\partial x_j} \frac{\partial R_i}{\partial x_k} \cdot \text{cov}(x_j, x_k)}. \quad (5.21)$$

$m = 4$ is the number of parameters R_i depends on, $\frac{\partial R_i}{\partial x_j}$ is the partial derivative of R_i with respect to parameter x_j with uncertainty Δx_j and $\text{cov}(x_j, x_k)$ is the covariance between parameters x_j and x_k , given by $\text{cov}(x_j, x_k) = \Delta x_j \cdot \Delta x_k \cdot \text{cor}_{jk}$ with the correlation factor cor_{jk} due to a certain number of events being shared in both samples. The correlation factors are given by $\sqrt{\min\left(\frac{N_i}{N_{\text{ref}}}, \frac{N_{\text{ref}}}{N_i}\right)}$ and $\sqrt{\min\left(\frac{\varepsilon_i}{\varepsilon_{\text{ref}}}, \frac{\varepsilon_{\text{ref}}}{\varepsilon_i}\right)}$. A systematic uncertainty is then obtained as the standard deviation σ_R of a weighted average of the ratios R_i according to

$$\sigma_R^2 = \frac{\sum_i \omega_i (1 - R_i)^2}{\sum_i \omega_i} \quad \text{with} \quad \omega_i = (\Delta R_i)^{-1}. \quad (5.22)$$

The sources of systematic effects for both processes $e^+e^- \rightarrow \phi K^+K^-$ and $e^+e^- \rightarrow \phi K_S^0 K_S^0$ are discussed in the following. The results are summarized in Table A.1.

5.6.1. Signal Region

A signal region is defined in which the signal part of the fit function is integrated to extract the number of observed events N_{obs} from data. This region was chosen to contain 95% of the respective signal. Since this value was initially chosen arbitrarily, the impact on the final result is investigated. No systematic behavior is observed in either final states.

5.6.2. Background Description

To study a potential systematic effect caused by the choice of a specific background function in case of ϕK^+K^- , higher order polynomials (2nd and 3rd order) instead of a 1st order polynomial are used to describe the background contribution. Results are shown in Figure 5.16 and listed in Table A.1. No systematic trend, but a distribution around the reference value is observed. The systematic uncertainty regarding the choice of a background function is determined to be 0.39% at $\sqrt{s} = 4.1784$ GeV.

5.6.3. Kinematic Fit

The nominal selection conditions of $\chi_{4C, \phi K^+K^-}^2 < 93$ and $\chi_{6C, \phi K_S^0 K_S^0}^2 < 227$ are varied in the ranges from $\chi_{4C}^2 < 43$ to $\chi_{4C}^2 < 143$ and from $\chi_{6C}^2 < 170$ to $\chi_{6C}^2 < 270$. Results are shown in Figures 5.16 and 5.17 and listed in Tables A.1 and A.3. No systematic trend,

but a distribution around the reference value is observed. The systematic uncertainty regarding the selection condition on the kinematic fit is determined to be 0.14% and 0.16% for the final states $\phi K^+ K^-$ and $\phi K_S^0 K_S^0$ at $\sqrt{s} = 4.1784$ GeV, respectively.

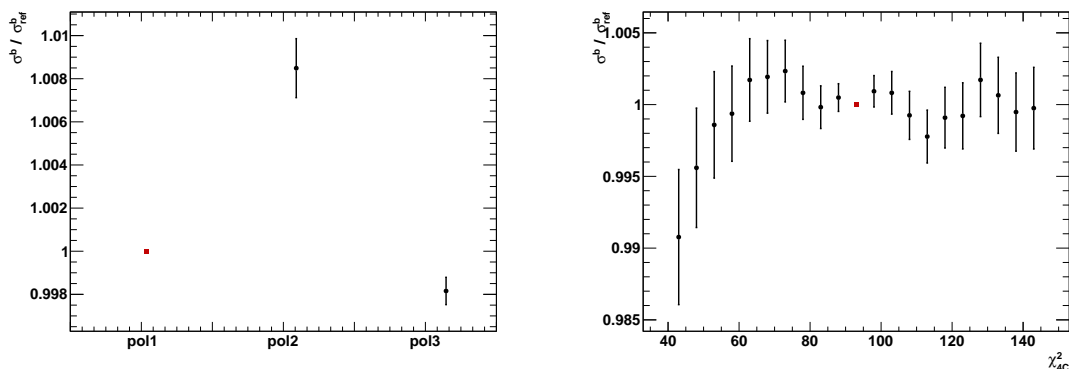


Figure 5.16.: Systematic studies of the functional form to describe the background part (**left**) and the selection condition on the χ^2_{4C} value of the kinematic fit (**right**) for $e^+e^- \rightarrow \phi K^+ K^-$ at $\sqrt{s} = 4.1784$ GeV. The nominal value, which is the reference value, is depicted as the red marker. The error bars are calculated using equation 5.21.

5.6.4. Partial Wave Model

To estimate a systematic uncertainty arising from the choice of the PWA model an additional $J^{PC} = 0^{++}$ as well as $J^{PC} = 2^{++}$ resonance is added. The deviation in the efficiency and hence Born cross section is used as the systematic uncertainty. It amounts to 1.00% for both the $\phi K^+ K^-$ and $\phi K_S^0 K_S^0$ final state for each center-of-mass energy.

5.6.5. K_S^0 Reconstruction

The systematic studies regarding the K_S^0 reconstruction are based on the linear piece wise function of [237], taking the momentum-dependence for the systematic uncertainty of the K_S^0 meson reconstruction into account. The momentum distribution obtained from the PWA is used as input for this linear piece wise function to determine a weight for each event. All event weights are summed up to obtain a value for the systematic uncertainty regarding the K_S^0 reconstruction, which is determined to be 1.98% at $\sqrt{s} = 4.1784$ GeV.

5.7. Partial Wave Analysis at $\sqrt{s} = m_{\psi(2S)}$

The data set at the $\psi(2S)$ resonance used in this work contains about $(448.1 \pm 2.9) \cdot 10^6$ events [249] and is therefore well suited to test the formalism introduced in Section 2.6 within a partial wave analysis. While the first application in [156] used data from

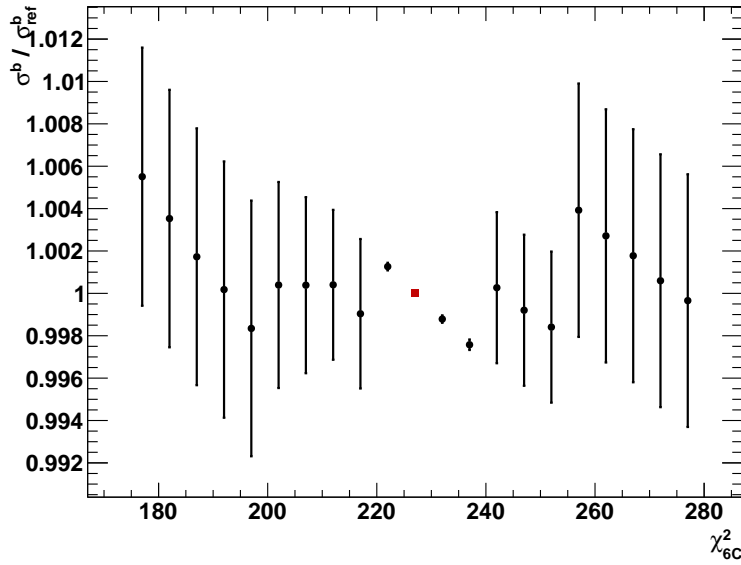


Figure 5.17.: Systematic studies of the selection condition on the χ_{6C}^2 value of the kinematic fit for $e^+e^- \rightarrow \phi K_S^0 K_S^0$ at $\sqrt{s} = 4.1784$ GeV. The nominal value, which is the reference value, is depicted as the red marker. The error bars are calculated using equation 5.21.

LHCb [52, 196] in terms of angular moments $Y_L^0(\sqrt{s})$, the BESIII data is directly available for all relevant coordinates $\vec{x} = \{p_\phi, \theta_\phi, \phi_\phi, p_{K\bar{K}}, \theta_{K\bar{K}}, \phi_{K\bar{K}}, \dots\}$. Hence, Equation (2.112) can be used as a parametrization for the S -wave scattering amplitude observed in data. In the following, the model used to perform the PWA is discussed briefly.

S -wave contributions ($J^{PC} = 0^{++}$) in the $K\bar{K}$ system recoiling off the ϕ meson are parametrized using the formalism discussed in Section 2.6. This already captures the physics of the $f_0(500)$ and $f_0(980)$ due to the dispersive approach and the incorporated Omnès matrix. Furthermore, two additional resonances representative for the $f_0(1500)$ and $f_0(2020)$ are included in order to extend the description onto the energy regime of $\sqrt{s} > 1.0$ GeV. All universal parameters, namely the bare resonance masses as well as the bare resonance-channel couplings are fixed in the fit to the values obtained in [156], incorporating the $\pi\pi$, $K\bar{K}$ and an effective 4π channel. The latter is modeled by $\rho\rho$ in this work. Note that some scalar isoscalar resonances above $\sqrt{s} = 1.0$ GeV have already been suggested to be dynamically generated by attractive ρ meson interactions [250–253]. The normalization of the form factors from Equation (2.124) can be fixed in the fit according to [123] to $c_1 = 0, c_2 = 1$ and $c_3 = 0$ for the $\pi\pi, K\bar{K}$ and 4π channel, respectively. Resonance-source couplings as well as a linear background term in the $K\bar{K}$ channel from Equation (2.124) are free parameters in the fit. The extraction of resonance poles on the nearest unphysical sheets using the framework of Padé approximants [254–256] is discussed in [156].

D -wave contributions ($J^{PC} = 2^{++}$) are parametrized using the K -matrix approach

of [177], including the four poles $f_2(1270)$, $f_2'(1525)$, $f_2(1810)$ and $f_2(1950)$ with the four channels $\pi\pi$, $K\bar{K}$, $\eta\eta$ and an effective 4π channel. Furthermore, constant background terms in the K -matrix (see Equation (2.99)) and in the P -vector (see Equation (2.101)), as well as linear terms in the latter are included. All parameters despite the P -vector background terms in the $K\bar{K}$ channel are fixed to the parametrization of [177]. Again, the extraction of resonance poles is discussed in [177].

Not only the $K\bar{K}$ system recoiling off the ϕ meson shows structures in the invariant mass spectra, but also the ϕK system. The fit quality can significantly be improved if excited kaons modeled by simple Breit-Wigner functions are included into the model, namely the $K_2(1820)$, recently observed by LHCb [257], as well as the $K_2(2250)$, representative for various peaks in strange meson systems reported in the 2150-2260 MeV region as well as for enhancements seen in the antihyperon-nucleon system [56]. Note that no excited kaons were found in the analysis of the XYZ data, as the statistics there were significantly lower.

The final results are shown in Figures 5.21 and 5.22 for invariant masses limited up to $m(K^+K^-) = 2.0$ GeV due to the parametrizations used. The data is well described by the respective partial wave projections in each of the kinematic variables. However, this approach has to be understood as a first step for an even more sophisticated analysis in the future. The goal in this work was to implement the form factor formalism [156] into the PAWIAN tool [240] as part of the GRK2149 theory project, which successfully have been achieved. The current assumptions concentrate on strong decays of the $\psi(2S)$ only, which conserve isospin. Actually, also decays via virtual photons γ^* are possible, which are not sensitive to isospin-conservation. Hence, also processes of the type $\psi(2S) \rightarrow \phi a_J$ with $a_J \rightarrow K\bar{K}$ may occur. In the $\phi K\bar{K}$ final state only, isospin can not be distinguished and, thus, analyzing this single channel is not able to disentangle the several isospin contributions. Including a_J waves with the data available in this work would therefore probably lead to unphysical results. As a next step in the future, the channels $\phi\pi^0\pi^0$ and $\phi\pi^0\eta$ should be investigated. Since in $\pi^0\pi^0$ only f_J and in $\pi^0\eta$ only a_J contributions are allowed due to conservation rules, a proper separation of isospin contributions could be achieved.

Additional improvements of the fit quality may be achieved by considering purely kinematic effects in the PWA model which can produce resonant structures in data. The S -matrix has kinematic singularities due to the on-shellness of intermediate particles for a process, such as two-body thresholds and triangle singularities (TS). For example, the position of the $K_2(1820)$ is close to the $K^*(892)\phi$ threshold which may have to be taken into account by using a Flattè formula to describe its lineshape. An introduction into the principles of TS and its applications for XYZ states can be found in [258] and [259], respectively. They basically describe the rescattering processes of intermediate particles (see Figure 5.18). The final state $\phi K\bar{K}$ may be produced via an intermediate K^* , which

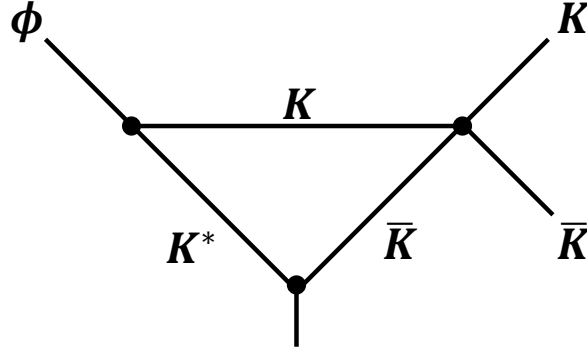


Figure 5.18.: A triangle diagram for the reaction $\psi(2S) \rightarrow \phi K\bar{K}$ via an intermediate K^* , denoting some excited kaon that decays to ϕK . For a triangle singularity to be operative one needs the K^* to be allowed to decay into ϕK on-shell.

generically stands for some excited kaon that decays to ϕK . For a triangle singularity to be operative one needs the K^* to be allowed to decay into ϕK on-shell. In fact, a resonant K^* contribution to the invariant mass of ϕK at $m_{\phi K} = 2.36$ GeV and re-scattering of the two K mesons in the scalar channel introduces a TS which leads to a cusp-like effect close to the $K\bar{K}$ threshold, which may interfere with the $f_0(980)$. Note that the broader the K^* , the smaller the strength of the TS because the on-shell requirement gets more and more meaningless. However, since the width is attached to the resonance which decays to ϕK , it will not smear out the cusp structure at the $K\bar{K}$ threshold, which is due to the opening of the $K\bar{K}$ channel. How large the effects of TS and therefore the proper description of the ϕK system to the full amplitude are has to be investigated in future analyses.

Comparing the two different final states ϕK^+K^- and $\phi K_S^0 K_S^0$, a significant difference can be observed especially in the invariant mass distributions of the kaons recoiling off the ϕ meson (not only at this energy point, but also at higher energies, see e.g. Figures 5.9 and 5.10). This behavior has also been observed in previous analyses, e.g. in amplitude analyses of $D_s^+ \rightarrow K^+K^-\pi^+$ [260, 261] and $D_s^+ \rightarrow K_S^0 K_S^0 \pi^+$ (BESIII preliminary). In case of $D_s^+ \rightarrow K^+K^-\pi^+$, the branching fraction of $D_s^+ \rightarrow S(980)\pi^+$ ($S(980)$ denotes the combined state of $a_0(980)$ and $f_0(980)$) was determined to be one order of magnitude larger as the branching fraction of $D_s^+ \rightarrow f_0(1710)\pi^+$. In case of $D_s^+ \rightarrow K_S^0 K_S^0 \pi^+$, almost no signal contribution is observed below 1.1 GeV/ c^2 in the $K_S^0 K_S^0$ mass spectrum. The authors of (BESIII preliminary) try to explain this suppression phenomenon with a destructive interference between the $a_0(980)$ and the $f_0(980)$. Surprisingly, an anomalous enhancement was observed around 1.7 GeV/ c^2 . The corresponding branching fraction of $D_s^+ \rightarrow f_0(1710)\pi^+$ with $f_0(1710) \rightarrow K_S^0 K_S^0$ results one order of magnitude larger than the expectation from [261] assuming only isospin symmetry. This may provide the evidence for a new resonance as a possible isospin one partner of the $f_0(1710)$, namely the $a_0(1710)$,

as proposed in [262] and recently observed in [263]. Since the f_0 and $(K^+K^- + K^0\bar{K}^0)$ have isospin zero while a_0 and $(K^+K^- - K^0\bar{K}^0)$ have isospin one, an opposite phase of both the f_0 and the a_0 would cause constructive and destructive interferences in the $K_S^0K_S^0$ and K^+K^- mass spectra, respectively. This is in agreement with the amplitude analysis of D_s^+ decays. Destructive and constructive interferences of f_0 and a_0 mesons may also be present in the analysis of the ϕK^+K^- and $\phi K_S^0K_S^0$ final states and need to be investigated in the future.

In principle, the form factor formalism may also be used as a parametrization of the D -wave contributions if proper phase-shifts would be available to describe the low-energy regime. However, the K -matrix approach and the form factor formalism are technically similar in the energy regime of $\sqrt{s} > 1.0$ GeV and so should be their results. The amount of data and therefore the statistics available at this center-of-mass energy is currently being increased fivefold which enables studies with even higher precision in the future.

5.7.1. Determination of $\mathcal{B}r(\psi(2S) \rightarrow \phi K\bar{K})$

The branching fractions $\mathcal{B}r(\psi(2S) \rightarrow \phi K\bar{K})$ are given by

$$\mathcal{B}r(\psi(2S) \rightarrow \phi K\bar{K}) = \frac{N_{\text{obs}}}{N_{\psi(2S)} \cdot \varepsilon \cdot \mathcal{B}r_{\text{rec}}}, \quad (5.23)$$

with N_{obs} being the number of observed signal events in data, $N_{\psi(2S)} = (448.1 \pm 2.9) \cdot 10^6$ being the number of $\psi(2S)$ mesons produced in e^+e^- annihilations at BESIII [249], ε being the detection efficiency and $\mathcal{B}r_{\text{rec}}$ being the product branching ratio of $\phi \rightarrow K^+K^-$ and, if present, subsequent $K_S^0 \rightarrow \pi^+\pi^-$ decays. Figure 5.19 shows the invariant mass distributions of ϕ meson candidates in data for $e^+e^- \rightarrow \phi K^+K^-$ and $e^+e^- \rightarrow \phi K_S^0K_S^0$. A maximum likelihood fit is performed in order to extract N_{obs} as described in Section 5.2. The detection efficiency ε is calculated using both the partial wave analysis results and the simple signal MC simulations from Section 5.7. Hence, two branching fractions $\mathcal{B}r_{\text{PWA}}$ and $\mathcal{B}r_{\text{PHSP}}$ are determined. Even though the result using the simple signal MC simulation is included here for the sake of completeness, only the reliable result from the PWA is discussed below. Results are listed in Table 5.3. The ratio $R_{\text{PWA}}(\phi K^+K^- / \phi K_S^0K_S^0)$ of the branching fractions $\mathcal{B}r(\psi(2S) \rightarrow \phi K^+K^-)$ and $\mathcal{B}r(\psi(2S) \rightarrow \phi K_S^0K_S^0)$ yields 2.78 ± 0.12 , which can be explained as in Sections 5.5 and 5.7. A more detailed discussion of the results can be found in Chapter 7.

In case of $\psi(2S) \rightarrow \phi K^+K^-$ a comparison with previous results listed in the PDG [56] is shown in Figure 5.20. The value of the branching fraction determined in this work matches the one from CLEO [264], but disagrees with the previous BES result [265]. The new, preliminary world average value determined in this work amounts to $(7.86 \pm 1.07) \cdot 10^{-5}$. No value for $\mathcal{B}r(\psi(2S) \rightarrow \phi K_S^0K_S^0)$ is stated in the PDG yet.

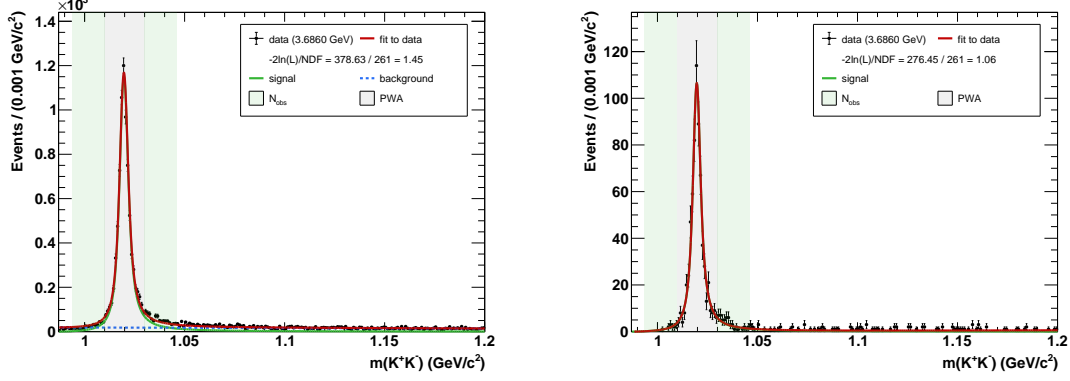


Figure 5.19.: Invariant mass spectrum of ϕ candidates for data (black dots with error bars) at $\sqrt{s} = m_{\psi(2S)}$. A fit (red line) with a Breit-Wigner function convolved with a Gaussian function as signal (green line) and a first-order polynomial as background (dashed blue line) is applied. The green and gray shaded areas depict the signal regions in which the number of observed events N_{obs} is extracted and for which a partial wave analysis (PWA) is performed to determine a global efficiency, respectively. **Left:** $e^+e^- \rightarrow \phi K^+K^-$. **Right:** $e^+e^- \rightarrow \phi K_S^0 K_S^0$.

Table 5.3.: Results for the branching fractions $\mathcal{B}r(\psi(2S) \rightarrow \phi K\bar{K})$ calculated using the PWA results and the simple signal MC simulation as well as their ratios R .

	$\psi(2S) \rightarrow \phi K^+K^-$	$\psi(2S) \rightarrow \phi K_S^0 K_S^0$
N_{obs}	$8408.52^{+99.84}_{-98.14}$	$721.59^{+28.00}_{-26.51}$
$\mathcal{B}r_{\text{rec}} / \%$	49.20	$49.20 \cdot 69.20^2$
$\varepsilon_{\text{PWA}} / \%$	39.93 ± 0.27	19.81 ± 0.19
$\varepsilon_{\text{PHSP}} / \%$	40.16 ± 0.16	20.98 ± 0.11
$\mathcal{B}r_{\text{PWA}} / \%$	$9.58^{+0.14}_{-0.14} \pm 0.45$	$3.45^{+0.14}_{-0.13} \pm 0.11$
$R_{\text{PWA}}(\phi K^+K^- / \phi K_S^0 K_S^0)$	2.78 ± 0.12	
$\mathcal{B}r_{\text{PHSP}} / \%$	$9.50^{+0.13}_{-0.13} \pm 0.44$	$3.26^{+0.13}_{-0.12} \pm 0.11$
$R_{\text{PHSP}}(\phi K^+K^- / \phi K_S^0 K_S^0)$	2.92 ± 0.12	

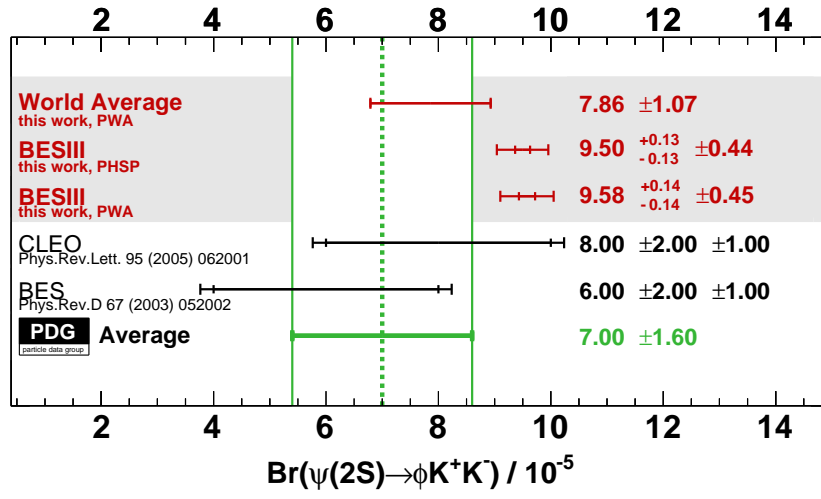


Figure 5.20.: Branching fraction of $\psi(2S) \rightarrow \phi K^+ K^-$ determined in this work (red) compared with previous results from the PDG [264, 265] (black) and the PDG world average value [56] (green).

5. Analysis of $e^+e^- \rightarrow \phi K\bar{K}$

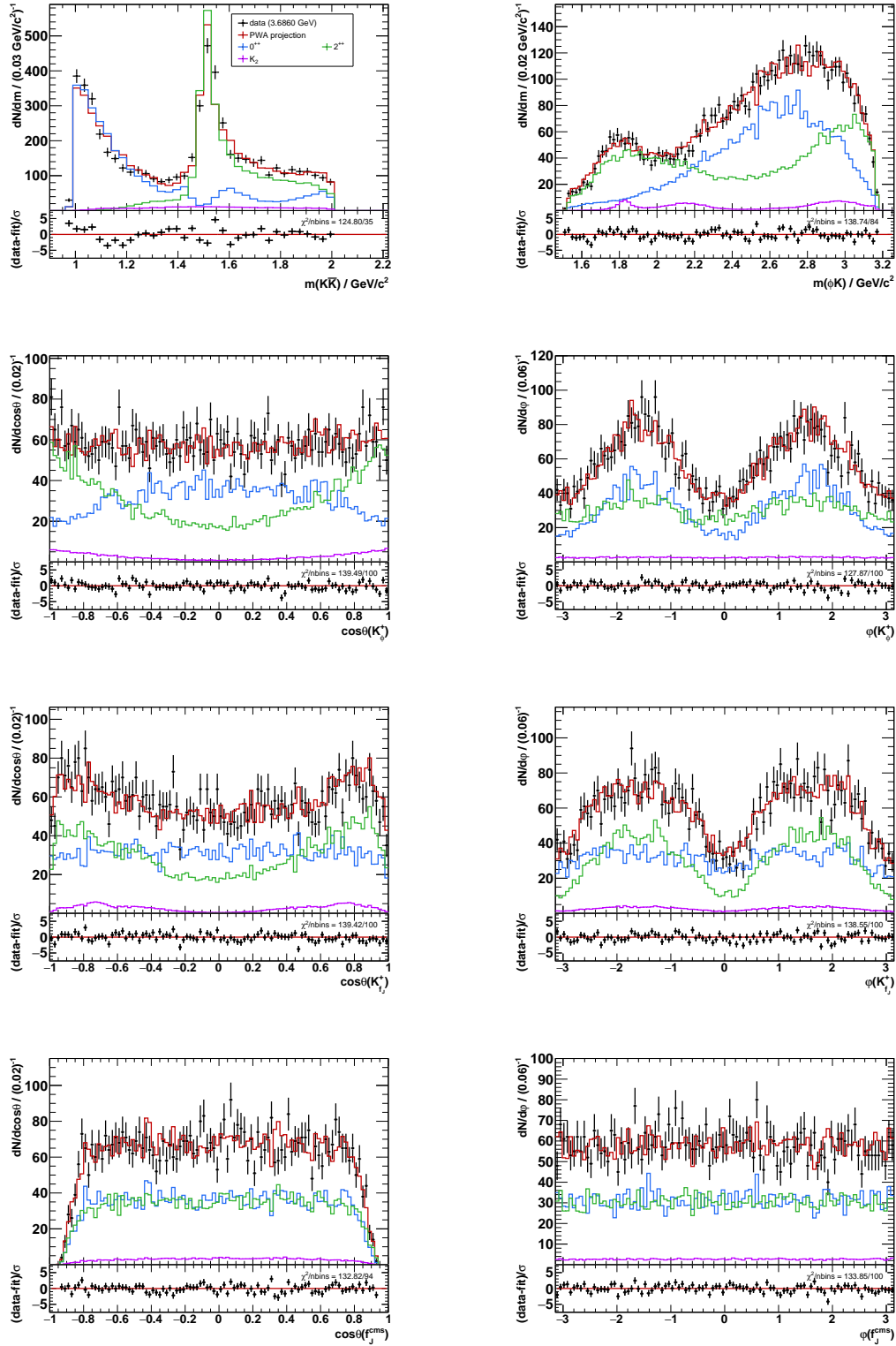


Figure 5.21.: Fit results of the partial wave analysis for $e^+e^- \rightarrow \phi K^+K^-$ at $\sqrt{s} = m_{\psi(2S)}$. Data (black dots with error bars), the total PWA projection (red solid line), the 0^{++} (blue solid line), the 2^{++} (green solid line) as well as the K_2 contributions (solid purple line) are shown.

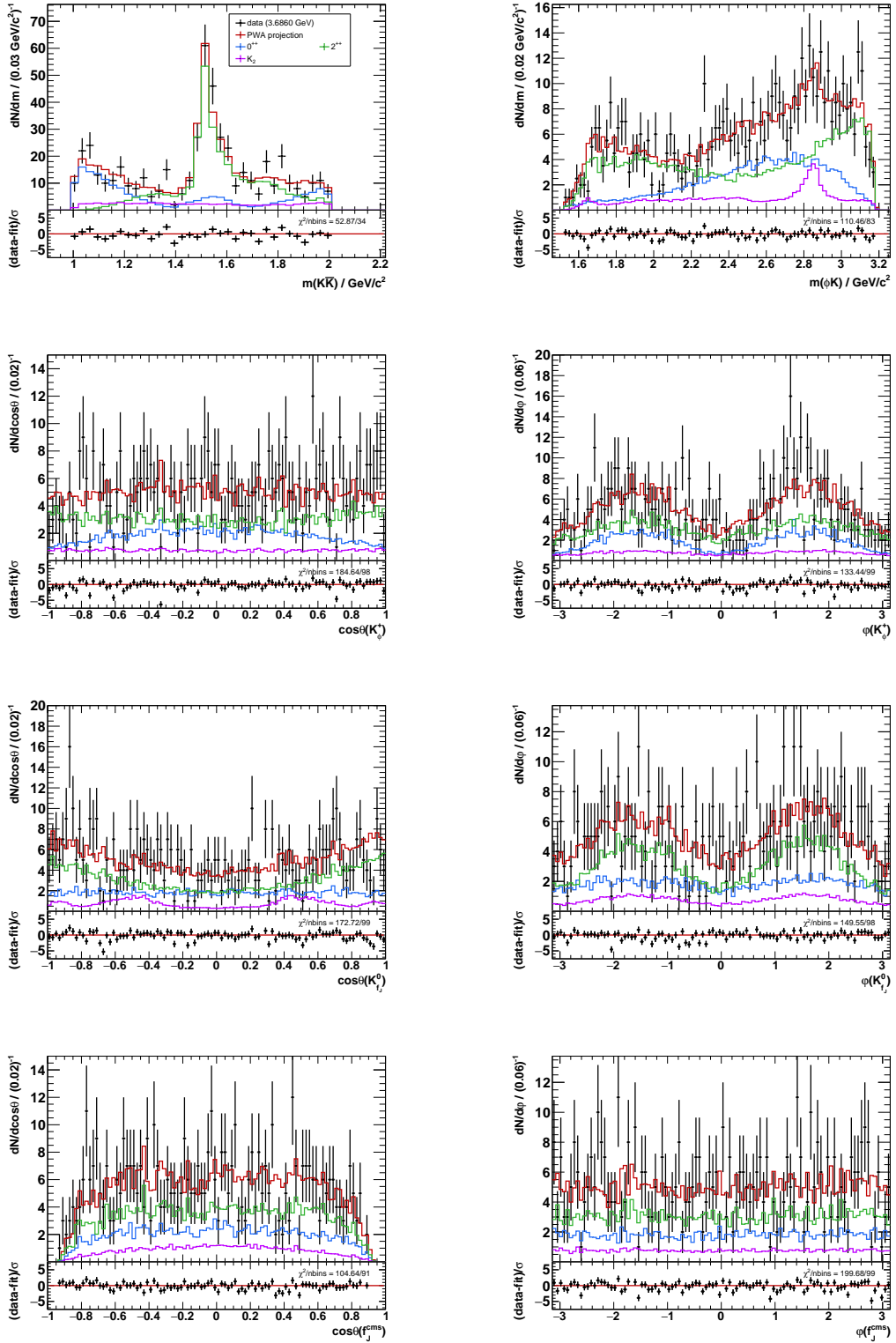


Figure 5.22.: Fit results of the partial wave analysis for $e^+e^- \rightarrow \phi K_S^0 K_S^0$ at $\sqrt{s} = m_{\psi(2S)}$. Data (black dots with error bars), the total PWA projection (red solid line), the 0^{++} (blue solid line), the 2^{++} (green solid line) as well as the K_2 contributions (solid purple line) are shown.

6. Analysis of $e^+e^- \rightarrow p\bar{p}\eta'$

The second part of this thesis deals with the lineshape study of the energy-dependent Born cross section $\sigma_b(e^+e^- \rightarrow p\bar{p}\eta')$ in the search for couplings of (exotic) vector charmonia to the investigated light hadron final state, using the same data as in Chapter 5. Born cross sections are calculated according to Equation (5.1).

While protons p and anti-protons \bar{p} can be directly measured with the BESIII detector, η' mesons are reconstructed in their decays $\eta' \rightarrow \eta\pi^+\pi^-$ with $\eta \rightarrow \gamma\gamma$ and $\eta' \rightarrow \gamma\pi^+\pi^-$. The respective branching fractions can be found in Table 4.1. All signal MC events are generated evenly distributed in phase space, except those of the decay $\eta' \rightarrow \gamma\pi^+\pi^-$, which are generated with the DIY generator taking $\rho - \omega$ interference and box anomaly into account [266–269].

6.1. Background Studies

η' meson candidates can be identified by investigating the invariant mass spectra of $\eta\pi^+\pi^-$ and $\gamma\pi^+\pi^-$ as shown in Figure 6.1. A clear resonant structure is observed in both channels. Compared to $\eta' \rightarrow \eta\pi^+\pi^-$, where the η mass constraint is applied to the reconstructed photon pair, the background increases drastically for $\eta' \rightarrow \gamma\pi^+\pi^-$ due to the single photon without additional constraints in the kinematic fit. Hence, an additional kinematic fit is performed, either including one extra photon from the event ($\chi_{+\gamma}^2$, e.g. π^0 meson contributions) or excluding an initially reconstructed one ($\chi_{-\gamma}^2$, e.g. processes leading to the $p\bar{p}\pi^+\pi^-$ final state to which photons have been incorrectly assigned). The kinematic χ_{NC}^2 value has to satisfy

$$\chi_{\text{NC}}^2 < \chi_{+\gamma}^2 \quad \text{and} \quad \chi_{\text{NC}}^2 < \chi_{-\gamma}^2. \quad (6.1)$$

Note that this will in principle also reduce the absolute number of signal events. In Figure 6.1, a maximum likelihood fit is performed to the invariant mass distributions before and after applying the selection conditions in Equation (6.1). Signal contributions are described by the signal MC shape convolved with a Gaussian function to account for possible differences in resolution between data and signal MC, while background contributions are described by a second-order and first-order polynomial for $\eta' \rightarrow \eta\pi^+\pi^-$ and $\eta' \rightarrow \gamma\pi^+\pi^-$, respectively. According to the fit results, the signal to background significance $S/\sqrt{S+B}$ has increased from 4.82 (3.60) to 7.10 (5.96) for the $p\bar{p}\eta\pi^+\pi^-$

6. Analysis of $e^+e^- \rightarrow p\bar{p}\eta'$

($p\bar{p}\gamma\pi^+\pi^-$) final state.

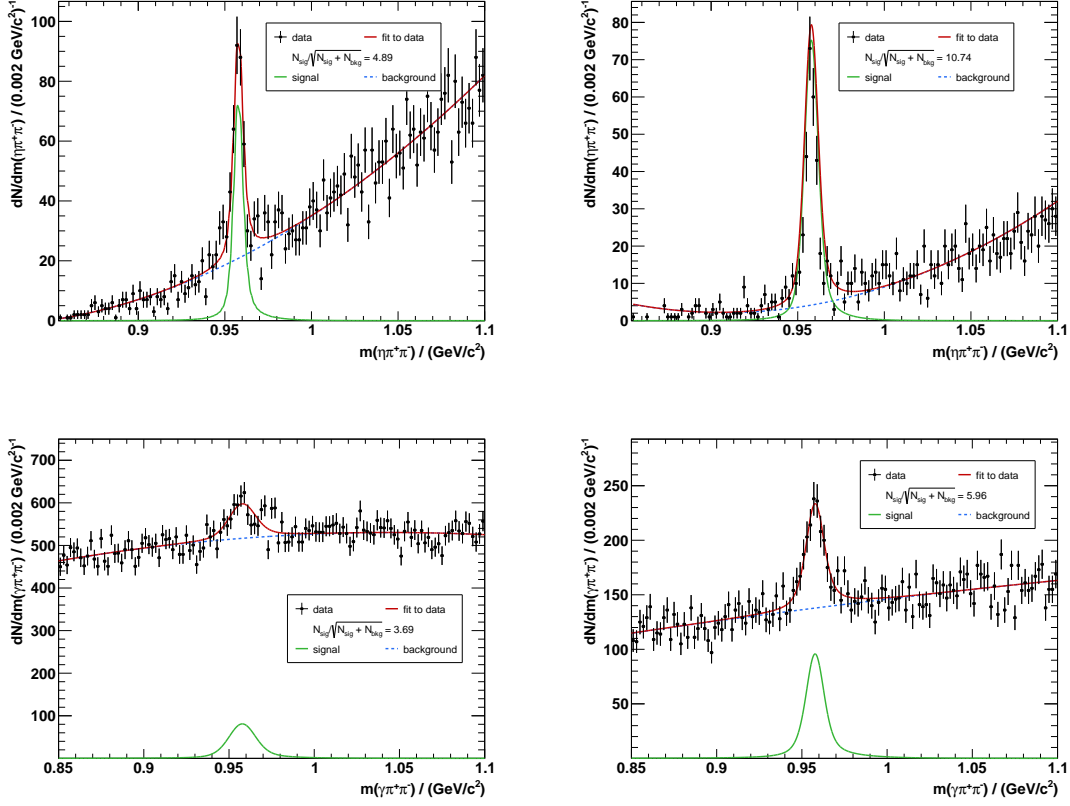


Figure 6.1.: Invariant mass spectrum of η' candidates for $\eta' \rightarrow \eta\pi^+\pi^-$ (**top**) and $\eta' \rightarrow \gamma\pi^+\pi^-$ (**bottom**) before (**left**) and after (**right**) the selection conditions $\chi_{\text{NC}}^2 < \chi_{+\gamma}^2$ and $\chi_{\text{NC}}^2 < \chi_{-\gamma}^2$ for all data sets used. A maximum likelihood fit as in Section 5.2 is performed to calculate the signal to background significance.

Similar to the strategy presented in Section 5.1, the inclusive Monte Carlo sample at $\sqrt{s} = 4.178$ GeV is used in order to identify reactions contributing to both the signal and to the background events left after the selection criteria applied so far. The extracted signal and background samples are scaled to data as shown in Figure 6.2. An overall good agreement between data and the inclusive MC sample is observed, showing no peaking background contributions at the mass of the η' meson, neither in $\eta' \rightarrow \eta\pi^+\pi^-$ nor in $\eta' \rightarrow \gamma\pi^+\pi^-$. In case of $\eta' \rightarrow \gamma\pi^+\pi^-$, the resonant background contribution at $m(\gamma\pi^+\pi^-) = 1.0$ GeV from the final state $p\bar{p}f_0(980)$ with $f_0(980) \rightarrow \gamma\pi^+\pi^-$ can be observed, which clearly does not match data.

Table 6.1 lists the composition of events from the inclusive MC sample, separated in signal and the main background contributions. Dominant background contributions contain processes leading to different final states as the signal hypotheses and thus may be suppressed by proper selection conditions on the kinematic χ_{NC}^2 value. The signal

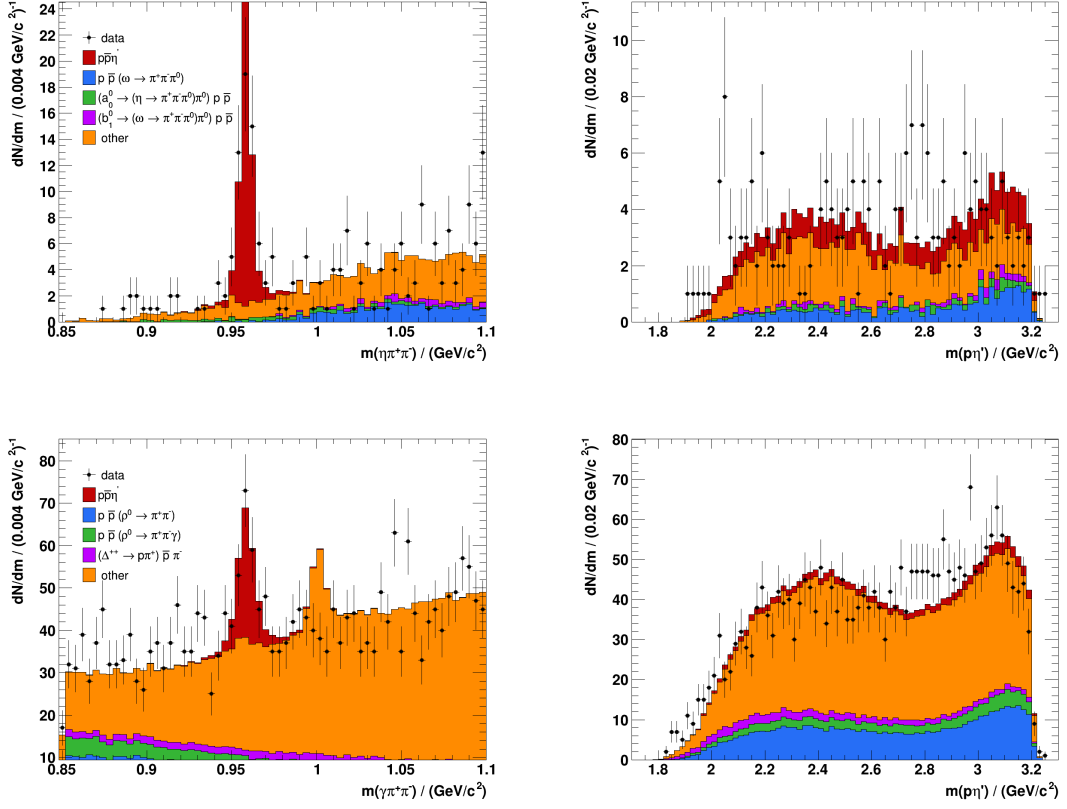


Figure 6.2.: Fit of the signal and background contributions extracted from the inclusive MC sample to the invariant mass spectrum of η' (**left**) and respective $\rho\eta'$ (**right**) candidates for $\eta' \rightarrow \eta\pi^+\pi^-$ (**top**) and $\eta' \rightarrow \gamma\pi^+\pi^-$ (**bottom**) at $\sqrt{s} = 4.178$ GeV. Data (black dots with error bars), the signal contribution (red) as well as main background contributions are shown.

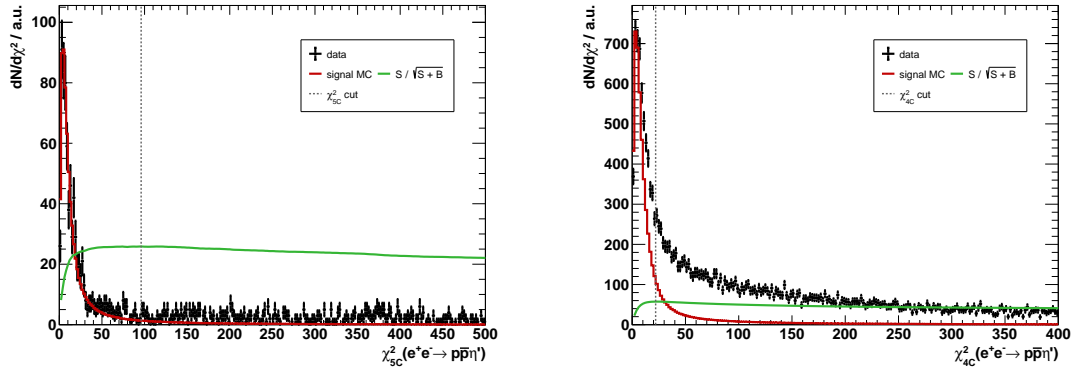


Figure 6.3.: χ^2_{NC} distributions for data sets used ($S + B$, black dots with error bars) and signal MC (S , red line) summed up over all center-of-mass energies analyzed, as well as the resulting FOM (green line) for the $\rho\bar{\rho}\eta\pi^+\pi^-$ (**left**) and $\rho\bar{\rho}\gamma\pi^+\pi^-$ final states (**right**). The vertical dashed gray line indicates the selection condition on the χ^2_{NC} value of the kinematic fit.

Table 6.1.: Inclusive MC events that survive the selection criteria identified as the $p\bar{p}(\eta' \rightarrow \eta\pi^+\pi^-)$ or $p\bar{p}(\eta' \rightarrow \gamma\pi^+\pi^-)$ final state. **Green:** Signal contributions. **White:** Background contributions. The listed processes are sorted according to their yield. Processes with lower yields are denoted by remaining.

Reaction	Number of events
$p\bar{p}(\eta' \rightarrow \eta\pi^+\pi^-)$	6777
$p\bar{p}(\omega \rightarrow \pi^+\pi^-\pi^0)$	8412
$p\bar{p}(b_1^0 \rightarrow (\omega \rightarrow \pi^+\pi^-\pi^0))\pi^0$	2665
$p\bar{p}(a_0^0 \rightarrow (\eta \rightarrow \pi^+\pi^-\pi^0))\pi^0$	2158
sum of remaining	10543
$p\bar{p}(\eta' \rightarrow \gamma\pi^+\pi^-)$	12752
$p\bar{p}(\rho^0 \rightarrow \pi^+\pi^-)$	38532
$p\bar{p}(\rho^0 \rightarrow \pi^+\pi^-\gamma)$	11193
$(\Delta^{++} \rightarrow p\pi^+)\bar{p}\pi^-$	8376
sum of remaining	132158

significance with respect to the background processes is again maximized using the figure of merit according to Equation (5.3). However, the χ_{NC}^2 distributions of the inclusive MC sample are in disagreement with data, so that they are not used for the optimization. Instead, signal MC (representing the χ_{NC}^2 distribution for signal S) and data (representing the χ_{NC}^2 distribution for the sum of signal S and background B ensuring a correct relative scaling) distributions are employed for the calculation of the figure of merit in Figure 6.3. This leads to maxima at $\chi_{5\text{C}}^2 = 96$ and $\chi_{4\text{C}}^2 = 22$ for $\eta' \rightarrow \eta\pi^+\pi^-$ and $\eta' \rightarrow \gamma\pi^+\pi^-$, respectively.

6.2. Number of Observed Events

Since overall statistics are rather limited, so that especially in data samples with lower luminosities no significant η' contributions can be observed, data from specific center-of-mass energy ranges is combined to subsets (see Table 6.2). A maximum likelihood fit is performed to each subset in order to extract the background shape for the respective energy regime, exemplary shown for the region from $\sqrt{s} = 4.2263$ GeV to $\sqrt{s} = 4.3964$ GeV in Figure 6.4. In subsequent fits to each individual data set, the parameters related to the background shape are fixed to the results from the fits to the corresponding subset. An additional free background scale parameter allows adjusting the background level according to data due to, i.e., different luminosities for each data set. As in Figure 6.1, signal contributions are described by the signal MC shape convolved with a Gaussian function to account for possible differences in resolution between data

and signal MC, while background contributions are described by a second-order and first-order polynomial for $\eta' \rightarrow \eta\pi^+\pi^-$ and $\eta' \rightarrow \gamma\pi^+\pi^-$, respectively. Results for all other individual data samples can be found in Appendix A.5.

Table 6.2.: Data subsets defined in a specific center-of-mass energy range \sqrt{s} with summed integrated luminosity L to extract the background shape.

Subset	\sqrt{s} / GeV	L / pb^{-1}
1	3.7730	2931.8
2	3.8695 – 4.2187	6788.4
3	4.2263 – 4.3964	6742.8
4	4.4156 – 4.7008	6233.4

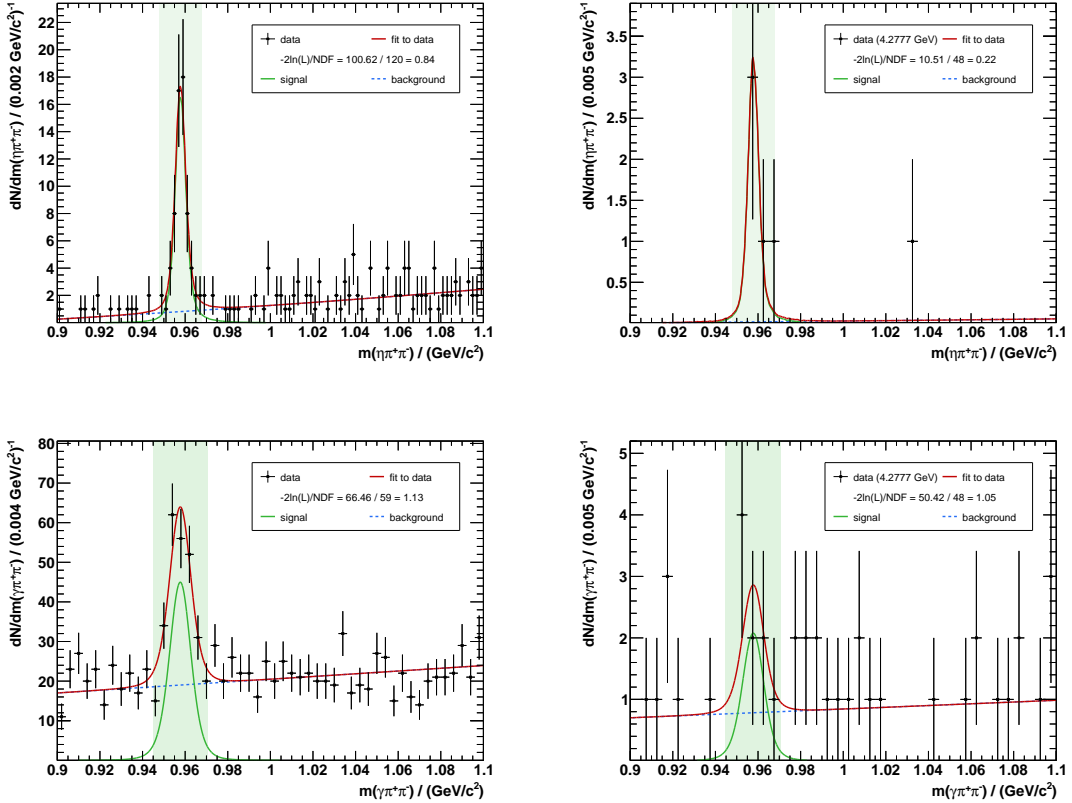


Figure 6.4.: Invariant mass spectrum of η' candidates for data (black dots with error bars) from $\sqrt{s} = 4.2263$ GeV to $\sqrt{s} = 4.3964$ GeV (**left**) and $\sqrt{s} = 4.2777$ GeV (**right**). A fit (red line) with the signal MC shape convolved with a Gaussian function as signal (green line) and a second-order and first-order polynomial as background for $\eta' \rightarrow \eta\pi^+\pi^-$ and $\eta' \rightarrow \gamma\pi^+\pi^-$ (dashed blue line) is applied, respectively. The green shaded area depicts the signal region in which the number of observed events N_{obs} is extracted. **Top:** $\eta' \rightarrow \eta\pi^+\pi^-$. **Bottom:** $\eta' \rightarrow \gamma\pi^+\pi^-$.

As can be seen in Figure 6.4 for the data set at $\sqrt{s} = 4.2777$ GeV, only a few events survive the selection criteria. In such cases, a significant η' contribution may not be observed in data and, thus, the nominal value of N_{obs} , extracted for each data set as described in Section 5.2, is compatible with zero within the 3σ interval of statistical uncertainty. The results for N_{obs} are listed in Table A.5.

6.3. Efficiency

The reconstruction and selection efficiency is determined according to Equation (5.7). However, since the available statistics is limited, a partial wave analysis can not be carried out in order to extract a re-weighted signal MC sample as an effective description of data. Hence, the efficiency is determined by integrating the reconstructed invariant mass distributions $m(\eta\pi^+\pi^-)$ and $m(\gamma\pi^+\pi^-)$ using the simple signal MC samples containing events evenly distributed in phase space and divide the results by the number of generated events. The radiative corrections factors are obtained as described in Section 5.4 and results are summarized in Table A.5.

6.4. Systematic Uncertainties

The strategy to determine the systematic uncertainties is equal to the one presented in Section 5.6. Systematic uncertainties which have been determined by the BESIII collaboration in previous studies [214, 248, 270] are summarized in Table 6.3. Additional

Table 6.3.: Systematic uncertainties for the luminosity [214], the tracking efficiency [248], the photon detection [270] as well as the branching ratio [56] in % for the reaction $e^+e^- \rightarrow p\bar{p}\eta'$.

	$\eta' \rightarrow \eta\pi^+\pi^-$	$\eta' \rightarrow \gamma\pi^+\pi^-$
Luminosity	1.0	1.0
Tracking efficiency	4.0	4.0
Photon detection	2.0	1.0
Branching ratio	1.3	1.4
Total	4.8	4.5

systematic effects are studied according to Equations (5.20) and (5.21). A systematic uncertainty is again obtained as the standard deviation σ_R of a weighted average of the ratios R_i using Equation (5.22). Due to the low statistics in data, the evaluation of systematic effects is performed based on the subsets listed in Table 6.2. A systematic uncertainty obtained from a subset is then assigned to each corresponding individual data set. Results are shown in Figures 6.5 and 6.6 and summarized in Table 6.4.

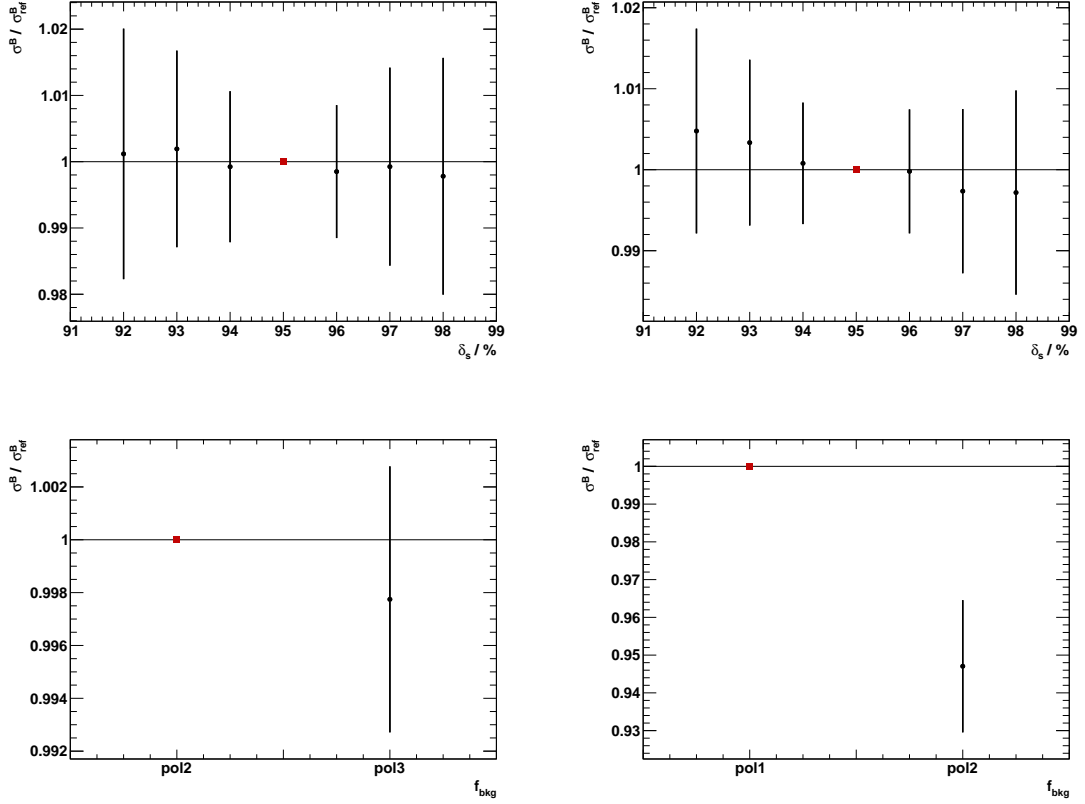


Figure 6.5.: Systematic studies of the arbitrarily chosen signal region containing a certain signal portion δ_s (**top**) and the functional form to describe the background part (**bottom**) for $\eta' \rightarrow \eta\pi^+\pi^-$ (**left**) and $\eta' \rightarrow \gamma\pi^+\pi^-$ (**right**) for subset 2. The nominal value, which is the reference value, is depicted as the red marker. The error bars are calculated using Equation (5.21).

Table 6.4.: Systematic uncertainties in % for each data subset for $\eta' \rightarrow \eta\pi^+\pi^-$ and $\eta' \rightarrow \gamma\pi^+\pi^-$ obtained from this analysis due to the choice of the signal region δ_s , of the background shape f_{Bkg} , and of the selection condition on the χ_{NC}^2 value, as well as the total systematic uncertainty, including the sources from Table 6.3.

Subset	$\eta' \rightarrow \eta\pi^+\pi^-$				$\eta' \rightarrow \gamma\pi^+\pi^-$			
	δ_s	f_{Bkg}	χ_{5C}^2	Total	δ_s	f_{Bkg}	χ_{4C}^2	Total
1	0.21	0.35	0.77	4.84	0.22	5.48	2.24	7.41
2	0.14	0.23	0.61	4.80	0.26	5.30	0.68	6.96
3	0.18	0.00	0.75	4.82	0.25	6.40	3.53	8.56
4	0.19	0.00	0.61	4.80	0.22	1.32	3.15	5.62

6.5. Born Cross Sections

Since the η' meson is reconstructed in its decay to both $\eta\pi^+\pi^-$ and $\gamma\pi^+\pi^-$, a combined Born cross section is determined in the following. As in Section 5.5, the likelihood

6. Analysis of $e^+e^- \rightarrow p\bar{p}\eta'$

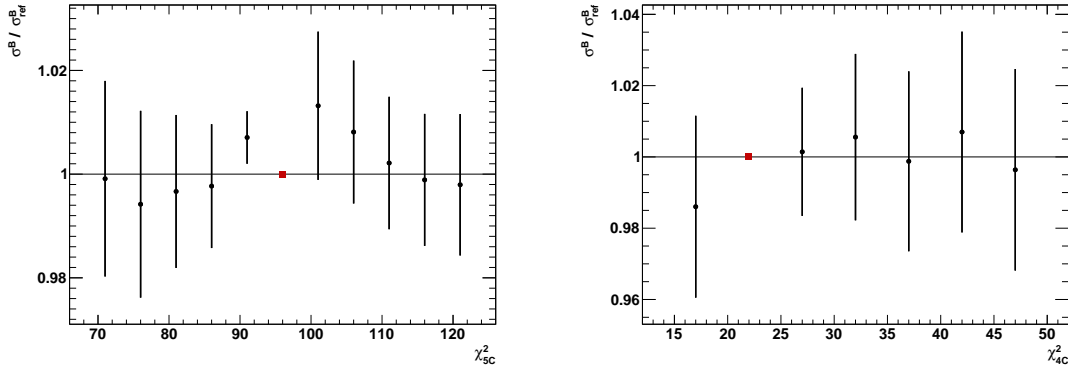


Figure 6.6.: Systematic studies of the selection condition on the χ_{NC}^2 value of the kinematic fit for $\eta' \rightarrow \eta\pi^+\pi^-$ (left) and $\eta' \rightarrow \gamma\pi^+\pi^-$ (right) for subset 2. The nominal value, which is the reference value, is depicted as the red marker. The error bars are calculated using Equation (5.21).

distribution of a single Born cross section measurement is assumed to be properly described by an asymmetric Gaussian function. In case of combining two measurements, the resulting vector-valued random variable $\sigma_{\text{b,comb}} = [\sigma_{\text{b},\eta' \rightarrow \eta\pi^+\pi^-}, \sigma_{\text{b},\eta' \rightarrow \gamma\pi^+\pi^-}]^T$ is said to have a multivariate Gaussian distribution with mean $\mu \in \mathbb{R}^n$ and the symmetric positive definite $n \times n$ covariance matrix $\Sigma \in \mathbb{S}_{++}^n$ ¹, if its probability density function is given by [271]

$$p(\vec{x}; \vec{\mu}, \Sigma) = \frac{1}{(2\pi)^{n/2}(\det \Sigma)^{1/2}} \exp\left(-\frac{1}{2}(\vec{x} - \vec{\mu})^T \Sigma^{-1}(\vec{x} - \vec{\mu})\right). \quad (6.2)$$

Here, $n = 2$ and the corresponding matrices read

$$\vec{x} = \begin{pmatrix} N_{\eta' \rightarrow \eta\pi^+\pi^-} \\ N_{\eta' \rightarrow \gamma\pi^+\pi^-} \end{pmatrix} \quad \vec{\mu} = \begin{pmatrix} \mu_{\eta' \rightarrow \eta\pi^+\pi^-} \\ \mu_{\eta' \rightarrow \gamma\pi^+\pi^-} \end{pmatrix} \quad \Sigma = \begin{pmatrix} \sigma_1^2 & \text{cov}(x_1, x_2) \\ \text{cov}(x_2, x_1) & \sigma_2^2 \end{pmatrix}, \quad (6.3)$$

with σ_1 and σ_2 being the total uncertainty for $\eta' \rightarrow \eta\pi^+\pi^-$ and $\eta' \rightarrow \gamma\pi^+\pi^-$, respectively, calculated by taking the squared sum of statistical and systematic uncertainties, and $\text{cov}(x_1, x_2) = \text{cov}(x_2, x_1) = x_1 \cdot \rho_{12} \cdot x_2 \cdot \rho_{21}$ being the covariance between channels 1 and 2, including the measured values x and their common relative systematic uncertainties ρ . Equation (6.2) reduces to the product of two independent Gaussian densities in case of vanishing covariances between both channels the η' meson is reconstructed in. Furthermore, the multivariate Gaussian function can be set up asymmetrically as in Equation (5.13) to account for Poisson-like distributed statistical uncertainties.

In order to obtain a value for the combined Born cross section for a single data set, a likelihood scan is performed as described in Section 5.5. Instead of the parametrizations

¹ \mathbb{S}_{++}^n is the space of symmetric positive definite $n \times n$ matrices, defined as $\mathbb{S}_{++}^n = \{A \in \mathbb{R}^{n \times n} : A = A^T \text{ and } x^T A x > 0 \text{ for all } x \in \mathbb{R}^n \text{ such that } x \neq 0\}$.

given in Equations (5.14), (5.16) and (5.17), a single parameter is used representing the Born cross section value. The common relative systematic uncertainties between channel 1 and 2 include the luminosity as well as the tracking efficiency and photon detections due to a shared number of charged tracks and photon candidates, respectively. Results are shown exemplary for $\sqrt{s} = 4.1784$ GeV and $\sqrt{s} = 4.2777$ GeV in Figure 6.7. Additionally, the 90% confidence level according to Equation (5.18) can be stated in case no significant η' contribution is observed. Results for each data set are listed in Table A.5.

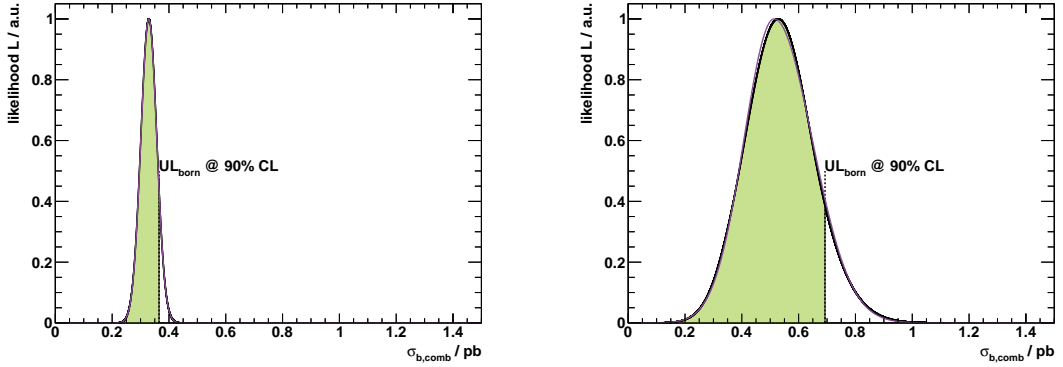


Figure 6.7.: Fit results (purple line) to the likelihood scans of the combined Born cross sections (black dots) at $\sqrt{s} = 4.1784$ GeV (**left**) and $\sqrt{s} = 4.2776$ GeV (**right**) for $e^+e^- \rightarrow p\bar{p}\eta'$. Upper limits indicated by the dashed lines are calculated at 90% *C.L.* according to Equation (5.18).

After having determined the results for the individual data sets, couplings of (exotic) vector charmonia ψ to the hadron final state $p\bar{p}\eta'$ are investigated following the same procedure as in Section 5.5. Hence, three maximum likelihood fits to the Born cross section at each center-of-mass energy from $\sqrt{s} = 3.7730$ GeV to $\sqrt{s} = 4.7008$ GeV are performed according to Equations (5.14), (5.16) and (5.17). The mass and width of the resonance described by the Breit-Wigner function in Equation (5.15) are fixed to the world average values from the PDG [56] $m_\psi = 4.2187$ GeV/ c^2 and $\Gamma_\psi = 0.044$ GeV, respectively. If the results for channel 1 (2) of all energies n_{ecms} are combined, the common systematic uncertainty due to the branching ratios $\mathcal{B}r(\eta' \rightarrow \eta\pi^+\pi^-)$ and $\mathcal{B}r(\eta \rightarrow \gamma\gamma)$ (or $\mathcal{B}r(\eta' \rightarrow \gamma\pi^+\pi^-)$) must be taken into account. In this case, the $n \times n$ covariance matrix with $n = n_{\text{channel}} \cdot n_{\text{ecms}}$ reads

$$\Sigma = \left(\begin{array}{cc|cc|c} \sigma_{11}^2 & \text{cov}(x_{11}, x_{21}) & \text{cov}(x_{12}, x_{11}) & 0 & \cdots \\ \text{cov}(x_{21}, x_{11}) & \sigma_{21}^2 & 0 & \text{cov}(x_{22}, x_{21}) & \cdots \\ \hline \text{cov}(x_{11}, x_{12}) & 0 & \sigma_{12}^2 & \text{cov}(x_{22}, x_{12}) & \cdots \\ 0 & \text{cov}(x_{21}, x_{22}) & \text{cov}(x_{12}, x_{22}) & \sigma_{22}^2 & \cdots \\ \hline \vdots & \vdots & \vdots & \vdots & \ddots \end{array} \right). \quad (6.4)$$

6. Analysis of $e^+e^- \rightarrow p\bar{p}\eta'$

The diagonal elements σ_{ik} and $\text{cov}(x_{ik}, x_{jk}) = \text{cov}(x_{jk}, x_{ik}) = x_{ik} \cdot \rho_{ijk} \cdot x_{jk} \cdot \rho_{jik}$ denote the total uncertainty for channel i at energy k and the covariance between channel i and j at energy k with measured values x_{ik}, x_{jk} and common relative systematic uncertainties $\rho_{ijk} = \rho_{jik}$. Covariances due to the energy-coupling are described by $\text{cov}(x_{ik}, x_{il}) = \text{cov}(x_{il}, x_{ik}) = x_{ik} \cdot \rho_{iik} \cdot x_{il} \cdot \rho_{iil}$ for channel i at energies k and l . The covariance due to energy-coupling of different channels is $\text{cov}(x_{ik}, x_{jl}) = \text{cov}(x_{jl}, x_{ik}) = 0$, because they share no common relative systematic uncertainties. Accordingly, the measured values \vec{x} and means $\vec{\mu}$ become $1 \times n$ vectors.

A hint for a resonant structure can be seen in data at $\sqrt{s} = 4.20$ GeV, which can be described by the hypothesis of a coherent resonant contribution of the $\psi(4230)$ with a significance of 2.43σ compared to the continuum production only.

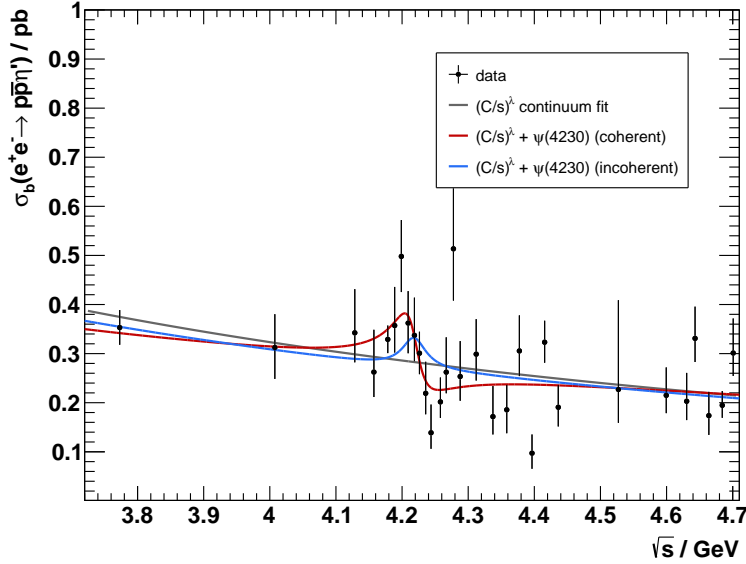


Figure 6.8.: Combined Born cross section (black dots with error bars, denoting the combined statistical and systematic uncertainties) for $e^+e^- \rightarrow p\bar{p}\eta'$ at center-of-mass energies from $\sqrt{s} = 3.7730$ GeV to $\sqrt{s} = 4.7008$ GeV. Maximum likelihood fits are performed according to Equations (5.14), (5.16) and (5.17), assuming pure continuum production (gray line) and an additional coherent (red line) or incoherent (blue line) resonant contribution of the $\psi(4230)$.

6.5.1. Upper Limit on $e^+e^- \rightarrow \psi \rightarrow p\bar{p}\eta'$

Since no significant coupling of the $\psi(4230)$ to the final state $p\bar{p}\eta'$ was observed, upper limits on $e^+e^- \rightarrow \psi(4230) \rightarrow p\bar{p}\eta'$ are set, following the procedure described in Subsection 5.5.1. Figure 6.9 shows the resulting likelihood scans for the hypothesis of a resonant $\psi(4230)$ contribution. The upper limits are obtained as $\sigma_{\psi, \text{coh}}^{\text{UL}} = 0.069$ eV and $\sigma_{\psi, \text{incoh}}^{\text{UL}} = 0.0069$ eV.

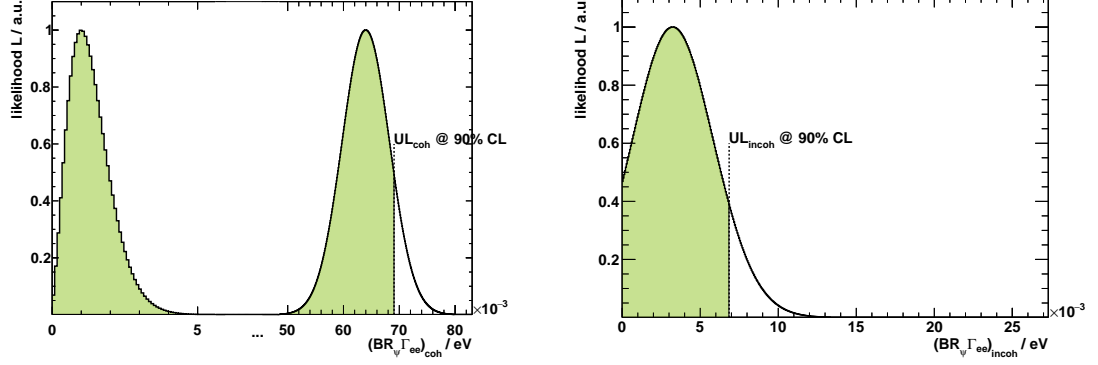


Figure 6.9.: Likelihood distribution for a coherent (**left**) and incoherent (**right**) resonant contribution of the $\psi(4230)$ to the Born cross section of $e^+e^- \rightarrow p\bar{p}\eta'$. Upper limits indicated by the dashed lines are calculated at 90% *C.L.* according to Equation (5.18).

6.6. Comparison with $e^+e^- \rightarrow J/\psi\eta'$

The Born cross section of $e^+e^- \rightarrow p\bar{p}\eta'$ calculated in Section 6.5 includes all processes which lead to the investigated final state $p\bar{p}\eta'$, e.g. its production via intermediate resonances such as J/ψ decaying into $p\bar{p}$. In principle, also the process $e^+e^- \rightarrow h_c\eta'$ with $h_c \rightarrow p\bar{p}$ can contribute. However, the PDG [56] only states an upper limit for $Br(h_c \rightarrow p\bar{p})$ of $< 1.5 \cdot 10^{-4}$, whereas the branching fraction of J/ψ decaying into $p\bar{p}$ is $Br(J/\psi \rightarrow p\bar{p}) = (2.12 \pm 0.03)^{-3}$. Thus, the process $e^+e^- \rightarrow h_c\eta'$ is not considered in this work.

In [57], the Born cross section of $e^+e^- \rightarrow J/\psi\eta'$ with $J/\psi \rightarrow e^+e^-$ and $J/\psi \rightarrow \mu^+\mu^-$ has been measured at center-of-mass energies from $\sqrt{s} = 4.1784$ GeV to $\sqrt{s} = 4.5995$ GeV by the BESIII collaboration. Their results are in agreement with a resonant contribution of both the $\psi(4160)$ and the $\psi(4230)$, as shown in Figure 6.10. Here, a maximum likelihood fit of a coherent and an incoherent sum of Breit-Wigner amplitudes according to

$$\sigma_{\text{coh},2B,2B} = \left| \mathcal{A}_1 \cdot \text{PHSP}_1 \cdot e^{i\phi_1} + \mathcal{A}_2 \cdot \text{PHSP}_2 \right|^2 \quad (6.5)$$

and

$$\sigma_{\text{incoh},2B,2B} = |\mathcal{A}_1 \cdot \text{PHSP}_1|^2 + |\mathcal{A}_2 \cdot \text{PHSP}_2|^2 \quad (6.6)$$

has been performed, respectively, with \mathcal{A}_i being the Breit-Wigner amplitude from Equation (5.15), PHSP_i being the two-body (2B) phase space factor for the two-particle decay $\psi \rightarrow J/\psi\eta'$

$$\text{PHSP} = \frac{\Phi^{\frac{3}{2}}(\sqrt{s})}{\Phi^{\frac{3}{2}}(M_\psi)} = \frac{\left(\frac{p(\sqrt{s})}{\sqrt{s}}\right)^{\frac{3}{2}}}{\left(\frac{p(M_\psi)}{M_\psi}\right)^{\frac{3}{2}}}, \quad (6.7)$$

6. Analysis of $e^+e^- \rightarrow p\bar{p}\eta'$

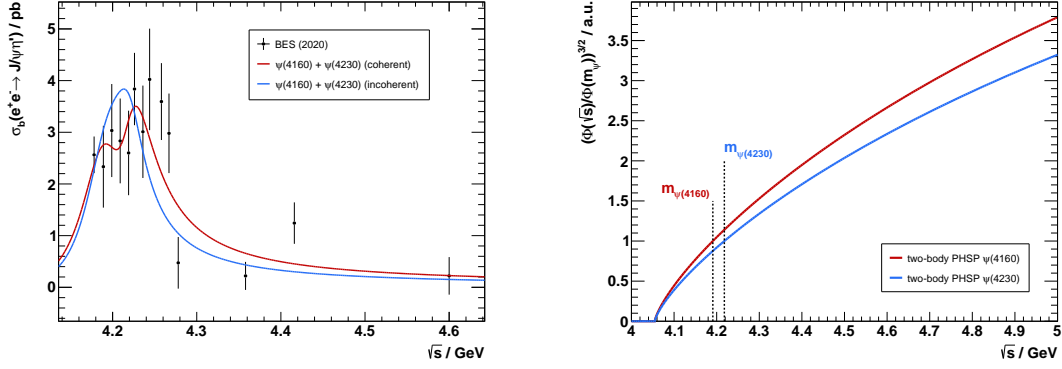


Figure 6.10.: **Left:** Born cross section of $e^+e^- \rightarrow J/\psi\eta'$ measured by the BESIII collaboration [57] at center-of-mass energies from $\sqrt{s} = 4.1784$ GeV to $\sqrt{s} = 4.5995$ GeV. A maximum likelihood fit is performed, assuming resonant contributions only of both the $\psi(4160)$ and the $\psi(4230)$ with (red line) and without (blue line) interference. **Right:** Two-body phase space factors for the decays $\psi(4160) \rightarrow J/\psi\eta'$ (red line) and $\psi(4230) \rightarrow J/\psi\eta'$ (blue line).

$p(x)$ being the momentum of the η' or J/ψ meson in the center-of-mass system at the energy \sqrt{s} or in the system of the ψ with mass M_ψ

$$p(x) = \sqrt{\left(x^2 - \left(M_{J/\psi} + M_{\eta'}\right)^2\right) \cdot \left(x^2 - \left(M_{J/\psi} - M_{\eta'}\right)^2\right)} \cdot \frac{1}{2x}, \quad (6.8)$$

and ϕ being a phase allowing for interferences between both resonant contributions. Figure 6.10 shows also the two-body phase space factor for both the $\psi(4160)$ and the $\psi(4230)$. At center-of-mass energies below the mass of the resonance M_ψ , the amplitude \mathcal{A} is reduced (PHSP<1), whereas at larger energies the decay of $\psi \rightarrow J/\psi\eta'$ is kinematically more favored, yielding an amplification of the amplitude (PHSP>1)².

The results published in [57] can be used to cross check with the analysis procedure developed in this work. Figure 6.11 shows the invariant mass distribution of $p\bar{p}$ pairs summed up over all data samples used in this work. Since the J/ψ meson decaying into $p\bar{p}$ can be clearly observed, the Born cross section of $e^+e^- \rightarrow p\bar{p}\eta'$ determined in this work should contain contributions of the two-body decay $\psi \rightarrow J/\psi\eta'$. To be precise, a portion of the resonant structure seen in the Born cross section of $e^+e^- \rightarrow p\bar{p}\eta'$ with a significance of 2.43σ should come from the process $\psi \rightarrow J/\psi\eta'$. Therefore, the analysis is repeated without J/ψ contributions, which is realized by a veto in the invariant mass of $p\bar{p}$ pairs in the range from $m(p\bar{p}) \in [3.07 \text{ GeV}/c^2, 3.13 \text{ GeV}/c^2]$ (see the green shaded box in Figure 6.11). The range corresponds to the J/ψ signal region in [57]. Results of the Born cross section excluding processes with intermediate J/ψ resonances are shown

²Note that Equation (6.7) converges in case of very large center-of-mass energies ($s \gg (M_{J/\psi} + M_{\eta'})$) to $\text{PHSP} = \sqrt{1/(2^3\Phi^3(M_\psi))}$.

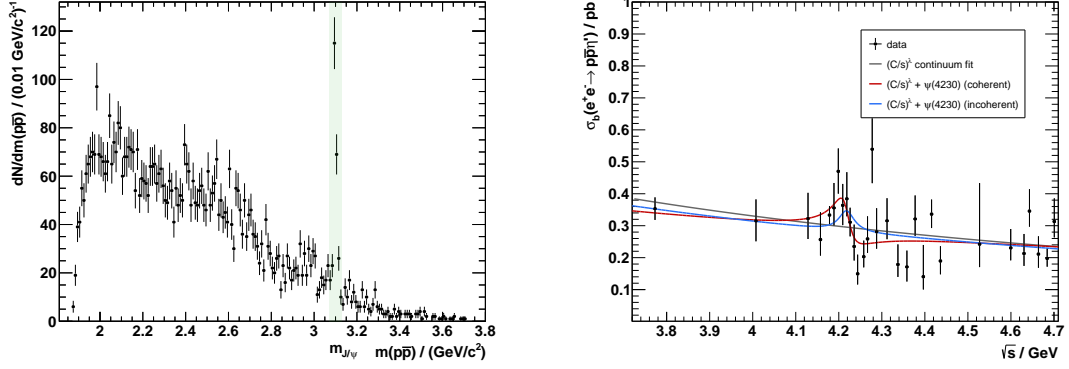


Figure 6.11.: **Left:** Invariant mass spectrum of $p\bar{p}$ pairs summed up over all data samples used in this work and channels the η' meson is reconstructed in. The green shaded box in the range from $m(p\bar{p}) \in [3.07 \text{ GeV}/c^2, 3.13 \text{ GeV}/c^2]$ represents the veto of the J/ψ meson. **Right:** Maximum likelihood fits to the Born cross section of $e^+e^- \rightarrow p\bar{p}\eta'$ excluding processes with intermediate J/ψ mesons assuming pure continuum production (gray line) and an additional coherent (red line) or incoherent (blue line) resonant contributions of the $\psi(4230)$.

in Figure 6.11. The significance of a coherent resonant contribution of the $\psi(4230)$ is 2.13σ and thus lower than in the case where J/ψ processes are involved. Even though no significant contribution of the $\psi(4230)$ can be observed in either case, the hint of such a structure remains with the veto on the J/ψ meson.

In [57], a significant contribution of not only the $\psi(4230)$ but also of the $\psi(4160)$ was observed. With the data available in this work, resonant contributions of the latter can also be searched for. Based on the results so far, it is interesting to additionally investigate whether the fit can distinguish between two- and three-body decays. Hence, in Figure 6.12 a maximum likelihood fit assuming coherent resonant contributions of both the $\psi(4160)$ and the $\psi(4230)$ decaying into $J/\psi\eta'$ or into $p\bar{p}\eta'$ is performed to the Born cross section determined in this work according to

$$\sigma_{\text{coh},2\text{B}} = \left| \sqrt{\sigma_{\text{cont}}} + \mathcal{A} \cdot \text{PHSP} \cdot e^{i\phi} \right|^2 \quad \text{and} \quad \sigma_{\text{coh},3\text{B}} = \left| \sqrt{\sigma_{\text{cont}}} + \mathcal{A} \cdot e^{i\phi} \right|^2. \quad (6.9)$$

Both fits describe the data equally well (note that the number of degrees of freedom is the same), but the background shapes change due to the asymmetric Breit-Wigner amplitudes caused by the two-body phase space factors. Therefore, this fit does not allow a distinction between two- and three-body decays when the resonances are implemented individually.

In a next step (see Figure 6.13), both resonances are included simultaneously, allowing for both two-body and three-body decays to check whether any interference (or only the presence in the incoherent case) of the $\psi(4160)$ and the $\psi(4230)$ favors one of the two

6. Analysis of $e^+e^- \rightarrow p\bar{p}\eta'$

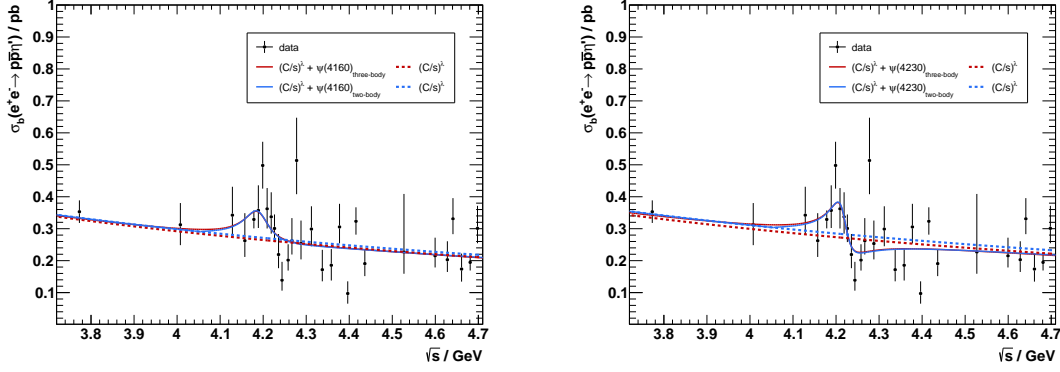


Figure 6.12.: Maximum likelihood fits to the Born cross section of $e^+e^- \rightarrow p\bar{p}\eta'$ determined in Section 6.5 assuming coherent resonant contributions of the $\psi(4160)$ (**left**) and the $\psi(4230)$ (**right**) decaying via a three-body decay into $p\bar{p}\eta'$ (red line) or via a two-body decay into $J/\psi\eta'$ (blue line). The corresponding continuum productions are drawn as dashed lines.

possibilities. In this case, the Born cross section for coherent contributions is described by

$$\begin{aligned} \sigma_{\text{coh},2B+3B,2B+3B} &= \left| \sqrt{\sigma_{\text{cont}}} \right. \\ &\quad + \tilde{\mathcal{A}}_1 \cdot \left(\sqrt{\sigma_{1,2B}} \cdot \text{PHSP}_1 + \sqrt{\sigma_{1,3B}} \right) e^{i\phi_1} \\ &\quad \left. + \tilde{\mathcal{A}}_2 \cdot \left(\sqrt{\sigma_{2,2B}} \cdot \text{PHSP}_2 + \sqrt{\sigma_{2,3B}} \right) e^{i\phi_2} \right|^2, \end{aligned} \quad (6.10)$$

with $\tilde{\mathcal{A}}_i$ being the Breit-Wigner amplitude of Equation (5.15) except from the product $\sigma_\psi = \Gamma_{e^+e^-} \mathcal{B}r(\psi \rightarrow \text{daughters})$, $\sigma_{i,2B} = \Gamma_{i,e^+e^-} \mathcal{B}r(\psi_i \rightarrow J/\psi\eta')$ and $\sigma_{i,3B} = \Gamma_{i,e^+e^-} \mathcal{B}r(\psi_i \rightarrow p\bar{p}\eta' \setminus J/\psi\eta')$. A comparison to the fit result shown in Figure 6.8 can be made where only the $\psi(4230)$ has been considered. The significance of an additional resonant contribution of the $\psi(4160)$ amounts to 0.44σ .

For incoherent contributions the amplitudes $\sigma_{i,2B}$ extracted from Figure 6.10 can be incorporated as a fixed contribution into the fit to the Born cross section of $e^+e^- \rightarrow p\bar{p}\eta'$. The fit function is given by

$$\begin{aligned} \sigma_{\text{incoh},2B+3B,2B+3B} &= \sigma_{\text{cont}} \\ &\quad + \left| \tilde{\mathcal{A}}_1 \cdot \left(\sqrt{\sigma_{1,2B}} \cdot \text{PHSP}_1 + \sqrt{\sigma_{1,3B}} \right) \right|^2 \\ &\quad + \left| \tilde{\mathcal{A}}_2 \cdot \left(\sqrt{\sigma_{2,2B}} \cdot \text{PHSP}_2 + \sqrt{\sigma_{2,3B}} \right) \right|^2. \end{aligned} \quad (6.11)$$

Table 6.5 summarizes the fit results presented in this section. As already indicated in Figure 6.12, no distinction between two- and three-body decays can be made with the data available. Each model listed in Table 6.5 has the same fit quality with and without

additional two-body phase space factors, why this notation is omitted in the following. The significance of a coherent resonant contribution of the $\psi(4160)$ or the $\psi(4230)$ compared to the continuum production is 1.78σ or 2.43σ , respectively. However, the significance of both contributions simultaneously is only 1.40σ due to the two additional free parameters in the fit. When the fixed contribution of $\psi \rightarrow J/\psi\eta'$ is built into the fit, no improvement of the fit quality can be achieved with an additional amplitude for three-body processes ($\sigma_{1,3B} = \sigma_{2,3B} = 0$). The significance of such model compared to the continuum production is 1.10σ . With the data available, the resonant production of the final state $p\bar{p}\eta'$ through (exotic) vector charmonia ψ occurs exclusively via the intermediate state $J/\psi\eta'$ with $J/\psi \rightarrow p\bar{p}$, although the resonant structure does not completely disappear in the case where the veto was made on the J/ψ (see Figure 6.11).

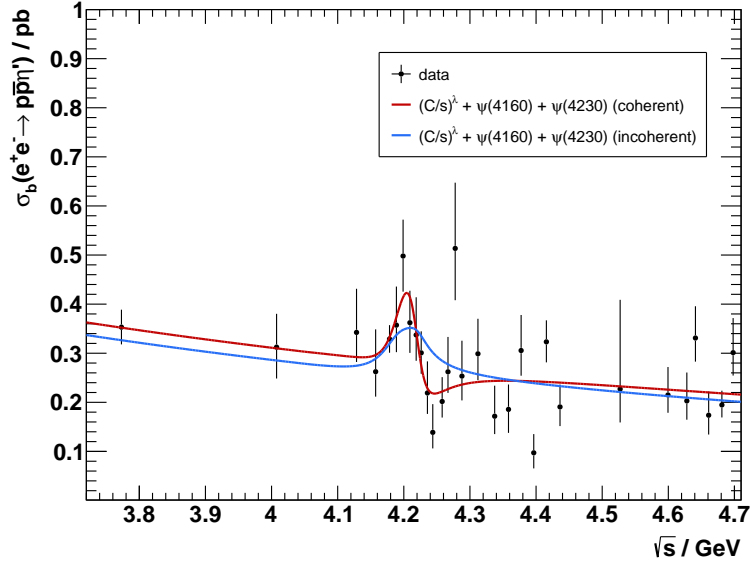


Figure 6.13.: Maximum likelihood fits to the Born cross section of $e^+e^- \rightarrow p\bar{p}\eta'$ determined in Section 6.5 assuming coherent (red line) and incoherent (blue line) resonant contributions of both the $\psi(4160)$ and the $\psi(4230)$ decaying via a three-body decay into $p\bar{p}\eta'$ or via a two-body decay into $J/\psi\eta'$.

6. Analysis of $e^+e^- \rightarrow p\bar{p}\eta'$

Table 6.5.: Fit model, $-2 \ln \mathcal{L}$ value of the minimization, number of free parameters n_{par} and significance calculated with respect to model 1, which considers the continuum production only.

Model	$-2 \ln \mathcal{L}$	n_{par}	σ
1 σ_{cont}	58.64	2	
2 + coherent $\psi(4230)$	50.24	4	2.43
3 + coherent $\psi(4160)$	53.48	4	1.78
4 + incoherent $\psi(4230)$	57.10	3	1.24
5 + coherent $\psi(4160), \psi(4230)$	49.40	6	1.40
6 + incoherent $\psi(4160), \psi(4230)$	56.03	4	1.10

7. Conclusions and Perspectives

In this work, Born cross sections of $e^+e^- \rightarrow \phi K^+K^-$, $e^+e^- \rightarrow \phi K_S^0 K_S^0$ and $e^+e^- \rightarrow p\bar{p}\eta'$ have been determined successfully using the high luminosity XYZ data sets accumulated with the BESIII detector at center-of-mass energies from $\sqrt{s} = 3.7730$ GeV to $\sqrt{s} = 4.7008$ GeV. By investigating the lineshape of the Born cross sections, possible couplings of exotic vector charmonia to these charmless meson final states have been studied. This thesis consists of two main parts, the results of which are summarized and discussed separately in the following.

$e^+e^- \rightarrow \phi K\bar{K}$

In the first part of this thesis, the processes $e^+e^- \rightarrow \phi K^+K^-$ and $e^+e^- \rightarrow \phi K_S^0 K_S^0$ have been analyzed. The ϕ meson was reconstructed in its decay into K^+K^- . K_S^0 mesons were reconstructed by their weak decays into $\pi^+\pi^-$, leading to a secondary vertex in the detector. For both the ϕK^+K^- and the $\phi K_S^0 K_S^0$ final state, the ϕ meson was observed in data nearly background free. The number of observed events was extracted precisely via maximum likelihood scans of the signal amplitude, taking Poisson-distributed statistics into account. An efficiency determination was performed in order to determine the Born cross sections properly. For this purpose, a partial wave analysis was carried out, allowing for the extraction of event weights to re-weight the signal MC sample to get an effective description of data. This was achieved with the PAWIAN software [240], developed by our colleagues from Bochum. The search for possible couplings of (exotic) vector charmonia, e.g. the $\psi(4230)$ to ϕK^+K^- and $\phi K_S^0 K_S^0$ was done by calculating the significance of an additional resonant contribution described by a Breit-Wigner amplitude based on the likelihood ratio for the hypotheses of continuum production and such additional resonant contribution. The significances are 0.57σ and 0.03σ (1.02σ and 1.37σ) for ϕK^+K^- (for $\phi K_S^0 K_S^0$) in the coherent and incoherent case, respectively, and, thus, the Born cross section of $e^+e^- \rightarrow \phi K\bar{K}$ in this energy regime is dominated by the continuum production of the respective channel. These results indicate that the $\psi(4230)$ strongly prefers to preserve its charm content in decays, as in charmonium transitions to $\psi(2S)$ or J/ψ under the emission of a $\pi\pi$ pair. Consequently, upper limits on the product of the electronic width and the branching fraction $\sigma_\psi = \Gamma_{e^+e^-} \cdot Br(\psi \rightarrow \phi K\bar{K})$ have been calculated. The results are $\sigma_{\psi,\text{coh}}^{\text{UL}} = 1.75$ eV and $\sigma_{\psi,\text{incoh}}^{\text{UL}} = 0.019$ eV for $e^+e^- \rightarrow \psi(4230) \rightarrow \phi K^+K^-$ and $\sigma_{\psi,\text{coh}}^{\text{UL}} = 0.47$ eV and $\sigma_{\psi,\text{incoh}}^{\text{UL}} = 0.025$ eV for $e^+e^- \rightarrow \psi(4230) \rightarrow \phi K_S^0 K_S^0$. Additionally,

the Born cross sections of $e^+e^- \rightarrow \phi K^+K^-$ and $e^+e^- \rightarrow \phi K_S^0 K_S^0$ have been compared, and a proportionality factor of 3.85 ± 0.01 has been found, which differs significantly from the value of two if assuming isospin symmetry.

Motivated by the still lacking knowledge of the masses and widths of ψ states around $m = 4.23 \text{ GeV}/c^2$, additional upper limit scans were performed for possible resonant contributions with masses $m \in [4.15 \text{ GeV}/c^2, 4.45 \text{ GeV}/c^2]$ and widths $\Gamma \in [0.04 \text{ GeV}, 0.24 \text{ GeV}]$. The results are shown in Figure 5.15. While the upper limit does not seem to depend on the mass for a fixed width bin, it increases with larger widths for a fixed mass bin. Furthermore, no obvious region could be observed in which the upper limits may show any discrepancy from these behaviors. Consequently, no specific pair of mass and width could be identified, which could be assigned to a possible resonant contribution.

Furthermore, the data set at the $\psi(2S)$ resonance including $(448.1 \pm 2.9) \cdot 10^6$ events [249] was used in order to study the $K\bar{K}$ system recoiling off the ϕ meson. The amount of data and therefore the statistics available at this center-of-mass energy is currently being increased fivefold which enables studies with even higher precision in the future. Possible quantum numbers the $K\bar{K}$ system could carry are, e.g. $J^{PC} = 0^{++}$, so that the scalar isoscalar sector (f_0 mesons) could be investigated. Simultaneously to the experimentally observed overpopulation of these states, lattice QCD calculations predict the lightest glueball to have quantum numbers $J^{PC} = 0^{++}$ and a mass around $1.6 - 1.7 \text{ GeV}/c^2$ [61–64]. This makes the study of the reaction $e^+e^- \rightarrow \phi K\bar{K}$ at BESIII particularly interesting. Due to many broad and overlapping resonances in the scalar isoscalar sector, analyticity and unitarity are violated if the dynamical parts of the amplitudes in a partial wave analysis are described by Breit-Wigner amplitudes, as extensively discussed in Chapter 2. Instead, more sophisticated approaches have to be used. An existing formalism based on dispersion theory [65], allowing for the proper description of both the low energy regime ($\sqrt{s} < 1.0 \text{ GeV}$) and the higher resonances between $1.0 \text{ GeV} \leq \sqrt{s} \leq 2.0 \text{ GeV}$ simultaneously, was successfully extended from the three channels $\pi\pi, KK$ and 4π up to five channels including $\eta\eta$ and $\eta\eta'$ and built into the PAWIAN software. Thereby, not only this analysis, but other analyses using PAWIAN can also benefit from this collaboration between experiment and theory.

The final results of the partial wave analysis using the $\psi(2S)$ data were shown in Figure 5.21. Overall, the data is well described by the respective partial wave projections in each of the kinematic variables. However, also suggestions for improvement have been discussed already. First, electromagnetic decays of the $\psi(2S)$ via virtual photons γ^* could be considered which do not require isospin conservation. Thus, processes such as $\psi(2S) \rightarrow \phi a_J$ with $a_J \rightarrow K\bar{K}$ may occur. Unfortunately, the final states $\phi K\bar{K}$ does not allow disentangling isospin contributions why more data is needed, e.g. for the $\phi\pi\pi$ and the $\phi\pi\eta$ channels. Second, purely kinematic effects such as triangle singularities may

influence especially the region at the $K\bar{K}$ threshold if excited kaons in the ϕK system are present, which has to be evaluated in the future.

Comparing the two different final states $\phi K^+ K^-$ and $\phi K_S^0 K_S^0$, a significant difference can be observed especially in the invariant mass distributions of the kaons recoiling off the ϕ meson. As already discussed in Section 5.7, this behavior has also been observed in previous analyses [260, 261] (BESIII internal), which might be due to constructive and destructive interferences between f_J and a_J mesons.

Using the partial wave analysis, an efficiency correction was applied in order to extract the branching fractions $\mathcal{B}r(\psi(2S) \rightarrow \phi K^+ K^-) = (9.58_{-0.14}^{+0.14} \pm 0.45) \cdot 10^{-5}$ and $\mathcal{B}r(\psi(2S) \rightarrow \phi K_S^0 K_S^0) = (3.45_{-0.13}^{+0.14} \pm 0.11) \cdot 10^{-5}$ with the ratio $R_{\mathcal{B}r} = 2.78 \pm 0.12$. Similar to the ratio $R_{\sigma_b} = 3.85 \pm 0.01$ for the Born cross sections in the XYZ regime, also $R_{\mathcal{B}r}$ is in disagreement with the value of two if assuming isospin symmetry. In case of the data at the $\psi(2S)$ resonance, the value is closer to the factor of two because strong decays of the $\psi(2S)$ also occur, whereas the final state is mainly produced by electromagnetic decays at center-of-mass energies in the XYZ region. The result of $\mathcal{B}r(\psi(2S) \rightarrow \phi K^+ K^-)$ was compared to previous results listed in the PDG [56]. In general, the precision is of a factor six times higher. While it is in agreement with the previous CLEO result [264], it deviates from the BES result from 2003 [265]. However, this can be explained by the huge improvements and upgrades made from BES to BESIII, e.g. an increase of the detection efficiency from $(13.4 \pm 1.6)\%$ [265] to $(39.9 \pm 0.3)\%$. The branching fraction $\mathcal{B}r(\psi(2S) \rightarrow \phi K_S^0 K_S^0)$ was determined in this work for the first time ever.

Since many inelasticities are present in the scalar isoscalar sector, such as the opening of other channels ($\pi\pi, KK, 4\pi, \eta\eta, \eta\eta'$), a coupled fit to these channels is sought. The preliminary ϕ , $\phi\pi$, $\pi^+\pi^-$ and $K\pi$ invariant mass spectra for the $\phi\pi^+\pi^-$ channel are shown in Figure 7.1 in the ϕ meson signal region. Compared to $\phi K\bar{K}$, the ϕ meson is observed on top of a non-negligible background. According to the inclusive MC sample, the main contributions are non-resonant $\psi(2S) \rightarrow K^+ K^- \pi^+ \pi^-$, $\psi(2S) \rightarrow K^+ \bar{K}^{*0}(892)\pi^-$ and $\psi(2S) \rightarrow K^- K^{*0}(892)\pi^+$. Especially the excited kaons decaying to $K\pi$ can be observed in Figure 7.1. Such contributions necessarily have to be taken into account in the partial wave analysis. The $\pi^+\pi^-$ system recoiling off the ϕ meson shows a significant resonant structure at the mass of the $f_0(980)$. In a future fit with multiple channels, this will help to better describe the KK system at the KK threshold.

In order to summarize the aforementioned results of the analysis of $e^+e^- \rightarrow \phi K\bar{K}$ and to draw a final conclusion, the two main objectives should be highlighted once again. The Born cross sections of both $e^+e^- \rightarrow \phi K^+ K^-$ and $e^+e^- \rightarrow \phi K_S^0 K_S^0$ have been successfully determined using the high luminosity XYZ data sets of BESIII. No significant couplings of (exotic) vector charmonia to these light hadron channels have been observed, which indicates that they strongly prefer to preserve their charm content in decays, as in charmonium transitions to $\psi(2S)$ or J/ψ under the emission of a $\pi\pi$ pair. This analysis

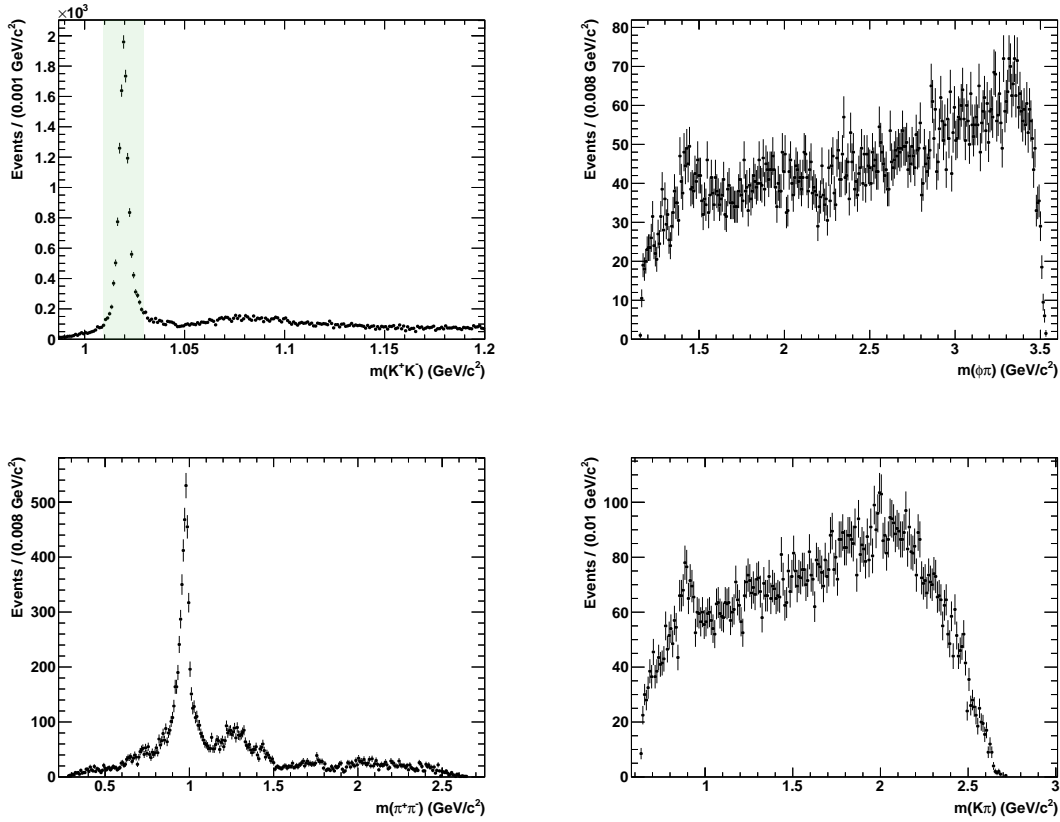


Figure 7.1.: Invariant mass spectra of ϕ (top left), $\phi\pi$ (top right), $\pi^+\pi^-$ (bottom left) and $K\pi$ (bottom right) candidates for the process $e^+e^- \rightarrow \phi\pi^+\pi^-$ at $\sqrt{s} = m_{\psi(2S)}$. The green shaded area denotes the signal region of the ϕ meson where the other spectra have been filled.

thus supports the assumption that exotic vector charmonia have $c\bar{c}$ content [35, 36]. In addition, the data set at $\sqrt{s} = m_{\psi(2S)}$ was investigated to study the scalar isoscalar sector using a partial wave analysis and a newly employed formalism which is in accordance with analyticity and unitarity. The analysis showed a clear discrepancy in the $K\bar{K}$ invariant mass spectra for ϕK^+K^- and $\phi K_S^0 K_S^0$ at $m(K\bar{K}) > 1.5$ GeV, which might be explained with interferences of f_J and a_J contributions. To disentangle these different isospin contributions, a coupled-channel approach has to be performed in the future. However, the partial wave analysis describes the data for both channels accurately, so that an efficiency correction could be applied to extract branching fractions for $\psi(2S) \rightarrow \phi K\bar{K}$. Compared to a previous BES result [265] a slight deviation is observed. This can be explained by the many improvements that have been made to BESIII, including an increase in efficiency through a 4π detector acceptance, as well as improved reconstruction algorithms and particle identification.

$e^+e^- \rightarrow p\bar{p}\eta'$

In the second part of this thesis, the process $e^+e^- \rightarrow p\bar{p}\eta'$ has been studied. The η' meson was reconstructed and significantly observed in its decays $\eta' \rightarrow \eta\pi^+\pi^-$ with $\eta \rightarrow \gamma\gamma$ and $\eta' \rightarrow \gamma\pi^+\pi^-$. While the reconstruction of both decay channels was strongly limited by statistics, the background for $\gamma\pi^+\pi^-$ increased drastically due to the single photon without additional constraints in the kinematic fit as in the case of $\eta\pi^+\pi^-$. Thus, no partial wave analysis could be performed. However, Born cross sections have been determined successfully for the first time in this energy regime. The significance of a coherent resonant contribution of the $\psi(4230)$ to the continuum production of $p\bar{p}\eta'$ was calculated to be 2.43σ . Hence, an upper limits were calculated as $\sigma_{\psi,\text{coh}}^{\text{UL}} = 0.069 \text{ eV}$ and $\sigma_{\psi,\text{incoh}}^{\text{UL}} = 0.0069 \text{ eV}$ for the coherent and incoherent case, respectively.

The results of this work have been compared to the Born cross section of $e^+e^- \rightarrow J/\psi\eta'$ with $J/\psi \rightarrow e^+e^-$ and $J/\psi \rightarrow \mu^+\mu^-$ determined previously by the BESIII collaboration [57]. Their results are in agreement with a resonant contribution of both the $\psi(4160)$ and the $\psi(4230)$, which was then included in the fit model to the Born cross section of $p\bar{p}\eta'$. Ultimately, no distinction between two-body decays into $J/\psi\eta'$ and three-body decays into $p\bar{p}\eta'$ could be made with the data available, limited by the statistical uncertainties. The fixed contribution extracted from a fit to the data of [57] describes the resonant contributions to the Born cross section of $e^+e^- \rightarrow p\bar{p}\eta'$ accurately, which serves as a good cross check for the analysis procedure developed in this work. Hence, the resonant production of the $p\bar{p}\eta'$ final state via the $\psi(4160)$ and the $\psi(4230)$ is assumed to happen solely via intermediate J/ψ resonances, which decay into $p\bar{p}$, indicating again that they strongly prefer to preserve their charm content in decays.

The Born cross sections of $e^+e^- \rightarrow p\bar{p}\eta'$ determined in this work are of special interest for the proton-antiproton annihilation experiment PANDA since the partial width of $\psi \rightarrow p\bar{p}h$, with h being a light unflavored meson, can be related to the production cross section for $p\bar{p} \rightarrow \psi h$. This may serve as information for the PANDA physics program, both to formulate detection strategies and to evaluate luminosity requirements, as well as for detailed detector simulations with theoretically preferred final states. Using an \bar{p} -beam with $p_{\text{max}} = 15 \text{ GeV}/c$, a maximal center-of-mass energy of $\sqrt{s} = 5.5 \text{ GeV}$ will be achieved at PANDA. The rest mass of $\psi(4230)\eta'$ is $m_{\psi(4230)\eta'} = 5.2 \text{ GeV}/c^2$ and thus could be produced in $p\bar{p}$ annihilation processes close to the production threshold. However, Equation (2.36) from [54] is exclusively based on the assumption of three-body decays of possible (exotic) vector charmonia, so that no proper estimates for the production cross section of $p\bar{p} \rightarrow \psi(4230)\eta'$ or $p\bar{p} \rightarrow \psi(4230)\eta'$ could be made in this work. Nevertheless, the analysis procedure developed in this work can be used to make predictions for the production cross section of lighter charmonia, e.g. the $\psi(2S)$ or the $\psi(3770)$ in association with an η' meson. Here, kinematically no decay to $J/\psi\eta'$ is allowed and Equation (2.36) can be employed. In that case, a cross-check with a previous BESIII

analysis of $\psi(3770) \rightarrow p\bar{p}\pi^0$ [272] could be made.

In summary, it should be said that the Born cross section of $e^+e^- \rightarrow p\bar{p}\eta'$ has been successfully determined for all data sets used in this work. Although the inclusion of the lineshape of the process $e^+e^- \rightarrow J/\psi\eta'$ from [57] fully describes the resonant contributions to the Born cross section of $e^+e^- \rightarrow p\bar{p}\eta'$, this process can not be significantly observed due to the total uncertainty of this measurement. However, the elaborated analysis strategy can be applied to the data set at $\sqrt{s} = m_{\psi(2S)}$ in order to make predictions on the production cross section of $p\bar{p} \rightarrow \psi(2S)\eta'$.

A. Appendix

A.1. The Least-Squares Method

The purpose of this section is to give an overview of the most commonly used method for parameter estimation, the so-called Least-Squares (LS) method. The following discussion mainly follows the ideas from [273].

Assume a set of N independent, experimental values y_1, y_2, \dots, y_N measured at the points x_1, x_2, \dots, x_N . A theoretical model exists, which predicts the true values $\eta_1, \eta_2, \dots, \eta_N$ of the observables y_i associated with each x_i through the functional dependence

$$f_i = f_i(\theta_1, \theta_2, \dots, \theta_L; x_i), \quad (\text{A.1})$$

with θ_i being a set of L a priori unknown parameters with $L \leq N$. The LS principle states that the best set of values $\hat{\theta} = \{\hat{\theta}_1, \hat{\theta}_2, \dots, \hat{\theta}_L\}$ of the parameters θ_i are those that minimizes

$$X^2 = \sum_{i=1}^N w_i (y_i - f_i)^2, \quad (\text{A.2})$$

with w_i being the weight assigned to the i -th observation. It expresses the accuracy in the measurement y_i . In case that all observations are equally accurate $w_i = 1$. If the uncertainty σ_i is different but known for each y_i the weight is usually set to $w_i = 1/\sigma_i^2$. In general, the observations may be correlated, with uncertainties and covariance terms given by the symmetric covariance matrix $V(y)$. Equation (A.2) then reads

$$X^2 = \sum_{i=1}^N \sum_{j=1}^N (y_i - f_i) V_{ij}^2 (y_j - f_j). \quad (\text{A.3})$$

It should be noted that the LS method is applicable regardless of the underlying distribution of the observed variables. If they are normally distributed, the minimum value X_{\min}^2 will be distributed as a χ^2 variable. The fit quality can then be evaluated based on the properties of a χ^2 distribution.

In principle, a distinction can be made between the two cases in which the theoretical model implies either a linear dependence (and, incidentally, no dependence of the weights on the parameters) or a non-linear dependence of the parameters. In the first case, the LS method provides an exact, unbiased solution for the parameters θ_i with minimum

variance.

Generally however, when the predicted values f_i have a non-linear dependence on the parameters, it is not possible to give an exact solution as in the linear case, but one has to perform the minimization by an iterative approach, e.g. the Newton's method.

A.1.1. Least-Squares Fit

The LS principle provides a prescription for how to find the best values of some unknown parameters θ . They are linked to the true observables η through the functional dependence f . However, the unknowns are often actually the observables η , although directly measurable. In an LS fit, the observations y with covariance matrix $V(y)$ may be taken as the initial estimate of the unknown η . Thus, the best estimate of η are those values which minimize

$$X^2 = \varepsilon^T V^{-1} \varepsilon, \quad (\text{A.4})$$

with $\varepsilon = y - \eta$ being the difference between the measured and true values. Accordingly, after the minimization, the final estimates $\hat{\eta}$ of the true η are called the *improved measurements*, or *fitted variables*, and the *residuals* $\hat{\varepsilon} = y - \hat{\eta}$ can be defined. The *weighted sum of squared residuals*, which is the minimum value obtained for X^2 in the fit, is then given as

$$X_{\min}^2 = \hat{\varepsilon}^T V^{-1} \hat{\varepsilon} = (y - \hat{\eta})^T V^{-1} (y - \hat{\eta}). \quad (\text{A.5})$$

So far, no assumptions have been made about the distribution of ε . In case that the uncorrelated ε_i are normally distributed centered at $x = 0$ with width σ_i^2 , the N measurements y_i are independent and normally distributed with mean η_i and width σ_i^2 . Hence, the quantity

$$X^2 = \sum_{i=1}^N \left(\frac{\varepsilon_i}{\sigma_i} \right)^2 = \sum_{i=1}^N \left(\frac{y_i - \eta_i}{\sigma_i} \right)^2 \quad (\text{A.6})$$

is a sum of N independent squared standard normal variables and thus equal to a chi-square variable with N degrees of freedom. Here, the estimated values $\hat{\eta}_i$ as obtained from the minimization instead of the unknown η_i can be used, leading to the weighted sum of squared residuals

$$X_{\min}^2 = \sum_{i=1}^N \left(\frac{\hat{\varepsilon}_i}{\sigma_i} \right)^2 = \sum_{i=1}^N \left(\frac{y_i - \hat{\eta}_i}{\sigma_i} \right)^2. \quad (\text{A.7})$$

Analogously, it can be shown that X_{\min}^2 is equal to a sum of $(N-L)$ independent squared standard normal variables and thus a chi-square variable with $(N-L)$ degrees of freedom. Note that this only applies to linear LS estimators. For a discussion of non-linear cases we refer to [273].

A.1.2. Goodness of Fit

Since the weighted sum of squared residuals X_{\min}^2 in Equation (A.7) for normally distributed measurements y_i follows a chi-square distribution, it provides a measure of the *goodness of fit*. In case of ν degrees of freedom (also called ν -constrained fit) the chi-square probability P_{χ^2} corresponding to the contents of the chi-square p. d. f $f(u; \nu)$ between the values $u = X_{\min}^2$ and $u = \infty$ can be obtained as

$$P_{\chi^2} = \int_{X_{\min}^2}^{\infty} f(u; \nu) du = 1 - F(X_{\min}^2; \nu), \quad (\text{A.8})$$

with $F(X_{\min}^2; \nu)$ being the cumulative chi-square distribution for ν degrees of freedom. P_{χ^2} corresponds to the probability for obtaining a higher value for X_{\min}^2 if a new minimization with similar measurements and the same model is performed. It follows that a large value for P_{χ^2} (corresponding to a small X_{\min}^2) means a good fit and vice versa.

However, a large value of X_{\min}^2 need not necessarily be due to an incorrect fit model, but may be due to a large contribution from a few of the N measurements. In such cases an investigation of the residuals $\hat{\varepsilon} = y_i - \hat{\eta}_i$ is helpful. In order to allow for different accuracies, the examination of the fit should be done in terms of the *pull*

$$z_i = \frac{\hat{\varepsilon}_i}{\sigma(\hat{\varepsilon}_i)}, \quad (\text{A.9})$$

which takes the standard deviation $\sigma(\hat{\varepsilon}_i)$ into account. If the observations are uncorrelated (note that y_i and $\hat{\eta}_i$ are fully, positively correlated), one can write

$$\begin{aligned} \sigma^2(\hat{\varepsilon}_i) &= V_{ii}(y - \hat{\eta}) = V_{ii}(y) - 2 \text{cov}(y, \hat{\eta})_{ii} + V_{ii}(\hat{\eta}) \\ &= V_{ii}(y) - V_{ii}(\hat{\eta}). \end{aligned} \quad (\text{A.10})$$

This leads to the i -th pull, which is in agreement with Equation (4.15):

$$z_i = \frac{y_i - \hat{\eta}_i}{\sqrt{\sigma^2(y_i) - \sigma^2(\hat{\eta}_i)}}. \quad (\text{A.11})$$

It is assumed to follow a Gaussian distribution with unit width centered at $x = 0$. A shift relatively to zero indicates a bias in the i -th observation, whereas a substantially broader (narrower) width indicates that the error in the i -th observation has probably consistently been taken too small (large).

In particle physics, the observables η in an LS estimation are usually connected by constraints, e.g. by energy and momentum conservation. In such cases, different approaches can be used to solve the new minimization problem. One approach is the method of *Lagrangian multipliers*, where the constrained X^2 minimization is reformulated

into an unconstrained minimization by increasing the number of unknowns by adding a set of Lagrange multipliers corresponding to the number of constraints. This method is used in the kinematic fit in BESIII [234].

A.2. Results for $e^+e^- \rightarrow \phi K^+K^-$, $e^+e^- \rightarrow \phi K_S^0 K_S^0$ and $e^+e^- \rightarrow p\bar{p}\eta'$

Table A.1.: Systematic uncertainties in % for each center-of-mass energy \sqrt{s} for the reaction $e^+e^- \rightarrow \phi K^+K^-$ obtained from this analysis due to the choice of the background shape f_{Bkg} and the selection condition on the χ_{4C}^2 value, as well as the total uncorrelated systematic uncertainty, including luminosity and tracking efficiency from Table 5.2.

\sqrt{s} / GeV	f_{Bkg}	χ_{4C}^2	Total	\sqrt{s} / GeV	f_{Bkg}	χ_{4C}^2	Total
3.7730	1.84	0.26	4.52	4.3121	0.18	0.92	4.23
3.8695	2.44	0.68	4.84	4.3374	1.00	0.52	4.28
4.0076	1.65	0.65	4.49	4.3583	0.09	0.30	4.13
4.1285	0.31	0.82	4.21	4.3774	0.50	0.81	4.23
4.1574	0.16	0.42	4.15	4.3964	0.13	0.82	4.21
4.1784	0.39	0.14	4.14	4.4156	0.39	0.61	4.19
4.1888	0.15	0.53	4.16	4.4362	0.06	1.14	4.28
4.1989	0.46	0.26	4.16	4.4671	2.03	0.41	4.62
4.2091	0.07	0.54	4.16	4.5271	2.25	0.51	4.73
4.2187	0.49	0.70	4.21	4.5995	0.17	0.75	4.19
4.2263	0.53	0.41	4.18	4.6151	1.82	1.79	4.85
4.2357	0.19	0.36	4.14	4.6304	0.25	0.88	4.22
4.2438	0.53	0.44	4.18	4.6431	0.09	0.87	4.22
4.2580	0.29	0.56	4.17	4.6639	0.94	0.49	4.26
4.2666	0.49	0.50	4.18	4.6842	0.49	0.56	4.19
4.2776	0.17	0.85	4.21	4.7008	0.99	0.94	4.34
4.2879	0.86	0.59	4.25				

Table A.2.: Center-of-mass energies \sqrt{s} , luminosities L , number of observed events N_{obs} , efficiencies ε , radiation correction factors $(1 + \delta_r)$, vacuum polarization correction factors $(1 + \delta_v)$ and calculated Born cross sections σ_b for the process $e^+e^- \rightarrow \phi K^+ K^-$, including lower and upper statistical as well as systematic uncertainties.

\sqrt{s} / GeV	L / pb $^{-1}$	N_{obs}	ε / %	$(1 + \delta_r)$	$(1 + \delta_v)$	σ_b / pb
3.7730	2931.8	7329.2 $^{+94.6}_{-92.9}$	35.8 \pm 0.2	0.8295	1.0560	16.19 $^{+0.24}_{-0.23}$ \pm 0.73
3.8695	224.0	452.5 $^{+24.1}_{-22.4}$	34.7 \pm 0.2	0.8889	1.0506	12.68 $^{+0.68}_{-0.63}$ \pm 0.61
4.0076	482.0	825.3 $^{+32.5}_{-30.8}$	33.7 \pm 0.2	0.9390	1.0441	10.53 $^{+0.43}_{-0.41}$ \pm 0.47
4.1285	401.5	590.3 $^{+27.4}_{-25.7}$	32.4 \pm 0.2	0.9675	1.0525	9.06 $^{+0.43}_{-0.41}$ \pm 0.38
4.1574	408.7	633.9 $^{+28.4}_{-26.7}$	32.4 \pm 0.2	0.9739	1.0533	9.48 $^{+0.44}_{-0.41}$ \pm 0.39
4.1784	3189.0	4572.5 $^{+74.9}_{-73.2}$	32.6 \pm 0.2	0.9783	1.0541	8.67 $^{+0.17}_{-0.17}$ \pm 0.36
4.1888	524.6	754.9 $^{+30.9}_{-29.2}$	32.6 \pm 0.2	0.9801	1.0558	8.68 $^{+0.37}_{-0.35}$ \pm 0.36
4.1989	526.0	785.2 $^{+31.6}_{-29.9}$	32.3 \pm 0.2	0.9823	1.0564	9.05 $^{+0.38}_{-0.36}$ \pm 0.38
4.2091	518.0	694.2 $^{+29.6}_{-27.9}$	31.6 \pm 0.2	0.9846	1.0568	8.28 $^{+0.37}_{-0.35}$ \pm 0.34
4.2187	514.6	673.6 $^{+29.2}_{-27.5}$	32.1 \pm 0.2	0.9866	1.0563	7.94 $^{+0.36}_{-0.34}$ \pm 0.33
4.2263	1056.4	1390.2 $^{+41.6}_{-39.9}$	33.1 \pm 0.2	0.9882	1.0564	7.74 $^{+0.25}_{-0.24}$ \pm 0.32
4.2357	530.3	715.6 $^{+30.1}_{-28.4}$	32.2 \pm 0.2	0.9902	1.0555	8.14 $^{+0.35}_{-0.34}$ \pm 0.34
4.2438	538.1	659.4 $^{+29.4}_{-27.7}$	32.1 \pm 0.2	0.9919	1.0555	7.42 $^{+0.34}_{-0.32}$ \pm 0.31
4.2580	828.4	978.9 $^{+35.4}_{-33.6}$	32.9 \pm 0.2	0.9951	1.0536	6.96 $^{+0.26}_{-0.25}$ \pm 0.29
4.2666	531.1	697.3 $^{+29.7}_{-28.0}$	32.7 \pm 0.2	0.9970	1.0532	7.76 $^{+0.34}_{-0.32}$ \pm 0.32
4.2776	175.7	241.6 $^{+17.5}_{-15.8}$	31.4 \pm 0.2	0.9990	1.0530	8.47 $^{+0.62}_{-0.56}$ \pm 0.36
4.2879	502.4	577.7 $^{+27.2}_{-25.5}$	31.4 \pm 0.2	1.0010	1.0527	7.07 $^{+0.34}_{-0.32}$ \pm 0.30
4.3121	501.2	583.1 $^{+27.5}_{-25.7}$	31.9 \pm 0.2	1.0056	1.0522	7.00 $^{+0.34}_{-0.32}$ \pm 0.30
4.3374	505.0	556.2 $^{+26.5}_{-24.8}$	31.0 \pm 0.2	1.0105	1.0508	6.81 $^{+0.33}_{-0.31}$ \pm 0.29
4.3583	543.9	604.6 $^{+27.6}_{-25.9}$	33.1 \pm 0.2	1.0141	1.0511	6.41 $^{+0.30}_{-0.28}$ \pm 0.27
4.3774	522.7	593.3 $^{+27.5}_{-25.8}$	32.4 \pm 0.2	1.0177	1.0513	6.65 $^{+0.32}_{-0.30}$ \pm 0.28
4.3964	507.8	530.2 $^{+26.1}_{-24.4}$	32.0 \pm 0.2	1.0214	1.0510	6.17 $^{+0.31}_{-0.29}$ \pm 0.26
4.4156	1043.9	1114.1 $^{+37.3}_{-35.6}$	32.4 \pm 0.2	1.0244	1.0524	6.21 $^{+0.22}_{-0.21}$ \pm 0.26
4.4362	569.9	619.2 $^{+28.2}_{-26.5}$	32.5 \pm 0.2	1.0275	1.0537	6.27 $^{+0.29}_{-0.28}$ \pm 0.27
4.4671	111.1	93.4 $^{+11.6}_{-9.9}$	32.6 \pm 0.2	1.0325	1.0548	4.81 $^{+0.60}_{-0.51}$ \pm 0.22
4.5271	112.1	97.8 $^{+11.5}_{-9.8}$	33.2 \pm 0.2	1.0427	1.0545	4.86 $^{+0.57}_{-0.49}$ \pm 0.23
4.5995	586.9	533.4 $^{+26.0}_{-24.3}$	32.2 \pm 0.2	1.0543	1.0546	5.16 $^{+0.26}_{-0.24}$ \pm 0.22
4.6151	102.5	69.3 $^{+9.9}_{-8.2}$	32.7 \pm 0.2	1.0569	1.0545	3.77 $^{+0.54}_{-0.45}$ \pm 0.18
4.6304	511.1	424.3 $^{+23.5}_{-21.8}$	32.4 \pm 0.2	1.0592	1.0544	4.66 $^{+0.26}_{-0.24}$ \pm 0.20
4.6431	541.4	407.0 $^{+23.0}_{-21.3}$	31.9 \pm 0.2	1.0612	1.0544	4.28 $^{+0.24}_{-0.23}$ \pm 0.18
4.6639	523.6	398.5 $^{+22.7}_{-21.0}$	31.9 \pm 0.2	1.0644	1.0544	4.32 $^{+0.25}_{-0.23}$ \pm 0.18
4.6842	1631.7	1295.0 $^{+40.5}_{-38.7}$	32.0 \pm 0.2	1.0677	1.0545	4.48 $^{+0.14}_{-0.14}$ \pm 0.19
4.7008	526.2	389.6 $^{+22.7}_{-21.0}$	31.9 \pm 0.2	1.0704	1.0545	4.18 $^{+0.24}_{-0.23}$ \pm 0.18

Table A.3.: Systematic uncertainties in % for each center-of-mass energy \sqrt{s} for the reaction $e^+e^- \rightarrow \phi K_S^0 K_S^0$ obtained from this analysis due to the selection condition on the χ_{6C}^2 value and the K_S^0 reconstruction efficiency, as well as the total uncorrelated systematic uncertainty, including luminosity and tracking efficiency from Table 5.2.

\sqrt{s} / GeV	χ_{6C}^2	K_S^0	Total	\sqrt{s} / GeV	χ_{6C}^2	K_S^0	Total
3.7730	0.23	2.11	3.08	4.3121	0.53	1.97	3.03
3.8695	0.54	2.00	3.05	4.3374	0.59	1.96	3.03
4.0076	0.31	1.99	3.01	4.3583	0.46	1.97	3.01
4.1285	0.56	1.98	3.04	4.3774	0.51	1.96	3.02
4.1574	0.41	1.97	3.01	4.3964	0.58	1.96	3.03
4.1784	0.16	1.98	2.99	4.4156	0.46	1.96	3.01
4.1888	0.49	1.98	3.02	4.4362	0.44	1.97	3.01
4.1989	0.52	1.97	3.03	4.4671	0.58	1.96	3.03
4.2091	0.47	1.98	3.02	4.5271	0.57	1.96	3.03
4.2187	0.15	1.98	2.99	4.5995	0.52	1.94	3.01
4.2263	0.56	1.98	3.04	4.6151	0.51	1.94	3.01
4.2357	0.54	1.98	3.03	4.6304	0.51	1.95	3.01
4.2438	0.50	1.97	3.03	4.6431	0.50	1.93	3.00
4.2580	0.31	1.97	3.00	4.6639	0.56	1.94	3.01
4.2666	0.38	1.97	3.00	4.6842	0.37	1.92	2.97
4.2776	0.59	1.97	3.04	4.7008	0.62	1.93	3.01
4.2879	0.46	1.96	3.01				

Table A.4.: Center-of-mass energies \sqrt{s} , luminosities L , number of observed events N_{obs} , efficiencies ε , radiation correction factors $(1 + \delta_r)$, vacuum polarization correction factors $(1 + \delta_v)$ and calculated Born cross sections σ_b for the process $e^+e^- \rightarrow \phi K_S^0 K_S^0$, including lower and upper statistical as well as systematic uncertainties.

\sqrt{s} / GeV	L / pb $^{-1}$	N_{obs}	ε / %	$(1 + \delta_r)$	$(1 + \delta_v)$	σ_b / pb
3.7730	2931.8	$360.8^{+20.9}_{-19.2}$	18.0 ± 0.1	0.8281	1.0560	$3.31^{+0.19}_{-0.18} \pm 0.10$
3.8695	224.0	$27.1^{+5.9}_{-4.3}$	17.6 ± 0.1	0.8864	1.0506	$3.14^{+0.69}_{-0.50} \pm 0.10$
4.0076	482.0	$56.6^{+8.2}_{-6.6}$	16.2 ± 0.2	0.9346	1.0441	$3.16^{+0.46}_{-0.37} \pm 0.09$
4.1285	401.5	$34.7^{+6.6}_{-5.0}$	15.8 ± 0.1	0.9611	1.0525	$2.30^{+0.44}_{-0.33} \pm 0.07$
4.1574	408.7	$27.1^{+5.9}_{-4.3}$	15.2 ± 0.1	0.9667	1.0533	$1.82^{+0.40}_{-0.29} \pm 0.05$
4.1784	3189.0	$289.6^{+18.6}_{-16.9}$	15.9 ± 0.1	0.9710	1.0541	$2.37^{+0.16}_{-0.14} \pm 0.07$
4.1888	524.6	$49.9^{+7.7}_{-6.1}$	16.1 ± 0.2	0.9727	1.0558	$2.44^{+0.38}_{-0.30} \pm 0.07$
4.1989	526.0	$42.3^{+7.2}_{-5.6}$	15.9 ± 0.1	0.9746	1.0564	$2.09^{+0.35}_{-0.28} \pm 0.06$
4.2091	518.0	$47.1^{+7.5}_{-5.9}$	16.2 ± 0.1	0.9765	1.0568	$2.31^{+0.37}_{-0.29} \pm 0.07$
4.2187	514.6	$48.0^{+7.6}_{-6.0}$	16.0 ± 0.1	0.9784	1.0563	$2.39^{+0.38}_{-0.30} \pm 0.07$
4.2263	1056.4	$79.4^{+9.5}_{-7.9}$	16.0 ± 0.1	0.9798	1.0564	$1.92^{+0.23}_{-0.19} \pm 0.06$
4.2357	530.3	$51.8^{+7.8}_{-6.3}$	16.5 ± 0.2	0.9820	1.0555	$2.43^{+0.37}_{-0.30} \pm 0.07$
4.2438	538.1	$35.7^{+6.7}_{-5.1}$	15.8 ± 0.1	0.9832	1.0555	$1.72^{+0.32}_{-0.25} \pm 0.05$
4.2580	828.4	$69.9^{+9.0}_{-7.4}$	16.1 ± 0.1	0.9867	1.0536	$2.14^{+0.28}_{-0.23} \pm 0.06$
4.2666	531.1	$33.8^{+6.5}_{-4.9}$	16.0 ± 0.1	0.9882	1.0532	$1.62^{+0.31}_{-0.24} \pm 0.05$
4.2776	175.7	$13.8^{+4.5}_{-2.9}$	17.0 ± 0.2	0.9898	1.0530	$1.88^{+0.61}_{-0.40} \pm 0.06$
4.2879	502.4	$37.6^{+6.8}_{-5.2}$	15.7 ± 0.1	0.9918	1.0527	$1.94^{+0.35}_{-0.27} \pm 0.06$
4.3121	501.2	$35.7^{+6.7}_{-5.1}$	15.8 ± 0.1	0.9955	1.0522	$1.82^{+0.34}_{-0.26} \pm 0.06$
4.3374	505.0	$25.2^{+5.7}_{-4.2}$	14.9 ± 0.1	1.0001	1.0508	$1.36^{+0.31}_{-0.22} \pm 0.04$
4.3583	543.9	$45.2^{+7.4}_{-5.8}$	16.7 ± 0.2	1.0032	1.0511	$2.01^{+0.33}_{-0.26} \pm 0.06$
4.3774	522.7	$41.4^{+7.1}_{-5.5}$	16.1 ± 0.1	1.0063	1.0513	$1.98^{+0.34}_{-0.27} \pm 0.06$
4.3964	507.8	$33.8^{+6.5}_{-4.9}$	16.0 ± 0.1	1.0094	1.0510	$1.67^{+0.32}_{-0.24} \pm 0.05$
4.4156	1043.9	$75.6^{+9.3}_{-7.7}$	16.7 ± 0.1	1.0118	1.0524	$1.72^{+0.21}_{-0.18} \pm 0.05$
4.4362	569.9	$32.8^{+6.4}_{-4.8}$	15.6 ± 0.1	1.0147	1.0537	$1.47^{+0.29}_{-0.22} \pm 0.04$
4.4671	111.1	$8.1^{+3.7}_{-2.1}$	18.7 ± 0.2	1.0193	1.0548	$1.55^{+0.69}_{-0.40} \pm 0.05$
4.5271	112.1	$3.4^{+2.7}_{-1.2}$	18.0 ± 0.2	1.0282	1.0545	$0.66^{+0.52}_{-0.22} \pm 0.02$
4.5995	586.9	$30.0^{+6.2}_{-4.6}$	16.5 ± 0.1	1.0382	1.0546	$1.20^{+0.25}_{-0.18} \pm 0.04$
4.6151	102.5	$4.3^{+2.9}_{-1.4}$	16.9 ± 0.1	1.0403	1.0545	$0.97^{+0.65}_{-0.31} \pm 0.03$
4.6304	511.1	$21.4^{+5.4}_{-3.8}$	15.5 ± 0.1	1.0424	1.0544	$1.04^{+0.26}_{-0.18} \pm 0.03$
4.6431	541.4	$19.5^{+5.2}_{-3.6}$	16.0 ± 0.1	1.0440	1.0544	$0.87^{+0.23}_{-0.16} \pm 0.03$
4.6639	523.6	$31.9^{+6.3}_{-4.8}$	15.6 ± 0.1	1.0466	1.0544	$1.50^{+0.30}_{-0.23} \pm 0.05$
4.6842	1631.7	$61.3^{+8.5}_{-6.9}$	15.3 ± 0.1	1.0492	1.0545	$0.94^{+0.13}_{-0.11} \pm 0.03$
4.7008	526.2	$22.4^{+5.5}_{-3.9}$	14.0 ± 0.1	1.0515	1.0545	$1.16^{+0.28}_{-0.20} \pm 0.04$

Table A.5.: Center-of-mass energies \sqrt{s} , radiation correction factors $(1 + \delta_r)$, number of observed events N_i , efficiencies ε_i , and combined Born cross sections σ_b for the process $e^+e^- \rightarrow p\bar{p}\eta'$ with $\eta' \rightarrow \eta\pi^+\pi^-$ (1) and $\eta' \rightarrow \gamma\pi^+\pi^-$ (2), including combined statistical and systematic uncertainties.

\sqrt{s} / GeV	$(1 + \delta_r)$	N_1	ε_1 / %	N_2	ε_2 / %	σ_b / pb
3.7730	0.8244	$5.3^{+6.7}_{-5.0}$	23.4 ± 0.1	$10.1^{+16.5}_{-14.8}$	31.5 ± 0.1	$0.35^{+0.04}_{-0.04}$
4.0076	0.9134	$1.5^{+2.6}_{-1.0}$	21.9 ± 0.1	$4.0^{+6.0}_{-4.4}$	29.0 ± 0.1	$0.31^{+0.07}_{-0.06}$
4.1285	0.9227	$2.3^{+3.3}_{-1.7}$	21.2 ± 0.1	$3.1^{+5.2}_{-3.5}$	28.1 ± 0.1	$0.34^{+0.09}_{-0.06}$
4.1574	0.9185	$1.8^{+2.8}_{-1.3}$	21.6 ± 0.1	$3.0^{+5.0}_{-3.3}$	28.3 ± 0.1	$0.26^{+0.09}_{-0.05}$
4.1784	0.9100	$6.7^{+7.9}_{-6.3}$	21.5 ± 0.1	$8.4^{+11.8}_{-10.1}$	28.3 ± 0.1	$0.33^{+0.03}_{-0.03}$
4.1888	0.9033	$2.7^{+3.5}_{-2.0}$	21.9 ± 0.1	$3.7^{+6.1}_{-4.4}$	28.7 ± 0.1	$0.36^{+0.08}_{-0.06}$
4.1989	0.8981	$2.1^{+3.3}_{-1.7}$	22.5 ± 0.1	$5.2^{+6.7}_{-5.1}$	29.2 ± 0.1	$0.50^{+0.07}_{-0.07}$
4.2092	0.9045	$2.9^{+3.7}_{-2.2}$	21.6 ± 0.1	$3.2^{+5.3}_{-3.6}$	28.8 ± 0.1	$0.36^{+0.07}_{-0.06}$
4.2187	0.9418	$2.3^{+3.3}_{-1.7}$	21.7 ± 0.1	$3.9^{+5.7}_{-4.0}$	27.8 ± 0.1	$0.34^{+0.08}_{-0.05}$
4.2263	0.9905	$2.7^{+3.9}_{-2.2}$	21.7 ± 0.1	$5.8^{+8.0}_{-6.3}$	27.5 ± 0.1	$0.30^{+0.04}_{-0.04}$
4.2357	1.0295	$2.2^{+3.2}_{-1.7}$	20.9 ± 0.1	$2.9^{+5.3}_{-3.6}$	26.2 ± 0.1	$0.22^{+0.06}_{-0.04}$
4.2438	1.0352	$1.7^{+2.7}_{-1.2}$	20.3 ± 0.1	$2.3^{+4.8}_{-3.2}$	25.5 ± 0.1	$0.14^{+0.06}_{-0.03}$
4.2580	1.0231	$2.5^{+3.6}_{-2.0}$	20.5 ± 0.1	$3.7^{+6.0}_{-4.3}$	26.1 ± 0.1	$0.20^{+0.05}_{-0.03}$
4.2668	1.0140	$2.2^{+3.0}_{-1.5}$	20.3 ± 0.1	$3.4^{+5.5}_{-3.8}$	26.0 ± 0.1	$0.26^{+0.07}_{-0.04}$
4.2777	1.0045	$2.0^{+2.8}_{-1.3}$	20.1 ± 0.1	$2.2^{+3.7}_{-2.2}$	25.9 ± 0.1	$0.51^{+0.13}_{-0.11}$
4.2879	0.9981	$1.9^{+2.9}_{-1.4}$	19.8 ± 0.1	$3.4^{+5.3}_{-3.7}$	26.2 ± 0.1	$0.25^{+0.07}_{-0.05}$
4.3121	0.9882	$1.9^{+3.0}_{-1.4}$	20.1 ± 0.1	$3.7^{+5.4}_{-3.7}$	26.4 ± 0.1	$0.30^{+0.07}_{-0.05}$
4.3374	0.9831	$1.5^{+2.4}_{-0.9}$	20.6 ± 0.1	$2.9^{+4.8}_{-3.1}$	26.9 ± 0.1	$0.17^{+0.06}_{-0.04}$
4.3583	0.9807	$1.1^{+2.2}_{-0.8}$	21.1 ± 0.1	$3.5^{+5.5}_{-3.9}$	27.4 ± 0.1	$0.19^{+0.05}_{-0.05}$
4.3774	0.9796	$2.2^{+3.1}_{-1.6}$	20.6 ± 0.1	$3.8^{+5.5}_{-3.9}$	26.9 ± 0.1	$0.31^{+0.07}_{-0.05}$
4.3965	0.9792	$1.6^{+2.6}_{-1.0}$	20.6 ± 0.1	$0.0^{+3.8}_{-50.5}$	27.2 ± 0.1	$0.10^{+0.04}_{-0.03}$
4.4156	0.9785	$2.9^{+3.8}_{-2.2}$	21.0 ± 0.1	$5.7^{+7.7}_{-6.1}$	27.2 ± 0.1	$0.32^{+0.04}_{-0.04}$
4.4362	0.9787	$2.3^{+3.2}_{-1.6}$	20.9 ± 0.1	$2.4^{+4.2}_{-2.6}$	27.2 ± 0.1	$0.19^{+0.05}_{-0.04}$
4.5271	0.9819	$0.9^{+2.0}_{-0.5}$	21.2 ± 0.1	$1.5^{+2.8}_{-1.4}$	27.4 ± 0.1	$0.23^{+0.18}_{-0.07}$
4.5995	0.9854	$2.0^{+2.8}_{-1.3}$	21.3 ± 0.1	$3.4^{+5.0}_{-3.4}$	27.2 ± 0.1	$0.21^{+0.06}_{-0.04}$
4.6304	0.9870	$2.1^{+2.9}_{-1.4}$	20.4 ± 0.1	$2.7^{+4.5}_{-2.9}$	26.9 ± 0.1	$0.20^{+0.06}_{-0.04}$
4.6431	0.9874	$2.7^{+3.5}_{-2.0}$	20.7 ± 0.1	$3.6^{+5.2}_{-3.6}$	27.1 ± 0.1	$0.33^{+0.06}_{-0.05}$
4.6639	0.9886	$1.2^{+2.1}_{-0.6}$	20.7 ± 0.1	$3.2^{+4.8}_{-3.2}$	26.8 ± 0.1	$0.17^{+0.05}_{-0.04}$
4.6842	0.9897	$3.0^{+3.9}_{-2.3}$	20.7 ± 0.1	$5.5^{+7.7}_{-6.0}$	27.2 ± 0.1	$0.19^{+0.03}_{-0.03}$
4.7008	0.9904	$2.2^{+3.5}_{-1.5}$	20.8 ± 0.1	$3.7^{+5.2}_{-3.5}$	26.9 ± 0.1	$0.30^{+0.07}_{-0.05}$

A.3. Invariant Mass Spectra of ϕ Meson Candidates for

$$e^+e^- \rightarrow \phi K^+K^-$$

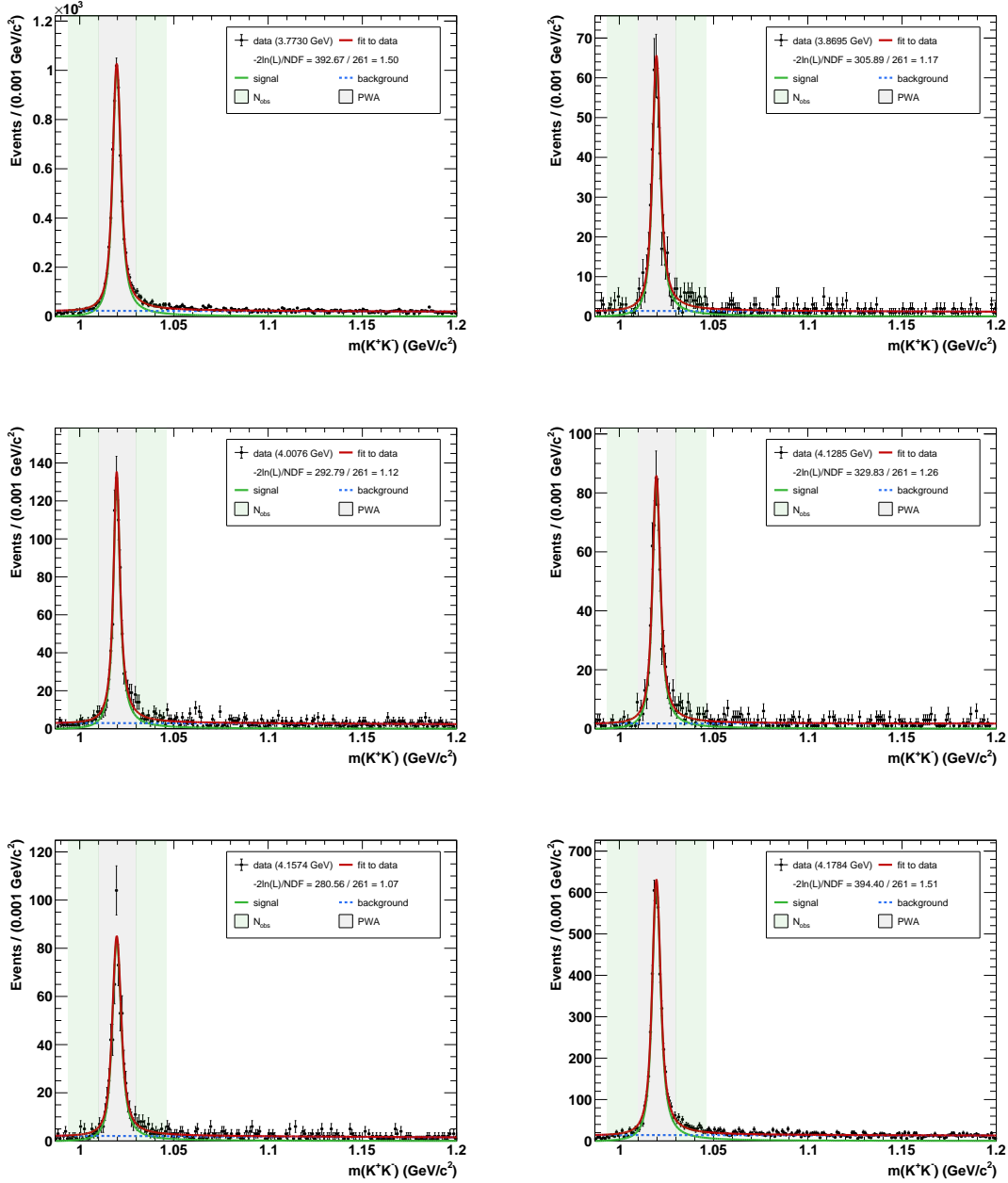


Figure A.1.: Invariant mass spectrum of ϕ candidates for data from $\sqrt{s} = 3.7730$ GeV to $\sqrt{s} = 4.1784$ GeV. A fit (red line) with a Breit-Wigner function convolved with a Gaussian function as signal (green line) and a first-order polynomial as background (dashed blue line) is applied. The green and blue shaded areas depict the signal regions in which the number of observed events N_{obs} is extracted and for which a PWA is performed to determine a global efficiency, respectively.

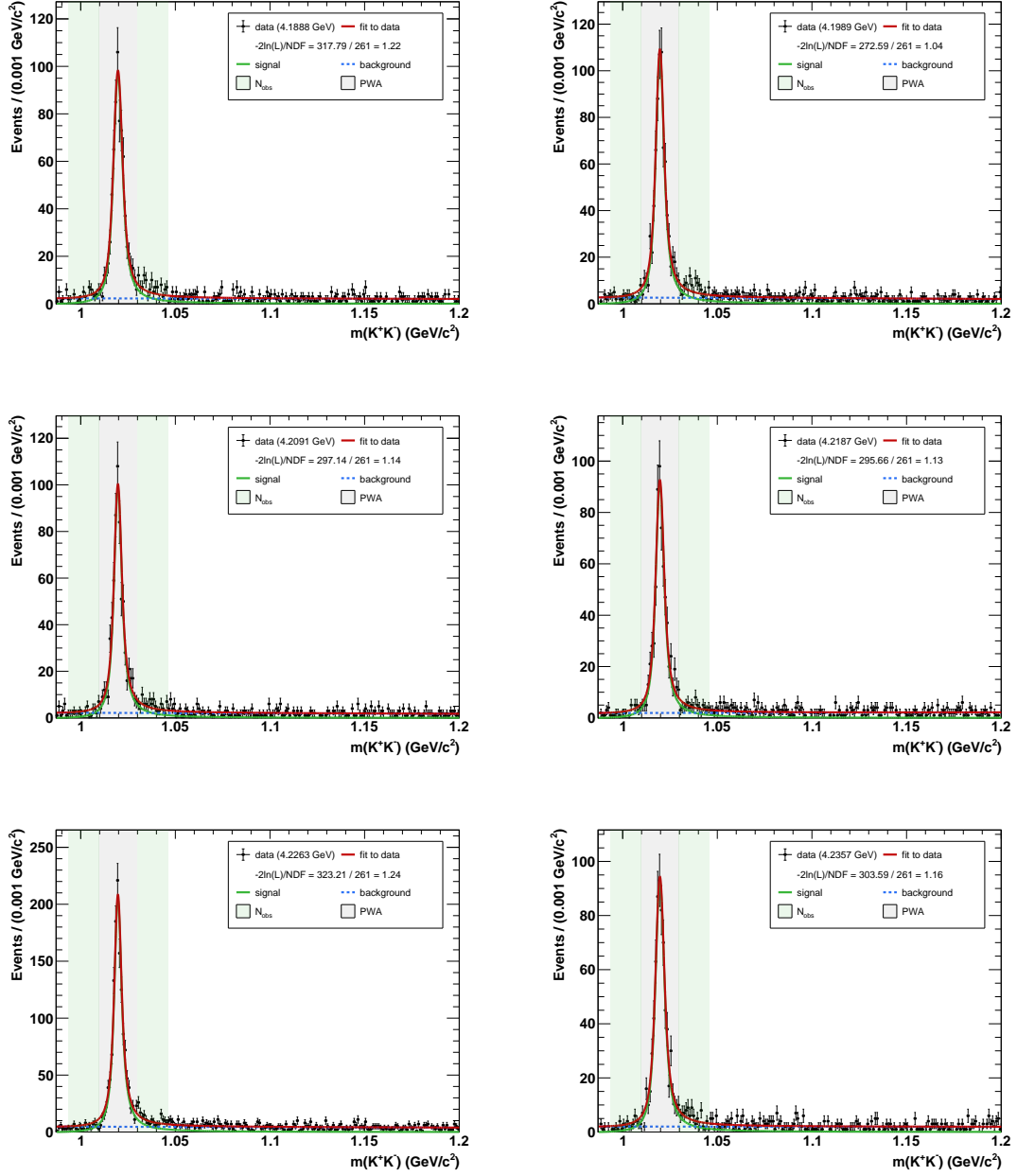


Figure A.2.: Invariant mass spectrum of ϕ candidates for data from $\sqrt{s} = 4.1888\text{ GeV}$ to $\sqrt{s} = 4.2357\text{ GeV}$. A fit (red line) with a Breit-Wigner function convolved with a Gaussian function as signal (green line) and a first-order polynomial as background (dashed blue line) is applied. The green and blue shaded areas depict the signal regions in which the number of observed events N_{obs} is extracted and for which a PWA is performed to determine a global efficiency, respectively.

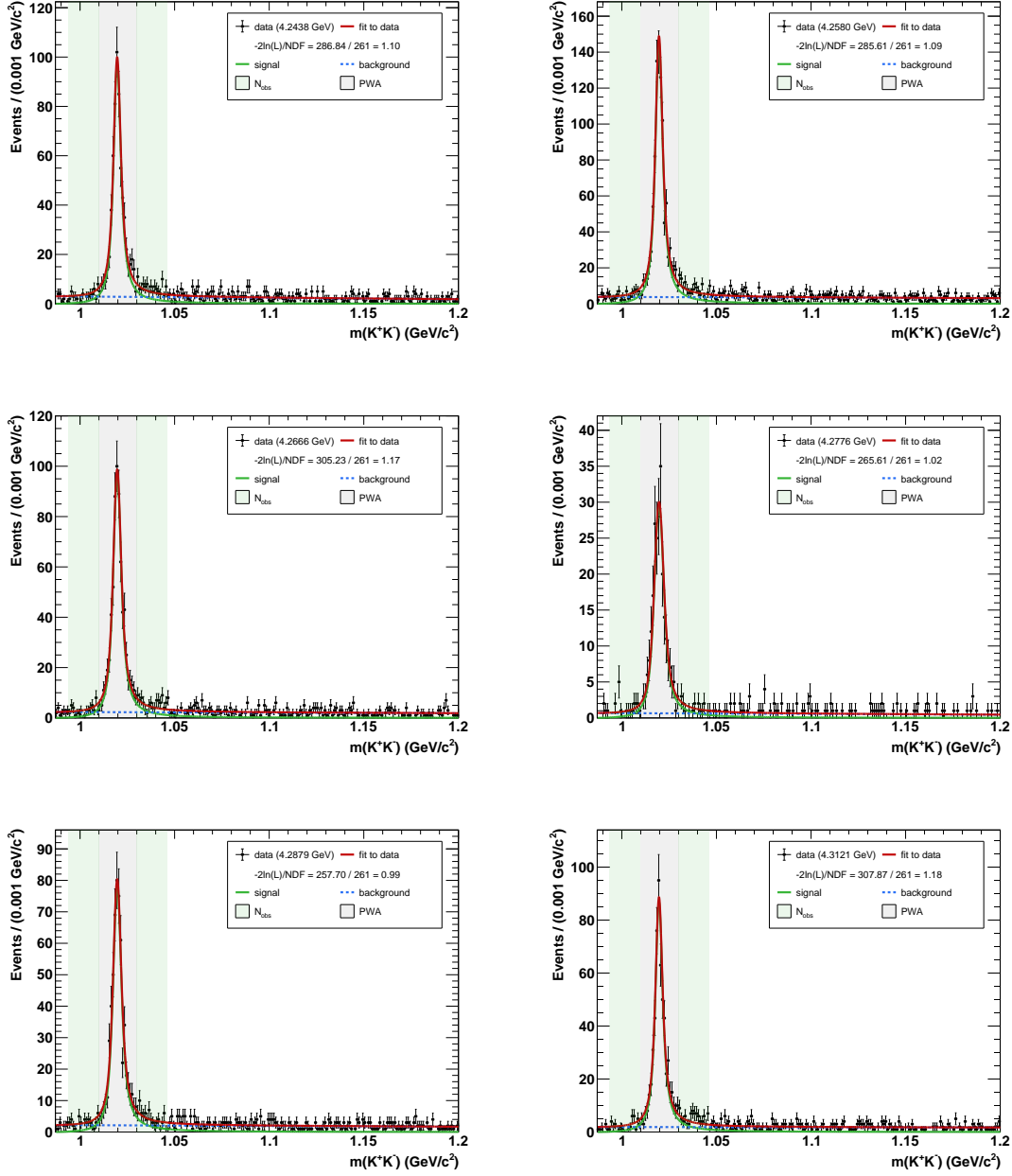


Figure A.3.: Invariant mass spectrum of ϕ candidates for data from $\sqrt{s} = 4.2438$ GeV to $\sqrt{s} = 4.3121$ GeV. A fit (red line) with a Breit-Wigner function convolved with a Gaussian function as signal (green line) and a first-order polynomial as background (dashed blue line) is applied. The green and blue shaded areas depict the signal regions in which the number of observed events N_{obs} is extracted and for which a PWA is performed to determine a global efficiency, respectively.

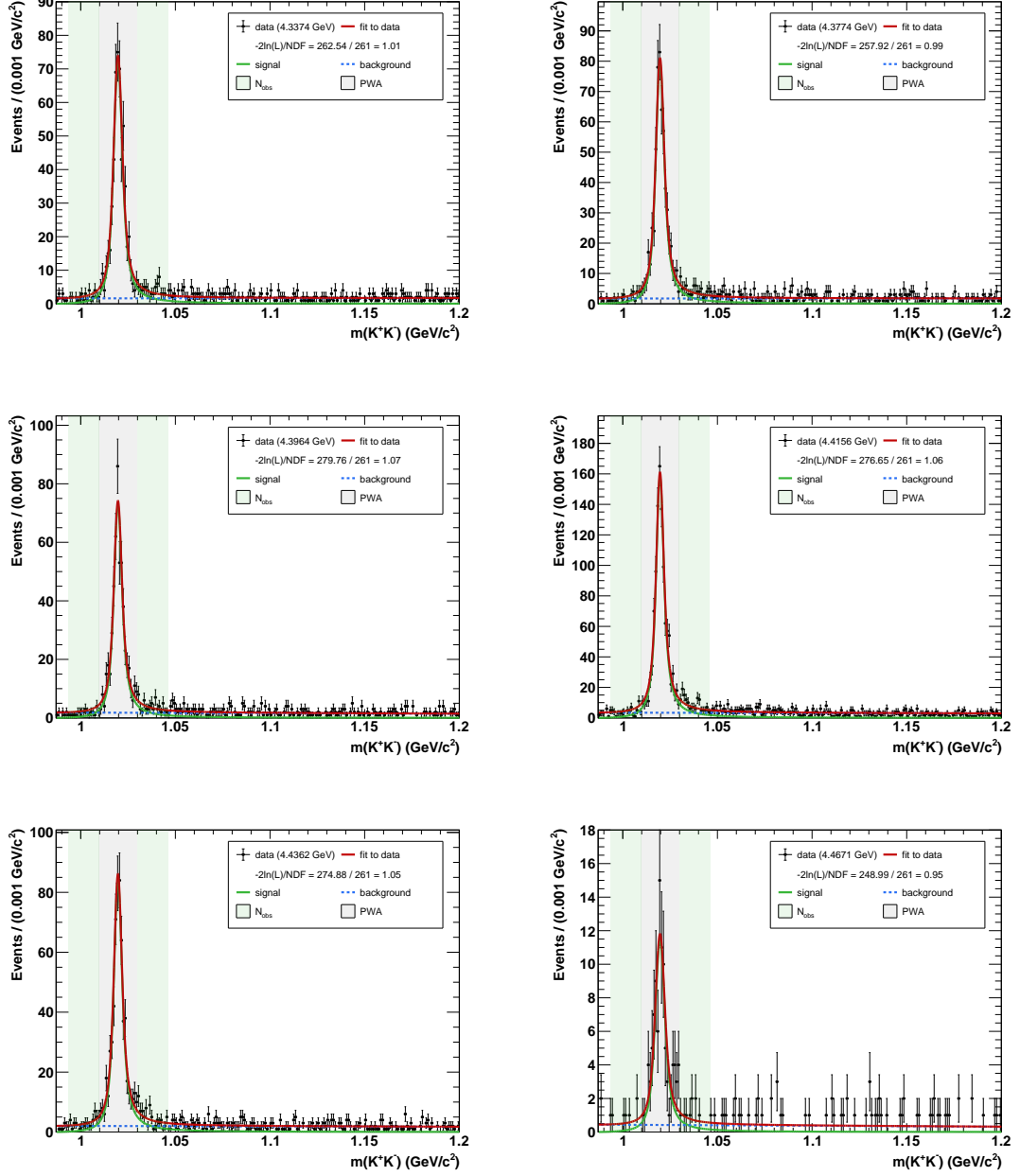


Figure A.4.: Invariant mass spectrum of ϕ candidates for data from $\sqrt{s} = 4.3374$ GeV to $\sqrt{s} = 4.4671$ GeV. A fit (red line) with a Breit-Wigner function convolved with a Gaussian function as signal (green line) and a first-order polynomial as background (dashed blue line) is applied. The green and blue shaded areas depict the signal regions in which the number of observed events N_{obs} is extracted and for which a PWA is performed to determine a global efficiency, respectively.

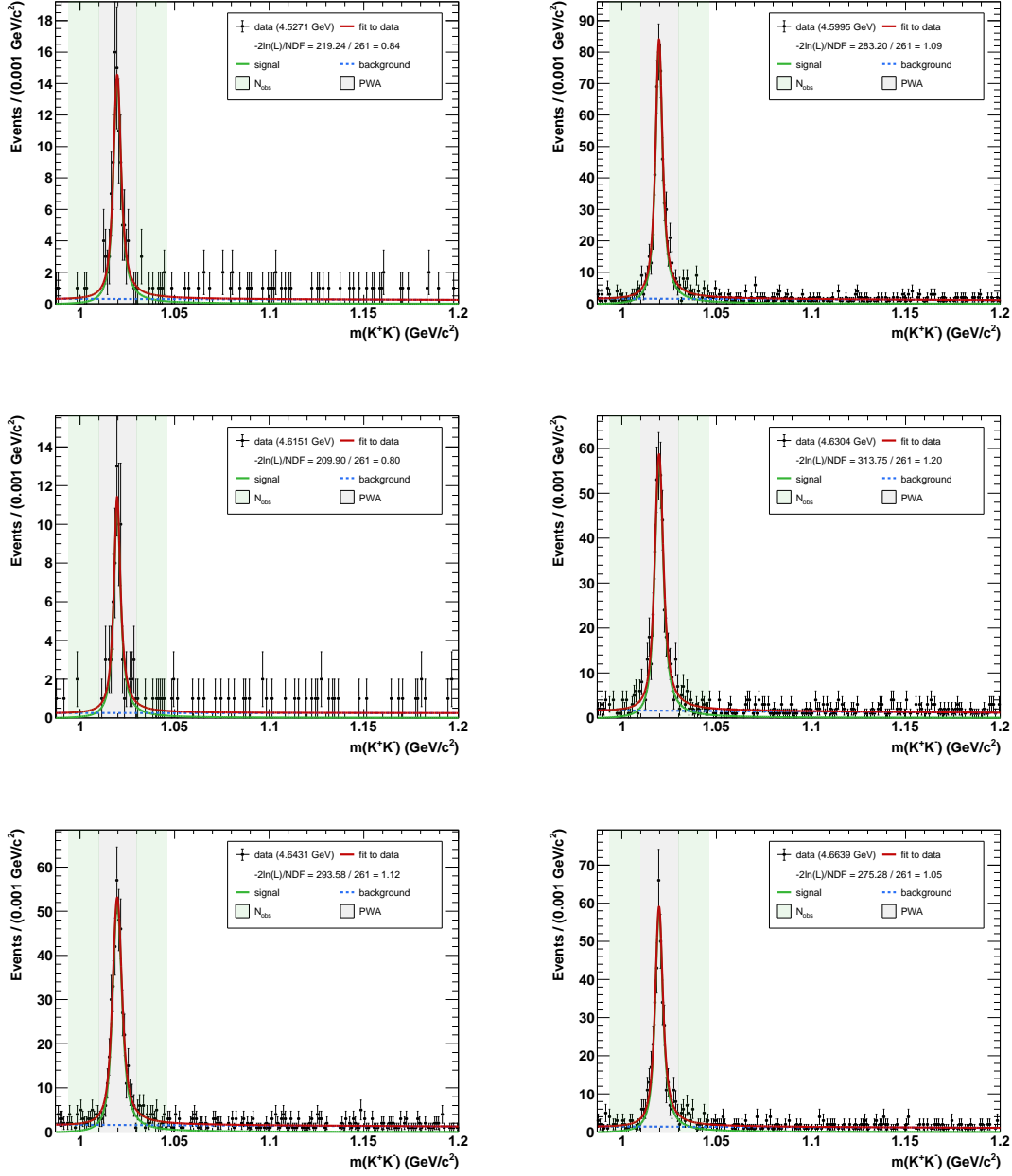


Figure A.5.: Invariant mass spectrum of ϕ candidates for data from $\sqrt{s} = 4.5271$ GeV to $\sqrt{s} = 4.6639$ GeV. A fit (red line) with a Breit-Wigner function convolved with a Gaussian function as signal (green line) and a first-order polynomial as background (dashed blue line) is applied. The green and blue shaded areas depict the signal regions in which the number of observed events N_{obs} is extracted and for which a PWA is performed to determine a global efficiency, respectively.

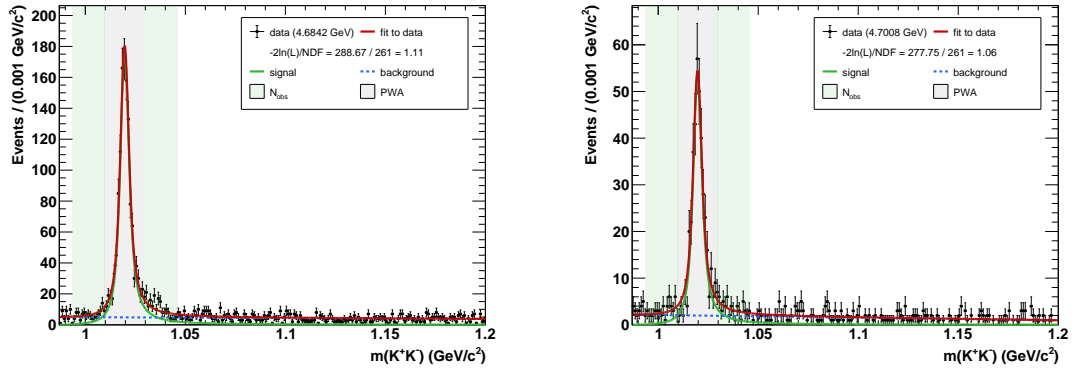


Figure A.6.: Invariant mass spectrum of ϕ candidates for data from $\sqrt{s} = 4.6842 \text{ GeV}$ to $\sqrt{s} = 4.7008 \text{ GeV}$. A fit (red line) with a Breit-Wigner function convolved with a Gaussian function as signal (green line) and a first-order polynomial as background (dashed blue line) is applied. The green and blue shaded areas depict the signal regions in which the number of observed events N_{obs} is extracted and for which a PWA is performed to determine a global efficiency, respectively.

A.4. Invariant Mass Spectra of ϕ Meson Candidates for

$$e^+e^- \rightarrow \phi K_S^0 K_S^0$$

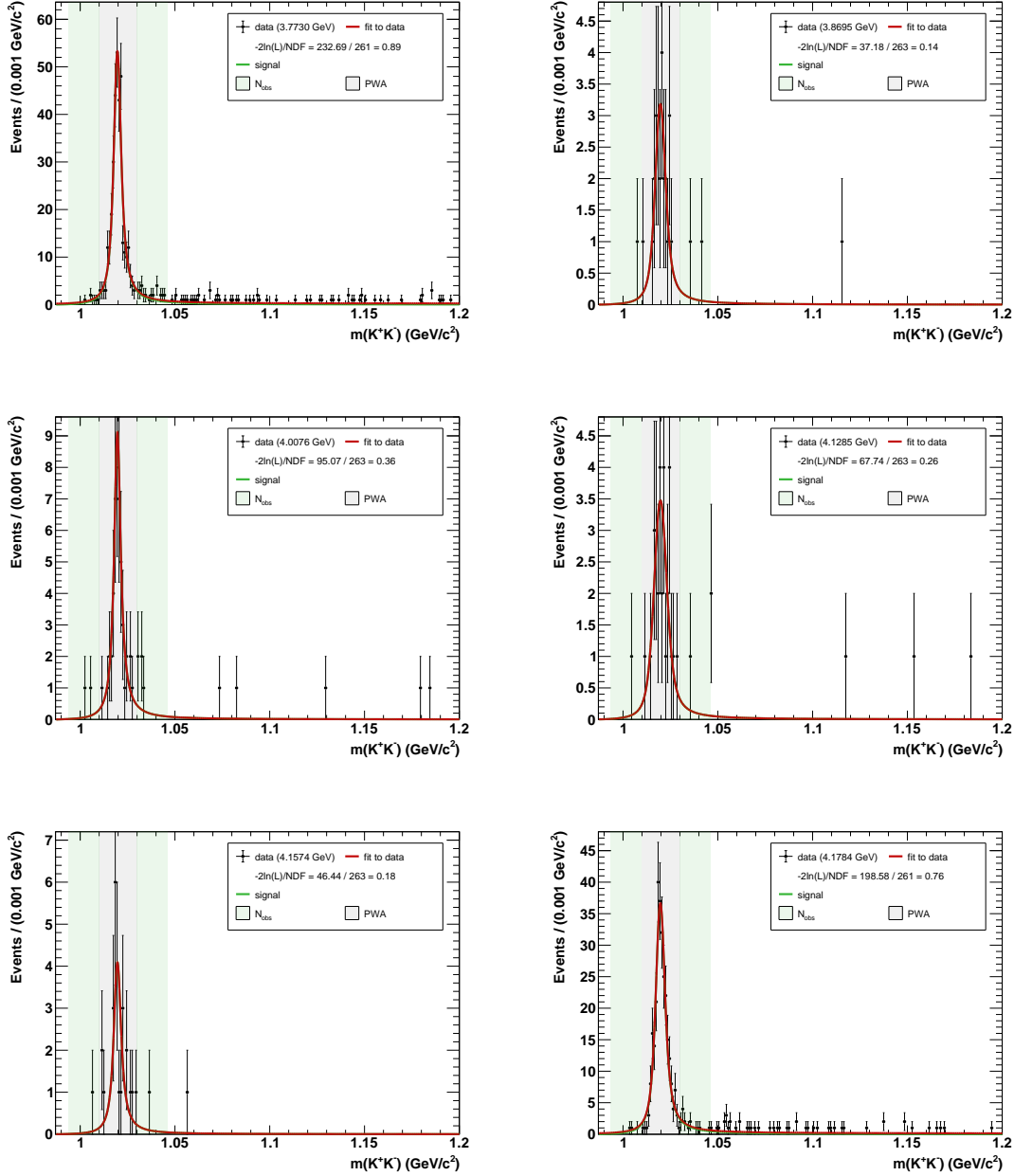


Figure A.7.: Invariant mass spectrum of ϕ candidates for data from $\sqrt{s} = 3.7730$ GeV to $\sqrt{s} = 4.1784$ GeV. A fit (red line) with a Breit-Wigner function convolved with a Gaussian function as signal is applied. The green and blue shaded areas depict the signal regions in which the number of observed events N_{obs} is extracted and for which a PWA is performed to determine a global efficiency, respectively.

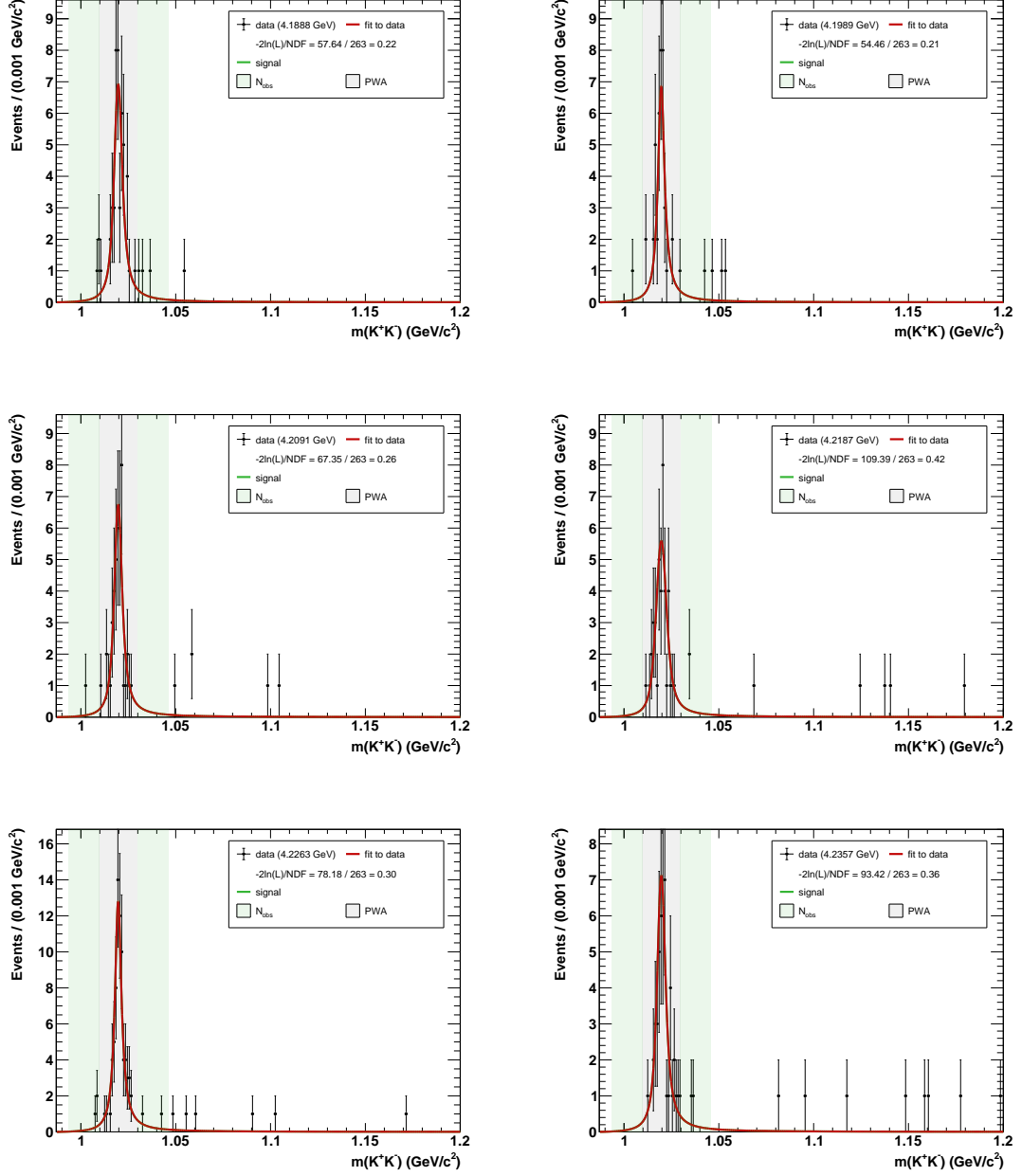


Figure A.8.: Invariant mass spectrum of ϕ candidates for data from $\sqrt{s} = 4.1888 \text{ GeV}$ to $\sqrt{s} = 4.2357 \text{ GeV}$. A fit (red line) with a Breit-Wigner function convolved with a Gaussian function as signal is applied. The green and blue shaded areas depict the signal regions in which the number of observed events N_{obs} is extracted and for which a PWA is performed to determine a global efficiency, respectively.

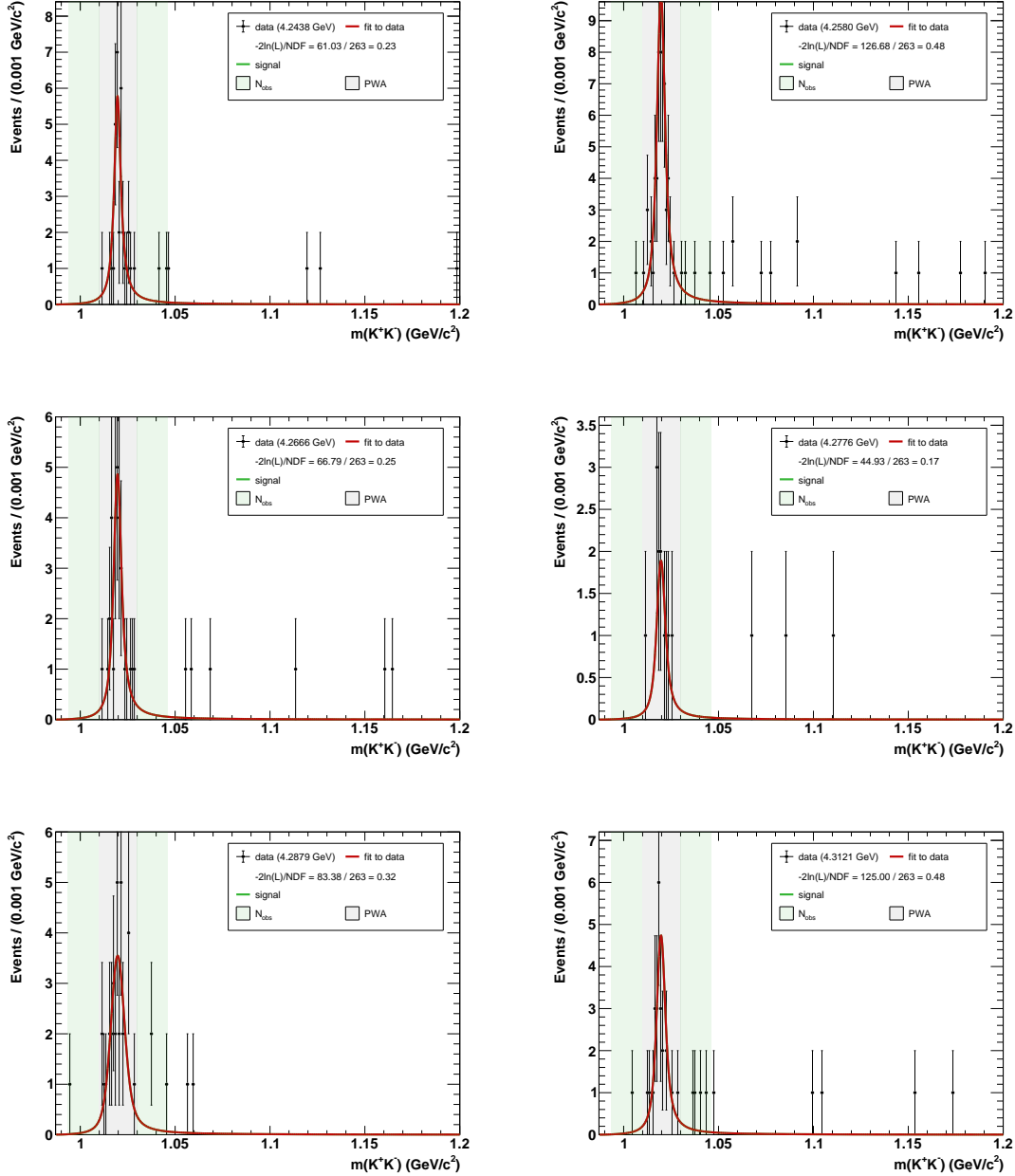


Figure A.9.: Invariant mass spectrum of ϕ candidates for data from $\sqrt{s} = 4.2438 \text{ GeV}$ to $\sqrt{s} = 4.3121 \text{ GeV}$. A fit (red line) with a Breit-Wigner function convolved with a Gaussian function as signal is applied. The green and blue shaded areas depict the signal regions in which the number of observed events N_{obs} is extracted and for which a PWA is performed to determine a global efficiency, respectively.

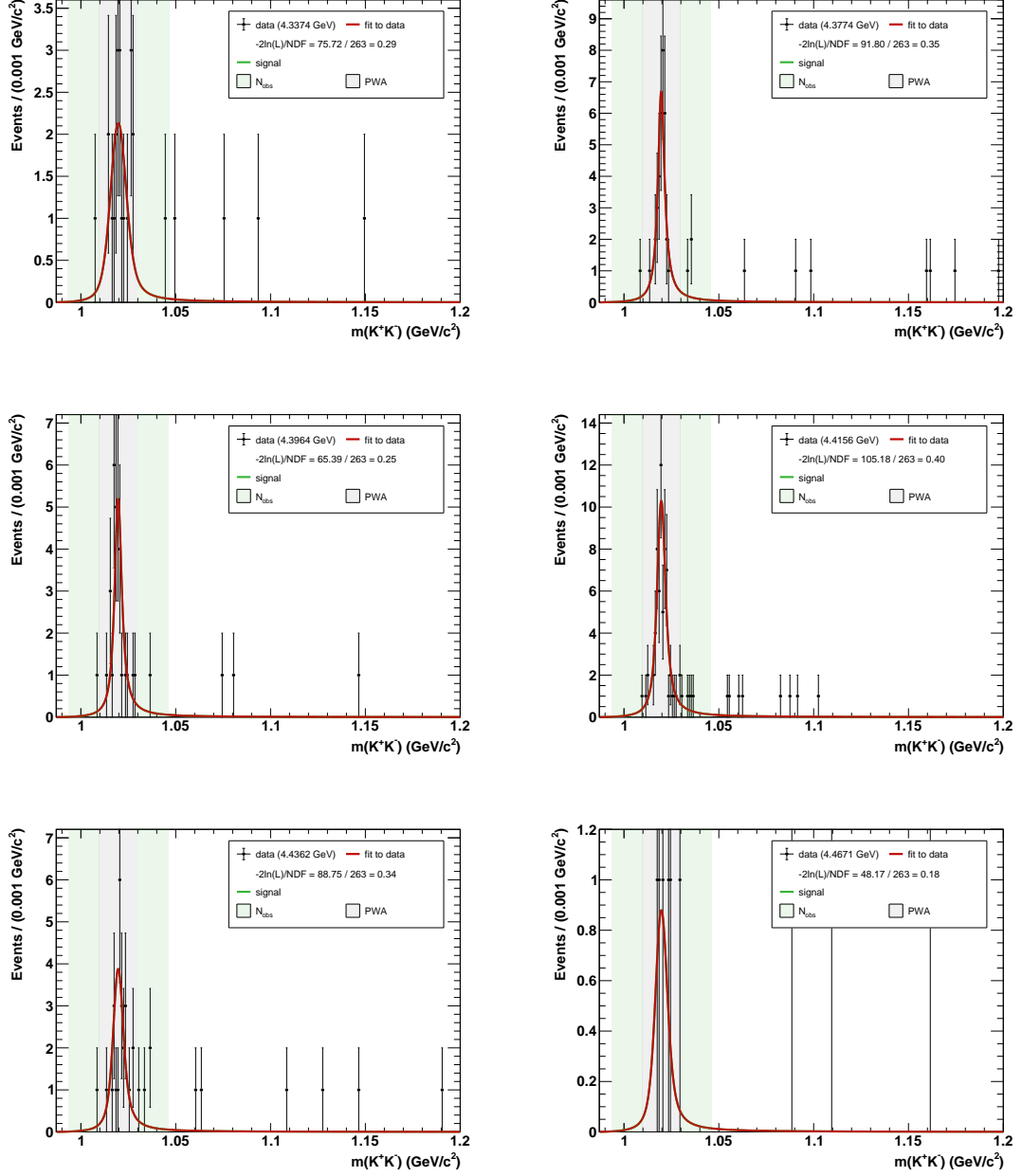


Figure A.10.: Invariant mass spectrum of ϕ candidates for data from $\sqrt{s} = 4.3374$ GeV to $\sqrt{s} = 4.4671$ GeV. A fit (red line) with a Breit-Wigner function convolved with a Gaussian function as signal is applied. The green and blue shaded areas depict the signal regions in which the number of observed events N_{obs} is extracted and for which a PWA is performed to determine a global efficiency, respectively.

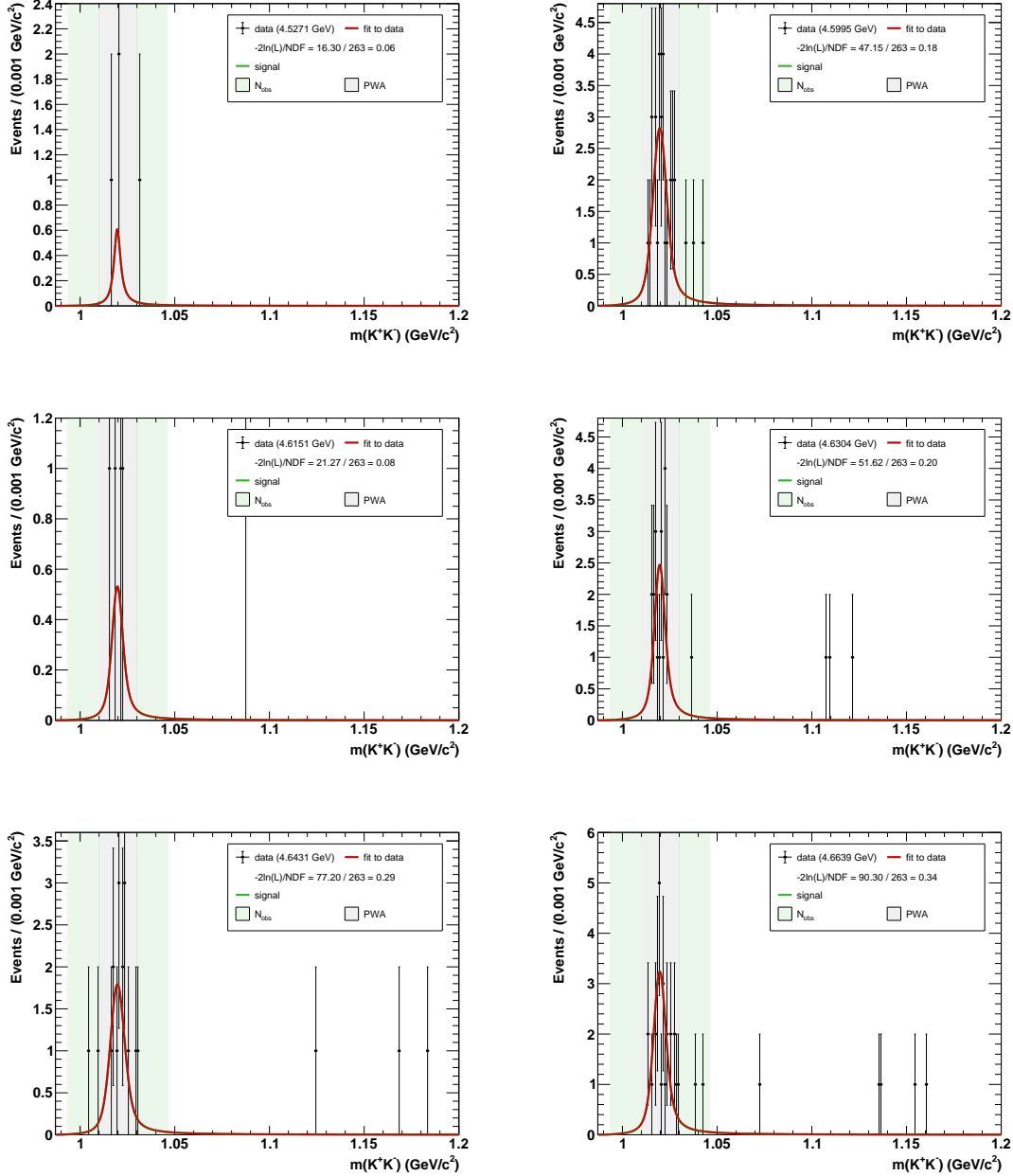


Figure A.11.: Invariant mass spectrum of ϕ candidates for data from $\sqrt{s} = 4.5271 \text{ GeV}$ to $\sqrt{s} = 4.6639 \text{ GeV}$. A fit (red line) with a Breit-Wigner function convolved with a Gaussian function as signal is applied. The green and blue shaded areas depict the signal regions in which the number of observed events N_{obs} is extracted and for which a PWA is performed to determine a global efficiency, respectively.

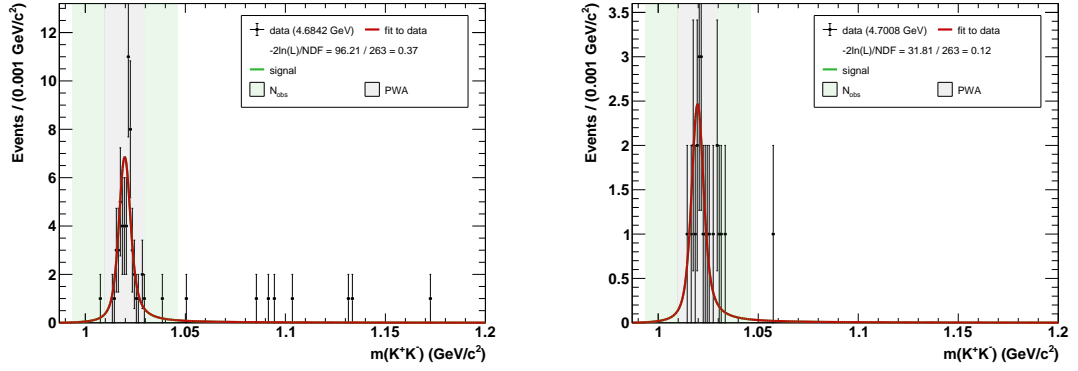


Figure A.12.: Invariant mass spectrum of ϕ candidates for data from $\sqrt{s} = 4.6842 \text{ GeV}$ to $\sqrt{s} = 4.7008 \text{ GeV}$. A fit (red line) with a Breit-Wigner function convolved with a Gaussian function as signal is applied. The green and blue shaded areas depict the signal regions in which the number of observed events N_{obs} is extracted and for which a PWA is performed to determine a global efficiency, respectively.

A.5. Invariant Mass Spectra of η' Meson Candidates for

$$\eta' \rightarrow \eta\pi^+\pi^-$$

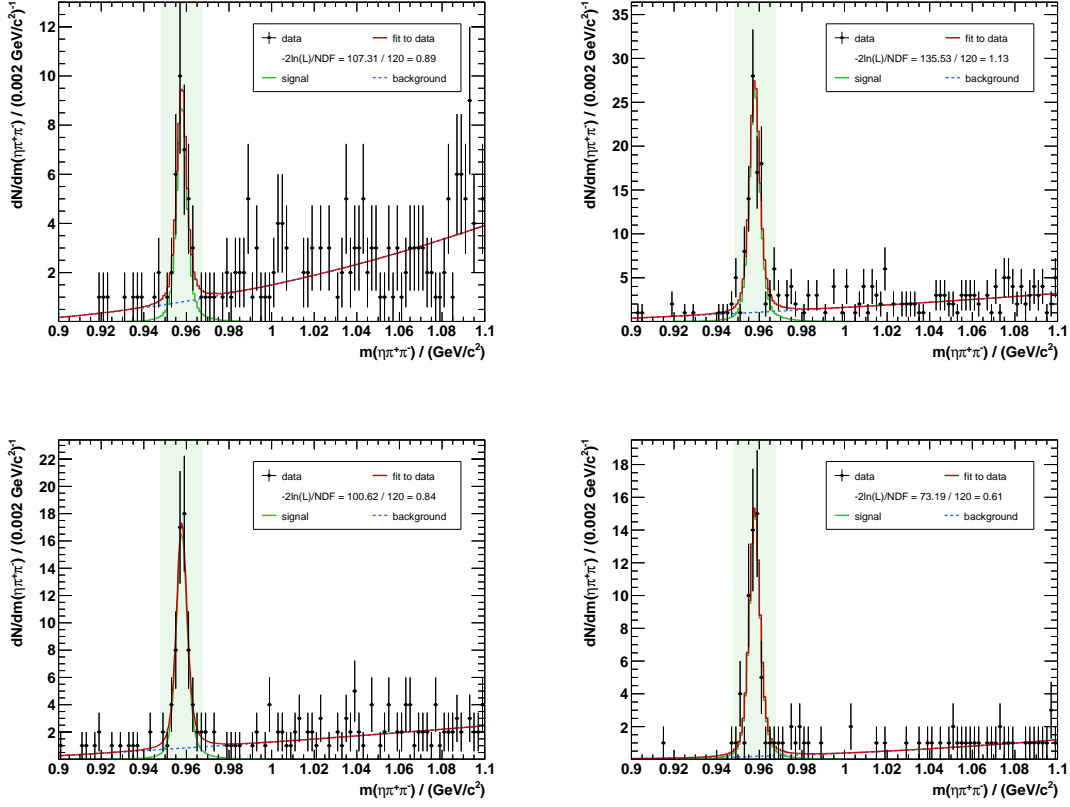


Figure A.13.: Invariant mass spectrum of $\eta' \rightarrow \eta\pi^+\pi^-$ candidates for data (black dots with error bars) subset 1 (**top left**), subset 2 (**top right**), subset 3 (**bottom left**) and subset 4 (**bottom right**). A fit (red line) with the signal MC shape convolved with a Gaussian function as signal (green line) and a second-order polynomial as background for (dashed blue line) is applied. The green shaded area depicts the signal region in which the number of observed events N_{obs} is extracted.

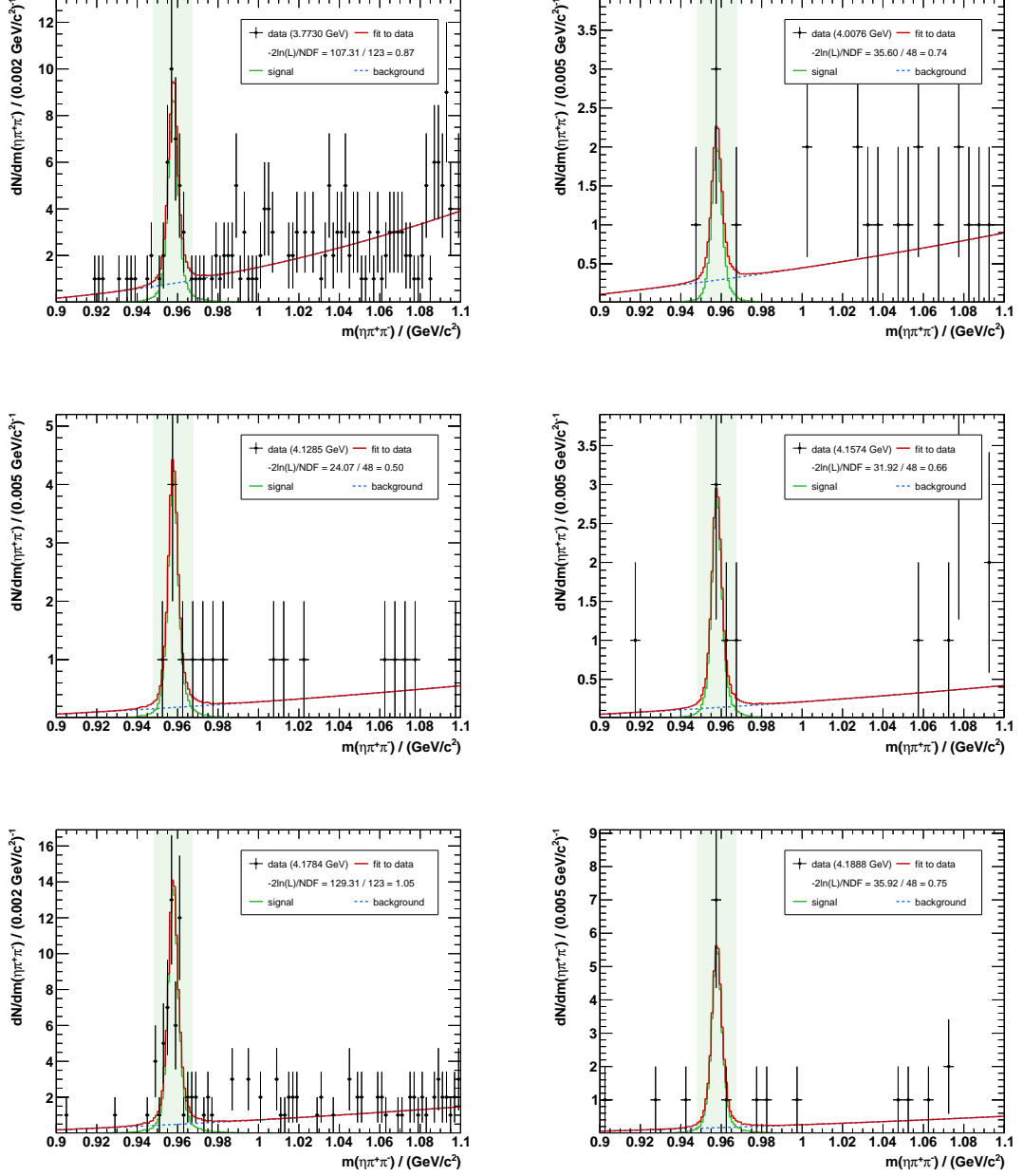


Figure A.14.: Invariant mass spectrum of $\eta' \rightarrow \eta\pi^+\pi^-$ candidates for data from $\sqrt{s} = 3.7730 \text{ GeV}$ to $\sqrt{s} = 4.1888 \text{ GeV}$. A fit (red line) with the signal MC shape convolved with a Gaussian function as signal (green line) and a second-order polynomial as background for (dashed blue line) is applied. The green shaded area depicts the signal region in which the number of observed events N_{obs} is extracted.

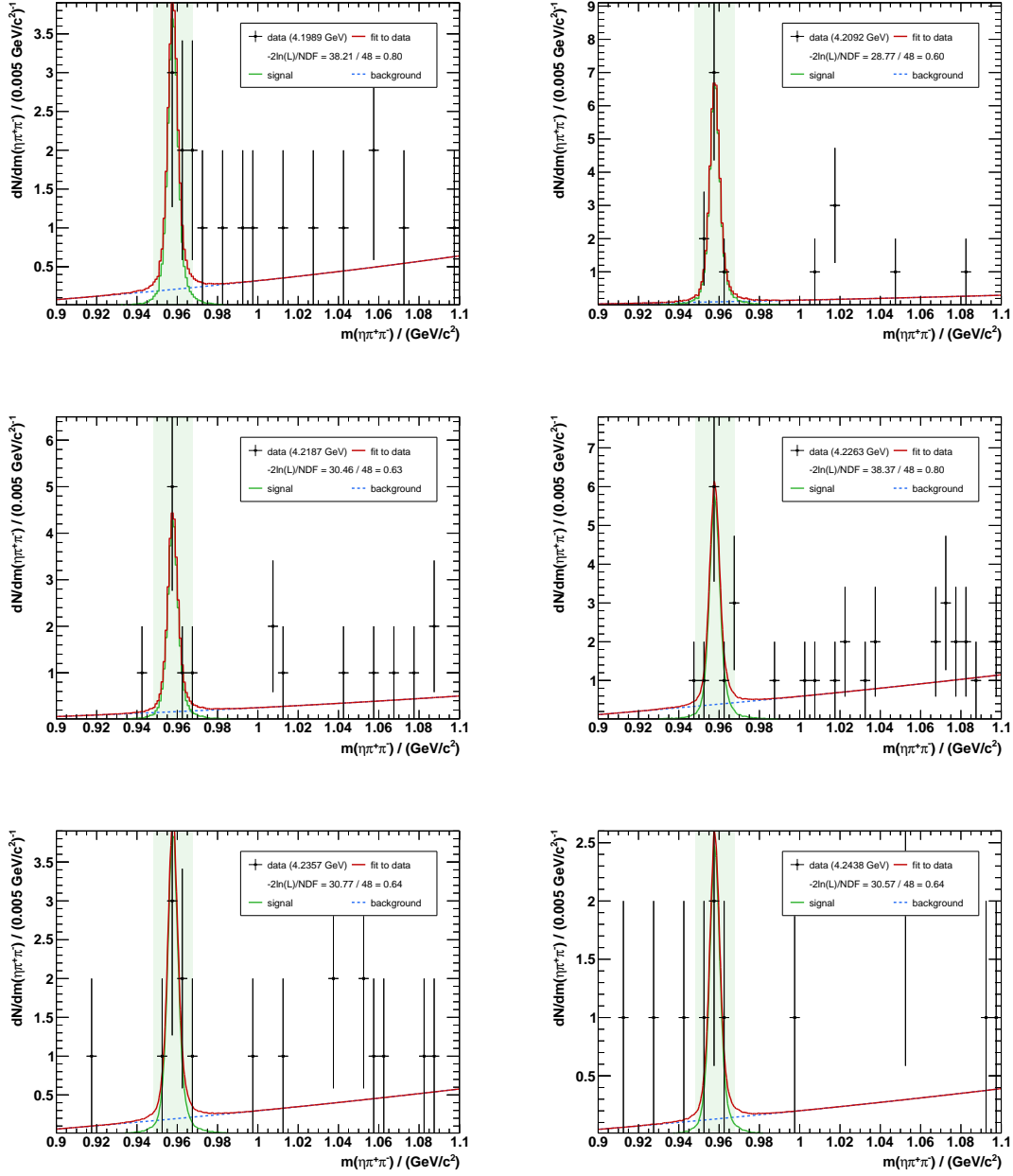


Figure A.15.: Invariant mass spectrum of $\eta' \rightarrow \eta\pi^+\pi^-$ candidates for data from $\sqrt{s} = 4.1989$ GeV to $\sqrt{s} = 4.2438$ GeV. A fit (red line) with the signal MC shape convolved with a Gaussian function as signal (green line) and a second-order polynomial as background for (dashed blue line) is applied. The green shaded area depicts the signal region in which the number of observed events N_{obs} is extracted.

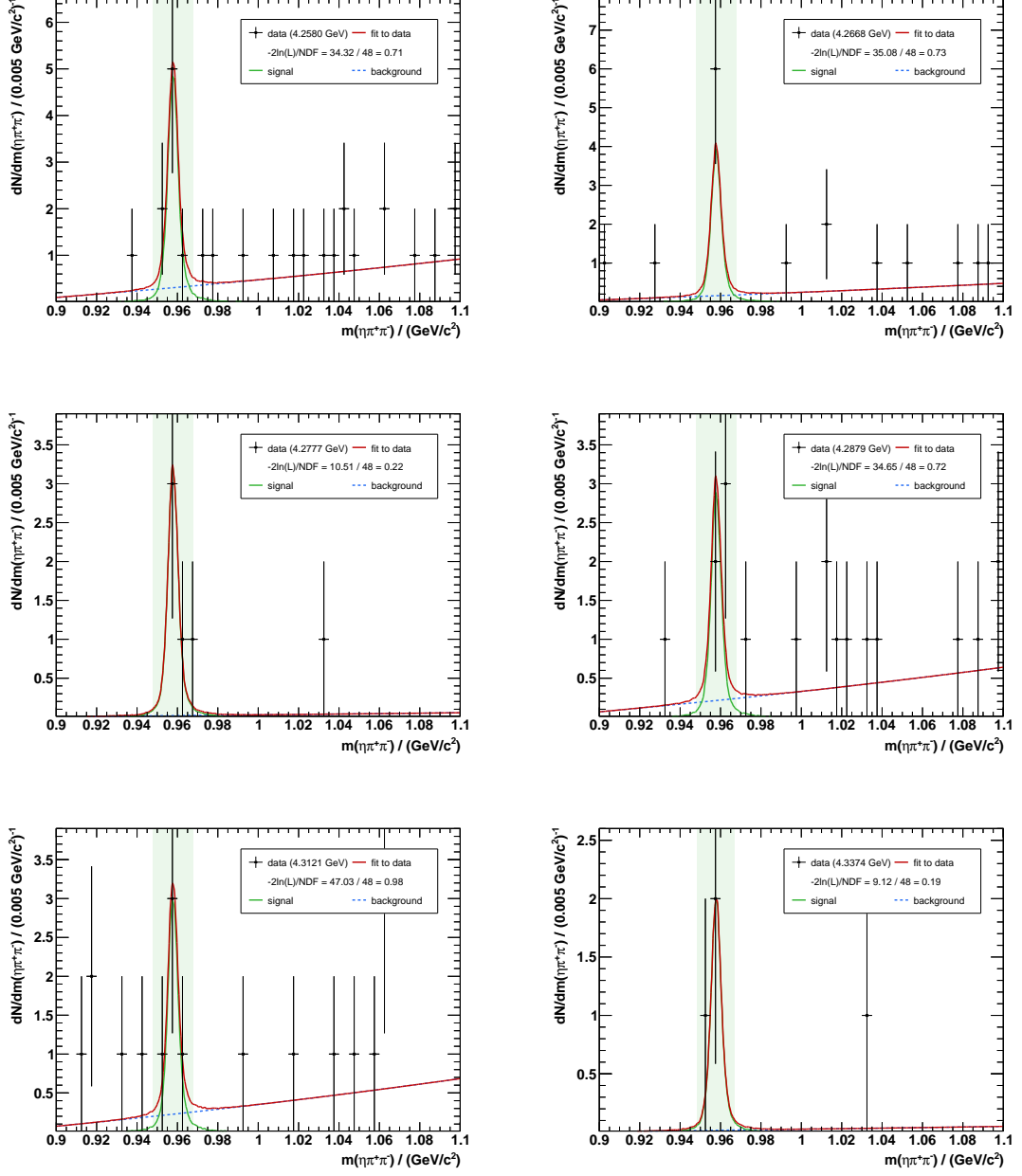


Figure A.16.: Invariant mass spectrum of $\eta' \rightarrow \eta\pi^+\pi^-$ candidates for data from $\sqrt{s} = 4.2580$ GeV to $\sqrt{s} = 4.3374$ GeV. A fit (red line) with the signal MC shape convolved with a Gaussian function as signal (green line) and a second-order polynomial as background for (dashed blue line) is applied. The green shaded area depicts the signal region in which the number of observed events N_{obs} is extracted.

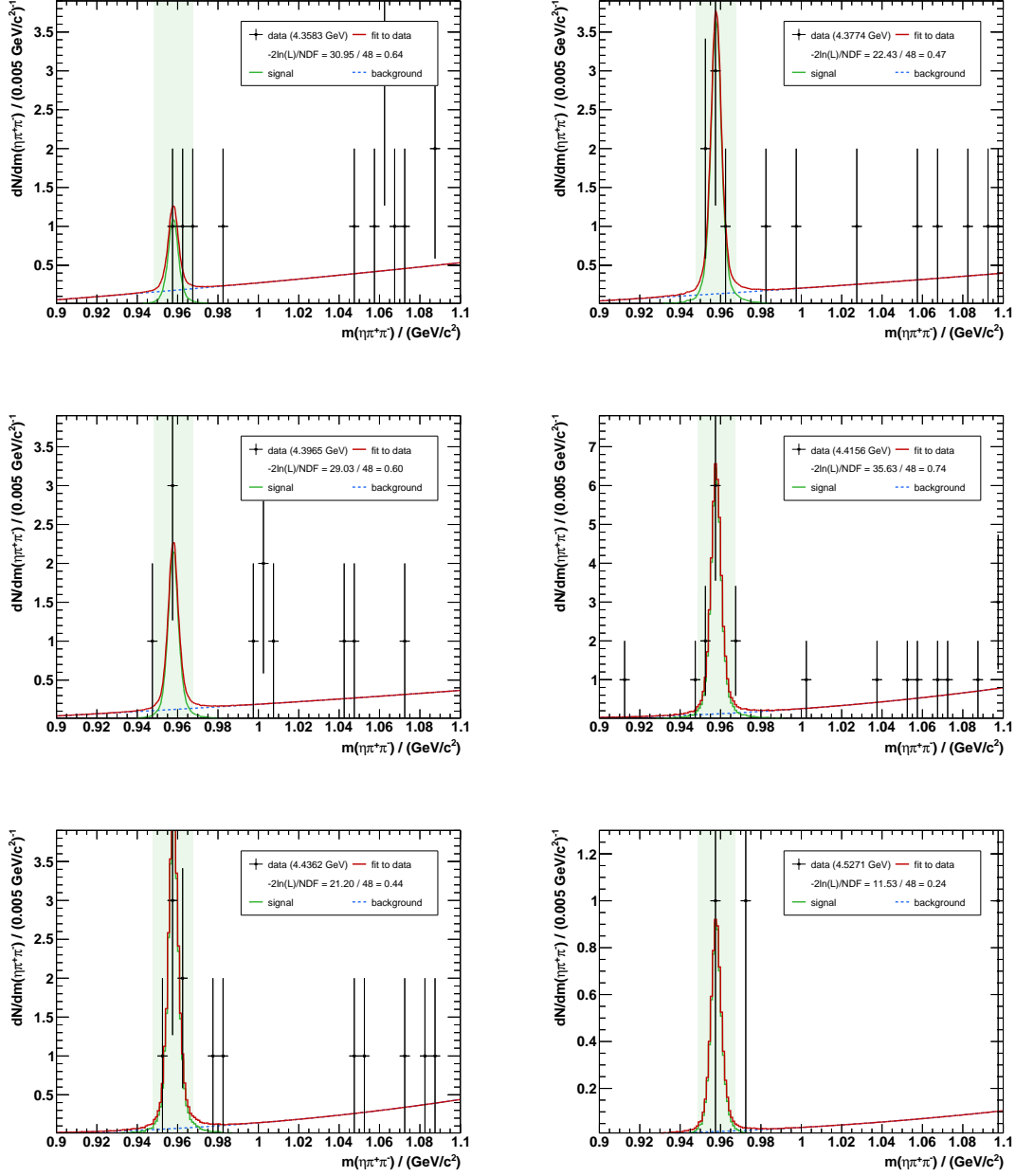


Figure A.17.: Invariant mass spectrum of $\eta' \rightarrow \eta\pi^+\pi^-$ candidates for data from $\sqrt{s} = 4.3583$ GeV to $\sqrt{s} = 4.5271$ GeV. A fit (red line) with the signal MC shape convolved with a Gaussian function as signal (green line) and a second-order polynomial as background for (dashed blue line) is applied. The green shaded area depicts the signal region in which the number of observed events N_{obs} is extracted.

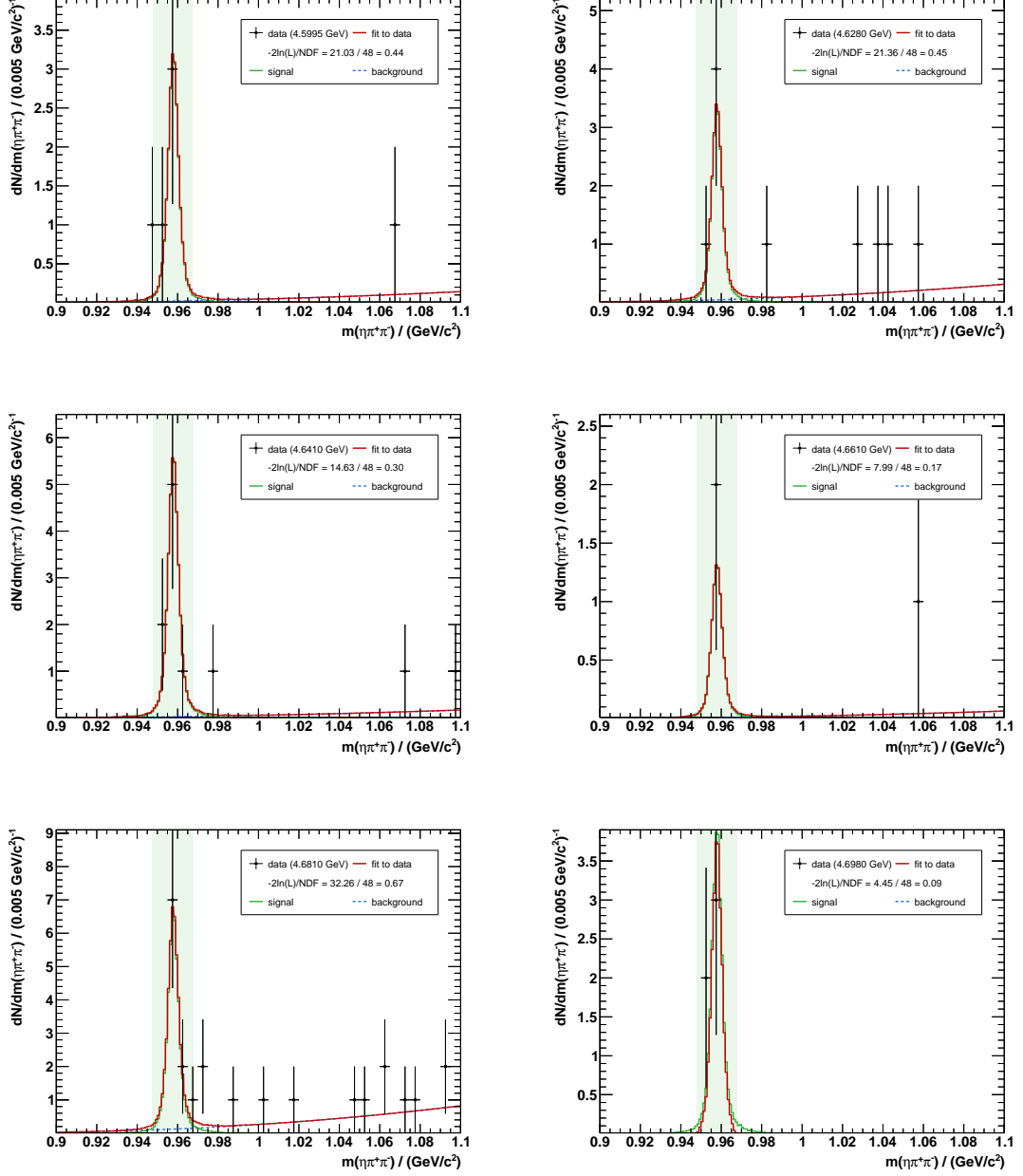


Figure A.18.: Invariant mass spectrum of $\eta' \rightarrow \eta\pi^+\pi^-$ candidates for data from $\sqrt{s} = 4.5995 \text{ GeV}$ to $\sqrt{s} = 4.7008 \text{ GeV}$. A fit (red line) with the signal MC shape convolved with a Gaussian function as signal (green line) and a second-order polynomial as background for (dashed blue line) is applied. The green shaded area depicts the signal region in which the number of observed events N_{obs} is extracted.

A.6. Invariant Mass Spectra of η' Meson Candidates for

$$\eta' \rightarrow \gamma\pi^+\pi^-$$

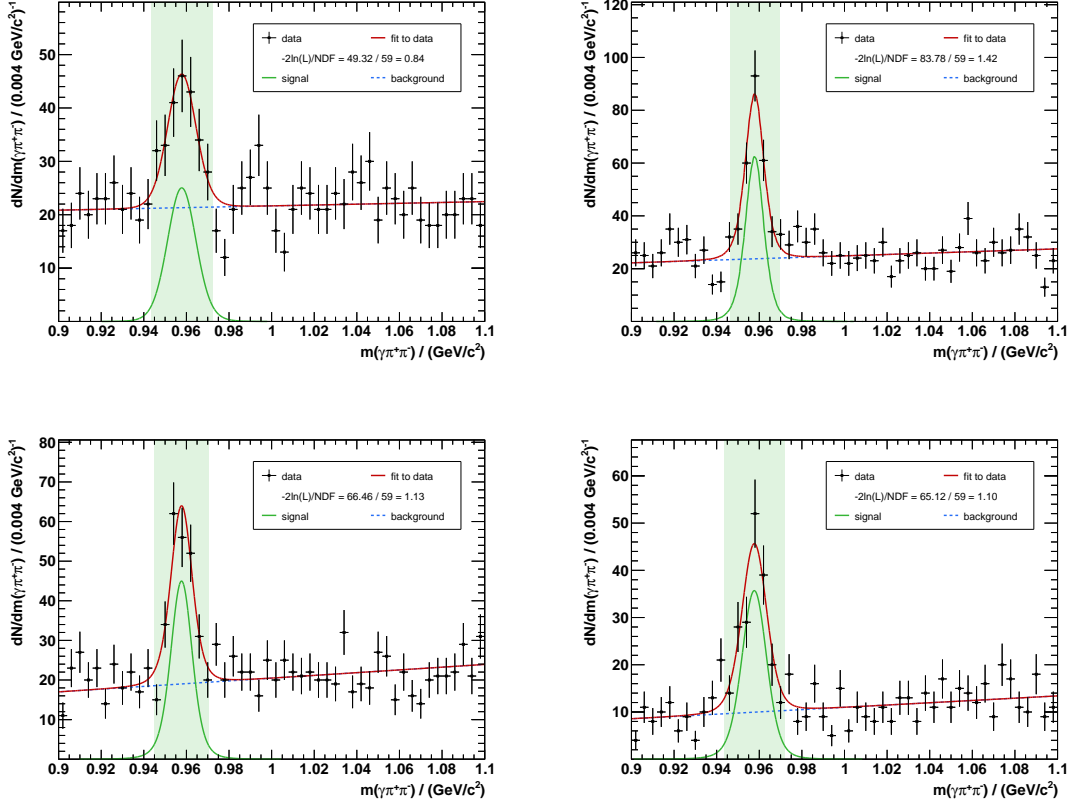


Figure A.19.: Invariant mass spectrum of $\eta' \rightarrow \gamma\pi^+\pi^-$ candidates for data (black dots with error bars) subset 1 (**top left**), subset 2 (**top right**), subset 3 (**bottom left**) and subset 4 (**bottom right**). A fit (red line) with the signal MC shape convolved with a Gaussian function as signal (green line) and a second-order polynomial as background for (dashed blue line) is applied. The green shaded area depicts the signal region in which the number of observed events N_{obs} is extracted.

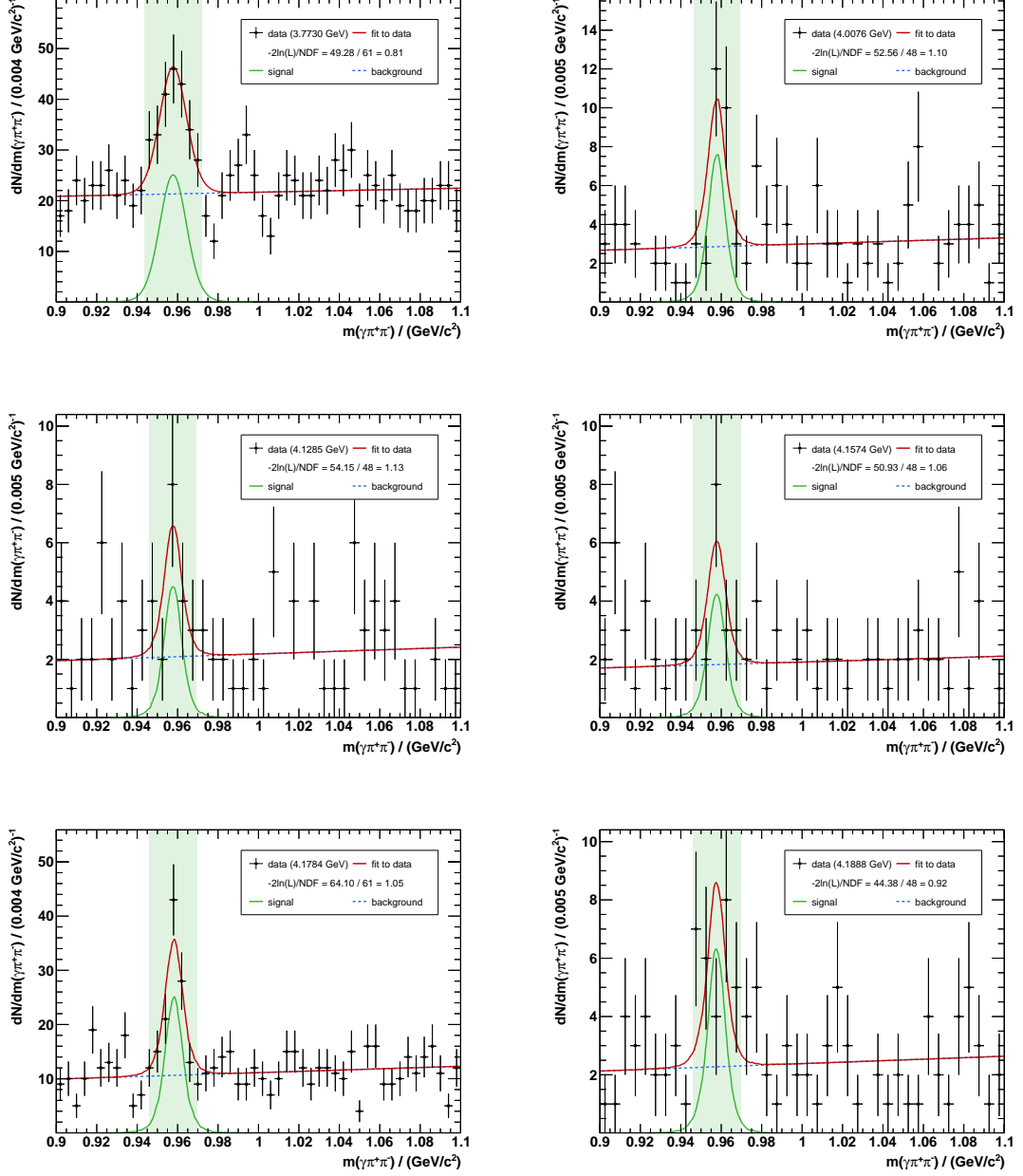


Figure A.20.: Invariant mass spectrum of $\eta' \rightarrow \gamma\pi^+\pi^-$ candidates for data from $\sqrt{s} = 3.7730$ GeV to $\sqrt{s} = 4.1888$ GeV. A fit (red line) with the signal MC shape convolved with a Gaussian function as signal (green line) and a second-order polynomial as background for (dashed blue line) is applied. The green shaded area depicts the signal region in which the number of observed events N_{obs} is extracted.

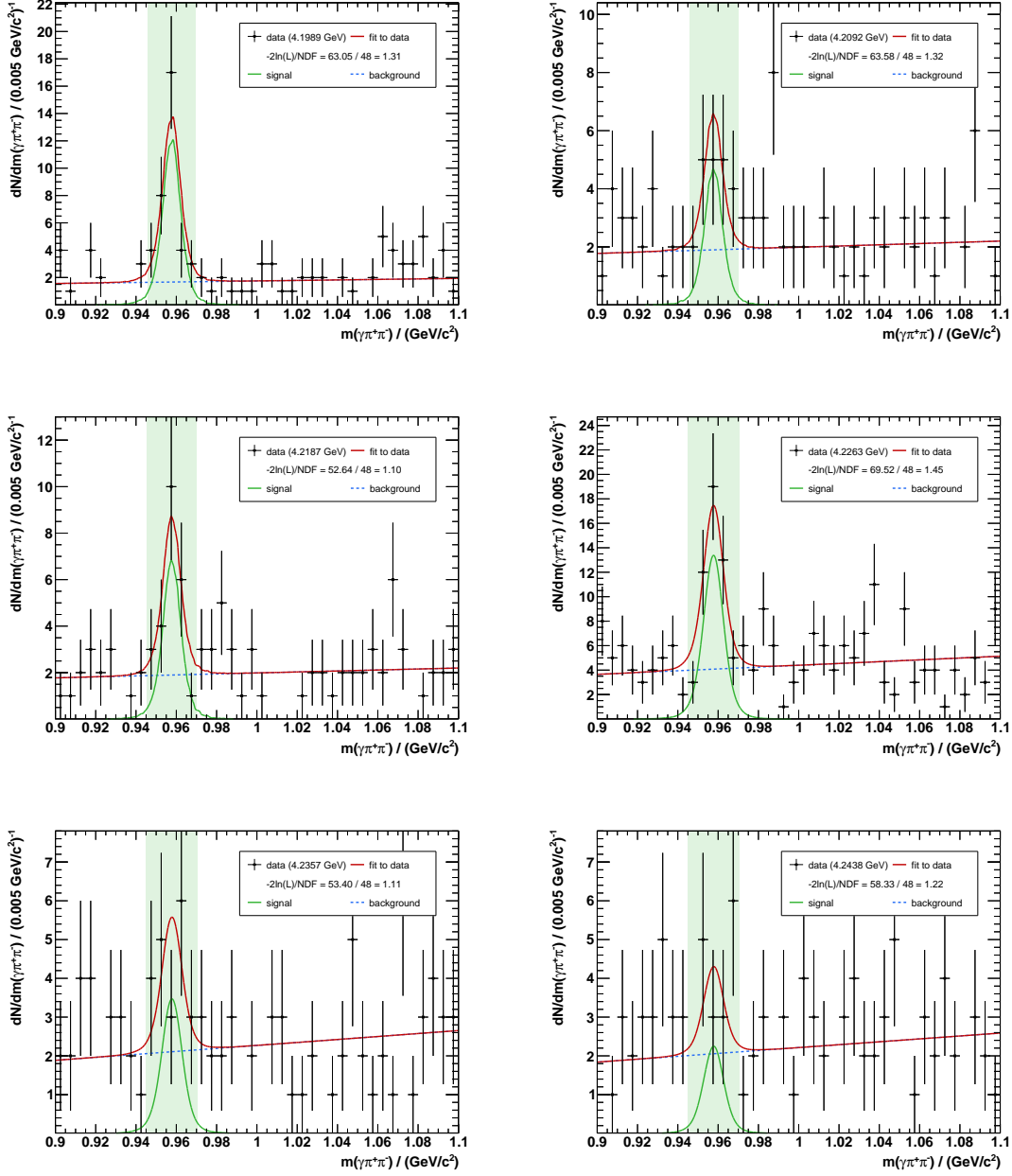


Figure A.21.: Invariant mass spectrum of $\eta' \rightarrow \gamma\pi^+\pi^-$ candidates for data from $\sqrt{s} = 4.1989 \text{ GeV}$ to $\sqrt{s} = 4.2438 \text{ GeV}$. A fit (red line) with the signal MC shape convolved with a Gaussian function as signal (green line) and a second-order polynomial as background for (dashed blue line) is applied. The green shaded area depicts the signal region in which the number of observed events N_{obs} is extracted.

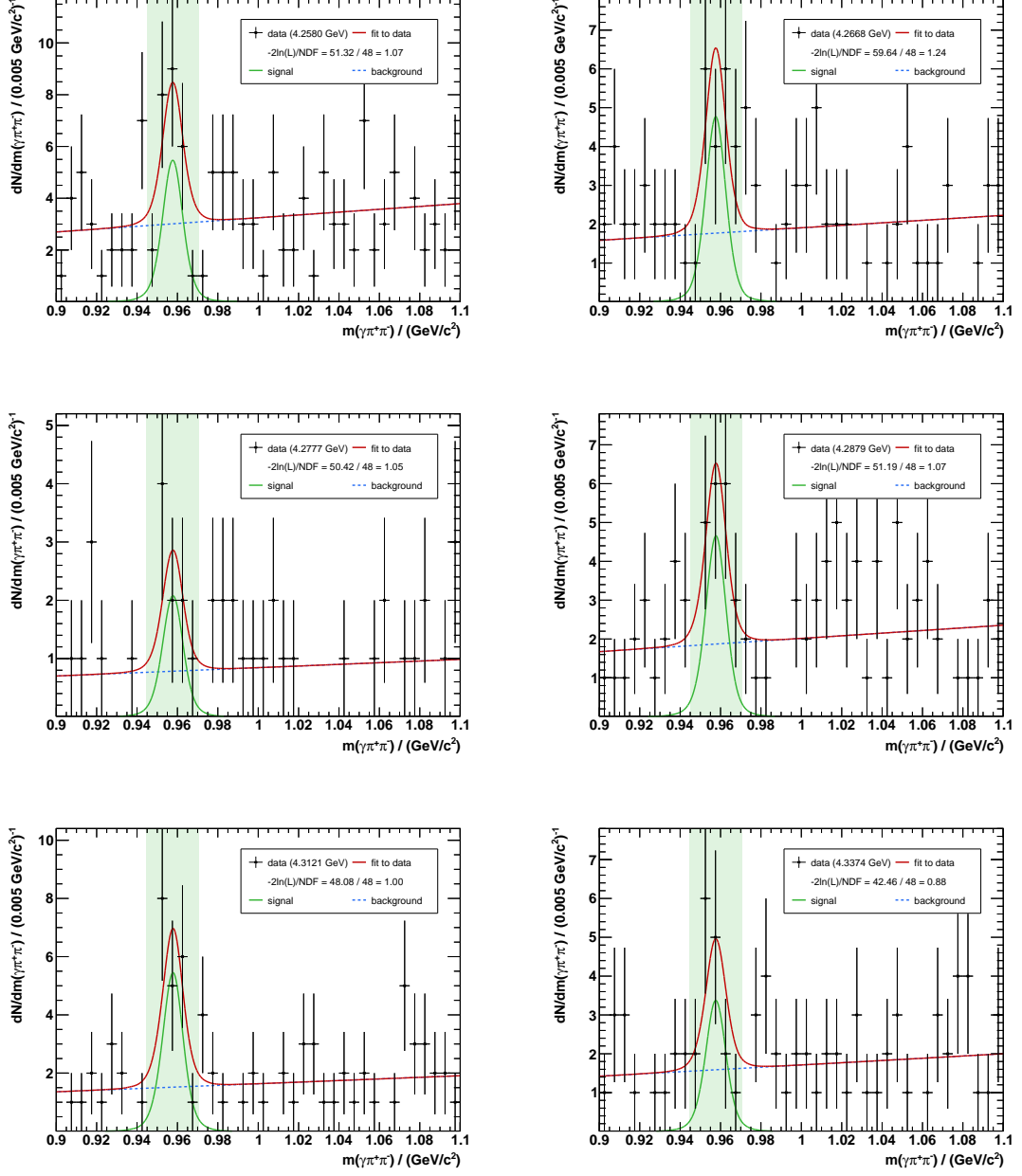


Figure A.22.: Invariant mass spectrum of $\eta' \rightarrow \gamma\pi^+\pi^-$ candidates for data from $\sqrt{s} = 4.2580$ GeV to $\sqrt{s} = 4.3374$ GeV. A fit (red line) with the signal MC shape convolved with a Gaussian function as signal (green line) and a second-order polynomial as background for (dashed blue line) is applied. The green shaded area depicts the signal region in which the number of observed events N_{obs} is extracted.

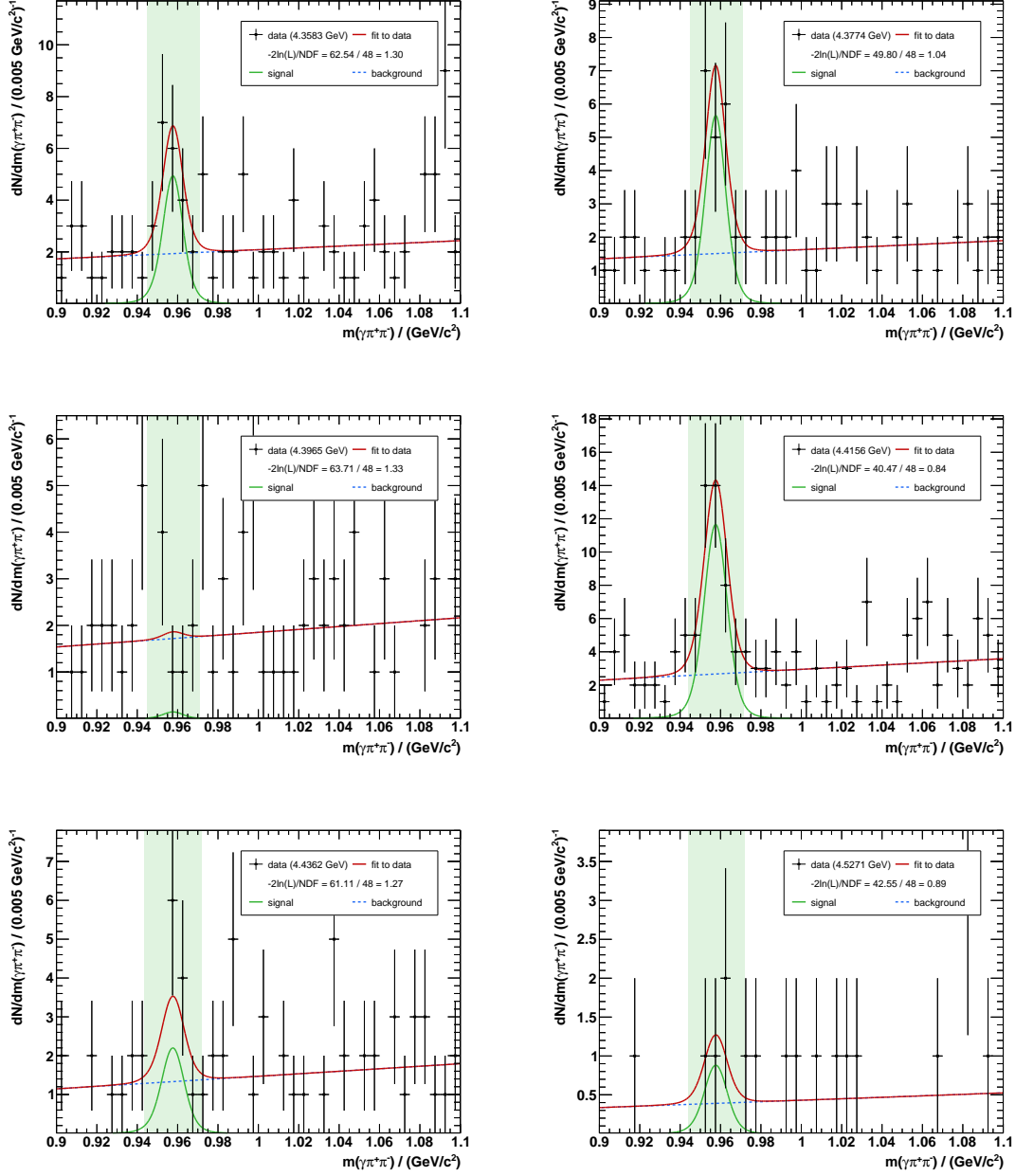


Figure A.23.: Invariant mass spectrum of $\eta' \rightarrow \gamma\pi^+\pi^-$ candidates for data from $\sqrt{s} = 4.3583$ GeV to $\sqrt{s} = 4.5271$ GeV. A fit (red line) with the signal MC shape convolved with a Gaussian function as signal (green line) and a second-order polynomial as background for (dashed blue line) is applied. The green shaded area depicts the signal region in which the number of observed events N_{obs} is extracted.

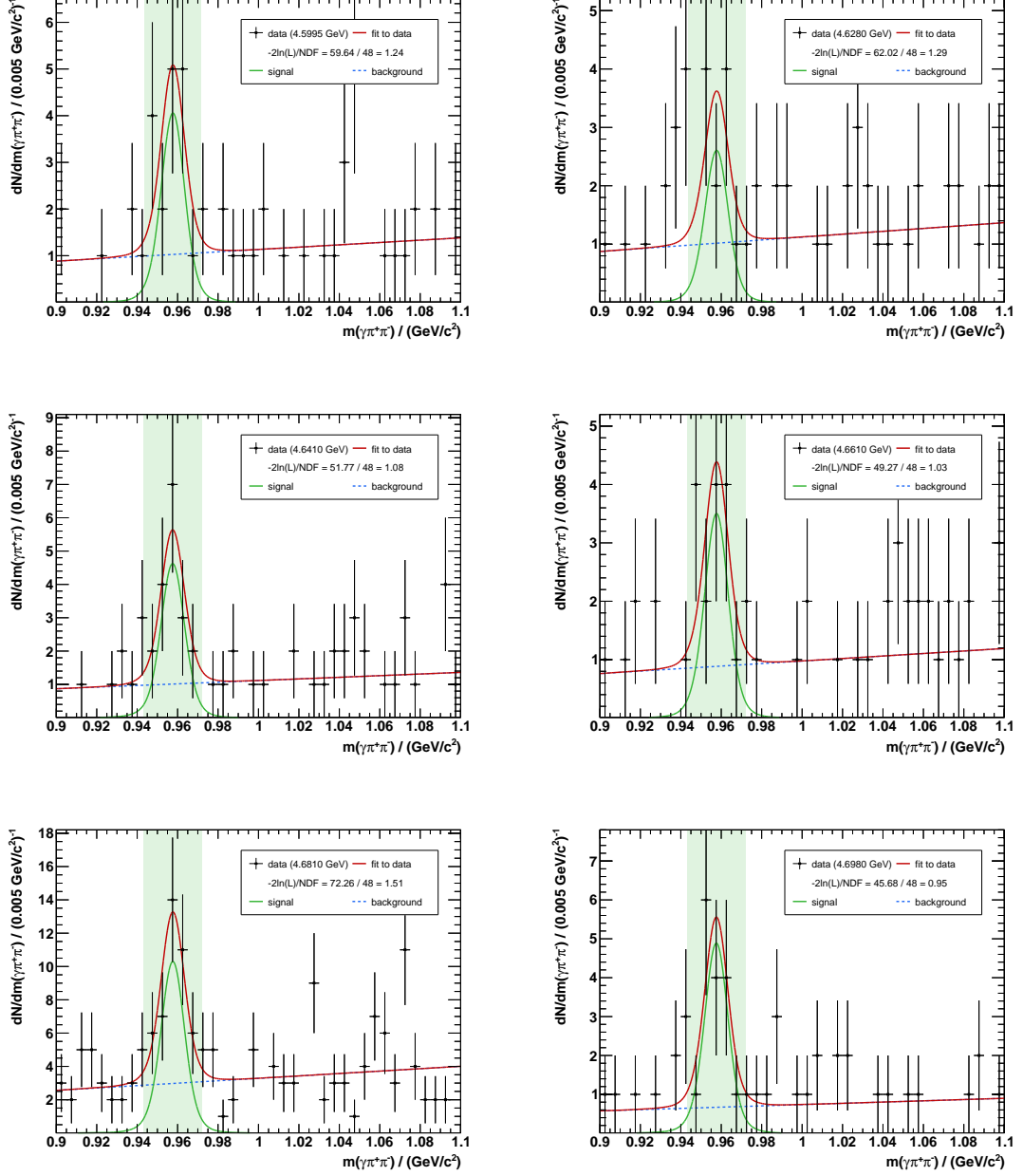


Figure A.24.: Invariant mass spectrum of $\eta' \rightarrow \gamma\pi^+\pi^-$ candidates for data from $\sqrt{s} = 4.5995$ GeV to $\sqrt{s} = 4.7008$ GeV. A fit (red line) with the signal MC shape convolved with a Gaussian function as signal (green line) and a second-order polynomial as background for (dashed blue line) is applied. The green shaded area depicts the signal region in which the number of observed events N_{obs} is extracted.

Bibliography

- [1] “Marathonlauf.” <https://de.wikipedia.org/wiki/Marathonlauf>. Accessed: 2021-09-21.
- [2] Belle Collaboration, S. K. Choi *et al.*, “Observation of a narrow charmonium-like state in exclusive $B^\pm \rightarrow K^\pm \pi^+ \pi^- J/\psi$ decays,” *Phys. Rev. Lett.* **91** (2003) 262001, [arXiv:hep-ex/0309032](https://arxiv.org/abs/hep-ex/0309032) [hep-ex].
- [3] S. L. Glashow, “Partial-symmetries of weak interactions,” *Nucl. Phys.* **22** no. 4, (1961) 579–588.
<https://www.sciencedirect.com/science/article/pii/0029558261904692>.
- [4] S. Weinberg, “A Model of Leptons,” *Phys. Rev. Lett.* **19** (Nov, 1967) 1264–1266.
<https://link.aps.org/doi/10.1103/PhysRevLett.19.1264>.
- [5] A. Salam, “Weak and Electromagnetic Interactions,” *Conf. Proc. C* **680519** (1968) 367–377.
- [6] H. Fritzsch, M. Gell-Mann, and H. Leutwyler, “Advantages of the color octet gluon picture,” *Phys. Lett. B* **47** no. 4, (1973) 365–368.
<https://www.sciencedirect.com/science/article/pii/0370269373906254>.
- [7] J. J. Thomson, “On bodies smaller than atoms,” *The Popular Science Monthly* **59** (1901) 323–335.
- [8] E. Rutherford, “The scattering of alpha and beta particles by matter and the structure of the atom,” *Phil. Mag. Ser.6* **21** (1911) 669–688.
- [9] A. Einstein, “Über einen die Erzeugung und Verwandlung des Lichtes betreffenden heuristischen Gesichtspunkt,” *Annalen der Physik* **322** no. 6, (1905) 132–148.
<https://onlinelibrary.wiley.com/doi/abs/10.1002/andp.19053220607>.
- [10] L. de Broglie *J. Phys. Radium* **3** (1922) 33–45.
- [11] L. de Broglie *Comptes Rendus* **177** (1923) 507–510.
- [12] L. de Broglie *Philos. Mag.* **47** (1924) 446–458.

- [13] J. Chadwick, “The Existence of a Neutron,” *Proc. Roy. Soc. Lond. A* **136** no. 830, (1932) 692–708.
- [14] H. Yukawa, “On the Interaction of Elementary Particles. I,” *Prog. Theor. Phys. Suppl.* **1** (01, 1955) 1–10. <https://doi.org/10.1143/PTPS.1.1>.
- [15] C. M. G. Lattes *et al.*, “Processes involving charged mesons,” *Nature* **159** no. 4047, (1947) 694–697. <https://doi.org/10.1038/159694a0>.
- [16] M. Gell-Mann, “A Schematic Model of Baryons and Mesons,” *Phys. Lett.* **8** (1964) 214–215.
- [17] G. Zweig, *An $SU(3)$ model for strong interaction symmetry and its breaking. Version 2.* 2, 1964.
- [18] J. I. Friedman and H. W. Kendall, “Deep Inelastic Electron Scattering,” *Annu. Rev. Nucl. Sci.* **22** no. 1, (1972) 203–254. <https://doi.org/10.1146/annurev.ns.22.120172.001223>.
- [19] **E598** Collaboration, J. J. Aubert *et al.*, “Experimental Observation of a Heavy Particle J,” *Phys. Rev. Lett.* **33** (1974) 1404–1406.
- [20] **SLAC-SP-017** Collaboration, J. E. Augustin *et al.*, “Discovery of a Narrow Resonance in e^+e^- Annihilation,” *Phys. Rev. Lett.* **33** (1974) 1406–1408. [Adv. Exp. Phys.5,141(1976)].
- [21] E. G. Cazzoli *et al.*, “Evidence for $\Delta S = -\Delta Q$ Currents or Charmed-Baryon Production by Neutrinos,” *Phys. Rev. Lett.* **34** (Apr, 1975) 1125–1128. <https://link.aps.org/doi/10.1103/PhysRevLett.34.1125>.
- [22] G. Goldhaber and F. M. o. Pierre, “Observation in e^+e^- Annihilation of a Narrow State at 1865 MeV/ c^2 Decaying to $K\pi$ and $K\pi\pi\pi$,” *Phys. Rev. Lett.* **37** (Aug, 1976) 255–259. <https://link.aps.org/doi/10.1103/PhysRevLett.37.255>.
- [23] I. Peruzzi and M. o. Piccolo, “Observation of a Narrow Charged State at 1876 MeV/ c^2 Decaying to an Exotic Combination of $K\pi\pi$,” *Phys. Rev. Lett.* **37** (Sep, 1976) 569–571. <https://link.aps.org/doi/10.1103/PhysRevLett.37.569>.
- [24] D. J. Gross and F. Wilczek, “Asymptotically Free Gauge Theories. I,” *Phys. Rev. D* **8** (Nov, 1973) 3633–3652. <https://link.aps.org/doi/10.1103/PhysRevD.8.3633>.
- [25] D. J. Gross and F. Wilczek, “Asymptotically free gauge theories. II,” *Phys. Rev. D* **9** (Feb, 1974) 980–993. <https://link.aps.org/doi/10.1103/PhysRevD.9.980>.

-
- [26] H. David Politzer, “Asymptotic freedom: An approach to strong interactions,” *Physics Reports* **14** no. 4, (1974) 129–180.
<https://www.sciencedirect.com/science/article/pii/0370157374900143>.
- [27] T. Barnes, S. Godfrey, and E. S. Swanson, “Higher charmonia,” *Phys. Rev. D* **72** (2005) 054026, [arXiv:hep-ph/0505002](https://arxiv.org/abs/hep-ph/0505002) [hep-ph].
- [28] **BaBar** Collaboration, B. Aubert *et al.*, “Observation of a broad structure in the $\pi^+\pi^-J/\psi$ mass spectrum around 4.26 GeV/c²,” *Phys. Rev. Lett.* **95** (2005) 142001, [arXiv:hep-ex/0506081](https://arxiv.org/abs/hep-ex/0506081) [hep-ex].
- [29] **BESIII** Collaboration, M. Ablikim *et al.*, “Precise measurement of the $e^+e^- \rightarrow \pi^+\pi^-J/\psi$ cross section at center-of-mass energies from 3.77 to 4.60 GeV,” *Phys. Rev. Lett.* **118** no. 9, (2017) 092001, [arXiv:1611.01317](https://arxiv.org/abs/1611.01317) [hep-ex].
- [30] **BESIII** Collaboration, M. Ablikim *et al.*, “Observation of a Charged Charmoniumlike Structure in $e^+e^- \rightarrow \pi^+\pi^-J/\psi$ at $\sqrt{s} = 4.26$ GeV,” *Phys. Rev. Lett.* **110** (2013) 252001, [arXiv:1303.5949](https://arxiv.org/abs/1303.5949) [hep-ex].
- [31] **Belle** Collaboration, Z. Q. Liu *et al.*, “Study of $e^+e^- \rightarrow \pi^+\pi^-J/\psi$ and Observation of a Charged Charmoniumlike State at Belle,” *Phys. Rev. Lett.* **110** (2013) 252002, [arXiv:1304.0121](https://arxiv.org/abs/1304.0121) [hep-ex].
- [32] D. Ebert, R. N. Faustov, and V. O. Galkin, “Masses of heavy tetraquarks in the relativistic quark model,” *Phys. Lett. B* **634** (2006) 214–219, [arXiv:hep-ph/0512230](https://arxiv.org/abs/hep-ph/0512230) [hep-ph].
- [33] L. Maiani, V. Riquer, F. Piccinini, and A. D. Polosa, “Four quark interpretation of $Y(4260)$,” *Phys. Rev. D* **72** (2005) 031502, [arXiv:hep-ph/0507062](https://arxiv.org/abs/hep-ph/0507062) [hep-ph].
- [34] A. Ali *et al.*, “A new look at the Y tetraquarks and Ω_c baryons in the diquark model,” *Eur. Phys. J. C* **78** no. 1, (2018) 29.
- [35] X. Liu, X.-Q. Zeng, and X.-Q. Li, “Possible molecular structure of the newly observed $Y(4260)$,” *Phys. Rev. D* **72** (2005) 054023, [arXiv:hep-ph/0507177](https://arxiv.org/abs/hep-ph/0507177) [hep-ph].
- [36] C.-F. Qiao, “One explanation for the exotic state $Y(4260)$,” *Phys. Lett. B* **639** (2006) 263–265, [arXiv:hep-ph/0510228](https://arxiv.org/abs/hep-ph/0510228) [hep-ph].
- [37] Q. Wang, C. Hanhart, and Q. Zhao, “Decoding the riddle of $Y(4260)$ and $Z_c(3900)$,” *Phys. Rev. Lett.* **111** no. 13, (2013) 132003, [arXiv:1303.6355](https://arxiv.org/abs/1303.6355) [hep-ph].

- [38] F. E. Close and P. R. Page, “Gluonic charmonium resonances at BaBar and BELLE?,” *Phys. Lett. B* **628** (2005) 215–222, [arXiv:hep-ph/0507199](#) [hep-ph].
- [39] S.-L. Zhu, “The Possible interpretations of $Y(4260)$,” *Phys. Lett. B* **625** (2005) 212, [arXiv:hep-ph/0507025](#) [hep-ph].
- [40] **BaBar** Collaboration, B. Aubert *et al.*, “Study of the Exclusive Initial-State Radiation Production of the D anti-D System,” *Phys. Rev. D* **76** (2007) 111105, [arXiv:hep-ex/0607083](#).
- [41] **Belle** Collaboration, K. Abe *et al.*, “Measurement of the near-threshold $e^+e^- \rightarrow D^{(*)\pm}D^{(*)\mp}$ cross section using initial-state radiation,” *Phys. Rev. Lett.* **98** (2007) 092001, [arXiv:hep-ex/0608018](#) [hep-ex].
- [42] **BESIII** Collaboration, M. Ablikim *et al.*, “Evidence of Two Resonant Structures in $e^+e^- \rightarrow \pi^+\pi^-h_c$,” *Phys. Rev. Lett.* **118** no. 9, (2017) 092002, [arXiv:1610.07044](#) [hep-ex].
- [43] **BESIII** Collaboration, M. Ablikim *et al.*, “Measurement of $e^+e^- \rightarrow \pi^+\pi^-\psi(3686)$ from 4.008 to 4.600 GeV and observation of a charged structure in the $\pi^\pm\psi(3686)$ mass spectrum,” *Phys. Rev. D* **96** no. 3, (2017) 032004, [arXiv:1703.08787](#) [hep-ex]. [erratum: *Phys. Rev. D* **99**, no. 1, 019903 (2019)].
- [44] **BESIII** Collaboration, M. Ablikim *et al.*, “Observation of a near-threshold enhancement in the $\Lambda\bar{\Lambda}$ mass spectrum from $e^+e^- \rightarrow \phi\Lambda\bar{\Lambda}$ at \sqrt{s} from 3.51 to 4.60 GeV,” *Phys. Rev. D* **104** (Sep, 2021) 052006. <https://link.aps.org/doi/10.1103/PhysRevD.104.052006>.
- [45] M. Ablikim *et al.*, “Measurement of cross sections of the interactions $e^+e^- \rightarrow \phi\phi\omega$ and $e^+e^- \rightarrow \phi\phi\phi$ at center of mass energies from 4.008 to 4.600 GeV,” *Phys. Lett. B* **774** (2017) 78–86. <https://www.sciencedirect.com/science/article/pii/S0370269317307190>.
- [46] **BESIII** Collaboration, M. Ablikim *et al.*, “Precision measurements of the $e^+e^- \rightarrow K_S^0 K^\pm \pi^\mp$ Born cross sections at center-of-mass energies between 3.8 and 4.6 GeV,” *Phys. Rev. D* **99** (Apr, 2019) 072005. <https://link.aps.org/doi/10.1103/PhysRevD.99.072005>.
- [47] **BESIII** Collaboration, M. Ablikim *et al.*, “Measurements of $e^+e^- \rightarrow K_S^0 K^\pm \pi^\mp \pi^0$ and $K_S^0 K^\pm \pi^\mp \eta$ at center-of-mass energies from 3.90 to 4.60 GeV,” *Phys. Rev. D* **99** (Jan, 2019) 012003. <https://link.aps.org/doi/10.1103/PhysRevD.99.012003>.

-
- [48] **BESIII** Collaboration, M. Ablikim *et al.*, “Study of $e^+e^- \rightarrow 2(p\bar{p})$ at center-of-mass energies between 4.0 and 4.6 GeV,” *Phys. Rev. D* **103** no. 5, (2021) 052003, [arXiv:2012.11079](https://arxiv.org/abs/2012.11079) [hep-ex].
- [49] M. Ablikim *et al.*, “Measurements of cross section of $e^+e^- \rightarrow p\bar{p}\pi^0$ at center-of-mass energies between 4.008 and 4.600 GeV,” *Phys. Lett. B* **771** (2017) 45–51.
<https://www.sciencedirect.com/science/article/pii/S0370269317303969>.
- [50] M. Ablikim *et al.*, “Cross section measurement of $e^+e^- \rightarrow p\bar{p}\eta$ and $e^+e^- \rightarrow p\bar{p}\omega$ at center-of-mass energies between 3.773 GeV and 4.6 GeV” [arXiv:2102.04268](https://arxiv.org/abs/2102.04268) [hep-ex].
- [51] **BESIII** Collaboration, M. Ablikim *et al.*, “Determination of the Spin and Parity of the $Z_c(3900)$,” *Phys. Rev. Lett.* **119** (Aug, 2017) 072001.
<https://link.aps.org/doi/10.1103/PhysRevLett.119.072001>.
- [52] **LHCb** Collaboration, R. Aaij, B. Adeva, *et al.*, “Measurement of resonant and CP components in $\bar{B}_s^0 \rightarrow J/\psi\pi^+\pi^-$ decays,” *Phys. Rev. D* **89** (May, 2014) 092006. <https://link.aps.org/doi/10.1103/PhysRevD.89.092006>.
- [53] **LHCb** Collaboration, R. Aaij, B. Adeva, *et al.*, “Measurement of the resonant and CP components in $\bar{B}^0 \rightarrow J/\psi\pi^+\pi^-$ decays,” *Phys. Rev. D* **90** (Jul, 2014) 012003. <https://link.aps.org/doi/10.1103/PhysRevD.90.012003>.
- [54] A. Lundborg, T. Barnes, and U. Wiedner, “Charmonium production in $p\bar{p}$ annihilation: Estimating cross sections from decay widths,” *Phys. Rev. D* **73** (May, 2006) 096003.
<https://link.aps.org/doi/10.1103/PhysRevD.73.096003>.
- [55] P. Collaboration *et al.*, “Physics Performance Report for PANDA: Strong Interaction Studies with Antiprotons,” [arXiv:0903.3905](https://arxiv.org/abs/0903.3905) [hep-ex].
- [56] **Particle Data Group** Collaboration, P. Zyla *et al.*, “Review of Particle Physics,” *PTEP* **2020** no. 8, (2020) 083C01.
- [57] **BESIII** Collaboration, M. Ablikim *et al.*, “Cross section measurement of $e^+e^- \rightarrow \eta' J/\psi$ from $\sqrt{s} = 4.178$ to 4.600 GeV,” *Phys. Rev. D* **101** (Jan, 2020) 012008. <https://link.aps.org/doi/10.1103/PhysRevD.101.012008>.
- [58] M. Guagnelli, R. Sommer, and H. Wittig, “Precision computation of a low-energy reference scale in quenched lattice QCD,” *Nucl. Phys. B* **535** no. 1, (1998) 389–402.
<https://www.sciencedirect.com/science/article/pii/S0550321398005999>.

- [59] N. A. Tornqvist, “The lightest scalar nonet,”
<https://arxiv.org/abs/hep-ph/0201171f>.
- [60] J. R. Peláez, “From controversy to precision on the sigma meson: A review on the status of the non-ordinary resonance,” *Physics Reports* **658** (Nov, 2016) 1–111.
<http://dx.doi.org/10.1016/j.physrep.2016.09.001>.
- [61] W. Lee and D. Weingarten, “Scalar quarkonium masses and mixing with the lightest scalar glueball,” *Phys. Rev. D* **61** (Dec, 1999) 014015.
<https://link.aps.org/doi/10.1103/PhysRevD.61.014015>.
- [62] G. Bali *et al.*, “A comprehensive lattice study of SU(3) glueballs,” *Phys. Lett. B* **309** no. 3, (1993) 378–384.
<https://www.sciencedirect.com/science/article/pii/037026939390948H>.
- [63] C. J. Morningstar and M. Peardon, “Efficient glueball simulations on anisotropic lattices,” *Phys. Rev. D* **56** (Oct, 1997) 4043–4061.
<https://link.aps.org/doi/10.1103/PhysRevD.56.4043>.
- [64] Y. Chen *et al.*, “Glueball spectrum and matrix elements on anisotropic lattices,” *Phys. Rev. D* **73** (Jan, 2006) 014516.
<https://link.aps.org/doi/10.1103/PhysRevD.73.014516>.
- [65] Ropertz Stefan, Hanhart Christoph, and Kubis Bastian, “A new parametrization for the scalar pion form factors,” *Eur. Phys. J. C* **78** no. 12, (2018) 1000.
- [66] A. Einstein, “Die Grundlage der allgemeinen Relativitätstheorie,” *Annalen Phys.* **49** no. 7, (1916) 769–822.
- [67] Z. Maki, M. Nakagawa, and S. Sakata, “Remarks on the Unified Model of Elementary Particles,” *Prog. Theor. Phys.* **28** no. 5, (11, 1962) 870–880,
<https://academic.oup.com/ptp/article-pdf/28/5/870/5258750/28-5-870.pdf>.
<https://doi.org/10.1143/PTP.28.870>.
- [68] B. Pontecorvo, “Neutrino Experiments and the Problem of Conservation of Leptonic Charge,” *Zh. Eksp. Teor. Fiz.* **53** (1967) 1717–1725.
- [69] K. Hirata *et al.*, “Experimental study of the atmospheric neutrino flux,” *Phys. Lett. B* **205** no. 2, (1988) 416–420.
<https://www.sciencedirect.com/science/article/pii/0370269388916905>.
- [70] A. Salam and J. C. Ward, “Weak and electromagnetic interactions,” *Nuovo Cim.* **11** (1959) 568–577.

-
- [71] S. L. Glashow, “The renormalizability of vector meson interactions,” *Nucl. Phys.* **10** (1959) 107–117.
- [72] M. E. Peskin and D. V. Schroeder, *An Introduction To Quantum Field Theory*. Westview Press, 1995.
- [73] J. Schwinger, “On Quantum-Electrodynamics and the Magnetic Moment of the Electron,” *Phys. Rev.* **73** (Feb, 1948) 416–417.
<https://link.aps.org/doi/10.1103/PhysRev.73.416>.
- [74] J. Schwinger, “Quantum Electrodynamics. I. A Covariant Formulation,” *Phys. Rev.* **74** (Nov, 1948) 1439–1461.
<https://link.aps.org/doi/10.1103/PhysRev.74.1439>.
- [75] J. Schwinger, “Quantum Electrodynamics. II. Vacuum Polarization and Self-Energy,” *Phys. Rev.* **75** (Feb, 1949) 651–679.
<https://link.aps.org/doi/10.1103/PhysRev.75.651>.
- [76] J. Schwinger, “Quantum Electrodynamics. III. The Electromagnetic Properties of the Electron—Radiative Corrections to Scattering,” *Phys. Rev.* **76** (Sep, 1949) 790–817. <https://link.aps.org/doi/10.1103/PhysRev.76.790>.
- [77] H. Fukuda and Y. Miyamoto,
“On the γ -Decay of Neutral Meson,” *Prog. Theor. Phys.* **4** no. 3, (09, 1949) 347–357,
<https://academic.oup.com/ptp/article-pdf/4/3/347/5335979/4-3-347.pdf>.
<https://doi.org/10.1143/ptp/4.3.347>.
- [78] R. P. Feynman, “Relativistic Cut-Off for Quantum Electrodynamics,” *Phys. Rev.* **74** (Nov, 1948) 1430–1438.
<https://link.aps.org/doi/10.1103/PhysRev.74.1430>.
- [79] R. P. Feynman, “Space-Time Approach to Quantum Electrodynamics,” *Phys. Rev.* **76** (Sep, 1949) 769–789.
<https://link.aps.org/doi/10.1103/PhysRev.76.769>.
- [80] F. J. Dyson, “The Radiation Theories of Tomonaga, Schwinger, and Feynman,” *Phys. Rev.* **75** (Feb, 1949) 486–502.
<https://link.aps.org/doi/10.1103/PhysRev.75.486>.
- [81] F. J. Dyson, “The S Matrix in Quantum Electrodynamics,” *Phys. Rev.* **75** (Jun, 1949) 1736–1755. <https://link.aps.org/doi/10.1103/PhysRev.75.1736>.
- [82] F. Englert and R. Brout, “Broken Symmetry and the Mass of Gauge Vector Mesons,” *Phys. Rev. Lett.* **13** (Aug, 1964) 321–323.
<https://link.aps.org/doi/10.1103/PhysRevLett.13.321>.

- [83] P. W. Higgs, “Broken Symmetries and the Masses of Gauge Bosons,” *Phys. Rev. Lett.* **13** (Oct, 1964) 508–509.
<https://link.aps.org/doi/10.1103/PhysRevLett.13.508>.
- [84] **CMS** Collaboration, S. Chatrchyan *et al.*, “Observation of a new boson at a Mass of 125 GeV with the CMS Experiment at the LHC,” *Phys. Lett. B* **716** (2012) 30–61, [arXiv:1207.7235](https://arxiv.org/abs/1207.7235) [hep-ex].
- [85] **ATLAS** Collaboration, G. Aad *et al.*, “Observation of a new particle in the search for the Standard Model Higgs boson with the ATLAS detector at the LHC,” *Phys. Lett. B* **716** (2012) 1–29, [arXiv:1207.7214](https://arxiv.org/abs/1207.7214) [hep-ex].
- [86] M. Mikhasenko, “A triangle singularity and the LHCb pentaquarks,” [arXiv:1507.06552](https://arxiv.org/abs/1507.06552) [hep-ph].
- [87] A. Bazilevsky, “The RHIC spin program overview,” *J. Phys.: Conf. Ser.* **678** (Feb, 2016) 012059. <https://doi.org/10.1088/1742-6596/678/1/012059>.
- [88] D. V. Bugg, ed., *Hadron spectroscopy and the confinement problem. Proceedings, NATO Advanced Study Institute, London, Swansea, UK, June 27-July 8, 1995*, vol. 353. 1996.
- [89] M. Aghasyan *et al.*, “Light isovector resonances in $\pi^-p \rightarrow \pi^- \pi^- \pi^+ p$ at 190 GeV/c ,” *Phys. Rev. D* **98** (Nov, 2018) 092003.
<https://link.aps.org/doi/10.1103/PhysRevD.98.092003>.
- [90] **COMPASS** Collaboration, M. G. Alekseev *et al.*, “Observation of a $J^{PC} = 1^{-+}$ exotic resonance in diffractive dissociation of 190 GeV/c $\pi^- \rightarrow \pi^- \pi^- \pi^+$,” *Phys. Rev. Lett.* **104** (Jun, 2010) 241803.
<https://link.aps.org/doi/10.1103/PhysRevLett.104.241803>.
- [91] C. Adolph *et al.*, “Odd and even partial waves of $\eta\pi^-$ and $\eta'\pi^-$ in $\pi^-p \rightarrow \eta^{(\prime)}\pi^-p$ at 191 GeV/c ,” *Phys. Lett. B* **740** (2015) 303–311.
<https://www.sciencedirect.com/science/article/pii/S0370269314008685>.
- [92] A. D. Martin, “An Introduction to Quarks and Partons,” *Physics Bulletin* **30** no. 12, (Dec, 1979) 523–524. <https://doi.org/10.1088/0031-9112/30/12/034>.
- [93] J. H. Christenson, J. W. Cronin, V. L. Fitch, and R. Turlay, “Evidence for the 2π Decay of the K_2^0 Meson,” *Phys. Rev. Lett.* **13** (Jul, 1964) 138–140.
<https://link.aps.org/doi/10.1103/PhysRevLett.13.138>.
- [94] **BABAR** Collaboration, B. Aubert *et al.*, “Observation of CP Violation in the B^0 Meson System,” *Phys. Rev. Lett.* **87** (Aug, 2001) 091801.
<https://link.aps.org/doi/10.1103/PhysRevLett.87.091801>.

-
- [95] Belle Collaboration, K. Abe *et al.*, “Observation of Large CP Violation in the Neutral B Meson System,” *Phys. Rev. Lett.* **87** (Aug, 2001) 091802.
<https://link.aps.org/doi/10.1103/PhysRevLett.87.091802>.
- [96] NA31 Collaboration, H. Burkhardt *et al.*, “First Evidence for Direct CP Violation,” *Phys. Lett. B* **206** (1988) 169–176.
- [97] E. Gamiz, “Kaon Physics: CP Violation and Hadronic Matrix Elements,”
<https://arxiv.org/pdf/hep-ph/0401236.pdf>.
- [98] E. de Rafael, “Chiral Lagrangians and Kaon CP -Violation,”
<https://arxiv.org/pdf/hep-ph/9502254.pdf>.
- [99] KTeV Collaboration, A. Alavi-Harati *et al.*, “Measurement of the K_L Charge Asymmetry,” *Phys. Rev. Lett.* **88** (Apr, 2002) 181601.
<https://link.aps.org/doi/10.1103/PhysRevLett.88.181601>.
- [100] KLOE Collaboration, G. D’Ambrosio and G. Isidori, “Determination of CP and CPT violation parameters in the neutral kaon system using the Bell-Steinberger relation and data from the KLOE experiment,” *JHEP* **12** (2006) 011,
[arXiv:hep-ex/0610034](https://arxiv.org/abs/hep-ex/0610034).
- [101] G. Buchalla, A. J. Buras, and M. E. Lautenbacher, “Weak decays beyond leading logarithms,” *Rev. Mod. Phys.* **68** (Oct, 1996) 1125–1244.
<https://link.aps.org/doi/10.1103/RevModPhys.68.1125>.
- [102] S. Bosch *et al.*, “Standard model confronting new results for ε'/ε ,” *Nucl. Phys. B* **565** no. 1, (2000) 3–37.
<https://www.sciencedirect.com/science/article/pii/S055032139900694X>.
- [103] S. Bertolini, M. Fabbrichesi, and J. O. Eeg, “Theory of the CP -violating parameter ε'/ε ,” *Rev. Mod. Phys.* **72** (Jan, 2000) 65–93.
<https://link.aps.org/doi/10.1103/RevModPhys.72.65>.
- [104] C. Amsler and N. A. Törnqvist, “Mesons beyond the naive quark model,” *Physics Reports* **389** no. 2, (2004) 61–117.
<https://www.sciencedirect.com/science/article/pii/S0370157303003351>.
- [105] M. Melis, F. Murgia, and J. Parisi, “Glueball production in radiative J/ψ , Υ decays,” *Phys. Rev. D* **70** (2004) 034021, [arXiv:hep-ph/0404070](https://arxiv.org/abs/hep-ph/0404070).
- [106] C. Amsler and F. E. Close, “Is $f_0(1500)$ a scalar glueball?,” *Phys. Rev. D* **53** (Jan, 1996) 295–311. <https://link.aps.org/doi/10.1103/PhysRevD.53.295>.

- [107] N. A. Törnqvist and M. Roos, “Confirmation of the Sigma Meson,” *Phys. Rev. Lett.* **76** (Mar, 1996) 1575–1578.
<https://link.aps.org/doi/10.1103/PhysRevLett.76.1575>.
- [108] A. Anisovich, V. Anisovich, and A. Sarantsev, “ 0^{++} -glueball/qq-state mixing in the mass region near 1500 MeV,” *Phys. Lett. B* **395** no. 1, (1997) 123–127.
<https://www.sciencedirect.com/science/article/pii/S0370269397000063>.
- [109] M. Boglione and M. R. Pennington, “Unquenching the Scalar Glueball,” *Phys. Rev. Lett.* **79** (Sep, 1997) 1998–2001.
<https://link.aps.org/doi/10.1103/PhysRevLett.79.1998>.
- [110] H.-Y. Cheng, C.-K. Chua, and K.-F. Liu, “Scalar glueball, scalar quarkonia, and their mixing,” *Phys. Rev. D* **74** (Nov, 2006) 094005.
<https://link.aps.org/doi/10.1103/PhysRevD.74.094005>.
- [111] R. L. Jaffe, “Multiquark hadrons. II. Methods,” *Phys. Rev. D* **15** (Jan, 1977) 281–289. <https://link.aps.org/doi/10.1103/PhysRevD.15.281>.
- [112] M. Alford and R. Jaffe, “Insight into the scalar mesons from a lattice calculation,” *Nucl. Phys. B* **578** no. 1, (2000) 367–382.
<https://www.sciencedirect.com/science/article/pii/S0550321300001553>.
- [113] L. Maiani *et al.*, “New Look at Scalar Mesons,” *Phys. Rev. Lett.* **93** (Nov, 2004) 212002. <https://link.aps.org/doi/10.1103/PhysRevLett.93.212002>.
- [114] L. Maiani, A. Polosa, and V. Riquer, “Structure of light scalar mesons from D_s and D_0 non-leptonic decays,” *Phys. Lett. B* **651** no. 2, (2007) 129–134.
<https://www.sciencedirect.com/science/article/pii/S0370269307006144>.
- [115] J. Weinstein and N. Isgur, “ $K\bar{K}$ molecules,” *Phys. Rev. D* **41** (Apr, 1990) 2236–2257. <https://link.aps.org/doi/10.1103/PhysRevD.41.2236>.
- [116] A. Aloisio, F. Ambrosino, *et al.*, “Study of the decay $\phi \rightarrow \eta\pi^0\gamma$ with the KLOE detector,” *Phys. Lett. B* **536** no. 3, (2002) 209–216.
<https://www.sciencedirect.com/science/article/pii/S037026930201821X>.
- [117] A. Aloisio, F. Ambrosino, *et al.*, “Study of the decay $\phi \rightarrow \pi^0\pi^0\gamma$ with the KLOE detector,” *Phys. Lett. B* **537** no. 1, (2002) 21–27.
<https://www.sciencedirect.com/science/article/pii/S0370269302018385>.
- [118] R. Akhmetshin, E. Anashkin, *et al.*, “First observation of the $\phi \rightarrow \pi^+\pi^-\gamma$ decay,” *Phys. Lett. B* **462** no. 3, (1999) 371–379.
<https://www.sciencedirect.com/science/article/pii/S0370269399009193>.

-
- [119] M. Achasov, S. Baru, *et al.*, “The $\phi \rightarrow \eta\pi^0\gamma$ decay,” *Phys. Lett. B* **479** no. 1, (2000) 53–58.
<https://www.sciencedirect.com/science/article/pii/S0370269300003348>.
- [120] F. Close, N. Isgur, and S. Kumano, “Scalar mesons in ϕ radiative decay: Their implications for spectroscopy and for studies of CP violation at ϕ factories,” *Nucl. Phys. B* **389** no. 2, (1993) 513–533.
<https://www.sciencedirect.com/science/article/pii/055032139390329N>.
- [121] N. N. Achasov, V. V. Gubin, and V. I. Shevchenko, “Production of scalar $K\bar{K}$ molecules in φ radiative decays,” *Phys. Rev. D* **56** (Jul, 1997) 203–211.
<https://link.aps.org/doi/10.1103/PhysRevD.56.203>.
- [122] S. Stone and L. Zhang, “Use of $B \rightarrow J/\psi f_0$ Decays to Discern the $q\bar{q}$ or Tetraquark Nature of Scalar Mesons,” *Phys. Rev. Lett.* **111** (Aug, 2013) 062001.
<https://link.aps.org/doi/10.1103/PhysRevLett.111.062001>.
- [123] Daub J. T., Hanhart C., and Kubis B., “A model-independent analysis of final-state interactions in $\bar{B}_{d/s}^0 \rightarrow J/\psi\pi\pi$,” *J. High Energ. Phys.* **2016** no. 2, (2016) 9.
- [124] D. Barberis, F. Binon, *et al.*, “A spin analysis of the 4π channels produced in central pp interactions at 450 GeV/c,” *Phys. Lett. B* **471** no. 4, (2000) 440–448.
<https://www.sciencedirect.com/science/article/pii/S0370269399014136>.
- [125] **WA102** Collaboration, D. Barberis *et al.*, “A Study of the $f(0)(1370)$, $f(0)(1500)$, $f(0)(2000)$ and $f(2)(1950)$ observed in the centrally produced 4π final states,” *Phys. Lett. B* **474** (2000) 423–426, [arXiv:hep-ex/0001017](https://arxiv.org/abs/hep-ex/0001017).
- [126] **WA102** Collaboration, D. Barberis *et al.*, “A Coupled channel analysis of the centrally produced $K^+ K^-$ and $\pi^+ \pi^-$ final states in $p p$ interactions at 450-GeV/c,” *Phys. Lett. B* **462** (1999) 462–470, [arXiv:hep-ex/9907055](https://arxiv.org/abs/hep-ex/9907055).
- [127] **Crystal Barrel** Collaboration, C. Amsler *et al.*, “Proton anti-proton annihilation at 900-MeV/c into $\pi^0 \pi^0 \pi^0$, $\pi^0 \pi^0 \eta$ and $\pi^0 \eta \eta$,” *Eur. Phys. J. C* **23** (2002) 29–41.
- [128] C. Amsler *et al.*, “Study of $K\bar{K}$ resonances in $p\bar{p} \rightarrow KK\pi$ at 900 and 1640 MeV/c,” *Phys. Lett. B* **639** (08, 2006) 165–171.
- [129] N. Isgur and H. B. Thacker, “Origin of the Okubo-Zweig-Iizuka rule in QCD,” *Phys. Rev. D* **64** (Oct, 2001) 094507.
<https://link.aps.org/doi/10.1103/PhysRevD.64.094507>.

- [130] F. E. Close and Q. Zhao, “Production of $f_0(1710)$, $f_0(1500)$, and $f_0(1370)$ in J/ψ hadronic decays,” *Phys. Rev. D* **71** (2005) 094022, [arXiv:hep-ph/0504043](#).
- [131] M. Acciarri *et al.*, “K0SK0S final state in two-photon collisions and implications for glueballs,” *Phys. Lett. B* **501** no. 3, (2001) 173–182.
<https://www.sciencedirect.com/science/article/pii/S0370269301001162>.
- [132] Belle Collaboration, K. Abe *et al.*, “Measurement of $K^+ K^-$ production in two photon collisions in the resonant mass region,” *Eur. Phys. J. C* **32** (2003) 323–336, [arXiv:hep-ex/0309077](#).
- [133] S. Uehara *et al.*, “High-statistics study of K_S^0 pair production in two-photon collisions,” *Prog. Theor. Exp. Phys.* **2013** no. 12, (12, 2013) ,
<https://academic.oup.com/ptep/article-pdf/2013/12/123C01/4436591/ptt097.pdf>.
<https://doi.org/10.1093/ptep/ptt097.123C01>.
- [134] ALEPH Collaboration, R. Barate *et al.*, “Search for the glueball candidates $f(0)(1500)$ and $f(J)(1710)$ in $\gamma\gamma$ collisions,” *Phys. Lett. B* **472** (2000) 189–199, [arXiv:hep-ex/9911022](#).
- [135] Belle Collaboration, S. Uehara, Y. Watanabe, *et al.*, “High-statistics measurement of neutral-pion pair production in two-photon collisions,” *Phys. Rev. D* **78** (Sep, 2008) 052004.
<https://link.aps.org/doi/10.1103/PhysRevD.78.052004>.
- [136] M. Ablikim *et al.*, “Study of $J/\psi \rightarrow \omega K^+ K^-$,” *Phys. Lett. B* **603** no. 3, (2004) 138–145.
<https://www.sciencedirect.com/science/article/pii/S0370269304014789>.
- [137] M. Ablikim *et al.*, “Resonances in $J/\psi \rightarrow \phi\pi^+\pi^-$ and $\phi K^+ K^-$,” *Phys. Lett. B* **607** no. 3, (2005) 243–253.
<https://www.sciencedirect.com/science/article/pii/S0370269304017265>.
- [138] M. Ablikim *et al.*, “Partial wave analyses of $J/\psi \rightarrow \gamma\pi^+\pi^-$ and $\gamma\pi^0\pi^0$,” *Phys. Lett. B* **642** no. 5, (2006) 441–448.
<https://www.sciencedirect.com/science/article/pii/S0370269306012573>.
- [139] BESIII Collaboration, M. Ablikim *et al.*, “Partial wave analysis of $J/\psi \rightarrow \gamma\eta\eta$,” *Phys. Rev. D* **87** (May, 2013) 092009.
<https://link.aps.org/doi/10.1103/PhysRevD.87.092009>.
- [140] V. Crede and W. Roberts, “Prog. Theor. Phys. towards understanding baryon resonances,” *Rept. Prog. Phys.* **76** (2013) 076301, [arXiv:1302.7299 \[nucl-ex\]](#).

-
- [141] **BABAR** Collaboration, B. Aubert *et al.*, “Study of the $B^- \rightarrow J/\psi K^- \pi^+ \pi^-$ decay and measurement of the $B^- \rightarrow X(3872)K^-$ branching fraction,” *Phys. Rev. D* **71** (Apr, 2005) 071103.
<https://link.aps.org/doi/10.1103/PhysRevD.71.071103>.
- [142] M. Cleven *et al.*, “ $Y(4260)$ as the first S -wave open charm vector molecular state?,” *Phys. Rev. D* **90** (Oct, 2014) 074039.
<https://link.aps.org/doi/10.1103/PhysRevD.90.074039>.
- [143] C. Hanhart, “Theory Concepts for Heavy Exotic Mesons,” *International Journal of Modern Physics: Conference Series* **46** (Jan, 2018) 1860004.
<http://dx.doi.org/10.1142/S2010194518600042>.
- [144] **BESIII** Collaboration, M. Ablikim *et al.*, “Observation of $e^+e^- \rightarrow \gamma X(3872)$ at BESIII,” *Phys. Rev. Lett.* **112** (Mar, 2014) 092001.
<https://link.aps.org/doi/10.1103/PhysRevLett.112.092001>.
- [145] Q. Wang, C. Hanhart, and Q. Zhao, “Decoding the Riddle of $Y(4260)$ and $Z_c(3900)$,” *Phys. Rev. Lett.* **111** (Sep, 2013) 132003.
<https://link.aps.org/doi/10.1103/PhysRevLett.111.132003>.
- [146] F.-K. Guo *et al.*, “Production of the $X(3872)$ in charmonia radiative decays,” *Phys. Lett. B* **725** no. 1, (2013) 127–133.
<https://www.sciencedirect.com/science/article/pii/S0370269313005285>.
- [147] F. E. Close and P. R. Page, “Gluonic charmonium resonances at BaBar and Belle?,” *Phys. Lett. B* **628** no. 3, (2005) 215–222.
<https://www.sciencedirect.com/science/article/pii/S0370269305012980>.
- [148] M. Berwein, N. Brambilla, J. Tarrús Castellà, and A. Vairo, “Quarkonium hybrids with nonrelativistic effective field theories,” *Phys. Rev. D* **92** (Dec, 2015) 114019.
<https://link.aps.org/doi/10.1103/PhysRevD.92.114019>.
- [149] E. Kou and O. Pene, “Suppressed decay into open charm for the $Y(4260)$ being an hybrid,” *Phys. Lett. B* **631** no. 4, (2005) 164–169.
<https://www.sciencedirect.com/science/article/pii/S0370269305013262>.
- [150] Y. S. Kalashnikova and A. V. Nefediev, “Spectra and decays of hybrid charmonia,” *Phys. Rev. D* **77** (Mar, 2008) 054025.
<https://link.aps.org/doi/10.1103/PhysRevD.77.054025>.
- [151] **BESIII** Collaboration, M. Ablikim *et al.*, “Observation of a Charged Charmoniumlike Structure $Z_c(4020)$ and Search for the $Z_c(3900)$ in

- $e^+e^- \rightarrow \pi^+\pi^-h_c$,” *Phys. Rev. Lett.* **111** (Dec, 2013) 242001.
<https://link.aps.org/doi/10.1103/PhysRevLett.111.242001>.
- [152] **BESIII** Collaboration, M. Ablikim *et al.*, “First measurement of $e^+e^- \rightarrow pK_S^0\bar{n}K^- + \text{c.c.}$ above open charm threshold,” *Phys. Rev. D* **98** (Aug, 2018) 032014. <https://link.aps.org/doi/10.1103/PhysRevD.98.032014>.
- [153] D. M. Asner *et al.*, “Physics at BES-III,” *Int. J. Mod. Phys. A* **24** (2009) S1–794, [arXiv:0809.1869](https://arxiv.org/abs/0809.1869) [hep-ex].
- [154] N. Brambilla *et al.*, “The XYZ states: Experimental and theoretical status and perspectives,” *Physics Reports* **873** (2020) 1–154.
<https://www.sciencedirect.com/science/article/pii/S0370157320301915>.
The XYZ states: experimental and theoretical status and perspectives.
- [155] K. J. Peters, “A Primer on partial wave analysis,” *Int. J. Mod. Phys. A* **21** (2006) 5618–5624, [arXiv:hep-ph/0412069](https://arxiv.org/abs/hep-ph/0412069) [hep-ph]. [,451(2004)].
- [156] Ropertz Stefan, Hanhart Christoph, and Kubis Bastian, “A new parametrization for the scalar pion form factors,” *Eur. Phys. J. C* **78** no. 12, (2018) 1000.
- [157] L. D. Landau, “On analytic properties of vertex parts in quantum field theory,” *Sov. Phys. JETP* **10** no. 1, (1959) 45–50.
- [158] G. F. Chew, “S-Matrix Theory of Strong Interactions without Elementary Particles,” *Rev. Mod. Phys.* **34** no. 3, (1962) 394–401.
- [159] H. P. Stapp, “Derivation of the CPT Theorem and the Connection between Spin and Statistics from Postulates of the S-Matrix Theory,” *Phys. Rev.* **125** (Mar, 1962) 2139–2162. <https://link.aps.org/doi/10.1103/PhysRev.125.2139>.
- [160] J. Gunson, “Unitarity and on-mass-shell analyticity as a basis for S-matrix theories. I” *j-J-MATH-PHYS* **6** no. 6, (June, 1965) 827–844.
http://jmp.aip.org/resource/1/jmapaq/v6/i6/p827_s1.
- [161] J. Gunson, “Unitarity and on-mass-shell analyticity as a basis for S-matrix theories. II,” *j-J-MATH-PHYS* **6** no. 6, (June, 1965) 845–851.
http://jmp.aip.org/resource/1/jmapaq/v6/i6/p845_s1.
- [162] J. Gunson, “Unitarity and on-mass-shell analyticity as a basis for S-matrix theories. III,” *j-J-MATH-PHYS* **6** no. 6, (June, 1965) 852–858.
http://jmp.aip.org/resource/1/jmapaq/v6/i6/p852_s1.

-
- [163] R. Eden, P. Landshoff, D. Olive, and J. Polkinghorne, *The Analytic S-Matrix*. Cambridge University Press, 2002.
<https://books.google.de/books?id=VWTn1TyjwjMC>.
- [164] A. R. White, “The Past and Future of the S -Matrix Theory,”
<https://arxiv.org/abs/hep-ph/0002303v1>.
- [165] S. U. Chung, “Spin formalisms,” *CERN-71-08* (1971).
- [166] J. D. Richman, “An Experimenter’s Guide to the Helicity Formalism,”
- [167] D. I. Olive, “Unitarity and the evaluation of discontinuities. — iii,” *Il Nuovo Cimento (1955-1965)* **37** (June, 1965) 1422–1445.
- [168] S. Mandelstam, “Determination of the Pion-Nucleon Scattering Amplitude from Dispersion Relations and Unitarity. General Theory,” *Phys. Rev.* **112** (Nov, 1958) 1344–1360. <https://link.aps.org/doi/10.1103/PhysRev.112.1344>.
- [169] S. Ropertz, *A formalism for a consistent treatment of two-pion interactions in heavy meson decays*. PhD thesis, Rheinischen Friedrich-Wilhelms-Universität Bonn, 2020.
- [170] J. Schwinger, “The Theory of Quantized Fields. I,” *Phys. Rev.* **82** (Jun, 1951) 914–927. <https://link.aps.org/doi/10.1103/PhysRev.82.914>.
- [171] G. Luders, “On the Equivalence of Invariance under Time Reversal and under Particle-Antiparticle Conjugation for Relativistic Field Theories,” *Kong. Dan. Vid. Sel. Mat. Fys. Med.* **28N5** no. 5, (1954) 1–17.
- [172] S. K. Allison, “Niels Bohr and the Development of Physics, edited by W. Pauli with the assistance of L. Rosenfeld and V. Weisskopf,” *j-BULL-AT-SCI* **12** no. 2, (Feb., 1956) 61–61.
- [173] J. S. Bell, “Time reversal in field theory,” *Proc. Roy. Soc. Lond. A* **231** (1955) 479–495.
- [174] C. Hanhart, “Amplitude analysis for mesons and baryons: Tools and technology,” <http://dx.doi.org/10.1063/1.4949383>.
- [175] D. J. Lange, “The EvtGen particle decay simulation package,” *Nucl. Instrum. Meth. A* **462** (2001) 152–155.
- [176] A. Ryd *et al.*, “EvtGen - A Monte Carlo Generator for B -Physics,” 2004.
<https://evtgen.hepforge.org/doc/EvtGenGuide.pdf>. found online on 10-11-2021 10:57.

- [177] M. Albrecht *et al.*, “Coupled channel analysis of $\bar{p}p \rightarrow \pi^0\pi^0\eta$, $\pi^0\eta\eta$ and $K^+K^-\pi^0$ at 900 MeV/c and of $\pi\pi$ -scattering data,” *Eur. Phys. J. C* **80** no. 5, (2020) 453.
- [178] E. Omnès, “On the solution of certain singular integral equations of quantum field theory,” *Il Nuovo Cimento (1955-1965)* **8** (Apr., 1958) 316–326.
- [179] J. F. Donoghue, J. Gasser, and H. Leutwyler, “The decay of a light Higgs boson,” *Nucl. Phys. B* **343** no. 2, (1990) 341–368.
<https://www.sciencedirect.com/science/article/pii/055032139090474R>.
- [180] J. Gasser and U. G. Meissner, “Chiral expansion of pion form-factors beyond one loop,” *Nucl. Phys. B* **357** (1991) 90–128.
- [181] F.-K. Guo, C. Hanhart, F. J. Llanes-Estrada, and U.-G. Meißner, “Quark mass dependence of the pion vector form factor,” *Phys. Lett. B* **678** no. 1, (Jul, 2009) 90–96. <http://dx.doi.org/10.1016/j.physletb.2009.05.052>.
- [182] C. Hanhart, “A new parameterization for the pion vector form factor,” *Phys. Lett. B* **715** no. 1-3, (Aug, 2012) 170–177.
<http://dx.doi.org/10.1016/j.physletb.2012.07.038>.
- [183] K. M. Watson, “Some General Relations between the Photoproduction and Scattering of π Mesons,” *Phys. Rev.* **95** (Jul, 1954) 228–236.
<https://link.aps.org/doi/10.1103/PhysRev.95.228>.
- [184] G. Colangelo, J. Gasser, and H. Leutwyler, “ $\pi\pi$ scattering,” *Nucl. Phys. B* **603** no. 1-2, (Jun, 2001) 125–179.
[http://dx.doi.org/10.1016/S0550-3213\(01\)00147-X](http://dx.doi.org/10.1016/S0550-3213(01)00147-X).
- [185] R. García-Martín *et al.*, “Pion-pion scattering amplitude. iv. improved analysis with once subtracted roy-like equations up to 1100 mev,” *Phys. Rev. D* **83** (Apr, 2011) 074004. <https://link.aps.org/doi/10.1103/PhysRevD.83.074004>.
- [186] B. Ananthanarayan *et al.*, “Roy equation analysis of $\pi\pi$ scattering,” *Physics Reports* **353** no. 4, (Nov, 2001) 207–279.
[http://dx.doi.org/10.1016/S0370-1573\(01\)00009-6](http://dx.doi.org/10.1016/S0370-1573(01)00009-6).
- [187] Caprini I., Colangelo G., and Leutwyler H., “Regge analysis of the $\pi\pi$ scattering amplitude,” *Eur. Phys. J. C* **72** no. 2, (2012) 1860.
- [188] P. Büttiker, S. Descotes-Genon, and B. Moussallam, “A new analysis of πK scattering from Roy and Steiner type equations,” *Eur. Phys. J. C* **33** no. 3, (Mar, 2004) 409–432. <http://dx.doi.org/10.1140/epjc/s2004-01591-1>.

-
- [189] Pelaez J. R. and Rodas A., “ $\pi\pi \rightarrow K\bar{K}$ scattering up to 1.47 GeV with hyperbolic dispersion relations,” *Eur. Phys. J. C* **78** no. 11, (2018) 897.
- [190] B. Moussallam, “ N_f dependence of the quark condensate from a chiral sum rule,” *Eur. Phys. J. C* **14** no. 1, (May, 2000) 111–122.
<http://dx.doi.org/10.1007/s100520000303>.
- [191] Hoferichter M., Ditsche C., Kubis B., and Meißner U.-G., “Dispersive analysis of the scalar form factor of the nucleon,” *J. High Energ. Phys.* **2012** no. 6, (2012) 63.
- [192] S. Descotes, “Zweig rule violation in the scalar sector and values of low-energy constants,” *J. High Energ. Phys.* **2001** no. 03, (Mar, 2001) 002–002.
<http://dx.doi.org/10.1088/1126-6708/2001/03/002>.
- [193] J. T. Daub *et al.*, “Improving the hadron physics of non-Standard-Model decays: example bounds on R-parity violation,” *J. High Energ. Phys.* **2013** no. 1, (2013) 179.
- [194] A. Celis, V. Cirigliano, and E. Passemar, “Lepton flavor violation in the Higgs sector and the role of hadronic τ -lepton decays,” *Phys. Rev. D* **89** (Jan, 2014) 013008. <https://link.aps.org/doi/10.1103/PhysRevD.89.013008>.
- [195] M. W. Winkler, “Decay and detection of a light scalar boson mixing with the higgs boson,” *Phys. Rev. D* **99** (Jan, 2019) 015018.
<https://link.aps.org/doi/10.1103/PhysRevD.99.015018>.
- [196] R. Aaij *et al.*, “Resonances and CP violation in $\bar{B}_s^0 \rightarrow J/\psi K^+ K^-$ decays in the mass region above the $\phi(1020)$,” *J. High Energ. Phys.* **2017** no. 8, (2017) 37.
- [197] L.-Y. Dai and M. R. Pennington, “Comprehensive amplitude analysis of $\gamma\gamma \rightarrow \pi^+\pi^-, \pi^0\pi^0$ and $K\bar{K}$ below 1.5 GeV,” *Phys. Rev. D* **90** (Aug, 2014) 036004.
<https://link.aps.org/doi/10.1103/PhysRevD.90.036004>.
- [198] **LHCb** Collaboration, R. Aaij *et al.*, “Analysis of the resonant components in $\bar{B}_s^0 \rightarrow J/\psi\pi^+\pi^-$,” *Phys. Rev. D* **86** (Sep, 2012) 052006.
<https://link.aps.org/doi/10.1103/PhysRevD.86.052006>.
- [199] S. Scherer, “Introduction to Chiral Perturbation Theory,” [arXiv:0210398](https://arxiv.org/abs/0210398) [hep-ph].
- [200] **BESIII** Collaboration, M. Ablikim *et al.*, “Future Physics Programme of BESIII,” *Chin. Phys. C* **44** no. 4, (2020) 040001, [arXiv:1912.05983](https://arxiv.org/abs/1912.05983) [hep-ex].
- [201] C. Zhang *et al.*, “Construction and Commissioning of BEPCII,” in *Particle accelerator. Proceedings, 23rd Conference, PAC’09, Vancouver, Canada, May 4-8*,

- 2009, p. MO3RAI03. 2010.
<http://accelconf.web.cern.ch/AccelConf/PAC2009/papers/mo3rai03.pdf>.
- [202] M. Aiba *et al.*, “Top-up injection schemes for future circular lepton collider,” *Nucl. Instrum. Meth. A* **880** (2018) 98–106.
- [203] Institute of High Energy Physics, CAS, “Photo/Video Gallery,” 2019.
<http://english.ihep.cas.cn/bes/chnl/132/index.html>. found online on 10-14-2019 17:43.
- [204] Institute of High Energy Physics, CAS, “BEPC & BEPCII,” 2019.
<http://english.ihep.cas.cn/doc/1840.html>. found online on 10-16-2019 14:47.
- [205] **BESIII** Collaboration, M. Ablikim *et al.*, “Design and Construction of the BESIII Detector,” *Nucl. Instrum. Meth. A* **614** (2010) 345–399, [arXiv:0911.4960](https://arxiv.org/abs/0911.4960) [physics.ins-det].
- [206] Q. Gang *et al.*, “Particle identification using artificial neural networks at BESIII,” *Chin. Phys. C* **32** (2008) 001.
- [207] M.-Y. Dong *et al.*, “Aging effect in the BESIII drift chamber,” *Chin. Phys. C* **40** no. 1, (Jan, 2016) 016001.
<http://dx.doi.org/10.1088/1674-1137/40/1/016001>.
- [208] S. Marcello *et al.*, “The new CGEM Inner Tracker and the new TIGER ASIC for the BES III Experiment,” *PoS EPS-HEP2017* (2017) 505.
- [209] Y. Guan, X.-R. Lü, Y. Zheng, and Y.-F. Wang, “Study of the efficiency of event start time determination at BESIII,” *Chin. Phys. C* **38** no. 1, (2014) 016201, [arXiv:1304.6177](https://arxiv.org/abs/1304.6177) [physics.ins-det].
- [210] X. Wang *et al.*, “The upgrade system of BESIII ETOF with MRPC technology,” *JINST* **11** no. 08, (2016) C08009, [arXiv:1604.02701](https://arxiv.org/abs/1604.02701) [physics.ins-det].
- [211] **BESIII** Collaboration, M. Ablikim *et al.*, “Measurement of the integrated luminosities of the data taken by BESIII at $\sqrt{s} = 3.650$ and 3.773 GeV,” *Chin. Phys. C* **37** (2013) 123001, [arXiv:1307.2022](https://arxiv.org/abs/1307.2022) [hep-ex].
- [212] **BESIII** Collaboration, M. Ablikim *et al.*, “Measurement of the center-of-mass energies at BESIII via the di-muon process,” *Chin. Phys. C* **40** no. 6, (2016) 063001, [arXiv:1510.08654](https://arxiv.org/abs/1510.08654) [hep-ex].

-
- [213] **BESIII** Collaboration, M. Ablikim *et al.*, “Study of $e^+e^- \rightarrow \gamma\omega J/\psi$ and Observation of $X(3872) \rightarrow \omega J/\psi$,” *Phys. Rev. Lett.* **122** no. 23, (2019) 232002, [arXiv:1903.04695 \[hep-ex\]](#).
- [214] **BESIII** Collaboration, M. Ablikim *et al.*, “Precision measurement of the integrated luminosity of the data taken by BESIII at center of mass energies between 3.810 GeV and 4.600 GeV,” *Chin. Phys. C* **39** no. 9, (2015) 093001, [arXiv:1503.03408 \[hep-ex\]](#).
- [215] W.-D. Li, Y.-J. Mao, and Y.-F. Wang, “The BES-III detector and offline software,” *Int. J. Mod. Phys. A* **24S1** (2009) 9–21.
- [216] G. Barrand *et al.*, “GAUDI - A software architecture and framework for building HEP data processing applications,” *Comput. Phys. Commun.* **140** (2001) 45–55.
- [217] **GEANT4** Collaboration, S. Agostinelli *et al.*, “GEANT4: A Simulation toolkit,” *Nucl. Instrum. Meth. A* **506** (2003) 250–303.
- [218] Z.-Y. DENG *et al.*, “Object-Oriented BESIII Detector Simulation System,” *Chin. Phys. C* **30** (2006) 006.
- [219] S. Jadach, B. F. L. Ward, and Z. Was, “The Precision Monte Carlo event generator KK for two fermion final states in e^+e^- collisions,” *Comput. Phys. Commun.* **130** (2000) 260–325, [arXiv:hep-ph/9912214 \[hep-ph\]](#).
- [220] R.-G. Ping, “Event generators at BESIII,” *Chin. Phys. C* **32** (2008) 599.
- [221] D. J. Lange, “The EvtGen particle decay simulation package,” *Nucl. Instrum. Meth. A* **462** (2001) 152–155.
- [222] S. Jadach *et al.*, “Coherent exclusive exponentiation for precision Monte Carlo calculations,” *Phys. Rev. D* **63** (2001) 113009, [arXiv:hep-ph/0006359 \[hep-ph\]](#).
- [223] B. Andersson *et al.*, “Parton Fragmentation and String Dynamics,” *Phys. Rept.* **97** (1983) 31–145.
- [224] B. Andersson and H.-m. Hu, “Few body states in Lund string fragmentation model,” [arXiv:hep-ph/9910285 \[hep-ph\]](#).
- [225] J. C. Chen *et al.*, “Event generator for J/psi and psi(2S) decay,” *Phys. Rev. D* **62** (2000) 034003.
- [226] R.-L. Yang, R.-G. Ping, and H. Chen, “Tuning and Validation of the Lundcharm Model with J/ψ Decays,” *Chin. Phys. Lett.* **31** no. 6, (Jun, 2014) 061301. <https://doi.org/10.1088/0256-307x/31/6/061301>.

- [227] R. E. Kalman, “A New Approach to Linear Filtering and Prediction Problems,” *J. Basic Eng.* **82** (1960) 35–45.
- [228] C. M. Bishop, *Neural Networks for Pattern Recognition*. Oxford University Press, USA, 1996.
- [229] R. Brun and F. Rademakers, “ROOT: An object oriented data analysis framework,” *Nucl. Instrum. Meth. A* **389** (1997) 81–86.
- [230] I. Antcheva *et al.*, “ROOT: A C++ framework for petabyte data storage, statistical analysis and visualization,” *Comput. Phys. Commun.* **182** (2011) 1384–1385.
- [231] Ohnishi Yukiyoishi, “Track Parametrization,” 1997. <https://citeseerx.ist.psu.edu/viewdoc/download?doi=10.1.1.23.2827&rep=rep1&type=pdf>. found online on 02-19-2021 18:19.
- [232] X. Min *et al.*, “Primary vertex reconstruction based on the Kalman filter technique at BESIII,” *Chin. Phys. C* **34** no. 1, (Jan, 2010) 92–98. <https://doi.org/10.1088/1674-1137/34/1/017>.
- [233] M. He, “Simulation and reconstruction of the BESIII EMC,” *J. Phys. Conf. Ser.* **293** (2011) 012025.
- [234] L. Yan *et al.*, “Lagrange multiplier method used in BESIII kinematic fitting,” *Chin. Phys. C* **34** (2010) 204–209.
- [235] **BESIII** Collaboration, M. Ablikim *et al.*, “Study of $e^+e^- \rightarrow \omega\chi_{cJ}$ at center-of-mass energies from 4.21 to 4.42 GeV,” *Phys. Rev. Lett.* **114** no. 9, (2015) 092003, [arXiv:1410.6538](https://arxiv.org/abs/1410.6538) [hep-ex].
- [236] **BESIII** Collaboration, M. Ablikim *et al.*, “Search for hadronic transition $\chi_{cJ} \rightarrow \eta_c\pi^+\pi^-$ and observation of $\chi_{cJ} \rightarrow K\bar{K}\pi\pi$,” *Phys. Rev. D* **87** (Jan, 2013) 012002. <https://link.aps.org/doi/10.1103/PhysRevD.87.012002>.
- [237] B. internal, “BESIII memo ”Determination of K_S^0 Efficiency Systematics”,”. <https://docbes3.ihep.ac.cn/cgi-bin/DocDB/ShowDocument?docid=520>.
- [238] S. U. Chung, “Formulas for Angular-Momentum Barrier Factors”, *BNL-QGS-06-101* (2015).
- [239] V. Anisovich and A. Sarantsev, “K-matrix analysis of the (IJPC = 00+ +)-wave in the mass region below 1900 MeV,” *Eur. Phys. J. A* **16** no. 2, (Feb, 2003) 229–258. <http://dx.doi.org/10.1140/epja/i2002-10068-x>.

-
- [240] B. Kopf, H. Koch, J. Pychy, and U. Wiedner, “Partial wave analysis for $\bar{p}p$ and e^+e^- annihilation processes,” *Hyperfine Interact.* **229** no. 1-3, (2014) 69–74.
- [241] **BESIII** Collaboration, M. Ablikim *et al.*, “Observation of $\eta_c \rightarrow \omega\omega$ in $J/\psi \rightarrow \gamma\omega\omega$,” *Phys. Rev. D* **100** (Sep, 2019) 052012.
<https://link.aps.org/doi/10.1103/PhysRevD.100.052012>.
- [242] F. Jegerlehner, “Electroweak effective couplings for future precision experiments,” *Nuovo Cim.* **C034S1** (2011) 31–40, [arXiv:1107.4683](https://arxiv.org/abs/1107.4683) [hep-ph].
- [243] F. James and M. Roos, “Minuit: A System for Function Minimization and Analysis of the Parameter Errors and Correlations,” *Comput. Phys. Commun.* **10** (1975) 343–367.
- [244] L. Moneta *et al.*, “The RooStats Project,” *PoS ACAT2010* (2010) 057, [arXiv:1009.1003](https://arxiv.org/abs/1009.1003) [physics.data-an].
- [245] C. Rover, C. Messenger, and R. Prix, “Bayesian versus frequentist upper limits,” in *Proceedings, PHYSTAT 2011 Workshop on Statistical Issues Related to Discovery Claims in Search Experiments and Unfolding, CERN, Geneva, Switzerland 17-20 January 2011*, pp. 158–163, CERN. CERN, Geneva, 2011. [arXiv:1103.2987](https://arxiv.org/abs/1103.2987) [physics.data-an].
- [246] A. Gelman *et al.*, *Bayesian Data Analysis*. Chapman and Hall/CRC, 2013.
- [247] K. Zhu, X. H. Mo, C. Z. Yuan, and P. Wang, “A mathematical review on the multiple-solution problem,” *Int. J. Mod. Phys. A* **26** (2011) 4511–4520, [arXiv:1108.2760](https://arxiv.org/abs/1108.2760) [hep-ex].
- [248] W.-L. Yuan *et al.*, “Study of tracking efficiency and its systematic uncertainty from $J/\psi \rightarrow p\bar{p}\pi^+\pi^-$ at BESIII,” *Chin. Phys. C* **40** no. 2, (2016) 026201, [arXiv:1507.03453](https://arxiv.org/abs/1507.03453) [hep-ex].
- [249] M. Ablikim *et al.*, “Determination of the number of $\psi(3686)$ events at BESIII,” *Chin. Phys. C* **42** no. 2, (Feb, 2018) 023001.
<https://doi.org/10.1088/1674-1137/42/2/023001>.
- [250] R. Molina, D. Nicmorus, and E. Oset, “ $\rho\rho$ interaction in the hidden gauge formalism and the $f_0(1370)$ and $f_2(1270)$ resonances,” *Phys. Rev. D* **78** (Dec, 2008) 114018. <https://link.aps.org/doi/10.1103/PhysRevD.78.114018>.
- [251] L. S. Geng and E. Oset, “Vector meson-vector meson interaction in a hidden gauge unitary approach,” *Phys. Rev. D* **79** (Apr, 2009) 074009.
<https://link.aps.org/doi/10.1103/PhysRevD.79.074009>.

- [252] Gülmez D., Meißner U.-G., and Oller J. A., “A chiral covariant approach to $\rho\rho$ scattering,” *Eur. Phys. J. C* **77** no. 7, (2017) 460.
- [253] M.-L. Du *et al.*, “Interactions between vector mesons and dynamically generated resonances,” *Eur. Phys. J. C* **78** no. 12, (2018) 988.
- [254] Masjuan Pere and Sanz-Cillero Juan José, “Padé approximants and resonance poles,” *Eur. Phys. J. C* **73** no. 10, (2013) 2594.
- [255] P. Masjuan, J. Ruiz de Elvira, and J. J. Sanz-Cillero, “Precise determination of resonance pole parameters through padé approximants,” *Phys. Rev. D* **90** (Nov, 2014) 097901. <https://link.aps.org/doi/10.1103/PhysRevD.90.097901>.
- [256] I. Caprini *et al.*, “Uncertainty estimates of the σ -pole determination by Padé approximants,” *Phys. Rev. D* **93** (Apr, 2016) 076004. <https://link.aps.org/doi/10.1103/PhysRevD.93.076004>.
- [257] **LHCb** Collaboration, R. Aaij *et al.*, “Observation of $J/\psi\phi$ structures consistent with exotic states from amplitude analysis of $B^+ \rightarrow J/\psi\phi K^+$ decays,” *Phys. Rev. Lett.* **118** no. 2, (2017) 022003, [arXiv:1606.07895](https://arxiv.org/abs/1606.07895) [hep-ex].
- [258] F.-K. Guo, X.-H. Liu, and S. Sakai, “Threshold cusps and triangle singularities in hadronic reactions,” *Prog. Theor. Phys. in Particle and Nucl. Phys.* **112** (2020) 103757. <https://www.sciencedirect.com/science/article/pii/S0146641020300041>.
- [259] F.-K. Guo, “Triangle Singularities and Charmonium-like XYZ States,” *Nucl. Phys. Rev.* **37** (2020) 406–413, [arXiv:2001.05884](https://arxiv.org/abs/2001.05884) [hep-ph].
- [260] **BABAR** Collaboration, P. del Amo Sanchez *et al.*, “Dalitz plot analysis of $D_s^+ \rightarrow K^+ K^- \pi^+$,” *Phys. Rev. D* **83** (Mar, 2011) 052001. <https://link.aps.org/doi/10.1103/PhysRevD.83.052001>.
- [261] **BESIII** Collaboration, M. Ablikim *et al.*, “Amplitude analysis and branching fraction measurement of $D_s^+ \rightarrow K^+ K^- \pi^+$,” *Phys. Rev. D* **104** (Jul, 2021) 012016. <https://link.aps.org/doi/10.1103/PhysRevD.104.012016>.
- [262] E. Klempt, “Scalar mesons and the fragmented glueball,” *Phys. Lett. B* **820** (2021) 136512. <https://www.sciencedirect.com/science/article/pii/S0370269321004524>.
- [263] **BaBar** Collaboration, J. P. Lees *et al.*, “Light meson spectroscopy from Dalitz plot analyses of η_c decays to $\eta' K^+ K^-$, $\eta' \pi^+ \pi^-$, and $\eta \pi^+ \pi^-$ produced in two-photon interactions,” [arXiv:2106.05157](https://arxiv.org/abs/2106.05157) [hep-ex].

-
- [264] **CLEO** Collaboration, R. A. Briere *et al.*, “Observation of Thirteen New Exclusive Multibody Hadronic Decays of the $\psi(2S)$,” *Phys. Rev. Lett.* **95** (Aug, 2005) 062001. <https://link.aps.org/doi/10.1103/PhysRevLett.95.062001>.
- [265] **BES** Collaboration, J. Z. Bai *et al.*, “ $\psi(2S)$ two- and three-body hadronic decays,” *Phys. Rev. D* **67** (Mar, 2003) 052002. <https://link.aps.org/doi/10.1103/PhysRevD.67.052002>.
- [266] **BESIII** Collaboration, M. Ablikim *et al.*, “Precision Study of $\eta' \rightarrow \gamma\pi^+\pi^-$ Decay Dynamics,” *Phys. Rev. Lett.* **120** (Jun, 2018) 242003. <https://link.aps.org/doi/10.1103/PhysRevLett.120.242003>.
- [267] E. Witten, “Global aspects of current algebra,” *Nucl. Phys. B* **223** no. 2, (1983) 422–432. <https://www.sciencedirect.com/science/article/pii/0550321383900639>.
- [268] Benayoun M. *et al.*, “Experimental evidence for the box anomaly in η/η' decays and the electric charge of quarks,” *Z. Phys. C* **58** no. 1, (1993) 31–53.
- [269] Benayoun M. *et al.*, “A global treatment of VMD physics up to the ϕ ; I: e^+e^- annihilations, anomalies and vector meson partial widths,” *Eur. Phys. J. C* **65** no. 1, (2009) 211.
- [270] **BESIII** Collaboration, M. Ablikim *et al.*, “Branching fraction measurements of χ_{c0} and χ_{c2} to $\pi^0\pi^0$ and $\eta\eta$,” *Phys. Rev. D* **81** (2010) 052005, [arXiv:1001.5360](https://arxiv.org/abs/1001.5360) [hep-ex].
- [271] D. Chuong, B. “The multivariate gaussian distribution,” 2004. <http://cs229.stanford.edu/section/cs229-gaussians.pdf>.
- [272] **BESIII** Collaboration, M. Ablikim *et al.*, “Study of $e^+e^- \rightarrow p\bar{p}\pi^0$ in the vicinity of the $\psi(3770)$,” *Phys. Rev. D* **90** (Aug, 2014) 032007. <https://link.aps.org/doi/10.1103/PhysRevD.90.032007>.
- [273] A. G. Frodesen, O. Skjeggstad, and H. M. Tofte, “Probability and statistics in particle physics,” 1979.

List of Figures

2.1.	Schematic illustration of the Standard Model of Particle Physics.	6
2.2.	Running coupling constant.	9
2.3.	Schematic representation of the nonet of pseudoscalar and vector mesons.	12
2.4.	Schematic representation of the baryon decuplet and the baryon octet.	20
2.5.	Schematic representation of the charmonium spectrum.	21
2.6.	Mandelstam plane.	30
2.7.	Integration contours for the dispersive representation in the complex s -plane.	36
2.8.	Dominant tree-level diagram for the weak transition on the quark level for the decay process $\bar{B}_s^0 \rightarrow J/\psi \pi^+ \pi^-$	39
2.9.	Schematic illustration of the production and decay reference frames.	42
3.1.	Pictures of the BESIII and BEPCII facilities.	47
3.2.	Schematic drawing of the BESIII detector.	48
3.3.	Luminosities of BESIII data sets at center-of-mass energies above 3.7 GeV.	52
4.1.	Schematic representation of the helix parametrization.	57
4.2.	Illustration of the vertex fit for two charged tracks.	58
5.1.	Invariant mass spectrum of ϕ candidates for $e^+e^- \rightarrow \phi K\bar{K}$	64
5.2.	Inclusive Monte Carlo scaling to ϕ and ϕK invariant mass distributions.	65
5.3.	χ_{NC}^2 distributions for $e^+e^- \rightarrow \phi K\bar{K}$	67
5.4.	Invariant mass spectrum of ϕ candidates for $e^+e^- \rightarrow \phi K\bar{K}$ for the integrated data set.	68
5.5.	Invariant mass spectrum of ϕ candidates for data at $\sqrt{s} = 3.7730$ GeV and $\sqrt{s} = 4.2776$ GeV.	69
5.6.	Likelihood scans of the number of observed events at $\sqrt{s} = 3.7730$ GeV and $\sqrt{s} = 4.2776$ GeV.	70
5.7.	Comparison of the efficiencies from PWA and PHSP.	72
5.8.	Momentum distributions of the $K\bar{K}$ system recoiling off the ϕ meson.	73
5.9.	PWA for $e^+e^- \rightarrow \phi K^+ K^-$ at $\sqrt{s} = 4.1784$ GeV.	74
5.10.	PWA for $e^+e^- \rightarrow \phi K_S^0 K_S^0$ at $\sqrt{s} = 4.1784$ GeV.	75
5.11.	Schematic drawings of the main processes included in the measured cross section for the reaction $e^+e^- \rightarrow \phi K\bar{K}$	76

5.12. Fit to the Born cross sections of $e^+e^- \rightarrow \phi K^+K^-$ and $e^+e^- \rightarrow \phi K_S^0 K_S^0$. . .	80
5.13. Comparison of the Born cross sections of $e^+e^- \rightarrow \phi K^+K^-$ and $e^+e^- \rightarrow \phi K_S^0 K_S^0$	80
5.14. Likelihood distributions for a resonant contribution of the $\psi(4230)$ to the Born cross sections of $e^+e^- \rightarrow \phi K\bar{K}$	82
5.15. Upper limit maps for a possible coherent resonant contribution ψ to the Born cross sections of $e^+e^- \rightarrow \phi K\bar{K}$	82
5.16. Systematic studies for $e^+e^- \rightarrow \phi K^+K^-$	85
5.17. Systematic studies for $e^+e^- \rightarrow \phi K_S^0 K_S^0$	86
5.18. A triangle diagram for the reaction $\psi(2S) \rightarrow \phi K\bar{K}$	88
5.19. Invariant mass of the ϕ meson for data at $\sqrt{s} = m_{\psi(2S)}$	90
5.20. Comparison of the branching fractions of $\psi(2S) \rightarrow \phi K^+K^-$	91
5.21. PWA for $e^+e^- \rightarrow \phi K^+K^-$ at $\sqrt{s} = m_{\psi(2S)}$	92
5.22. PWA for $e^+e^- \rightarrow \phi K_S^0 K_S^0$ at $\sqrt{s} = m_{\psi(2S)}$	93
6.1. Invariant mass spectrum of η' candidates for $e^+e^- \rightarrow p\bar{p}\eta'$	96
6.2. Invariant mass spectrum of η' and $p\eta'$ candidates in data compared to inclusive MC.	97
6.3. χ^2_{NC} distributions $e^+e^- \rightarrow p\bar{p}\eta'$	97
6.4. Invariant mass spectrum of η' candidates from $\sqrt{s} = 4.2263$ GeV to $\sqrt{s} = 4.3964$ GeV.	99
6.5. Systematic studies for $e^+e^- \rightarrow p\bar{p}\eta'$	101
6.6. Systematic studies for $e^+e^- \rightarrow p\bar{p}\eta'$	102
6.7. Likelihood scans of the combined Born cross section at $\sqrt{s} = 4.1784$ GeV and $\sqrt{s} = 4.2776$ GeV.	103
6.8. Fit to the Born cross section of $e^+e^- \rightarrow p\bar{p}\eta'$	104
6.9. Likelihood distributions for a resonant contribution of the $\psi(4230)$ to the Born cross section of $e^+e^- \rightarrow p\bar{p}\eta'$	105
6.10. Born cross section of $e^+e^- \rightarrow J/\psi\eta'$ and two-body phase space factors. . .	106
6.11. Maximum likelihood fits to the Born cross section of $e^+e^- \rightarrow p\bar{p}\eta'$ excluding processes with intermediate J/ψ mesons.	107
6.12. Maximum likelihood fits to the Born cross section of $e^+e^- \rightarrow p\bar{p}\eta'$ assuming two- and three-body decays of the $\psi(4160)$ or the $\psi(4230)$	108
6.13. Maximum likelihood fits to the Born cross section of $e^+e^- \rightarrow p\bar{p}\eta'$ assuming two- and three-body decays of the $\psi(4160)$ and the $\psi(4230)$. . .	109
7.1. Invariant mass spectra for $e^+e^- \rightarrow \phi\pi^+\pi^-$	114
A.1. Invariant mass spectrum of ϕ candidates for data from $\sqrt{s} = 3.7730$ GeV to $\sqrt{s} = 4.1784$ GeV.	126

A.2. Invariant mass spectrum of ϕ candidates for data from $\sqrt{s} = 4.1888$ GeV to $\sqrt{s} = 4.2357$ GeV.	127
A.3. Invariant mass spectrum of ϕ candidates for data from $\sqrt{s} = 4.2438$ GeV to $\sqrt{s} = 4.3121$ GeV.	128
A.4. Invariant mass spectrum of ϕ candidates for data from $\sqrt{s} = 4.3374$ GeV to $\sqrt{s} = 4.4671$ GeV.	129
A.5. Invariant mass spectrum of ϕ candidates for data from $\sqrt{s} = 4.5271$ GeV to $\sqrt{s} = 4.6639$ GeV.	130
A.6. Invariant mass spectrum of ϕ candidates for data from $\sqrt{s} = 4.6842$ GeV to $\sqrt{s} = 4.7008$ GeV.	131
A.7. Invariant mass spectrum of ϕ candidates for data from $\sqrt{s} = 3.7730$ GeV to $\sqrt{s} = 4.1784$ GeV.	132
A.8. Invariant mass spectrum of ϕ candidates for data from $\sqrt{s} = 4.1888$ GeV to $\sqrt{s} = 4.2357$ GeV.	133
A.9. Invariant mass spectrum of ϕ candidates for data from $\sqrt{s} = 4.2438$ GeV to $\sqrt{s} = 4.3121$ GeV.	134
A.10. Invariant mass spectrum of ϕ candidates for data from $\sqrt{s} = 4.3374$ GeV to $\sqrt{s} = 4.4671$ GeV.	135
A.11. Invariant mass spectrum of ϕ candidates for data from $\sqrt{s} = 4.5271$ GeV to $\sqrt{s} = 4.6639$ GeV.	136
A.12. Invariant mass spectrum of ϕ candidates for data from $\sqrt{s} = 4.6842$ GeV to $\sqrt{s} = 4.7008$ GeV.	137
A.13. Invariant mass spectrum of $\eta' \rightarrow \eta\pi^+\pi^-$ candidates for all data subsets. .	138
A.14. Invariant mass spectrum of $\eta' \rightarrow \eta\pi^+\pi^-$ candidates for data from $\sqrt{s} =$ 3.7730 GeV to $\sqrt{s} = 4.1888$ GeV.	139
A.15. Invariant mass spectrum of $\eta' \rightarrow \eta\pi^+\pi^-$ candidates for data from $\sqrt{s} =$ 4.1989 GeV to $\sqrt{s} = 4.2438$ GeV.	140
A.16. Invariant mass spectrum of $\eta' \rightarrow \eta\pi^+\pi^-$ candidates for data from $\sqrt{s} =$ 4.2580 GeV to $\sqrt{s} = 4.3374$ GeV.	141
A.17. Invariant mass spectrum of $\eta' \rightarrow \eta\pi^+\pi^-$ candidates for data from $\sqrt{s} =$ 4.3583 GeV to $\sqrt{s} = 4.5271$ GeV.	142
A.18. Invariant mass spectrum of $\eta' \rightarrow \eta\pi^+\pi^-$ candidates for data from $\sqrt{s} =$ 4.5995 GeV to $\sqrt{s} = 4.7008$ GeV.	143
A.19. Invariant mass spectrum of $\eta' \rightarrow \gamma\pi^+\pi^-$ candidates for all data subsets. .	144
A.20. Invariant mass spectrum of $\eta' \rightarrow \gamma\pi^+\pi^-$ candidates for data from $\sqrt{s} =$ 3.7730 GeV to $\sqrt{s} = 4.1888$ GeV.	145
A.21. Invariant mass spectrum of $\eta' \rightarrow \gamma\pi^+\pi^-$ candidates for data from $\sqrt{s} =$ 4.1989 GeV to $\sqrt{s} = 4.2438$ GeV.	146

A.22.Invariant mass spectrum of $\eta' \rightarrow \gamma\pi^+\pi^-$ candidates for data from $\sqrt{s} =$ 4.2580 GeV to $\sqrt{s} = 4.3374$ GeV.	147
A.23.Invariant mass spectrum of $\eta' \rightarrow \gamma\pi^+\pi^-$ candidates for data from $\sqrt{s} =$ 4.3583 GeV to $\sqrt{s} = 4.5271$ GeV.	148
A.24.Invariant mass spectrum of $\eta' \rightarrow \gamma\pi^+\pi^-$ candidates for data from $\sqrt{s} =$ 4.5995 GeV to $\sqrt{s} = 4.7008$ GeV.	149

List of Tables

2.1.	Additive quantum numbers of the quarks.	11
2.2.	Quark content of the lightest pseudoscalar and vector mesons.	13
3.1.	Relevant operational parameters of BEPCII.	46
3.2.	Expected event rates of the BESIII trigger system.	51
4.1.	Branching fractions and reconstruction patterns of the analyzed light hadron final states.	61
5.1.	Inclusive MC events separated in signal and background contributions. . .	66
5.2.	Systematic uncertainties at BESIII for $e^+e^- \rightarrow \phi K\bar{K}$	83
5.3.	Results for $\mathcal{B}r(\psi(2S) \rightarrow \phi K\bar{K})$	90
6.1.	Inclusive MC events separated in signal and background contributions. . .	98
6.2.	Definition of the data subsets.	99
6.3.	Systematic uncertainties at BESIII for $e^+e^- \rightarrow p\bar{p}\eta'$	100
6.4.	Systematic uncertainties for $\eta' \rightarrow \eta\pi^+\pi^-$ and $\eta' \rightarrow \gamma\pi^+\pi^-$	101
6.5.	Comparison of the fits to the Born cross section of $e^+e^- \rightarrow p\bar{p}\eta'$	110
A.1.	Systematic uncertainties for $e^+e^- \rightarrow \phi K^+K^-$	120
A.2.	Results of the Born cross section of $e^+e^- \rightarrow \phi K^+K^-$	121
A.3.	Systematic uncertainties for $e^+e^- \rightarrow \phi K^+K^-$	122
A.4.	Results of the Born cross section of $e^+e^- \rightarrow \phi K_S^0 K_S^0$	123
A.5.	Results of the combined Born cross section for $e^+e^- \rightarrow p\bar{p}\eta'$	124

Who made this work possible

It is time to acknowledge the help I have received and to highlight it as a necessary condition for producing this work. This includes a whole range of people whom I would like to mention by name in the following. Many, many thanks to all of you!

Alfons, for converting me from neutrino physics to hadron spectroscopy. The four years in your working group have been incredibly fun. Not only through regular feedback on the analyses, but also through your trust and mentoring, you have pushed my work forward. **Nyls**, for letting me drive you up the wall. You always tried to get the best out of the students you supervised, no matter how much diligence and effort it took. I appreciate that very much.

Slim, for always being a good sparring partner in the office and, of course, for proofreading most of my work. Without you, everything would have gemacht less sense. **The whole working group now and then** (everyone knows who is meant!), especially CF and Andre, for always providing a working atmosphere in which one — let me put it this way — never gets bored!

Anton & Jochen, for taking over the responsibility as second and third examiner for my dissertation. I hope you liked it.

Christoph & Stefan, for welcoming and mentoring me so nicely in Jülich. I enjoyed the time of my theory project very much.

Karin, for taking the time for our joint project. Unfortunately, the stay in Uppsala was denied. Some systematic uncertainties cannot be eliminated.

The GRK2149, for offering me the position as a doctoral student. Through your program and opportunities provided, I was able to enjoy a unique education.

Hanni, for whatever. Jokes aside — I think a friendship like ours gives someone the support they need for stressful times during the dissertation. Thank you for the wonderful years since the 2nd bachelor semester! Some things last forever. Hopefully this one will too.

My family, which mainly includes Jana, Mum, Dad and my three brothers, for existing. I love you.

Curriculum Vitæ

Personal Details

First Name Johannes
Last Name Bloms
Date of Birth November 30th, 1995
Place of Birth Lingen (Ems), Germany
Nationality German

Academic Education

- Autumn 2020 **Theory project**, Forschungszentrum Jülich, *A new parameterization for the pion vector form factor*, supervised by Prof. Dr. C. Hanhart.
- since 2018 **PhD student**, Westfälische Wilhelms-Universität Münster, *From Exotic Charmonia to Scalar Glueballs - Light Hadron Final States at BESIII*, supervised by Prof. Dr. A. Khoukaz.
- since 2018 **Full member of the Research Training Group (Graduiertenkolleg) 2149 "Strong and Weak Interactions - from Hadrons to Dark Matter"**, Westfälische Wilhelms-Universität Münster, *Journal Club, Student Seminar, GRK Colloquium*.
- 2016–2018 **Master of Science**, Westfälische Wilhelms-Universität Münster, *Search for exotic states in $e^+e^- \rightarrow p\bar{p}\eta$ at center-of-mass energies above 4 GeV at BESIII*, supervised by Prof. Dr. A. Khoukaz.
- 2013–2016 **Bachelor of Science**, Westfälische Wilhelms-Universität Münster, *Kalibration und Dunkelratenmessungen von Photomultipliern für optische Module in IceCube-Gen2*, supervised by Prof. Dr. A. Kappes.
- 2005–2013 **Secondary School**, Gymnasium Marianum Meppen.